TUNING RIGID PARTICLE MOTION IN SIMPLE SHEAR FLOW AND SOFT PARTICLE ON A CURVED SURFACE

A Dissertation

Presented to the Faculty of the Graduate School

of Cornell University

in Partial Fulfillment of the Requirements for the Degree of

Doctor of Philosophy

by

Vikram Singh

August 2013

TUNING RIGID PARTICLE MOTION IN SIMPLE SHEAR FLOW AND SOFT PARTICLE ON A CURVED SURFACE

Vikram Singh, Ph.D.

Cornell University 2013

This thesis focuses on problems in microhydrodynamics involving both rigid and deformable particles. Two problems deal with the rotational behavior of thin particles at low aspect ratio in linear flows. Two other problems focus on studying the collision and aggregation dynamics of non-spherical particles. Another problem involves studying the motion of a deformable particle on a rigid curved surface.

In chapter 2, the ideal collision rate of cylindrical particles of circular cross-section in simple shear flow is studied. The work extends Smoluchowski's results for spherical particles to cylindrical particles. Asymptotic solutions are obtained for collision rate of particles of very large and very low aspect ratio. Numerical simulations are performed to obtain collision rate of particles of finite aspect ratio.

In chapter 3, the rotational behavior of thin disks in linear flow at low Reynolds number is studied. Using numerical simulations and asymptotic analysis, the work estimates the effective aspect ratio of thin particles.

In chapter 4, a class of rigid thin particles is identified which stops rotating in simple shear flow. Numerical simulations and analytical results are used to estimate the aspect ratio at which the particle stops tumbling and the angle at which the particle will align.

In chapter 5, aggregation kinetics of red blood cells in the presence of macro-

molecules is studied. Experiments are performed to study red blood cell dimer formation in microchannels to estimate the dependence of rate constant of aggregation of deformable particles on shear rate and macromolecule concentration.

In chapter 6, dynamics of a deformable particle on a rigid curved surface is studied. It is shown that the colloidal interaction energy of a deformable particle on a rigid surface can be tuned by tuning its curvature. Migration velocity of the particle on the rigid surface due to its change in curvature is estimated analytically in some asymptotic limits.

BIOGRAPHICAL SKETCH

Vikram was born on 16th October, 1984 in Jind, a small town in Haryana. He was soon brought to Delhi by his parents. He spent most of his childhood in one of the most populous and colorful parts of the capital, the old Delhi. In his early days, he got attracted towards the two traditional sporting activities of the region: flying kites and pigeons. He spent most of his childhood flying kites but his inability to whistle never allowed him to rear pigeons.

On the academic front, Vikram showed little interest in math and sciences until calculus and classical physics were introduced in high school. After finishing high school, he joined the Chemical Engineering department at IIT Delhi. At IIT Delhi, he enjoyed studying transport phenomena and pursued a number of projects in fluid mechanics which got him interested in the field. He then joined Cornell University to pursue Ph.D. in chemical engineering and started working with Abe and Don on topics discussed in this thesis.

Having lived in a city of 15 million people and never seen snow in his life, he had reservations about moving to Ithaca. With time though he started enjoying life in Ithaca and considers it at his second home. He is currently reluctantly learning the art of living in the real world.

Dedicated to my parents, Kamal and Kuldeep, and sister, Kamini.

ACKNOWLEDGEMENTS

First and foremost, I would like to thank my advisors: Abe and Don for their help, support and immense patience with me in my research. Their rigor in scientific research and instinct to ask the right question is something I would like to emulate throughout my life. Beyond research, they both have been very inspirational to me in their own ways. I have also learned a lot from numerous lengthy emails from my collaborator Prof. Ganesh Subramanian and would like to thank him for that. I would also like to thank Michael King for serving in my thesis committee and for some very useful comments about this thesis.

I must also thank members of my group, who helped keep me sane in the office. It was an absolute pleasure to work and share office space with them. In particular, I would like to thank Pavithra for sharing the same perils at work and giving me strength in difficult times, Dave and Vinay for keeping the coffee table full of delicacies and teaching me to brew, Ying and Anthony for teaching me how to grow networks, Nak Won for some insightful presentations, Joe and Eugene for being helpful lab and office mates. I would also like to thank other graduate students in the department for their friendly presence.

A number of friends in Ithaca have made the last five years as one of the best time of my life. It's almost impossible to name each and every one of them here. Thanks go to Tushar, Krishna, Rebecca, Ananth, Franny, Sasi, Ami, Sam, Prateek, Hitesh for all the laughs and good times together. Special thanks to Ami for providing bed and breakfast whenever needed. Thanks also go to Taimoor, Goose, and Umang for giving me a hard time at squash. Thanks go to members of Cornell cricket club for keeping cricket alive in Ithaca, and Cornell cinema and Cinemapolis for its great taste in movies.

Special thanks to Jean and Stu for inviting me to all those vegetarian dinners and providing a family away from home.

Thanks also go to my high school teacher, Anil Kumar; my undergrad advisor, Shantanu Roy, and all my other teachers and lecturers for their support and encouragement in my pre-grad school life.

Finally, I would like to thank my family: papa, mummy, and sister for the immense love I have received from them and for an atmosphere at home in which I (almost) never had to worry about doing well or bad.

TABLE OF CONTENTS

LIST OF TABLES

LIST OF FIGURES

CHAPTER 1

INTRODUCTION

Particles in fluid are ubiquitous in industrial, biological and natural systems. Examples include: oil droplets and catalyst particles in fluidized beds, packed beds, liquid crystals, polymer molecules in liquid solutions, gels, red blood cells and blood platelets in blood, microorganisms in fluid, clouds containing small water droplets, aerosols and colloidal suspensions [69, 126, 83, 29, 22, 91, 52, 141, 105] . A good understanding of the motion of particles is fundamental to understand the behavior of these particle laden systems. Of particular interest is the behavior of particles at low Reynolds number (Re) where tiny objects (L) flow at low speeds (u) in a viscous fluid (ν) such that $Re = \frac{uL}{\nu} << 1$. For example, glaciers moving at very low speed, lava flow at high viscosity, and microrganisms movement at small length scale. In low Reynolds number flows, importance of inertial terms is negligible compared to the viscous terms in the Navier-Stokes equations.

In this work, the role of shape and deformability of the particle in tuning its response is studied. The first half of the thesis deals with the behavior of non-spherical particles in linear flow. The particles here are assumed to be rigid, the fluid is assumed to be Newtonian, and the Reynolds number to be small. The motion of the particle is a response to the fluid motion. This study is most relevant to understanding the behavior of dilute suspensions. The next three chapters are devoted to this. In the other half of the thesis, the role of deformability of the particle on its motion on surfaces is studied in the context of self-assembly. The particle motion is no longer in free fluid but on a surface with which it can interact. In particular, migration of deformable particle on curved

surfaces in the presence of colloidal interactions is studied. The driving force for the motion of the particle is no longer external fluid flow but colloidal forces on the surface. The deformability of the particle is used to direct its motion and search for the most stable position. Aggregation of red blood cells is studied experimentally as a particular example of assembly of soft particles.

The general solution approach adopted in all chapters (barring chapter 5) is to use asymptotic and numerical methods. Asymptotic analysis is performed to derive solutions in a limiting case. Numerical computations are performed to aid analytical analysis and in conditions when analytical techniques cannot be applied. The results from the numerical methods can determine under what conditions results from the limiting case no longer hold. A question that one can ask is, what is the benefit of performing asymptotic analysis in a limiting condition when the complete numerical solution can yield results in the non-limiting conditions which is what one needs in most applications? Is asymptotic analysis a useless mathematical exercise made popular in an age when computational tools were not as easily available as today? Although, it is true that the results of asymptotic analysis are valid in some extreme limiting conditions, the value of the analysis lies in understanding the mechanism underlying the physical phenomena in those limiting conditions. Even in the simplified form, the problem has all the relevant elements responsible for the physical phenomena at study, the problem solved via asymptotic analysis is simple but not simpler! Solutions via numerical methods of the complete problem tend to hide the physical mechanism governing the phenomena. By understanding the physical mechanisms through the analysis, the results can be extrapolated to other situations not being solved for. A more detailed discussion of the thesis follows now.

1.1 Rigid non-spherical particles in simple shear flow at low Re number

A number of diverse properties of suspension flows emerge from the dynamics of particles in fluid. Particle size, shape [72, 9, 73], rigidity [29], diffusivity [97, 63], surface, electrical, and magnetic properties [69, 126, 26] can all influence mechanical and transport properties of a suspension. Apart from the size, the shape is another generic feature which can be used to influence fluid property and is not a property of the material of the particle. For example, non-spherical particles can affect the properties of a fluid by degrees of magnitudes compared to spherical particles for the same volume concentration [49, 40] , non-spherical particles can provide directional properties to the fluid [7, 93, 105] and due to the periodic rotational motion, non-spherical particles can also influence properties in a time dependent manner [92].

The central problem in particulate suspension flows is to determine the motion of a particle in fluid flow. Stokes [132] was the first to study the motion of a particle in fluid. Stokes calculated the drag force acting on a spherical particle when it is moving in a stationary fluid. At low Reynolds number, the balance between the drag force and the external force acting on the particle determines the translational velocity of the particle.

Einstein [43] used the motion of a spherical particle in simple shear flow to calculate the viscosity of the suspension at small dilution. A spherical particle in simple shear flow translates with the velocity of the flow at its center and rotates with the angular velocity of the flow. Behavior of non-spherical shapes at low Reynolds number was first studied by Jeffery [72, 41]. Jeffery showed

that the center of the particle translates with the velocity of the fluid and the axis of symmetry of the particle rotates with the angular velocity (figure 1.1):

$$\dot{\mathbf{p}} = p.\omega + \lambda(\mathbf{p}.\mathbf{E} - \mathbf{ppp} : \mathbf{E}), \tag{1.1}$$

where p is the orientation of the axis of symmetry of the particle, ω is the vorticity tensor, $\mathbf{E}$ is the strain tensor, and λ is a constant which depends on the shape of the particle. In terms of velocity $\mathbf{v}$, vorticity and strain tensors are given by:

$$\omega = \nabla\mathbf{v} - \nabla\mathbf{v}^{\mathbf{T}}$$

$$\mathbf{E} = \nabla\mathbf{v} + \nabla\mathbf{v}^{\mathbf{T}}. \tag{1.2}$$

For the case of a spheroid, the constant $\lambda = \frac{\kappa^2-1}{\kappa^2+1}$ where $\kappa = \frac{l}{d}$ is the aspect ratio of the particle with a characteristic length l and a characteristic diameter d. Bretherton [20] later showed that all axis-symmetric particles follow the same equation of motion ((4.1)) as spheroids as long as effective aspect ratio (κ_e) is used instead of aspect ratio (κ) in the definition of λ.

Understanding the motion of a particle in Jeffery orbit is essential to understanding a bulk of the work presented in this thesis. Here we discuss in some details, behavior of a particle following Jeffery rotational motion (4.1). A single particle rotating in a viscous, Newtonian fluid at low Reynolds number follows one of the set of closed Jeffery orbits illustrated in 1.1. Here C is called the orbit constant of the particle, for a non-Brownian particle without any hydrodynamic interactions C depends on the initial orientation of the particle.

One obvious peculiarity in the trajectory of the particle is that although the angular velocity of the undisturbed fluid is only in the z direction, the angular velocity of the axis of the particle has all three components (except when the

particle rotates in the flow gradient plane or is oriented in the vorticity direction). At small aspect ratio, particle move towards the gradient direction when approaching the gradient-vorticity plane and at high aspect ratio particle move towards the flow direction when approaching the flow-vorticity plane. One might ask the question why does the axis of symmetry moves out of one $x - y$ plane to another or what imparts a z velocity to the axis of symmetry when the flow is in the x direction and gradient is in the y direction. The answer to these questions lies in understanding the interaction of the particle with the extensional component of the flow. The rotational component of simple shear flow does not make the particle move across the $x - y$ planes as it does not produce any strain. On the other hand, extensional flow has a non-zero strain component which tries to deform the particle and the particle resists this deformation. The movement across the $x - y$ plane is then a resultant of the flow trying to deform the particle and the particle trying to resist the deformation. The result of this is the movement of the particle across the $x - y$ planes. In (4.1), $\mathbf{ppp} : \mathbf{E}$ term, which clearly depends on the extensional flow, gives rise to a non-zero velocity of the axis of symmetry in the z direction.

Another thing to note in the rotational motion of the particle, which is not evident in figure 1.1, is the magnitude of the angular velocity at different points in the trajectory of the particle. The long axis of the particle spends more time aligned in the flow-vorticity plane i.e for a fiber the axis of symmetry spends more time aligned in the flow direction and for a disk the axis of symmetry spends more time aligned in the gradient direction. The particle spends minimum amount of time with its long axis in the gradient direction. This change in angular velocity with orientation could be understood by the torque or the angular velocity induced by the extensional component of the flow on the particle

since the angular velocity induced by the rotational component is constant. Extensional flow when acting alone tries to orient the particle along the principal direction of the flow. When the particle is oriented along these principal directions, net torque due to extensional flow acting on the particle is zero. On the other hand, when the particle is oriented at an angle $\pm\pi/4$ ($\mathbf{e}_x$ or $\mathbf{e}_y$) to the principal direction of extensional flow, the torque acting on the particle due to the extensional flow is maximum. The direction of the torque due to the extensional flow is along the vorticity direction when the long axis is closer to the gradient direction and the direction of the torque is opposite to the vorticity direction when the long axis is closer to the flow direction. Since the angular velocity of the particle is constant in an orbit due to the rotational component of the shear flow and is always in the vorticity direction, the overall angular velocity of the particle is minimum when the long axis of the particle is in the flow direction where the torque acting on it due to the extensional component of the flow is maximum and is in a direction opposite to the vorticity direction.

Since the work of Jeffery and Bretherton a lot of work has been done to understand motion of non-spherical particles at low Reynolds number [16, 19, 17, 64, 80, 54]. Apart from spheroidal shape particles, the other particle shapes that have been analytically rigorously studied are long slender shape particles with different type of cross sections. Slender body theory used to study these particles of large aspect ratio with variable cross section [6, 34]. Simulation techniques like Stokesian dynamics [15] has been used extensively recently to study non spherical particles [150, 32, 104]. In this work we use boundary element method and perturbation methods to study low aspect ratio particle motion.

The next three chapters of the thesis are devoted to understanding different aspects of rigid non-spherical particles at low Re number. In all these studies no colloidal or hydrodynamic interactions are taken into account.

In chapter two, the ideal collision rate of cylindrical particles is studied. The calculations shown here are along the lines of the work done by Smoluchowski [146] for spherical particles about 100 years ago. The ideal collision rate for cylindrical particles is calculated over a broad range of particle aspect ratios κ defined as the ratio of length to diameter. Unlike spherical shape particles, for cylindrical particles rotation motion plays an important role in determining their collision rate. Monte Carlo simulations are performed with initial relative positions and orientations that model the rate of approach of non-interacting particles following Jeffery orbits with several choices of the orbit distribution. A collision is detected when two particles overlap geometrically. Using asymptotic analysis, scaling of collision rate at high and low aspect ratio is derived and verified with simulation results. In addition to deriving the total collision rate, collisions are characterized as side-side, edge-side and face-edge based on the initial point of contact.

In the third and fourth chapter, motion of axis-symmetric particles at low aspect ratio in simple shear flow is studied. It is interesting that despite so much work done in the field of single particle motion [95] in Stokes flow, the motion of particles at low aspect ratio is still unknown. In Stokes flow, for any shape axis-symmetric particle center with the fluid velocity and motion of axis of symmetry depends on the exact shape of the particle. Bretherton [72, 20] showed that the rotational motion of all axis-symmetric particles in linear flows can be described based on its shape using only one constant called effective aspect ratio, κ_e. Here,

the effective aspect ratio is defined as the aspect ratio of the spheroid having the same period of rotation as the particle.

In chapter three, the motion of thin disks of shapes given by a family of shapes is studied and the dependence of the effective aspect ratio, κ_e on the actual aspect ratio of the particle is derived using asymptotic analysis aided by boundary element simulations. For certain shapes, it is shown that the rotation rate of the particle to the leading order is governed by the shape of the edge. Cylindrical thin disk is one particular shape of interest for which effective aspect ratio is determined.

In chapter four, a special case of motion of a particle at low aspect ratio is studied. As mentioned above, most particles in simple shear flow undergo rotation motion in the vorticity direction and the rate of this rotational motion can be tuned by changing the shape of the particle. But surprisingly it is not known if there are any particles which can stop rotating and align in simple shear flow at finite aspect ratio. Though particle alignment can be achieved for droplets [142], vesicles with fluid or with solid inclusions [39, 75, 88], for fibers due to steric effects[114] or electrostatic interactions [27], and for organisms like chlamydomonas [122] in simple shear flow. Alignment of particles can also be achieved in flows where the magnitude of the extensional component of the flow is more than the rotational component [53]. But there are no known rigid particles which can align in simple shear flow without any interparticle or external interactions. In this chapter, a ring shape particle with some characteristic family of shape of the cross-section which can stop rotating in simple shear flow in presented.

1.2 Assembly of soft particles

Self assembly is the process of organization of small building blocks into well-defined larger structures without any external intervention. A typical self assembly process has two characteristics : 1) presence of a sampling mechanism, which helps in sampling of the entire configuration space of the system and 2) presence of a binding mechanism, which determines the most favorable configuration of assembly. The building blocks for self assembly may comprise atoms, molecules, colloids and macroscopic objects. At sub micron scale strong Brownian forces serve the purpose of a sampling mechanism and weak non covalent interactions like van der Waal, electrostatic forces, hydrogen bonds, hydrophobic forces etc act as a binding force. Inherent to this description is a powerful bottom-up approach for assembling matter, which is driven at least in part by non-covalent interactions and enables the synthesis of complex architectures with little to no waste. The reversible aspect of the synthesis is critical because it allows the system to correct misassembled building blocks by essentially reverting that portion back to the disassembled state and reassembling. To keep the assembly reversible, it is necessary that the energy associated with the binding mechanism and the sampling mechanism are of the same order. Traditionally self assembly has been very successful with building blocks smaller than $1\mu m$. At meso and macroscale ($> 1\mu m$), due to the absence of any natural sampling mechanism like Brownian motion, self assembly is much more challenging. Only a very careful control of interactions and external sampling mechanisms can lead to self assembly.

In chapter five and six of the thesis, example of using deformability as a sampling mechanism for self assembly is studied. To deform a material from

its equilibrium shape some amount of work needs to be done which is stored as potential energy for elastic materials. This increase in the potential energy is compensated by the decrease in the colloidal surface energy where the surface area is provided by the deformation of the material. This gives deformable particles a means to sample its environment (of the order of size of the particle) to find the the minimum energy state.

In chapter five, assembly of red blood cells is discussed. Red blood cell (rbc) aggregation is unique in the sense that rbcs form well defined linear stack coin like structures upon aggregation where as other rigid particle systems undergoing aggregation with a particle size of the range of rbcs form random structures. The well defined structures formed during rbc aggregation are not expected for particle size larger than few microns (meso scale) as they are too big to undergo significant Brownian motion which is generally important to search for the minimum energy state in an aggregate. For the case of rbc aggregation though, the high deformability [131] of the cells allow the particles to form minimum energy structures after aggregation. The objective of this work is to use rbc as a model system to understand kinetics of assembly of soft particles in simple shear flow. Experiments are done with horse red blood cells at different shear rates to understand the role of hydrodynamics in aggregation. The scaling of the aggregation rate constant of a rbc dimer formation with respect to shear rate is determined for different binding forces by changing the concentration of polymer solution. The dependence of the rate constant to shear rate is compared with that of non-deformable particles. It is shown that the dependence of collision efficiency of soft particles on the shear rate is weaker than that of hard colloids with van der Waal interactions [38] or depletion interactions [1].

In chapter six, an analogous problem on migration of a particle (vesicle) aided by its deformability on a rigid curved surface is studied. A deformable particle undergoing attractive colloidal interactions with a surface tries to maximize its area of contact. It is shown that the energy of interaction decreases with increase in the curvature of the rigid surface. This change in energy of the vesicle can be used to move the particle from low to high curvatures on the rigid surface. Interesting asymptotic results are presented in the limit when the colloidal interaction energy is large compared to the bending energy and curvature of the rigid surface and the area of interaction between the particle and surface are small. In particular, migration velocity of the particle on the surface is estimated.

Figure 1.1: Jeffery's orbits for various orbit constants for a particle of κ = 10. In all orbits, the particle moves towards the flow direction when approaching the flow vorticity plane.

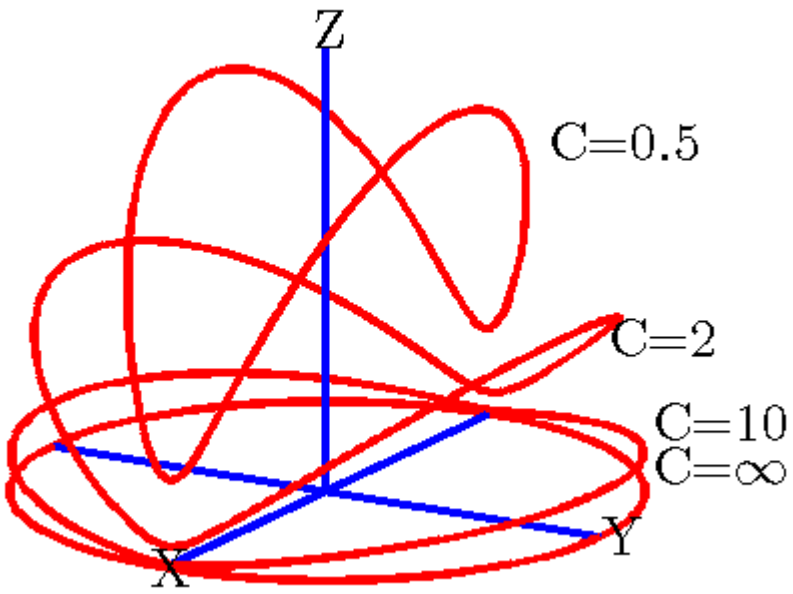

CHAPTER 2

IDEAL RATE OF COLLISION OF CYLINDERS IN SIMPLE SHEAR FLOW

The collision of particles influences the behavior of suspensions through the formation of aggregates for adhesive particles or through the contributions of solid-body contacts to the stress for non-adhesive particles. The simplest estimate of the collision rate, termed the ideal collision rate, is obtained when particles translate and rotate with the flow but have no hydrodynamic or colloidal interactions. Smoluchowski calculated the ideal collision frequency of spherical particles in 1917. So far little work has been done to understand rate of collision for non-spherical particles. In this work, we calculate the ideal collision rate for cylindrical particles over a broad range of particle aspect ratios r defined as the ratio of length to diameter. Monte Carlo simulations are performed with initial relative positions and orientations that model the rate of approach of non-interacting particles following Jeffery orbits with several choices of the orbit distribution. The role of rotational motion of particles on collision frequency is elucidated by comparing the ideal collision rate calculations with similar calculations for non-rotating particles. It is shown that the ratio of the collision rate of cylinders to that of spheres that circumscribe the cylinders is proportional to $1/rr_e$ for $r >> 1$ and r_e for $r << 1$. Here, r_e is the effective aspect ratio defined as the aspect ratio of a spheroid having the same period of rotation as the cylinder. The effective aspect ratio of the cylindrical particles was determined using finite element calculations of the torque on non-rotating cylinders with their axes parallel to the velocity and velocity gradient directions. In addition to deriving the total collision rate, we categorize collisions as side-side, edge-side and face-edge based on the initial point of contact. Most collisions are found to be side-edge for $r \gg 1$ and face-edge for $r \ll 1$, suggesting that nonlinear aggregates will

develop if particles stick at the point of first contact.

2.1 Introduction

Particulate flows involving cylindrical particles are encountered in a variety of contexts: clay particles in drilling mud, glass-fiber-filled thermoplastics, fibers in paper manufacturing, fibers and disks in gelation applications, red blood cells, and blood platelets [56, 91]. At small concentrations, well stabilized particles do not interact with one another and contribute to the properties of bulk suspensions in proportion to their volume fraction [44, 18]. At higher concentration, hydrodynamic interactions and collisions between particles start influencing the behavior of the suspension [103, 9]. Collisions of two particles in a suspension could either lead to a non-adhesive contact with contact forces that influence the bulk stress or adhesive contacts leading to the formation of permanent aggregates. In this work we calculate the ideal rate of collision of cylindrical particles in simple shear flow using numerical simulations. This work extends the classical result of Smoluchowski [146] for spheres in shear flow to cylindrical particles in shear flow.

The rate of collisions per unit volume per unit time in a suspension of singlet particles with number concentration, n, is given by:

$$J = kn^2, \tag{2.1}$$

where k is the collision rate constant that depends on the driving force pushing the particles together, the particle geometry, and the interparticle interactions. A fundamental assumption leading to this equation is that collision is a second-order rate process, in which the rate is proportional to the product of the concentrations of two colliding species. This assumption breaks down

for dense systems. Collisions can be driven by various mechanisms, such as Brownian motion, shear flow, or differential settling. The most important difference in rate constants obtained from these different transport mechanisms is the dependence on size. In the presence of all three mechanisms, size can determine the dominant mechanism for collision of particles. For spherical particles, this dependence is well known, but for cylinders undergoing Brownian motion[118, 144] , results are known only in the limiting case of low (disks) and high (fibers) aspect ratio. The calculation of a collision rate for sedimenting cylinders would be complicated by the fact that a homogeneous suspension of sedimenting non-spherical particles is known to be unstable to variations in particle concentration [82, 62].

In sheared suspensions of cylinders, mechanical contacts between the particles can significantly increase the average stress of the suspension. While lubrication forces prevent contact between pairs of smooth particles in dilute suspensions, the sharp edges of cylinders can allow interparticle contact to occur. Simulations have explored the effects of mechanical contact in the limiting case of cylinders of high aspect ratio [138, 102], but no general results have been presented for cylindrical particles. An estimate of the stress contribution from collisions can be obtained from a product of the rate of collision of particles and the time integral of the stresslet over a single collision. A similar strategy can also be used to estimate the stress contribution when there are hydrodynamic and colloidal interactions between the particles without any mechanical contact [9, 126]. Apart from the increase in interparticle interactions, the collision of particles can also lead to aggregation. This aggregation can further affect the properties of the suspension [26, 55] by changing the size distribution of the particles.

To describe the kinetics of aggregation processes, Smoluchowski developed a generic second order rate equation assuming that only binary collisions lead to aggregation:

$$\frac{dn_i}{dt} = \frac{1}{2}\sum_{k=1}^{i-1}\sum_{j=i-k} k_{jk}p_{jk}n_j n_k - \sum_{j=1}^{\infty} k_{ij}p_{ij}n_i n_j, \tag{2.2}$$

where n_i is the number of aggregates of size i per unit volume, k_{ij} is the ideal rate constant for collision of aggregates of size i and j, and p_{ij} is the collision efficiency of aggregates of size i and j. The ideal rate constant characterizes collisions in the absence of particle interactions, while the collision efficiency is the ratio of the collision rates in the presence and absence of hydrodynamic and colloidal interactions. The primary contribution of the present paper is to predict the rate constant k_{11} for collision of two singlet cylinders to form a doublet facilitating the description of the initial stages of aggregation when particle interactions are neglected . When the particle size is more than 1 μm and the density difference between the fluid and the particle is small, shear is the dominant mechanism driving collisions. For the case of shear induced collision of spherical particles undergoing van der Waal attractions and hydrodynamic interactions, the collision efficiency, p, for doublet formation is given by de Ven and Mason[38].

The description of the later stages of aggregation is more complex. In principle, the change in the aggregate size distribution can be predicted from the Smoluchowski equation if p_{ij} is known. In practice, as the size and shape of aggregates evolves, values of the rate constant are not available except in the case of liquid droplets, where coalescence leads to a change in size but preserves the shape. When the shape of the aggregate is not preserved, a fractal dimension is commonly used to describe the size of the aggregate as a function of number of particles in the aggregate. A fractal dimension close to 1 means the aggregate

is more like a cylinder and a fractal dimension of 3 corresponds to a spherical geometry. For simplicity, the rate constant for the aggregation of fractals is generally estimated to be equal to that of the spheres that circumscribe the fractal clusters. This approximation is made even for aggregates with low fractal dimension. For example, in the aggregation of red blood cells (RBCs), disks of RBCs aggregate to form stacked coin like structures of different aspect ratio but maintain the original cylindrical geometry. Even in this case, the rate constant has been calculated using the results for a sphere [101]. Calculations of the ideal collision rate presented here for cylindrical particles could be used in cases like the aggregation of RBCs in which the fractal dimension remains close to one. In the more general case, one might use the collision rates of circumscribing spheres and of cylinders having lengths equal to the cluster diameters as upper and lower bounds on the actual collision rate of two clusters.

Calculation of the ideal collision rate constant has been known for spherical particles for about a century, but there are no analogous results for cylindrical particles. The rotational motion of cylindrical particles in shear flow combined with their relatively complex geometry makes it difficult to estimate collision rates analytically. Spherical particles also undergo rotational motion in simple shear flow, but due to their symmetric geometry about all axes passing through their center, the rotational motion does not affect collision rate. In this paper, we calculate the ideal collision rate of cylindrical particles undergoing rotational motion in simple shear flow using numerical simulations (Figure 2.1). Jeffery's [72, 20] solution for the motion of force- and torque-free rigid axisymmetric particles in a uniform shear flow of a Newtonian fluid is used to describe the rotational motion of cylindrical particles.

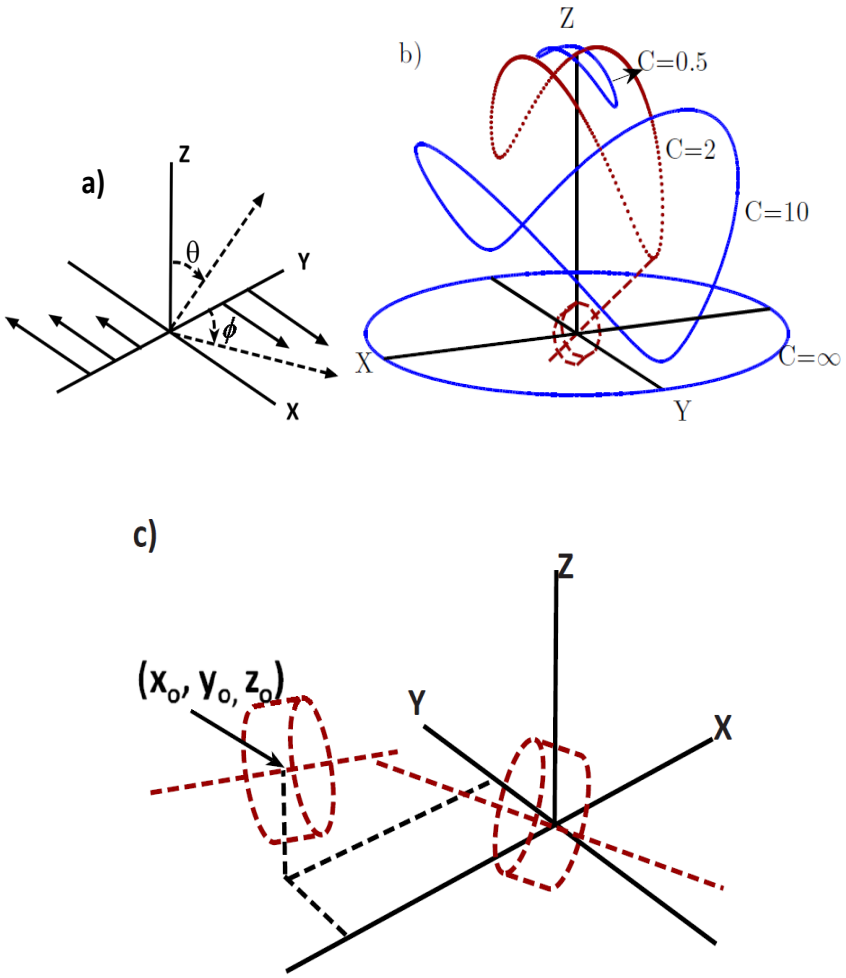

Figure 2.1: (a) Spherical coordinate system for a particle centered at the origin and subjected to a simple shear flow in the x-y plane. (b) Jeffery's orbits for various orbit constants for aspect ratio of 0.1. At small aspect ratios, the particle's axis of symmetry moves towards the gradient direction when approaching the gradient-vorticity plane and at high aspect ratio the particle's axis tends to move towards the flow direction when approaching the flow-vorticity plane.(c) Schematic diagram of the collision process between two cylindrical particles in simple shear flow.

Apart from calculating the collision frequency we have also characterized collisions as side-side (Figure 2.2 (b)), side-edge (Figure 2.2 (c, e)), or face-edge (Figure 2.2 (d, f)), depending on the point of contact of the particles at the time of first contact. The point of contact could be of interest in problems involving particles with asymmetric surface properties. For example, clay particles under appropriate conditions have different surface charge densities on their flat and lateral surfaces [141] and hence can form only side-face aggregates when surface charge effects dominate over van der Waal forces. Thus, due to heterogeneous surface properties, there could be a different collision efficiency for different types of collisions. Particles having uniform surface properties can also have different collision efficiencies depending on the point of contact. Certain types of collisions will lead to stronger colloidal interaction at the time of collision; the relative orientation during a collision along with the aspect ratio of the particles will influence the likelihood that aggregation will occur. For example, in systems involving attractive colloidal forces, the collision efficiency will be high for collisions of the flat faces of cylinders as the colloidal forces will be acting over a larger surface area during collision. Badaire et al. [4] showed that for cylindrical colloids experiencing polymer depletion mediated attractive forces the energy reduction due to aggregation of cylindrical particles in different orientations changed with changes in aspect ratio. In general, both aspect ratio and the length scale associated with the attractive force determine whether face-face, side-face or side-side aggregates are favored. Momentum transfer by contacts could also be affected by the orientation of the particle at collision. For example, high aspect ratio fibers undergo face-face collisions when they are aligned and side-edge or side-side collisions when one fiber is flipping. The side-side and side-edge collisions between flipping fibers have higher relative velocities

leading to larger collisional stresses.

2.2 Problem Formulation

The force-free, torque-free particles are suspended in a simple shear flow whose velocity components in a Cartesian coordinate system are given by -

$$v_x = \gamma y, v_y = 0, v_z = 0, \tag{2.3}$$

where, v_x, v_y and v_z are the velocity components of the fluid in the Cartesian coordinate system defined in Figure 2.1 (a), and γ is the shear rate. In the absence particle interactions, simple shear flow can bring the particles together, resulting in collisions. Smoluchowski derived the rate of collision of spherical particles of diameter D in simple shear flow, assuming particles follow straight fluid streamlines. The collision frequency in this case can be calculated by considering a stationary particle at the origin and calculating the flux of the particles passing through a circle of diameter $2D$ which is the projection of the excluded volume of the particle onto the yz plane. The area of this circle is called the collision cross-section. The resulting rate constant for binary collisions of spheres in simple shear flow is:

$$k_s = \frac{4}{3}\gamma D^3. \tag{2.4}$$

The rate constant of collision for cylindrical particles in theory can also be calculated in a similar manner, i.e. calculating the flux of the particles crossing the collision cross-section and then equating it to the second order rate law. However, this calculation is difficult as cylindrical particles undergo rotational motion in shear flow. An analytical expression is available for the rotational

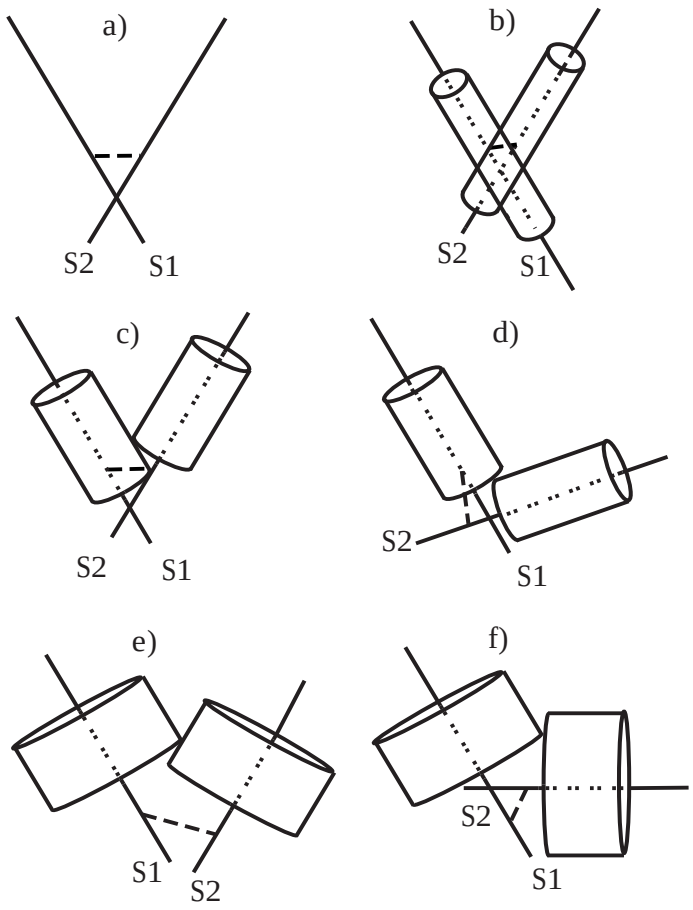

Figure 2.2: Schematic diagram of the type of collisions and the algorithm used for detection of collision between cylinders. a) Distance between the axes as the first step in determining collision. b) Side-side collision when both cylinders are On. c) Side-edge collision when one cylinder is On and other is Off. d) Face-edge collision when one cylinder is On and other is Off. e) Side-edge collision when both cylinders are Off. f) Face-edge collision when both cylinders are Off.

motion, but the analytical calculation would involve a five-dimensional integral in the space of the relative position and orientations of the particles. We have chosen instead to use Monte Carlo simulations to calculate the rate constant for cylindrical particles. Since we already know the solution for a sphere, we choose it as a comparison case for our simulations. We express the rate constant of collision of cylindrical particles in terms of the rate constant of collision for two spherical particles that circumscribe the cylindrical particles:

$$k = fk_s = f\frac{4}{3}\gamma D^3, \tag{2.5}$$

where f is a fractional collision frequency and D is the diameter of the circumscribing sphere which is given by $(L^2 + d^2)^{\frac{1}{2}}$ for a cylinder of diameter, d and length, L. This fraction, f is a function of the aspect ratio of the particle and also depends on the nature of the particles' rotational motions.

The equations of rotational motion for spheroidal particles in simple shear flow were first derived by Jeffery [72]. Although the original derivation was for spheroidal particles, Bretherton [20] later showed that the same equations are valid for all axisymmetric particles as long as the aspect ratio, $r = \frac{L}{d}$ of the spheroidal particles in the equation of motion is replaced by an effective aspect ratio, r_e, of the axisymmetric particle. The general equations of motion for axisymmetric particles in simple shear flow is then given by:

$$\tan(\theta) = \frac{Cr_e}{(r_e^2 cos^2\phi + \sin^2\phi)^{\frac{1}{2}}}, \tag{2.6}$$

$$\tan(\phi) = r_e \tan(\frac{\gamma t}{r_e + r_e^{-1}} + \kappa), \tag{2.7}$$

where θ is the angle of the particle orientation relative to the vorticity direction and ϕ is the angle of the projection of the particle orientation into the flow-gradient plane relative to the velocity gradient direction (see Figure 2.1 (a)).

Here, κ is the phase angle, and C the orbit constant. For a spheroidal particle r_e in the above equations is equal to r. In general the effective aspect ratio, r_e depends on the shape of the particle and can be determined by solving the flow problem around the particle. Effective aspect ratio values used in the simulations performed here are obtained by simulating fluid flow around stationary cylindrical particles in simple shear flow using Comsol 3.5 software as explained in the simulation section of the paper.

In Jeffery's rotational motion, a particle's center translates with the velocity of the fluid and the axis of symmetry rotates in a periodic motion in one of an infinite set of possible orbits (Figure 2.1 (b)). The location of the particle's orientation along the orbit at $t = 0$ can be characterized by a phase angle. According to Jeffery's equation of rotational motion, particles remain in the same orbit with the same phase angle indefinitely. Therefore, the orbit that a particle is going to follow is purely determined by the initial orientation of the particle and hence depends on how the particles were initially suspended. Jeffery's analysis neglects Brownian motion and hydrodynamic interactions among the particles. If the particle size is small, Brownian diffusion can lead to changes in a particle's orbit and eventually gives an orbit distribution that is completely independent of initial conditions. Leal and Hinch [97] have analytically determined the orbit distributions for particles undergoing weak Brownian motion. Jeffery postulated an orbit distribution that would result from an initially isotropic orientation distribution. Such an initial condition would lead to a non-uniformly distributed phase angle and a time-dependent orientation distribution. However, phase mixing due to a small polydispersity of aspect ratio can quickly remove this time dependence. In the experiment on dilute sheared fiber suspensions by Ankzuorowski and Mason[2], this initial phase mixing occurs within about 3

Jeffery periods and is followed by a much slower change in the orbit distribution due to hydrodynamic interactions. In the present work, we consider the following steady orientation distributions while calculating the collision frequency: 1) Jeffery orbit distribution with a uniform phase angle. and 2) Leal and Hinch orbit distribution for weakly Brownian particles. When we do not specify the orbit distribution explicitly we will use the Jeffery orbit distribution. To further illustrate the effect of orbit distribution on collision rate, two other extreme cases have been studied: 3) All particles in $C = 0$ orbit which corresponds to the alignment of the symmetry axis in the vorticity direction (log rolling) and 4) All particles in $C = \infty$ orbit which corresponds to the motion of the symmetry axis in the flow-gradient plane. The latter cases are of interest because particles have been observed to migrate into these extreme orbits when weak viscoelastic or inertial effects are important. In the presence of weak viscoelastic or inertial effects, particles still undergo approximate Jeffery orbits, but they drift slowly across orbits of different orbit constant. For the case of slender bodies, orbital drift towards the vorticity direction is observed due to elastic effects [50, 94, 60] and towards the shear gradient plane due to inertial effects [77, 136]. For oblate spheroids, orbit drift towards the vorticity direction is observed due to inertial effects [77] and towards the shear gradient plane is reported due to elastic effects [50]. Only the motion of individual particles is taken into account in these simulations without considering hydrodynamic and colloidal interactions.

Apart from obtaining f, we have also characterized the collisions based on the first point of contact between the colliding cylinders. We have broadly identified three types of points on a cylinder: points on the lateral surface (side points), points on the flat face (face points), and points on the rim joining the flat surface and the curved surface (edge points). Based on this classification of

points on the cylinder, all collisions have been categorized into three types:
1) Side-side (Figure 2.2 (b)): The lateral surfaces of the two cylinders come into contact. This type of collision is more prominent for high aspect ratio particles with large lateral surface area.
2) Side-edge (Figure 2.2 (c, e)): This includes collisions in which the lateral surface area of one cylinder comes into contact with the edge of the other cylinder. This type of collision is also more prominent at large aspect ratio. At large aspect ratio, as shown later, rotational motion of the particle determines whether side-side or side-edge collisions will dominate.
3) Face-edge (Figure 2.2 (d, f)): This group includes collisions in which the flat surface of one cylinder comes into contact with edge points on the other cylinder. This type of collision is more prominent for particles of low aspect ratio for which a large flat surface area is available for collision.

We note that there are no face-face collisions tracked here because for a face-face collision to occur, both cylinders need to be exactly parallel to each other. There are also no face-side collisions because these require the cylinders to be exactly perpendicular to each other. The probability of two cylinders to be exactly parallel or perpendicular is infinitesimally small. The classification of collisions presented above is valid only when cylinders have sharp edges. For particles with rounded edges, there is no distinct edge. In the limiting case of very high aspect ratio, edge points might be considered part of the face or end of the fiber. At low aspect ratio, edge point might be considered a part of the lateral surface area.

2.3 Simulation

This section is divided into two parts: in the first we explain how the effective aspect ratio of cylindrical particles is obtained using finite element simulations (Comsol 3.5), and in the second we explain the Monte Carlo simulation procedure for calculating the fractional collision frequency.

(I) Effective aspect ratio calculations

Jeffery's equations of rotational motion (2.6, 2.7) for cylinders are valid as long as an effective aspect ratio, r_e, for cylinders is used in place of the actual aspect ratio. Cox [34] showed using Jeffery's solutions that the effective aspect ratio for any axisymmetric body can be obtained in terms of the torques, T_x and T_y, acting on a non-rotating particle when the particle's axis is oriented in the flow (or x) and velocity gradient (or y) direction, respectively:

$$r_e = (\frac{T_x}{T_y})^{\frac{1}{2}} \tag{2.8}$$

We used this result to determine the effective aspect ratio of cylinders with a range of aspect ratios. The torques were computed by solving Stokes equations in the geometries illustrated in Figure 2.3 using the finite element commercial software Comsol 3.5. We used the symmetry of the problem under reflection through the plane $z = 0$ to reduce the size of the domain by half. The outer boundaries of the domain enclosing the particle were at least five times the largest dimension of the cylinder. We found that further increasing the size of the domain changed the torque insignificantly. For all simulations the largest mesh size used on the surface of the particle was smaller than the size of the smallest dimension of the cylinder. The boundary conditions used for the problem are as follows: The inlet and outlet boundaries (planes 1 and 6) were specified with a constant pressure, $P = 0$ which ensures that pressure is not a driving

force. The top and bottom walls (planes 2 and 5) were moved with velocity $+Y$ and $-Y$ to create a simple shear flow with shear rate, $\gamma = 1$ where Y is the half side length of the domain in y direction. Symmetry boundary conditions were applied on the planes 3 and 4, specifying that there is no velocity component perpendicular to the planes and no shear stress acting on the planes. These conditions are satisfied exactly on the plane of symmetry (3) of the problem and approximately on the far-field planar boundary (4) that is parallel to the flow-gradient plane.

(II) Collision frequency calculations

Monte carlo simulations were used to determine the fractional collision frequency, f of cylindrical particles. In each computation a pair of cylindrical particles was initialized. Assuming that the center of mass of the particle follows fluid streamlines, 2.3 was used for the translation motion and 2.6 and 2.7 were used for the rotational motion of the axis of symmetry of the particle. A check was performed at each time step to determine if there was a collision. A large number of such computations were performed from which f was determined by calculating the ratio of the total number of collisions to the total number of trajectories calculated.

The basic strategy behind initialization (Figure 2.1 (c)) was that all the possible base cases were included that model the rate of approach of non-interacting particles following Jeffery orbits with several choices of the orbit distribution. The initialization process involved specifying the positions of the centers of mass and the initial orientations of the particles. One particle was placed at the origin, while the other particle position was chosen such that the spheres circumscribing the two particles would collide with a probability 1 in simple shear

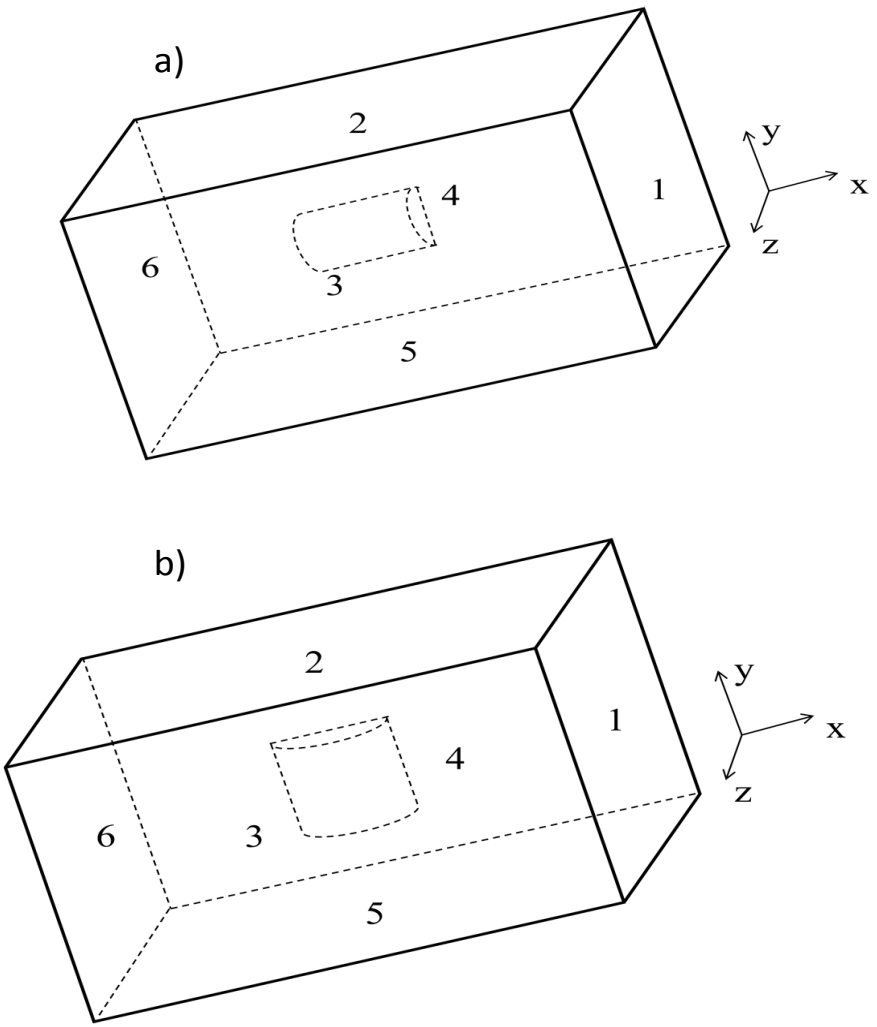

Figure 2.3: Geometry used for the calculation of the torque on a cylinder in Comsol 3.5. Reflection symmetry around the $z = 0$ plane was used. The total torque acting on the particle is twice the torque obtained from these simulations. a) Cylinder with its axis in the direction of flow. b) Cylinder with its axis in the velocity gradient direction.

flow. The initial position of the center of mass of the second particle (x_o, y_o, z_o) was chosen with $x_o = -D$. The position of the second particle within the collision cross-section was chosen from a region $z_o^2 + y_o^2 < D^2$ with a probability weighted by y_0 to account for the variation of the flux of particles due to the simple shear translational motion. Equivalent results would have been obtained by choosing any position further upstream, $x_o \leq -D$. No collision can occur between particles separated by a distance larger than D and the orientation distributions of the particles before collision are time independent.

The initial orientation was picked independently for each particle by following the following procedure. The orientation was chosen by picking the orbit constant C and the phase angle κ in the Jeffery rotational motion equations (2.6,2.7). The phase angle was chosen at random from 0 to 2π, a requirement for obtaining a time independent orientation distribution. Leal and Hinch's orbit distribution [97] was specified by the probability distribution derived in their paper. For the Jeffery orbit distribution, we generated an orientation at random on the unit sphere and specified the particle orbit constant C corresponding to this initial orientation from 2.6. We also considered cases where all particles were chosen to have $C = 0$ or $C = \infty$ with randomly chosen phase angle. In addition, to highlight the role of Jeffery rotation in influencing the collision efficiency, we have computed the collision efficiency of particles that translate with a simple shear flow but have an isotropic orientation distribution and do not rotate with the flow.

Once the initialization was complete the motion of the particles was determined using the equations of motion. The centers of the particles were moved based on the simple shear flow and the orientations were changed based on

Jeffery's solution using a short time step, dt. This process was continued until either a collision was detected or the center of mass reached $x_0 = D$ beyond which no collision would be possible. To obtain statistically accurate results, a sufficient number of trials were performed so that at least 10^4 collisions were detected; this sample size corresponds to a statistical error of about 1%. In all the results presented here, $dt < \frac{r}{10}$ for aspect ratios smaller than 1 and $dt < \frac{1}{10r}$ for aspect ratios larger than 1 was used. Decreasing dt further by a factor of 5 did not result in a significant change in collision frequency with the maximum change being 2%.

Collision detection was carried out using the algorithm proposed by Ketchel and Larochelle [79] which uses line geometry to determine whether two cylindrical particles have collided or not. The same algorithm [79] was also used for determining the type of collisions, i.e. whether the collision was side-side, side-edge or face-edge although in the paper they don't explicitly say when a collision is any of these types. A short summary of the algorithm is as follows. The first step in detecting the collision between the cylinders was to determine the shortest distance between the axes of the cylinders (Figure 2.2 (a)). If the shortest distance between the two axes (S1,S2) was less than the sum of the radii of the cylinders, the possibility of a collision was considered. If the point of shortest distance (N1 or N2) lies within the line segment in the cylinder, the cylinder was denoted as an On cylinder otherwise it was called an Off cylinder. This distinction resulted in three possible cases: both cylinders On, one cylinder On and the other cylinder Off, and both cylinders Off in which case they were called Off1 and Off2. If both the cylinders were On, then a side-side collision between the cylinders was detected (Figure 2.2 (b)). If only one cylinder was On, then side-side contact of the cylinders was not possible and the distance

between the axes of the cylinder was no longer sufficient to determine whether a collision had occurred. Instead, the shortest distance between the edge of the Off cylinder and axis of the On cylinder was calculated. If this distance was less than the radius of the Off cylinder then a possibility of a collision was considered. If the point of shortest distance on the axis of the On cylinder lay inside the cylinder then a side-edge (Figure 2.2 (c)) collision was detected. Otherwise a check for the intersection of the edge of the Off cylinder with the face of the On cylinder was made. If the edge intersects the face, a face-edge (Figure 2.2 (d)) collision was detected; otherwise the cylinders were not colliding. If both cylinders were Off, then the minimum distance between the edge of Off1 cylinder and the axis of Off2 cylinder was calculated. If the point of shortest distance on the axis of the Off2 cylinder lay inside the cylinder and the shortest distance was less than the radius of the Off2 cylinder, then a side-edge (Figure 2.2 (e)) collision was detected. Otherwise a check was made to determine if the edge of the Off1 cylinder intersected with the face of the Off2 cylinder. If the edge intersected the face then a face-edge (Figure 2.2 (f)) collision was detected; otherwise the same procedure was followed with roles of the two cylinders interchanged.

2.4 Results and Discussion

A. Effective aspect ratio of cylinders

The ratio of the effective aspect ratio obtained from our finite element simulations to the actual aspect ratio of the cylinders is compared with experimental results of Mason and coworkers [58, 57, 2] and Stokesian dynamic simulation results from Meng and Higdon [104] in Figure 2.4 for $r = 0.04$ to 10. From the

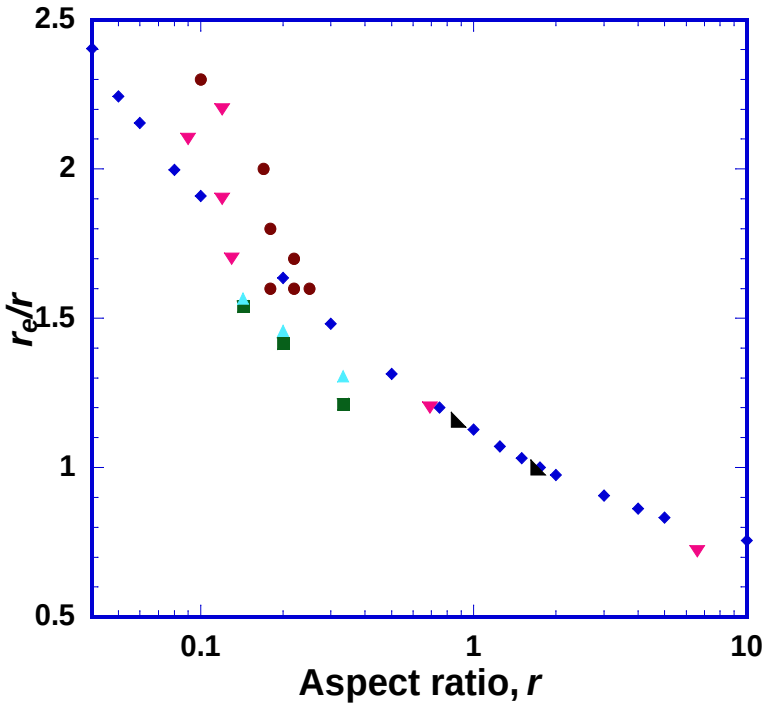

Figure 2.4: Ratio of the effective aspect ratio to the actual aspect ratio obtained from FEM simulations (⋄) compared with various experimental results: a) Goldsmith and Mason [58] (∘), b) Goldsmith and Mason [57] (▽), and c) Anczurowski and Mason [2] (right triangle). Meng and Higdon [104] (□) results for disks approximated by planar arrays of spheres are compared with FEM simulations for disks with semi-circular edges (△).

experimental results reported by Anczurowski and Mason [2], $r_e = 1$ occurs for disks of aspect ratio 0.86; our FEM simulations agree. The aspect ratio at which $r_e = r$ is obtained differs slightly in our simulations and previous experiments. Our simulations show this to occur at $r = 1.75$ whereas experiments report the aspect ratio to be $r = 1.68$ [2].

Meng and Higdon do not report effective aspect ratios directly, but they pro-

vide results for the average stresslet in a dilute suspension of particles subject to simple shear as a function of time. The average stresslet oscillates as the particles rotate and the effective aspect ratio was determined from the period of oscillation. Our simulation results are in fairly good agreement with experimental results and are larger than the effective aspect ratio obtained from Meng and Higdon's simulations. Meng and Higdon used a planar assembly of spherical particles to approximate a cylindrical disk. We suspected that the primary source of the difference in the effective aspect ratio might come from the curved edges of the disks in the Stokesian dynamic simulations. We therefore performed finite element simulations for particles consisting of cylindrical disks with semi-circular edges with the radius of curvature of the edge equal to the half-height of the cylinder. These results represented by the symbol $\triangle$ in the plot are closer to Meng and Higdon's results although still slightly higher with the difference increasing with increasing aspect ratio. The remaining difference probably results from the roughness of the face of the disk of spheres and the deviations from a perfectly circular shape of the disk. These effects become larger for the higher aspect ratio assemblages which include smaller numbers of spheres.

At high aspect ratios, $r > 10$, our simulation results agree with the theoretical scaling predicted by Cox [34]:

$$\frac{r_e}{r} = \frac{A}{ln(r)}. \tag{2.9}$$

By comparing his results with experimental measurements, Cox found the constant A to be 1.24. Figure 2.5 shows the agreement of our simulation with this scaling and with the results of a number of experimental studies [143, 112, 68, 117].

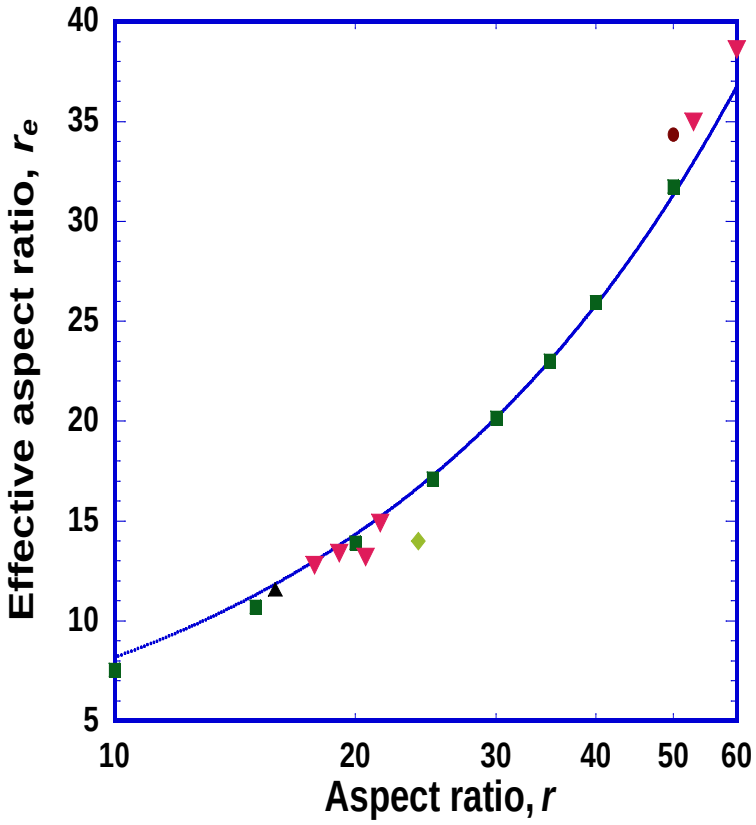

Figure 2.5: Effective aspect ratio of high aspect ratio particles from the simulations (□) compared with the analytical asymptotic scaling of Cox [34] (dotted line) and experimental results of Trevelyan and Mason [143] (▽), Okagawa and Mason [112] (△), Petrich, Koch and Cohen [117] (○), and Iso, Koch and Cohen [68] (⋄). The simulation results match well with the analytical results for $15 \leq r \leq 50$.

The effective aspect ratio values obtained from our simulations and used in the study of collision rate are tabulated with the actual aspect ratio in Table 2.1. In order to further check the limitations of our FEM simulations at high and low aspect ratio, we performed simulations for spheroids with the same aspect ratios as the cylinders considered in our study. For spheroids, we know that $r_e = r$ and we found this to be true of our calculations within an error of 2% for $0.1 \leq r \leq 50$ and 5.3% for $0.04 \leq r \leq 0.1$.

B. Asymptotic analysis of collision rate

The scaling of the fractional collision frequency, f, can be determined analytically for the cases of high (fibers) and low (disks) aspect ratio. To reason qualitatively about the collisions among high aspect ratio fibers, we should be aware of the nature of Jeffery orbits in this limit. Rahnama et al. [123] used similar considerations to describe the hydrodynamic interactions among fibers in simple shear flows. At any given instant of time, an $O(1)$ fraction of fibers undergoing Jeffery rotation at steady state are within an $O(\frac{1}{r_e})$ angle of the direction of flow. The cross-sectional area of these flow aligned fibers in the plane perpendicular to the flow direction (i.e., their collision cross-section) is O(d^2). The relative velocity of such fibers as they collide is $O(d\gamma)$ since the distance between the center of mass of these fibers in the velocity gradient direction is $O(d)$. The collision frequency of these aligned fibers with one another is then the product of a collision cross section of $O(d^2)$ and a relative speed of $O(d\gamma)$ yielding $k \sim O(d^3\gamma)$. The collision frequency of the corresponding circumscribing sphere is $O(L^3\gamma)$. The fractional collision frequency of the fibers is thus $f = O(\frac{d^3}{L^3}) = O(\frac{1}{r^3})$. Apart from the particles aligned in the direction of flow there is another set of particles that is flipping. At very high aspect ratio, using 2.7, it can be shown that a particle

spends an $O(\frac{r_e}{\gamma})$ time aligned in the flow-vorticity plane and an $O(\frac{1}{\gamma})$ time flipping. Hence, the fraction of particles flipping at any instant at high aspect ratio is O($\frac{1}{r_e}$). The cross sectional area of these fibers in the direction of flow is O(Ld) and the associated relative velocity is $O(L\gamma)$ since the distance between the center of mass of the fibers is $O(L)$. The scaling of the fractional collision frequency for a pair of flipping fibers is the product of an $O(\frac{1}{r_e^2})$ probability of finding such a pair with the associated collision cross-section and relative velocity yielding $f \sim O(\frac{1}{r_e^2 r})$. When a flipping fiber collides with an aligned fiber, the collision cross-section and relative velocity remain the same as for flipping-flipping collisions whereas the probability of such collisions is $O(\frac{1}{r_e})$ rather than $O(\frac{1}{r_e^2})$ so that $f = O(\frac{1}{rr_e})$ and is larger than that for either aligned-aligned or flipping-flipping collisions. This prediction that most collisions at high aspect ratio are between an aligned and a flipping fiber is supported by the experimental observations of Blakeney [14, 102]. At high aspect ratio, Lindstrom and Uesaka [102] have proposed a collision scaling of $O(\frac{ln(r_e)}{rr_e})$ for $C = \infty$ orbits which differs from our scaling by a factor of $ln(r_e)$. The results from our simulation for $C = \infty$ are better fit by the scaling of $O(\frac{1}{rr_e})$ although the distinction is not certain because $ln(r_e)$ is a weak scaling and we have only explored aspect ratios as high as 50. Since $r_e \sim O(\frac{r}{ln(r)})$ for high-aspect-ratio fibers, the scaling of the overall rate constant for collision is given by:

$$k_{fiber} \sim O(\gamma d^2 L ln(r)). \tag{2.10}$$

Hence in simple shear flow, k is approximately proportional to the volume of the fiber. For fibers undergoing Brownian motion, the rate constant of collision is given by [118]:

$$k_{B,fiber} = \frac{8kT ln(r)}{3\mu}. \tag{2.11}$$

In the derivation of the above relation the assumption of ideal collision was also

made. One interesting difference between the Brownian collision constant of fibers and the shear induced collision constant is the dependence on the size of the fiber. In Brownian diffusion, the rate constant is independent of the absolute size, whereas in shear induced collisions, the rate constant is proportional to the volume of the fiber. In both cases the rate constant has a lograthmic dependence on aspect ratio.

Thin disks rotating in Jeffery orbits tend to align such that their axis of symmetry is in the velocity gradient direction. This alignment gives an available collision cross section of $O(Ld)$ and an associated relative velocity of $O(L\gamma)$. Thus, f for aligned-aligned collisions is $O(\frac{dL^2}{d^3}) = O(r^2)$. For disks that are flipping, the cross sectional area available for collision is O(d^2) and the associated velocity with collision is $O(d\gamma)$. The fraction of flipping disks is $O(r_e)$. Therefore, the fractional collision frequency of a flipping disk with an aligned disk is $O(r_e\frac{d^3}{d^3})$=$O(r_e)$. The fractional collision frequency of a pair of flipping disk, like that for a pair of flipping fibers, is one order smaller than the frequency for flipping-aligned collisions and is $O(r_e^2)$. The overall rate constant of collision is then given by:

$$k_{disk} \sim \ r_e d^3 \gamma. \tag{2.12}$$

Like fibers, the rate constant of collision for disks undergoing only Brownian motion is also independent of the size of the particle [144], implying that for the same collision efficiency bigger disks are easier to flocculate using shear flow.

The theoretical asymptotic scalings of f at high and low aspect ratios are compared with the simulation results in Figure 2.6 and Figure 2.7, respectively. Fibers follow the asymptotic scaling for $r > 15$. For disks, simulation results agree with analytical results for $r < 0.1$. Although the scaling laws derived above are for circular cross section cylindrical shape particles, we believe that

Actual aspect ratio, r	Effective aspect ratio, r_e (simulations)
0.04	0.096
0.05	0.112
0.06	0.129
0.08	0.156
0.1	0.191
0.2	0.327
0.3	0.444
0.5	0.656
0.75	0.900
1	1.127
1.25	1.339
1.5	1.547
1.75	1.751
2	1.952
3	2.719
4	3.450
5	4.160
10	7.560
20	13.923
25	17.133
30	20.176
35	23.020
40	25.963
50	31.740

Table 2.1: Effective aspect ratio, r_e as calculated from FEM simulations for various aspect ratio used in the Monte Carlo simulations.

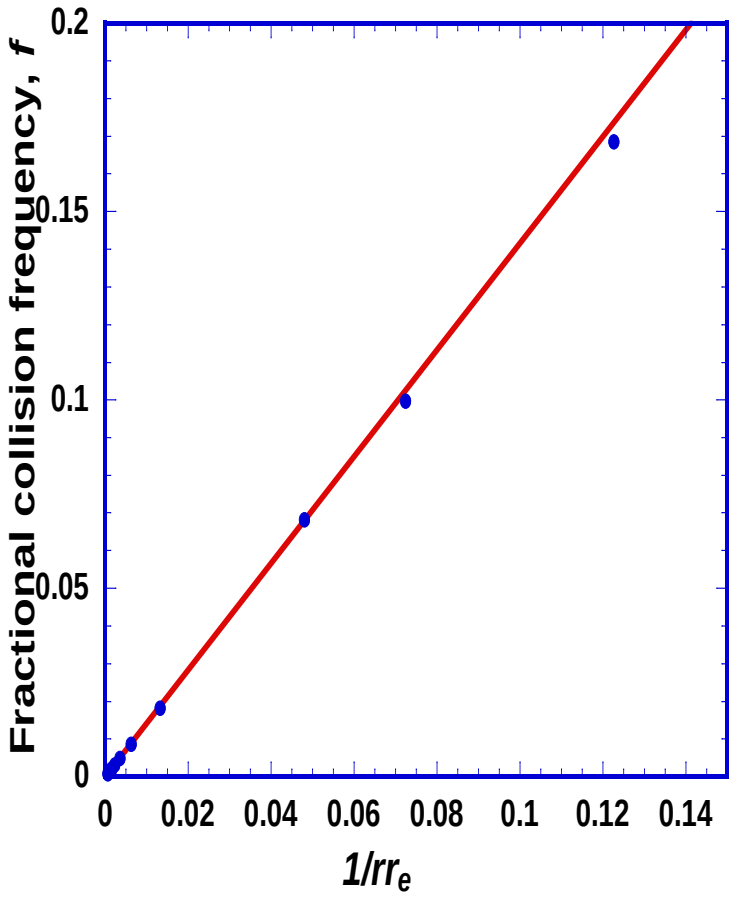

Figure 2.6: Fractional collision frequency of high aspect ratio particles from the simulations (∘) compared with the analytical scaling $f = 1.42/(rr_e)$ (line).

the same scaling laws will hold for other axisymmetric particle shapes such as spheroidal, double conical etc. as long as appropriate effective aspect ratio values are used. The predictions should hold true because the only quantities used in deriving the scalings are the rotational rate and the two length scales associated with the axisymmetric particle's shape.

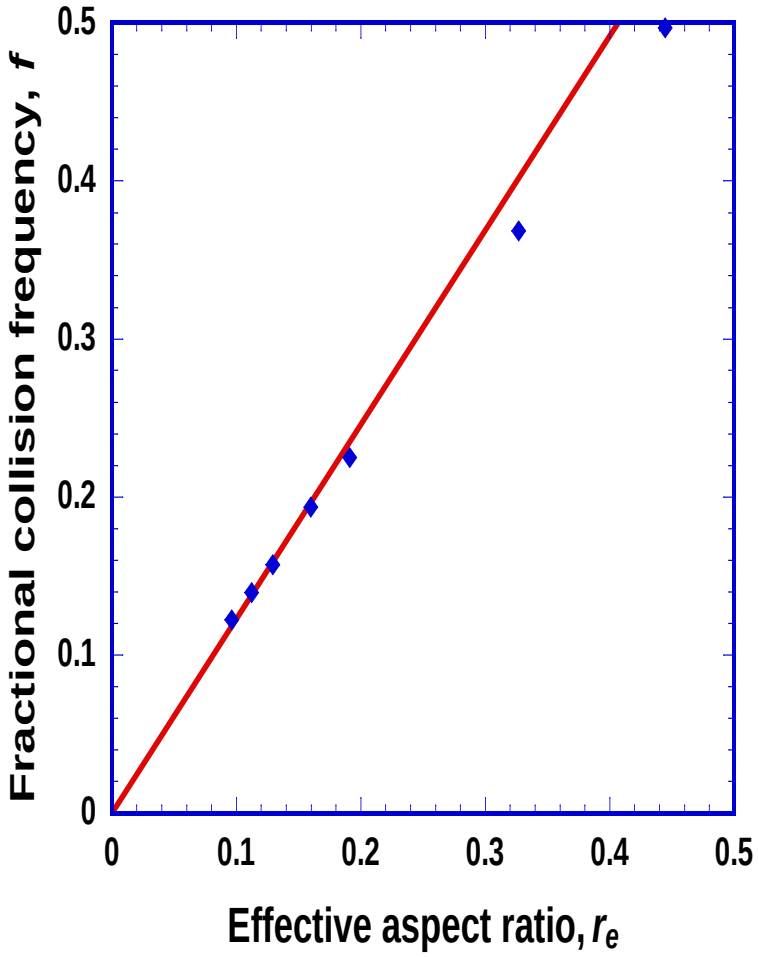

Figure 2.7: Fractional collision frequency of low aspect ratio particles from the simulations ($\diamond$) compared with the analytical scaling $f = 1.23r_3$ (line).

C. Fractional collision frequency for particles following Jeffery orbit distribution

The dependence of f on aspect ratio is shown in Figure 2.8 for particles undergoing rotation motion with Jeffery orbit distribution. As the aspect ratio increases at low aspect ratio, f also increases up to an aspect ratio of about 0.75. This is because with an increase in aspect ratio a cylinder occupies a larger fraction of a sphere's volume and hence collides more often. The presence of a max-

imum close to an aspect ratio of 0.75 is also interesting given that the maximum fractional volume of the cylinder inscribed in a sphere is obtained at an aspect ratio of 0.71. As the aspect ratio grows further, f starts decreasing because for $r > 0.71$ the volume fraction of the cylinder circumscribed by a sphere also starts decreasing . In the asymptotic case of high aspect ratio, we have already shown that the fractional collision frequency follows a scaling of $O(\frac{ln(r)}{r^2})$ whereas the fractional volume follows a scaling of $O(\frac{1}{r^2})$.

The effect of the Jeffery rotational motion of cylinders on the fractional collision frequency is studied by comparing the collision frequency for particles undergoing such motion with non-rotating particles undergoing only translational motion (Figure 2.8). Although there is no physical situation where particles do not rotate in simple shear flow, the non-rotating particle case is used as a reference to understand the effect of Jeffery type rotational motion on collisions. At all aspect ratio, particles undergoing rotational motion have a smaller collision frequency compared to non-rotating particles although both follow a similar qualitative trend. The lower collision frequency for rotating particles can be explained based on the fact that in Jeffery orbits particles spend more time aligned in the direction of the flow, i.e. fibers with their axis in the direction of the flow and disks with their axis in the gradient direction. Both these orientation have smaller cross-sectional area in the $y - z$ plane available for collisions than orientations in which particles are not aligned. In addition, it may be noted that the motion of a slender fiber resembles that of a line of dye in the fluid except that the length of the line of dye increases whereas the fiber length is fixed. Two lines of dye will not cross because the fluid velocity has a single value at each point in space. Thus, Jeffery motion induces less collisions than would be expected in the case of uncoupled rotational and translational motion such as Brownian

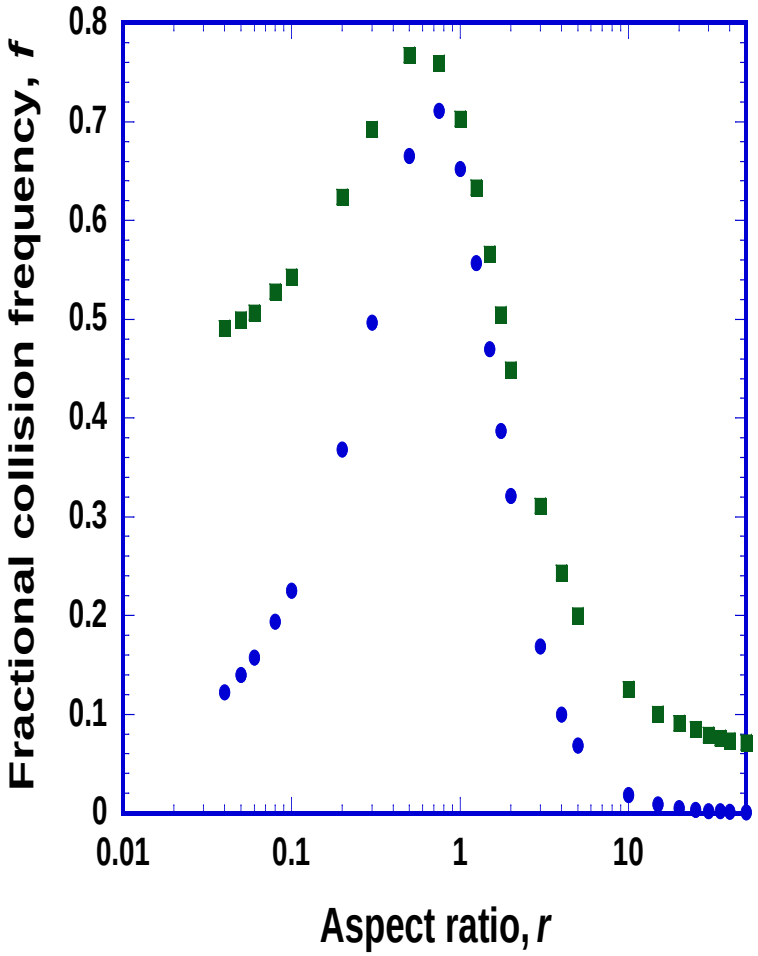

Figure 2.8: Comparison of fractional collision frequency, f of cylindrical particles undergoing Jeffery's rotational motion (○) and particles undergoing translational motion (□) without any rotation.

motion.

The ideal collision rate calculations performed in this work neglect hydrodynamic and colloidal interactions between the particles. However, in the case of unstable colloidal spherical particles, it is known that the viscous resistance to the approach of the particles is largely compensated by their van der Waals attraction leading to collision efficiencies (ratios of actual to ideal collision rate)

ranging from about 0.2 to 1 [24, 38]. The ideal collision rate may prove an even better estimate of the true collision rate for cylindrical particles than for spheres. Cylindrical particles have sharp corners and many of the collisions detected in our study are edge-face or edge-side collisions. The sharp corner would minimize the lubrication and colloidal forces acting as the particles approach and so we may expect collision efficiencies closer to one for cylinders than for smooth particles. High aspect ratio fibers are known to have weak hydrodynamic interactions; their fluid velocity disturbance is small in proportion to $1/ln(r)$ and experience indicates that the prefactor is also small [123].

Figure 2.9 shows the fraction of the collisions which are face-edge, side-edge and side-side based on the first point of contact at the time of collision. At low aspect ratio, most collisions are face-edge, the orientation favored by the flipping-aligned pair of disks which was predicted to dominate the collision rate. As the aspect ratio of the particle increases, side-side collisions increase and face-edge collisions decrease. This could be explained on the basis that increased aspect ratio results in more lateral surface area available for collisions. As the aspect ratio is increased further, the effect of increased lateral surface area is balanced by the increase in the tendency of the particles to spend more time in the direction of flow with their lateral surface area perpendicular to the flow direction thus decreasing side-side collisions. At higher aspect ratio, the leading order contribution to the collision frequency comes from one rotating and one aligned fiber as shown in the asymptotic analysis and these collisions are predominantly side-edge. Non-rotating particles do not preferentially align in the direction of flow and hence their fraction of side-side collisions continues to increase with aspect ratio at all aspect ratios. We expect particles undergoing uncoupled rotational and translational motion due to other mechanisms to also

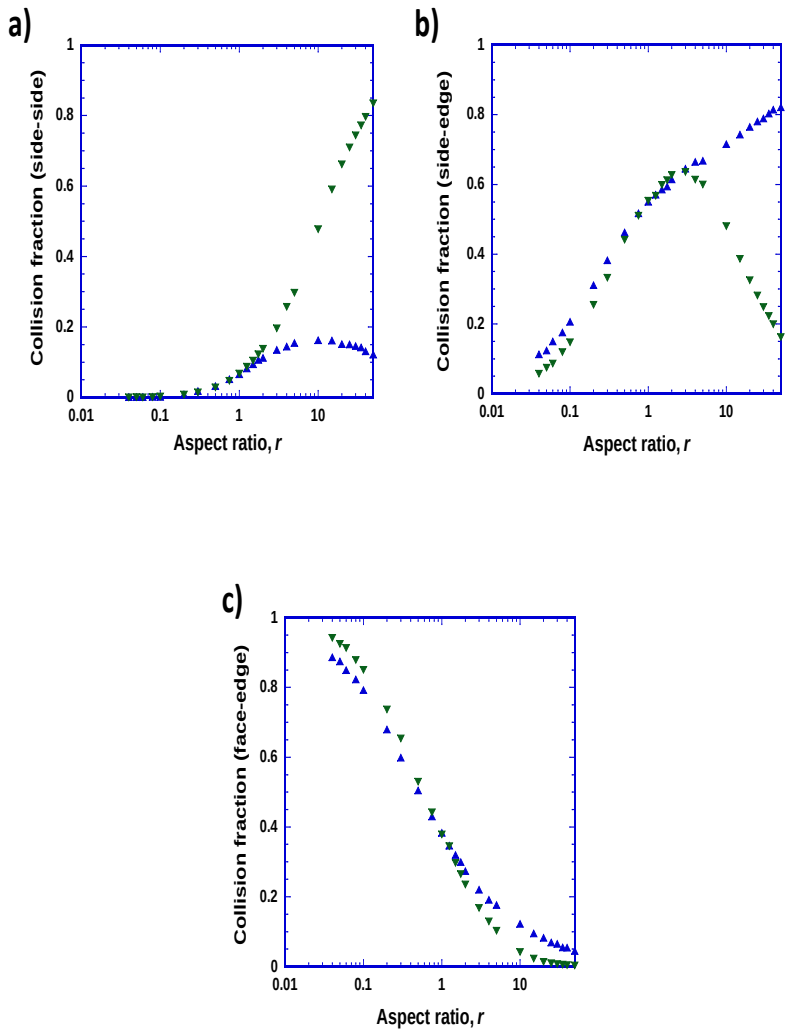

Figure 2.9: Fraction of the collisions with different orientations based on the first point of contact for rotating (▽) and non- rotating particles (△).

show a similar behavior.

Collisions between particles influence the average stress in the suspension as shown by Sundararajakumar and Koch [138] and Lindstrom and Uesaka [102]

for the case of fibers. Because of the high aspect ratio of the particles and the sharp edges of cylinders, lubrication forces do not prevent solid-body contacts from forming. The increased frequency of side-edge collisions at high aspect ratio suggests that the contribution of fiber-fiber contact to the stress will be large. This is due to the fact that the relative velocity of the center of the cylinders is substantial, O(γL), for side-edge collisions leading to large contact forces:

$$F_c \sim \frac{\mu L(L\gamma)}{ln(r)}. \tag{2.13}$$

The average stress resulting from these collisions is then given by :

$$\sigma_{collision} = n^2 f k_{sphere} t_c F_c r_c, \tag{2.14}$$

where $t_c = \gamma^{-1}$ is the characteristic time over which the shear flow drives the particles together and r_c is the size of the cluster which for the case of collision of two fibers is L. Substituting the value of f and k_{sphere} in the above expression we obtain the following expression for collisional stress,

$$\sigma_{collision} \sim \frac{4\mu\gamma(nL^2d)^2}{3ln(r)^{\frac{1}{2}}} \tag{2.15}$$

The collisional stress will contribute to the shear and normal stresses in the suspension. However, a suspension of purely hydrodynamically interacting fibers has no normal stress difference, a consequence of the linearity of Stokes flow. Thus, the effects of the collisional stress can be isolated by examining the first normal stress difference. In the absence of interparticle friction Lindstrom and Uesaka [102] found the normal stress difference to scale as $(nL^2d)^2$, cf. eqn (53)[102]. This scaling agrees within a weak logarithmic factor with that obtained above. Sundararajakumar and Koch's results [138] also indicate that the normal stress difference grows faster than linearly with nL^2d.

For low aspect ratio particles collisions between one flipping and one aligned

disk predominate, suggesting that again disk-disk contact will make a large contribution to the stress. Using a scaling analysis similar to that discussed above for fibers, we can estimate the collision stress for a suspension of disks as:

$$\begin{aligned}\sigma_{collision} &\sim n^2 f k_{sphere} t_c F_c r_c \\ &\sim n^2 f \frac{4}{3}\gamma d^3 \frac{\mu d^3 \gamma}{\gamma} \\ &\sim \mu\gamma n^2 r_e d^6. \end{aligned} \tag{2.16}$$

D. Effect of orbit distribution on the collision frequency

Before colliding, the cylindrical particles rotate according to Jeffery's rotational motion. However, since the orbit constant is not changed by this motion, we must specify a probability distribution for the particles among the orbits. In this section, we consider the effect of this distribution by examining cases corresponding to all particles with vorticity aligned axes of symmetry ($C = 0$ orbit), all particles with axis of symmetry tumbling in the flow-gradient plane ($C = \infty$ orbit), the distribution corresponding to weak Brownian motion (Leal and Hinch distribution), and that corresponding to isotropic initial orientation (Jeffery distribution).

The fractional collision frequency, f for particles in the $C = 0$ orbit can be calculated analytically using the same approach as Smoluchowski and has been found to be $f_{C=0} = \frac{3r}{2(r^2+1)^{(3/2)}}$. Our simulation results match very well with the analytical results for $C = 0$ orbit. The effect of the orbit distribution on collision frequency is illustrated in Figure 2.10 for particles following Leal and Hinch orbit distribution, Jeffery orbit distribution and $C = \infty$ orbit. Here, the fractional collision frequency is normalized using the analytical result for particles in $C = 0$. The non-monotonic nature of the plot at moderate aspect ratio can be

explained based on the fact that the collision frequency in $C = 0$ orbit depends only on aspect ratio and is independent of effective aspect ratio whereas for the other orbit distribution collision frequency depends on both the effective aspect ratio and the geometric aspect ratio. At all aspect ratios, the fractional collision frequency for Leal and Hinch orbit distribution and Jeffery orbit distribution are very close to one another with a maximum difference of 2.5%; this difference is close to the statistical error of 1% in our studies. This closeness could be due to the fact that neither the Leal and Hinch nor the Jeffery orbit distribution is strongly biased towards $C = 0$ or $C = \infty$ orbits. It can also be seen that all three orbit distributions have a higher collision frequency than the $C = 0$ orbit for the same aspect ratio, although the scaling at high aspect ratio is very similar and the scaling at low aspect ratio differs only by a factor of $\frac{r}{r_e}$. In the limit of high and low aspect ratios, $f_{C=0}$ reduces to $\frac{1.5}{r^2}$ and $1.5r$ respectively. Fibers in the $C = 0$ orbit do not flip and we noted in the scaling analysis above that flipping enhances the collision rate. However, the projection of fibers with $C = 0$ into the flow-gradient plane is larger than an aligned fiber in an orbit with $C > 0$.

The corresponding scaling for orbit distributions dominated by orbits with $C \sim O(1)$ is $f = O(r_e)$ at low aspect ratio and $O(\frac{1}{rr_e})$ at high aspect ratio, as shown earlier. Since at high aspect ratio $r_e \sim O(\frac{r}{ln(r)})$, we expect the collision frequency for all orbit distributions to scale similarly at high aspect ratio with a maximum variation of a factor of $ln(r)$ seen between the two extreme orbits $C = 0$ and $C = \infty$. Although the minimum collision frequency is obtained for $C = 0$ orbit distribution for the case of cylinders, it is not clear what orbit distribution would maximize the collision rate of cylinders. However, it seems likely that a distribution admitting both many vorticity aligned particles and many particles with axes in the flow-gradient plane would facilitate collision. In fact, we

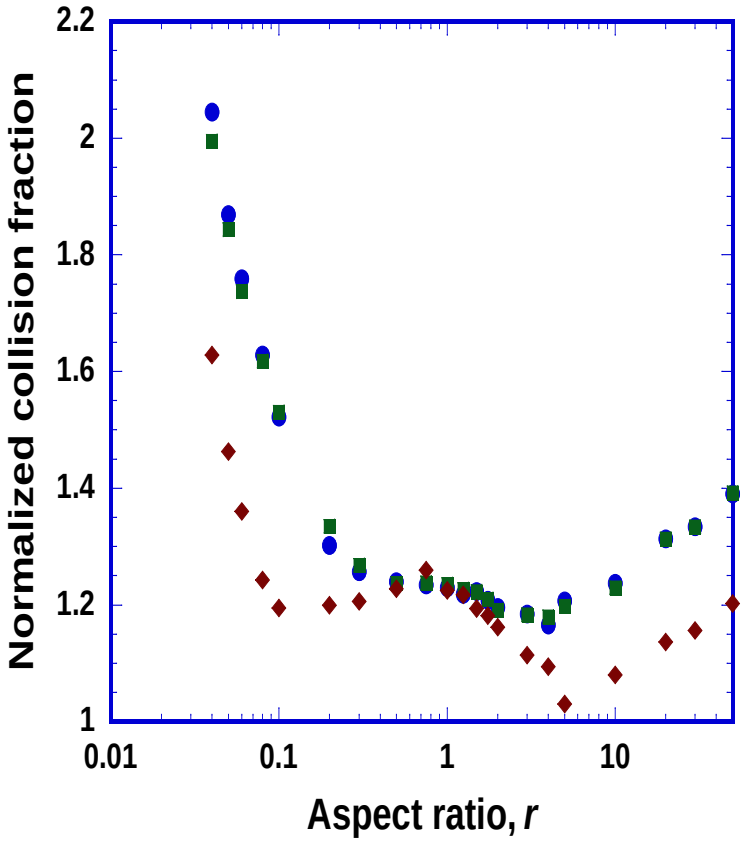

Figure 2.10: Fractional collision frequency, f of cylindrical particles for different orbit distributions - a) Jeffery orbit distribution (∘), b) Leal and Hinch orbit distribution (□), and c). $C = \infty$ (⋄). f is normalized by the analytical fractional collision frequency results for fibers in the $C = 0$ orbit.

have performed a few simulations with half the particles in $C = 0$ and half in $C = \infty$ and obtained higher collision rates than for any of the four distributions discussed above.

2.5 Summary

In this paper, we have determined the ideal collision rate for cylindrical particles in simple shear flow. The ideal collision rate is the rate at which particles intercept one another if they follow the motion associated with the imposed simple shear flow without interacting with one another through hydrodynamic or colloidal forces. While the calculation of the ideal collision rate for spheres [146] requires only a simple analytical derivation based on translational motion, the ideal collision rate of non-spherical particles depends on the way they rotate in the shear flow in addition to their relative translational motion.

Effective aspect ratio: The rotational motion of a particle is governed by its effective aspect ratio r_e, defined as the aspect ratio of a spheroid with the same period of rotation. We used finite element calculations (COMSOL 3.5) to compute the effective aspect ratio of cylinders with aspect ratios ranging from 0.04 to 50. This is the first computational determination of the effective aspect ratio for cylinders over a broad range of aspect ratios.The results are in good agreement with the available experimental and analytical results. The asymptotic scaling of r_e with r at small aspect ratios is unknown and is an interesting open question.

Fractional collision frequency for Jeffery orbit distribution: After determining the nature of the particles' rotational motion, we used Monte Carlo simulations to evaluate the collision rate constant. Scaling analyses for low and high aspect ratio particles indicated that the collision rate is dominated by collisions between one flipping and one flow-aligned particle. The overall collision rate constant scales as $O(Ld^2ln(r)\gamma)$ and $O(r_ed^3\gamma)$ at high and low aspect ratio, respectively. The

collision rate for particles of all aspect ratios was found to correlate reasonably closely with the volume of the particle. The scaling of the collision rate differs from the volumetric scaling by a logarithmic factor $ln(r)$ at high aspect ratio and by a factor of r_e/r at low aspect ratio. Although the simulations performed here are for cylindrical particles, the scaling arguments at both high and low aspect ratios would be expected to hold for any axisymmetric particle. The relatively high relative velocity of flipping and aligned particles leads to a large collisional stress which scales as $(nL^2d)^2$ for $r >> 1$ and $n^2r_ed^6$ for $r << 1$.

Type of collisions: Collisions were also characterized as side-side, edge-side and face-edge collisions based on the initial point of contact of the particles. For high and low aspect ratio particles, most collisions were found to be side-edge and face-edge, respectively, suggesting that if particles stick at the point of first contact, the resulting aggregates will be non linear.

Effect of orbit distribution: The orbit distribution was found to have a relatively weak effect on the collision rate. The Jeffery orbit distribution corresponding to isotropic initial orientations of non-Brownian particles and the Leal and Hinch orbit distribution corresponding to weak Brownian motion gave nearly identical results. Even the extreme distributions with all particles in $C = 0$ or all particles in $C = \infty$ orbits yielded collision rates within 50% of that for the Jeffery orbit distribution for $r = 0.04$ to 50.

Limitations: The ideal collision rate calculated here only serves as a reference and the true rate of collision depends on the detailed hydrodynamic and colloidal interactions between the particles. For a more accurate estimate of the collision rate these interactions should be taken into account. Another limitation of the present work is that the outcome of collisions between particles can-

not be determined based on it. Solid-body interactions between particles, that could lead to only transfer of stress[138] or aggregation[26, 107] determine the outcome of collisions, have not been been studied here.

2.6 Acknowledgement

V.S. is grateful to John Paul Bir Singh for helping with Comsol 3.5. We acknowledge support for a graduate fellowship from the Corning Foundation (V.S.), the NYSTAR J.D. Watson Investigator Program, and the National Science Foundation (CTS-0529042).

CHAPTER 3

ROTATIONAL MOTION OF A THIN AXISYMMETRIC DISK IN A LOW REYNOLDS NUMBER LINEAR FLOW

Most rigid, torque-free, low-Reynolds number, axisymmetric particles undergo a time periodic tumbling motion in a simple shear flow, with their axes of symmetry following a set of closed Jeffery orbits. We have identified a class of rigid, ring-like particles whose axes of symmetry instead reach a permanent alignment near the velocity gradient direction with the plane of the particle aligning near the flow-vorticity plane. An asymptotic analysis for small particle aspect ratio (ratio of length parallel to the axis of symmetry to diameter perpendicular to the axis) shows that an appropriate asymmetry of the ring cross-section with a thinner outer edge and thicker inner edge leads to a tendency to rotate in a direction opposite to the vorticity; this tendency can balance the usual rotation rate associated with the finite thickness of the particle. Boundary integral computations for finite particle aspect ratios are used to determine the conditions of aspect ratio and degree of asymmetry that lead to the aligning behavior and the final orientation of the axis of symmetry of the aligned particles. The aligning particle follows an equation of motion similar to the Leslie-Erickson equation for the director of a small molecule nematic liquid crystal. However, whereas the alignment of the director arises from intermolecular interactions, the ring-like particle aligns solely due to its intrinsic rotational motion in a low Reynolds number flow.

3.1 Introduction

The objective of this study is to understand the rotational motion of thin axisymmetric rigid particles at low Reynolds number in linear flows. The motion of axisymmetric particles in linear flows can be determined using a single scalar parameter called the effective aspect ratio, κ_e. Bretherton [20] derived the following general equation of motion for axisymmetric particles in linear flows:

$$\dot{\mathbf{p}} = \mathbf{p}.\Omega + \frac{\kappa_e^2 - 1}{\kappa_e^2 + 1}(\mathbf{p}.\mathbf{E} - \mathbf{ppp} : \mathbf{E}), \tag{3.1}$$

where $\mathbf{p}$ is the orientation of the axis of symmetry of the particle and $\dot{\mathbf{p}}$ is the rate of change of the orientation. $\mathbf{\Omega}$ and $\mathbf{E}$ are the vorticity and the strain tensors respectively, given by:

$$\mathbf{E} = \frac{1}{2}(\nabla\mathbf{v} + \nabla\mathbf{v}^T), \tag{3.2}$$

$$\mathbf{\Omega} = \frac{1}{2}(\nabla\mathbf{v} - \nabla\mathbf{v}^T), \tag{3.3}$$

where $\mathbf{v}$ is the fluid velocity. For simple shear flow, the time period of rotation, T, of the particle following the motion described in 3.1 is given by:

$$T = \frac{2\pi}{\gamma}\left(\kappa_e + \frac{1}{\kappa_e}\right). \tag{3.4}$$

Here γ is the shear rate. For a spheroid $\kappa_e = \kappa$ where κ, is defined as a ratio of the thickness (L) of the particle parallel to the axis of symmetry to its diameter (d) perpendicular to the axis of symmetry, and the effective aspect ratio can be defined as the aspect ratio of a spheroid having the same period of rotation as that of the particle. Although the effective aspect ratio is independent of the imposed flow and is only a property of the shape of the particle, to determine the effective aspect ratio generally two specific flow problems need to be solved. We consider a single stationary particle of low aspect ratio in simple

shear flow with its axis of symmetry aligned with the gradient axis (problem A) and with the flow axis (problem B). The suspending fluid is Newtonian. The simple shear flow applies a torque on the stationary particle to rotate it about the vorticity axis. The torque in problem A is small in the limit of small aspect ratio and controls the scaling of the effective aspect ratio with the aspect ratio. We determine the scaling of this torque for a family of axisymmetric shapes.

Non-spherical particles of extreme aspect ratio are commonly used to change the transport properties of fluids [8] and the mechanical and the mass transfer [36] properties of composite materials. Particles with extreme aspect ratios have a large influence on the properties of a suspension or composite relative to those of moderate aspect ratio since these properties usually scale with either the largest length or the surface area of the particle rather than the particle volume. Therefore, a small volume fraction of high or low aspect ratio particles can alter the properties of a suspension significantly. For dilute suspensions, the change in the properties of the fluid depends on the concentration [43] and the flow-induced rotational motion [72] of the particles.

The simplest non-spherical particles are axisymmetric particles. Jeffery was the first to study the rotational motion of axisymmetric particles in simple shear flow [72] . Jeffery showed that in the absence of inertial effects, a spheroidal particle's axis of symmetry rotates in a simple shear flow in a periodic motion with a period of rotation that depends on the aspect ratio of the particle. Bretherton later showed that most [129] axisymmetric particles follow the same equation of motion in simple shear flow as long as an effective aspect ratio, κ_e, is used instead of the actual aspect ratio. Extensive work has been done since Bretherton to understand the behavior of long particles [6, 33, 34, 120] , that is the limit of

large κ. Cox [34] analytically derived the scaling of the effective aspect ratio of long fibers of different shapes. Cox showed, via an analysis based on the viscous slender-body theory, that the effective aspect ratio of long tapered fibers is always proportional to the actual aspect ratio with logarithmically small corrections at the second order. The radius of the cross-section of a tapered fiber decreases to zero smoothly at either end over length scales on the order of the fiber half-length . For blunt-ended objects, on the other hand, Cox showed that the effective aspect ratio must be:

$$\kappa_e = \frac{1.24\kappa}{(ln\kappa)^{\frac{1}{2}}}, \tag{3.5}$$

where the prefactor was determined by comparison with experimental results [2] . For these particles (a finite cylinder being an example), the torque acting on the particle, when it is aligned in the direction of the flow, is dominated by forces of $O(\mu\gamma d^2)$ acting over an area of $O(d^2)$ at the blunt ends, and is $O(\mu\gamma d^2 L)$. We will see in this work that for thin disk shapes also with sufficiently blunt edges, the force density at the edge of the particle again creates the leading order torque on a particle with its long axis parallel to the velocity. Despite our good understanding of particle motion at large aspect ratio, we have little knowledge of the motion of thin particles in the limit $\kappa \to 0$. In this paper, we aim to redress this lack of knowledge.

Low aspect ratio disk-like particles are encountered in a number of systems like red blood cells and platelets in blood [29], clay or mica particles in suspensions [73, 105], and gas barrier materials [36] . In a number of previous experimental studies [143, 58, 111] , the motion of a single thin particle was studied to verify Jeffery and Bretherton's results at low Reynolds number, and establish the effective aspect ratio of the particle. Recently, experiments have been performed to understand the rheology of suspensions of hard disks [73, 23] . Most

of the experimental systems use clay particles as model hard disks. A route to a fundamental understanding of the behavior of a dilute particle suspensions is to understand the motion of a single particle which depends on the shape of the particle. Meng and Higdon [104] used Stokesian dynamics to study the motion of a planar assembly of spherical particles forming a disk-like shape. This assembly of spherical particles was then used to understand the rheology of a concentrated suspension of disk shaped particles ($\kappa > 0.13$). Recently, Singh et al. [128] used finite element simulations to calculate the effective aspect ratio at moderately small aspect ratio ($\kappa > 0.1$); these results were then used to determine the collision rate cylindrical particles in the dilute suspension limit. Previous experimental and numerical studies fail to predict the scaling of effective aspect ratio as $\kappa \to 0$. These studies [2, 58, 57, 128, 104] do show that as the aspect ratio of a cylinder decreases the ratio of effective aspect ratio to the aspect ratio grows. This observation raises the question of whether κ_e/κ will eventually approach a constant as $\kappa \to 0$, exhibit a weak logarithmic dependence on κ as in the case of a fiber, or grow as a stronger algebraic function of $1/\kappa$.

Before embarking on the detailed analysis, it is interesting to consider what one can say from simple scaling arguments about the period of rotation and the effective aspect ratio of particles of large ($\kappa >> 1$) and small ($\kappa << 1$) aspect ratio. Jeffery's solution for spheroids indicates that the period of rotation (3.4) is proportional to κ for $\kappa >> 1$ and proportional to κ^{-1} for $\kappa << 1$. This beautifully symmetric result, where the particle rotation slows down in a similar way as the particle becomes long and thin or flat and thin, might be thought to suggest that the factors governing the rotation of the particle are similar at large and small aspect ratio. We will find that while there are some analogies, the two cases are very different.

Cox[34] showed that one can estimate the effective aspect ratio of a particle in terms of the torque acting on a stationary particle in simple shear flow in two different orientations. We consider the following two orientations of the particle (figure 3.1) for this work: (i) the axis of the particle is in the gradient direction (orientation A) and (ii) the axis of the particle is in the flow direction (orientation B). In both these orientations the torque acting on the stationary particle must by symmetry be in the vorticity direction. Using Jeffery's equation of motion, Cox [34] obtained the following relationship for effective aspect ratio,

$$\kappa_e = \left(\frac{G_A}{G_B}\right)^{\frac{1}{2}}, \tag{3.6}$$

where G_A and G_B are the torques acting on the particle in orientation A and B respectively. When a particle's long axis is parallel to the gradient direction, it experiences variations of velocity on the order of the largest length, so that we may expect its dimensional torque to scale with the large dimension: $G_A = O(\mu\gamma L^3)$ for $\kappa >> 1$ and $G_B = O(\mu\gamma d^3)$ for $\kappa << 1$. We will see in section VA that this scaling argument for the torque on a thin disk is correct and that $G_B = -(32/3)\mu\gamma d^3$ independent of the detailed variation of its thickness with radial position. Cox showed that the aforementioned estimate for the torque on a high aspect ratio particle in orientation A is correct to within a logarithmic factor that might be expected to arise from matching the inner and outer solutions for the fluid velocity in a slender-body theory. Thus, $G_A = O(\mu\gamma L^3/\ln\kappa)$ for $\kappa \gg 1$. When the particle is aligned with its long axis in the flow direction, it makes a relatively small disturbance to the fluid flow so that we might expect the stress $\mathbf{f}$ to be predominantly in the x direction with $f_x = O(\mu\gamma)$. In a high aspect ratio particle, this stress acts with an $O(d)$ moment arm over an $O(dL)$ area, so that we might expect from this simple argument that $G_B = O(\mu\gamma d^2 L)$. Cox again showed that this estimate is correct to within a logarithmic factor so that $\kappa_e = O(\kappa)$ for

tapered and $\kappa_e = O(\kappa/(\ln\kappa)^(1/2))$ for blunt slender fibers. For a low aspect ratio particle, for orientation A, the stress acts with an $O(L)$ moment arm over an area of $O(d^2)$, so that the simple argument yields $G_A = O(\mu\gamma d^2 L)$ and an effective aspect ratio of $\kappa_e = \kappa^{\frac{1}{2}}$. Clearly this simple argument does not correctly predict the effective aspect ratio of a disk-like spheroid for which $\kappa_e = \kappa$. Thus, the naive argument that does not account for the shape of the particle in defining the leading order scaling is not sufficient to give the right order of torque for thin disks. We will see that the supposition that the leading order stress is $f_x = O(\mu\gamma)$ is correct. However, the leading order y stress, $f_y = O(\mu\gamma\kappa)$ will be seen to yield a torque that exactly cancels that due to the leading order x stress. It is then necessary to consider higher order corrections to the stresses in the outer region covering most of the disk and/or the stresses in a boundary layer near the edge of the particle to find the leading order torque and the effective aspect ratio for a this disk. We will find that this leads to an effective aspect ratio that is sensitive to the details of the particle shape.

The family of axisymmetric shapes with fore-aft symmetry considered in this work is given by:

$$y(\rho) = \kappa l(\rho) = \kappa(1-\rho^2)^{\alpha}. \tag{3.7}$$

Here polar coordinates are used with $\rho = (x^2 + z^2)^{\frac{1}{2}}$ as the radial coordinate in the $x-z$ plane with the center of the coordinate axis coinciding with the center of the particle, $y(\rho)$ is half the thickness of the particle at ρ, κ is equal to half the thickness of the particle at $\rho = 0$, and α is a non-negative parameter. By varying α, a number of shapes are obtained as shown in figure 3.2. In particular, for $\alpha = \frac{1}{2}$, 3.7 represents the shape of a spheroidal disk and for $\alpha \to 0$ it represents the shape of a cylindrical disk. As α gets smaller, the particle becomes more blunt around the edges. For $\alpha > 1$ the slope of the particle over the entire surface in

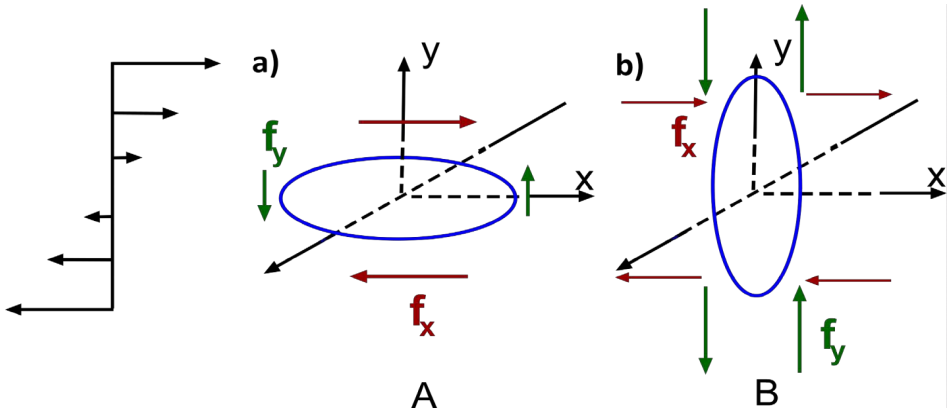

Figure 3.1: Schematic of forces acting on: a) An axisymmetric thin particle oriented with its axis of symmetry in the gradient direction (Orientation A) and b) An axisymmetric thin particle oriented with its axis of symmetry in the flow direction (Orientation B).

the radial direction is $O(\kappa)$. As will be shown later, the change in the slope of the particle as $\rho \to 1$ for different values of α, is an important factor in determining the rotational motion of the particle.

In this work, we use the integral formulation of Stokes equation as a starting point to calculate the stresses acting on the surface of a stationary particle. The stresses are then used to calculate the torque acting on the particle. From the torque, using 3.6, the effective aspect ratio as a function of aspect ratio of the particle is calculated. In section II, to set the context for the problem, we present some classical results describing the motion of axisymmetric particles and then introduce the governing equations for the present problem. Section III describes the general boundary element method and the details of the method pertinent to the present problem. In section IV, we perform a matched asymptotic analysis to obtain the stresses acting on the particle. The analytical description based on the distance from the edge of the particle and its geometry calls for dividing the surface into two regions, an outer region away from the edge and a boundary layer region close to the edge of the particle. The torque contribution from both these regions of interest is calculated separately. In section V, we present our BEM simulation results along with a comparison with the analytical results obtained in section IV. Finally in section VI, we summarize all our results along with a discussion of the role of the effective aspect ratio in the rheology of thin particles.

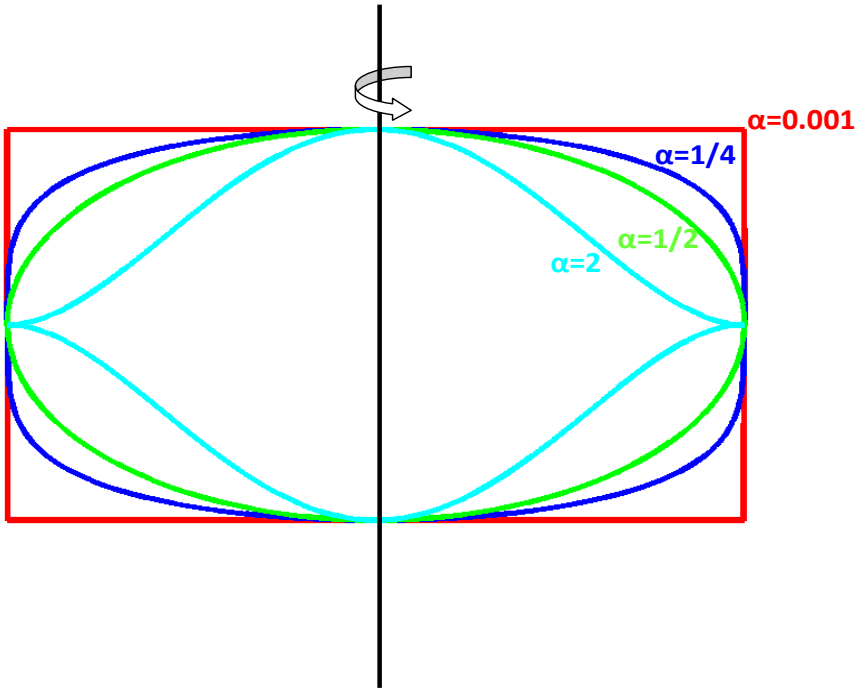

Figure 3.2: Different shapes given by $y = \pm\kappa(1-\rho^2)^\alpha$ for $\alpha = 10^{-3}$ (red), $\alpha = 1/4$ (blue), $\alpha = 1/2$ (green), and $\alpha = 2$ (cyan) for $\alpha = 1/2$.

3.2 Problem Formulation

The simplest possible flow in fluid mechanics is a steady uniform flow. When an axisymmetric particle is suspended in uniform flow, it undergoes translation motion based on its shape and orientation without undergoing any rotational [16] motion. In practice, most fluid flows are non-uniform in nature. A Taylor series expansion of any non-uniform flow can be written as a sum of a uniform, a linear, a quadratic and other higher order flows. When the particle size is small, one can approximate the flow as a combination of uniform and linear flows. The velocity gradient of a linear flow causes the particle to rotate about its center. In theory, any linear flow can be used to calculate the effective aspect ratio of an axisymmetric particle using Jeffery's [72, 20] theory. We use simple shear flow because in simple shear flow the torque in orientation A approaches zero as $\kappa \rightarrow 0$ while the torque in orientation B is still $O(1)$, this isolates the torque in orientation A which can be used to calculate the small non-zero κ_e. For other flows κ_e will depend on a small difference between the torques in the two orientations which will be harder to detect. The simple shear flow used in this work in a Cartesian coordinate system is given by (figure 3.3 (a)):

$$v_x = y, v_y = 0, v_z = 0, \tag{3.8}$$

where all the length scales are non-dimensionalized using the radius ($R = d/2$) of the particle and the time scales are non-dimensionalized using the shear rate, γ of simple shear flow. In the rest of the paper, we non-dimensionalize all length scales using R, time by $1/\gamma$, velocities by γR, and stresses by $\mu\gamma$.

The motion of axisymmetric particles in simple shear flow has been studied for over 100 years now. Einstein [43] was the first to use the motion of a sphere in simple shear flow to predict the viscosity of a dilute suspension of spheres.

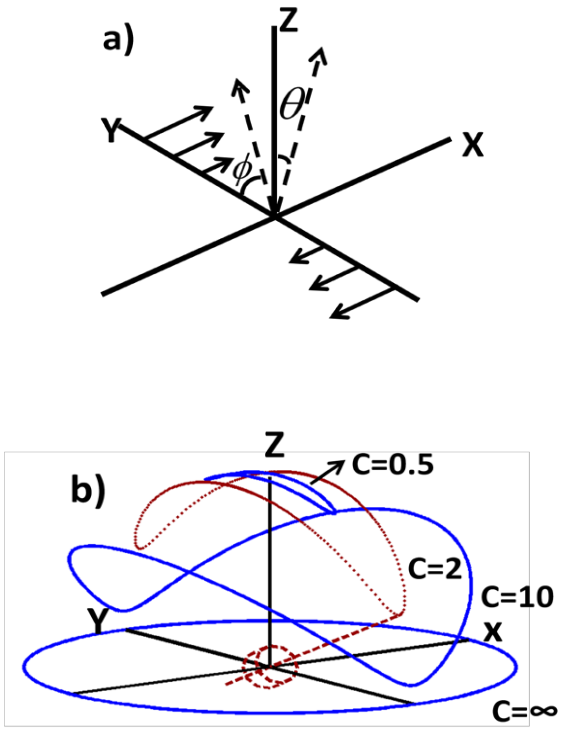

Figure 3.3: (a) Spherical coordinate system for a particle centered at the origin and subjected to a simple shear flow in the x-y plane. (b) Jeffery's orbits for various orbit constants for aspect ratio of 0.1. At small aspect ratios, the particle's axis of symmetry moves towards the gradient direction when approaching the gradient-vorticity plane and at high aspect ratio the particle's axis tends to move towards the flow direction when approaching the flow-vorticity plane.

The next level of complexity was added by changing the shape from spherical to spheroidal (ellipsoid with two equal semi-diameters). Jeffery [72] studied the motion of spheroidal particles in simple shear flow. Jeffery showed that in simple shear flow a spheroid translates with the undisturbed fluid velocity at its center and rotates in a periodic motion in closed orbits (Figure 3.3 (b)). The equation of motion of the axis of symmetry of the particle is given by:

$$\tan(\theta) = \frac{C\kappa}{(\kappa^2 \cos^2 \phi + \sin^2 \phi)^{\frac{1}{2}}}, \tag{3.9}$$

$$\tan(\phi) = \kappa \tan(\frac{t}{\kappa + \kappa^{-1}} + k), \tag{3.10}$$

where θ is the angle of the particle orientation relative to the vorticity direction and ϕ is the angle of the projection of the particle orientation into the flow-gradient plane relative to the velocity gradient direction. Here, k is the phase angle and C the orbit constant, both of which depend only on the initial orientation of the particle for non-Brownian particles in Newtonian fluid. Figure 3.2 (b) shows the trajectory of a particle's axis of symmetry with aspect ratio, $\kappa = 0.1$.

As noted in the introduction, Bretherton [20] later showed that most axisymmetric particles follow the same equation of rotational motion (3.1) as spheroids as long as the effective aspect ratio (κ_e) of the particles is used instead of the actual aspect ratio. In 3.1, the vorticity component of the flow causes solid body rotation of the particle and is independent of the shape of the particle. On the other hand, the extensional component of the flow tries to align the axis of symmetry of the particle along the extensional axis for fibers and along the compressional axis for thin disks. Unlike the rotational component of flow, the response of a particle to extensional component of flow depends on the shape (or effective aspect ratio) of the particle.

The general equation of rotational motion (3.1) can be used to determine the

motion of an axisymmetric particle as long as the effective aspect ratio of the particle is known. For a given external flow if one solves for the instantaneous angular velocity of the particle in a given orientation, using 3.1, the effective aspect ratio of the particle can be determined. Alternatively, Cox [34] showed using Jeffery's solution that the effective aspect ratio for any axisymmetric body can be determined based on the torques acting on the particle when it is held stationary in two different orientations in simple shear flow (3.6). We chose the alternate approach proposed by Cox [34] for this work since it depends on the torque acting on the particle which can be directly deduced from the force densities acting on the particle. As noted earlier, the nondimensional torque ($G_B = -32/3$) acting on the particle when it is oriented with its axis in the direction of flow is $O(1)$. Thus, 3.6 reduces to:

$$\kappa_e = \left(\frac{-3G_A}{32}\right)^{\frac{1}{2}}, \tag{3.11}$$

where G_A now is the non-dimensional torque. Thus to determine the effective aspect ratio of a particle with $\kappa \ll 1$, one needs to solve only for the stresses on the surface of the particle when it is stationary with its axis in gradient direction and then deduce the torque trying to rotate the particle.

Stokes equations can be used to solve for the disturbance velocity field around a particle in an external flow at low Reynolds number. The disturbance field can then be used to calculate the stresses on the surface of the particle. Alternatively, one can use the integral equation formulation of Stokes equation to directly solve for the stresses acting on the surface of the particle. These integral equations are used as the starting point for both the boundary element method and the asymptotic analysis performed in this work. The general integral representation of the creeping-flow problem was obtained by Ladyzhenskaya [89]. For the case of flow around rigid boundaries, the simplified integral equations

[81] of the creeping-flow problem can be written as:

$$\boldsymbol{v}(\boldsymbol{r}) = \boldsymbol{u}(\boldsymbol{r}) + \int_S \boldsymbol{J}(\boldsymbol{r} - \boldsymbol{r}').\boldsymbol{f}(\boldsymbol{r}')dS' \tag{3.12}$$

where $\boldsymbol{r}$ and $\boldsymbol{r}'$ are the position vectors in space, S represents the boundary of the flow domain, dS' indicates integration over S with respect to the point $\boldsymbol{r}'$, $\boldsymbol{v}$ is the velocity on the boundary, $\boldsymbol{u}$ is the undisturbed fluid velocity (simple shear here) in the absence of the boundary, $\boldsymbol{f}$ is the unknown surface stress and $\boldsymbol{J}$ is the Green's function. Here the integral term on the right hand side represents the velocity disturbance field at $\boldsymbol{r}$ created by the stresses acting on the fluid due to the surface of the particle at $\boldsymbol{r}'$. The surface stresses acting on the particle are equal and opposite in direction to the stresses acting on the fluid. The integration is performed on the surface of the particle. Using the integral equation approach, one can directly calculate stresses acting on the two dimensional boundary without solving for the entire disturbance field in the infinite three dimensional domain. Here the surface stress is given by:

$$f_i = \sigma_{ij} n_j \tag{3.13}$$

where σ_{ij} is the total stress tensor and n_j is the inward normal vector to the particle. For the Stokes problem, $\boldsymbol{J}$ is given by:

$$J_{ij} = \frac{1}{8\pi}\left(\frac{\delta_{ij}}{r} + \frac{r_i r_j}{r^3}\right). \tag{3.14}$$

Using the symmetry of the shape and orientation (A) of the particle and the anti-symmetry of the flow about the polar plane $(\rho - \theta)$, one can write the stresses on the surface of the particle as:

$$\begin{aligned} f_x(\boldsymbol{\rho}, +y(\rho)) &= -f_x(\boldsymbol{\rho}, -y(\rho)) \\ f_y(\boldsymbol{\rho}, +y(\rho)) &= f_y(\boldsymbol{\rho}, -y(\rho)) \\ f_z(\boldsymbol{\rho}, +y(\rho)) &= -f_z(\boldsymbol{\rho}, -y(\rho)) \end{aligned} \tag{3.15}$$

For both the analysis and the numerical simulation, f_z is considered to be zero as the contribution of the leading order f_z to the disturbance field and hence the stresses in the x and y direction is less than $O(\kappa^2)$ (shown in appendix A.1.). We will see later that the stresses responsible for the leading order torque, G_A are greater or equal to $O(\kappa^2)$ thus justifying the neglect of f_z. Using the above results and neglecting f_z, the integral equation on the surface of a stationary disk can then be written in polar coordinates as:

$$\begin{aligned}
0 &= \delta_{ix}\kappa l(\rho) \\
&+ \int_S dS'[J_{ix}(\boldsymbol{\rho} - \boldsymbol{\rho'} + \boldsymbol{e_y}\kappa(l(\rho) - l(\rho'))) - J_{ix}(\boldsymbol{\rho} - \boldsymbol{\rho'} + \boldsymbol{e_y}\kappa(l(\rho) + l(\rho')))]f_x(\boldsymbol{\rho'}) \\
&+ \int_S dS'[J_{iy}(\boldsymbol{\rho} - \boldsymbol{\rho'} + \boldsymbol{e_y}\kappa(l(\rho) - l(\rho'))) + J_{iy}(\boldsymbol{\rho} - \boldsymbol{\rho'} + \boldsymbol{e_y}\kappa(l(\rho) + l(\rho')))]f_y(\boldsymbol{\rho'}) \\
&= \delta_{ix}\kappa l(\rho) + I_{ix} + I_{iy}
\end{aligned} \tag{3.16}$$

where $\boldsymbol{\rho}$ and $\boldsymbol{\rho'}$ are radial position vectors in the $x-z$ plane, S now only represents the top ($+y$) surface of the particle, and $\boldsymbol{e_y}$ is a unit vector in the y direction. The integral terms in the above equation now represent the disturbance field due to a pair of forces per unit area separated by the thickness of the particle at ρ' with the first term being a force dipole per unit area due to the x stresses and the second being y forces of the same sign. In the next section, boundary element method simulations as applied to the present problem are described.

3.3 Numerical Simulations

In order to exactly determine the forces and hence torques acting on the particle, we use boundary element method simulations (BEM)[151] for particles at low aspect ratio. We use 3.16 as the starting point for the simulations to be performed in this work. The unknowns in the equation are the stresses, $f_x(\boldsymbol{\rho})$ and

$f_y(\boldsymbol{\rho})$ acting on the surface. The surface of the particle in BEM is discretized into small elements and the integral equation is then reduced to a system of linear algebraic equations with the unknown stress on each element of the surface being a constant over the entire element. The system of linear algebraic equations can then be solved by using any of the traditional schemes like Gauss elimination or matrix inversion. In this section, we now show how the numerical scheme was set up.

In BEM, integral equations are solved over the surface (two-dimensional) of the particle. For our case, the computational efforts can be greatly reduced if one can determine the dependence of the stress on the azimuthal (θ) angle. In that case, the integral involved in 3.16 can be analytically integrated in the azimuthal direction. Given the axisymmetry and the fore-aft symmetry of the particles we are studying, anti-symmetry of the external flow about the $x-z$ plane and the orientation (figure 3.1 (a)) of the particle with respect to the external flow, one can determine that the dependence of the stress on the θ direction should be the same for all shapes considered here. Using the finite element software package Comsol, we have determined the following functional dependence of stresses on θ:

$$\begin{aligned} f_x(\boldsymbol{\rho}) &= f_1(\rho) \\ f_y(\boldsymbol{\rho}) &= f_2(\rho)\cos\theta \end{aligned} \tag{3.17}$$

We performed the finite element Comsol simulations in a manner similar to the ones described in Singh et al [128] for determining effective aspect ratio of cylindrical disks. In addition to cylindrical disks, we have also performed finite element Comsol simulations for the case of spheroidal, and symmetrical double cone (two cones of same dimensions joined at their circular bases) shaped par-

ticles to verify the dependence of stress on θ. Asymptotic analysis is carried out later in this work where we show that $f_x(\boldsymbol{\rho})$ to $O(\kappa)$ and $f_y(\boldsymbol{\rho})$ to $O(\kappa^2)$ also agree with the above functional dependence of stresses on θ.

Using the above dependence of stresses on θ, the governing integral equation (3.16) can be reduced to the following equations with $f_1(\rho)$ and $f_2(\rho)$ from 3.17 being the unknowns now:

$$
\begin{aligned}
-y = &\int_0^1 \rho' ds' d\theta' (f_1(\rho'))\Big[\frac{1}{(\rho''^2 + (y(\rho) - y'(\rho'))^2)^{\frac{1}{2}}} \\
&+ \frac{(\rho\cos\theta - \rho'\cos\theta')^2}{(\rho''^2 + (y(\rho) - y'(\rho'))^2)^{\frac{3}{2}}} - \frac{1}{(\rho''^2 + (y(\rho) + y'(\rho'))^2)^{\frac{1}{2}}} - \frac{(\rho\cos\theta - \rho'\cos\theta')^2}{(\rho''^2 + (y(\rho) + y'(\rho'))^2)^{\frac{3}{2}}}\Big] \\
&+ \int_0^1 \rho' ds' d\theta' f_2(\rho')\cos(\theta')\Big[\frac{(\rho\cos\theta - \rho'\cos\theta')(y(\rho) - y'(\rho'))}{(\rho''^2 + (y(\rho) - y'(\rho'))^2)^{\frac{3}{2}}} \\
&+ \frac{(\rho\cos\theta - \rho'\cos\theta')(y(\rho) + y'(\rho'))}{(\rho''^2 + (y(\rho) + y'(\rho'))^2)^{\frac{3}{2}}}\Big]
\end{aligned} \tag{3.18}
$$

$$
\begin{aligned}
0 = &\int_0^1 \rho' ds' d\theta' f_1(\rho')\Big[\frac{(\rho\cos\theta - \rho'\cos\theta')(y(\rho) - y'(\rho'))}{(\rho''^2 + (y(\rho) - y'(\rho'))^2)^{\frac{3}{2}}} \\
&- \frac{(\rho\cos\theta - \rho'\cos\theta')(y(\rho) + y'(\rho'))}{(\rho''^2 + (y(\rho) + y'(\rho'))^2)^{\frac{3}{2}}}\Big] \\
&+ \int_0^1 \rho' ds' d\theta' f_2(\rho')\cos(\theta')\Big[\frac{1}{(\rho''^2 + (y(\rho) - y'(\rho'))^2)^{\frac{1}{2}}} + \frac{(y(\rho) - y'(\rho'))^2}{(\rho''^2 + (y(\rho) - y'(\rho'))^2)^{\frac{3}{2}}} \\
&+ \frac{1}{(\rho''^2 + (y(\rho) - y'(\rho'))^2)^{\frac{1}{2}}} + \frac{(y(\rho) + y'(\rho'))^2}{(\rho''^2 + (y(\rho) + y'(\rho'))^2)^{\frac{3}{2}}}\Big]
\end{aligned} \tag{3.19}
$$

where $\rho'' = (\rho^2 + \rho'^2 - 2\rho\rho'\cos\theta'')^{\frac{1}{2}}$ is the distance between the two points ρ and ρ' in the $x - z$ plane, $\theta'' = \theta - \theta'$, and $ds' = d\rho'\left[1 + \left(\kappa\frac{dl(\rho')}{d\rho'}\right)^2\right]^{1/2}$ is the arc-length of a small element on the surface. Since the unknowns stresses $(f_1(\rho'),\ f_2(\rho'))$ in the above 4.51 and 4.52 are now independent of θ', these equations can be integrated analytically along the azimuthal direction, resulting in complete elliptic integrals. The resulting integrals are shown in the appendix A.2. The remaining

problem is then reduced to integration over any of the cross-sectional curves of the surface in $y - \rho$ planes with constant θ. We use the curve at $\theta = 0$ for our simulations.

For the one dimensional integration performed over the curve on the surface of the particle, the curve is divided into N elements. For $\alpha < 1$, the stresses on the surface of the particle vary rapidly close to the edge of the particle over a region of $O(\kappa^{\frac{1}{1-\alpha}})$ and slowly away from the edge of the particle over an $O(1)$ region. The rapid variation of the stress close to the edge and the length scale involved with it was determined from the asymptotic analysis and is discussed in detail in section IV. For the purpose of numerics, it is important to understand that there are two different length scales involved and the size of the boundary elements also need to have two length scales to perform numerical integration appropriately. Since the boundary layer thickness is small ($\sim O(\kappa^{1/(1-\alpha)})$), the size of the elements in the boundary layer (closed to the edge) needs to be very small compared to the size of the elements in the outer region (away from the edge). The size of the largest element was maintained as $ds_l = 0.001$ while the smallest element within the boundary layer was $ds_s = 0.001\kappa^{\frac{1}{1-\alpha}}$. The transition from the very small length scale in the boundary region to the larger element size in the outer region is achieved by increasing the size of the element at each step using a geometric progression. Since close to the edge, the variation along the radial direction is much smaller compared to variation in the y direction for $\alpha < 1$, arc length is discretized instead of the radial coordinate. At each step the size of the element is then given by:

$$ds_{i+1} = \frac{1}{\frac{1}{ds_l} + \frac{1}{(ds_s\beta^i)}} \tag{3.20}$$

where β is a number slightly larger than 1. For the simulation results that we present $\beta = 1.02$ is used. Tests of accuracy showed that changing the value

of β from 1.02 to 1.01 and $\beta = 1.03$ changes the torque by less than 0.1% for a spheroid with $\kappa = 0.01$. Since the integral equations to be solved are based on the coordinates of the element in the cylindrical coordinate system (4.51,4.52), we need to determine the coordinates (ρ, y) of each element on the curve. To determine the coordinates of the element, at each step we calculate $d\rho$ and dy corresponding to the size (ds) of the element and the slope:

$$d\rho_i = ds_i/(1 + m_{i-1}^2)^{\frac{1}{2}} \tag{3.21}$$
$$dy_i = ds_i/(1 + 1/m_{i-1}^2)^{\frac{1}{2}}$$

where m_i is the slope of the ith element given by:

$$m_i = \frac{dy_i}{d\rho_i} = \begin{cases} \frac{2\alpha\kappa^{\frac{1}{\alpha}}}{y_i^{\frac{1-\alpha}{\alpha}}} & \text{if } m_{i-1} > 10 \\ \frac{2\alpha\kappa\rho_i}{l(\rho_i)^{1-\alpha}} & \text{if } m_{i-1} < 10 \end{cases} \tag{3.22}$$

Here, two different relations for the slope are used to avoid round-off error as $\rho \to 1$. In figure 3.4, we present the variation of the size of the boundary element as a function of radial position for $\alpha = 1/2$ and $\kappa = 0.001$. The size of the element at $\rho = 0$ is adjusted to make sure that one end of the last element lies at $\rho = 0$. For $\alpha > 1$, since the slope at the edge is $O(\kappa)$, the surface can be discretized in radial coordinates with a constant element size of $d\rho_l = 0.001$.

For $\alpha = 0$, there is a sharp corner at $y = \kappa$ and $\rho = 1$. The sharp corner leads to a singular velocity gradient, pressure and stress near the edge but this singular stress does not contribute to the net torque. To properly resolve the corner of the particle a range of discretizations of elements near the corner is used. At $\rho = 1$, element size of κ/h ($h = 20, 50, 100, 200,$ and 500) is used and on the flat surface ($y = \kappa$) element size given by 3.20 is used with the smallest element being κ/h. For the range of h used, the torque is found to change by less than 0.3%.

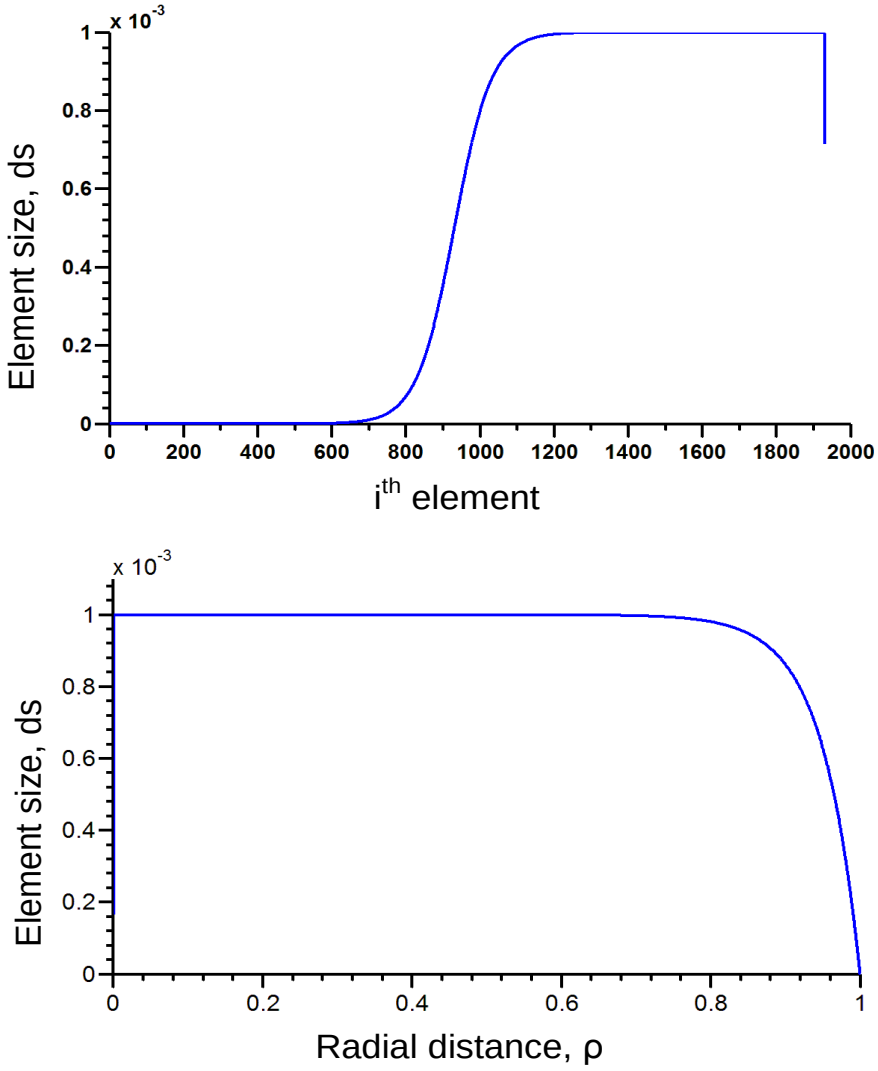

Figure 3.4: (a) Size of the ith element as given by 3.20 and (b) size of the elements as a function of the radial coordinate for $\rho = 1/2$ and $\kappa = 0.001$. The size of the last element is adjusted to make sure that one of its ends lies at $\rho = 1$.

4.51 and 4.52 are evaluated for ρ at the center of each of the N elements. Since the stress is considered constant within each element, these can be written as summation equations after carrying out the analytical integration in the θ direction as shown in appendix A.2. Each element is locally divided into N_{small} subelements. $N_{small} = 20$ is used when the element being integrated does not include the point ρ. When the element includes ρ, $N_{small} = 200$ is used for $\alpha < 1$. For $\alpha > 1$, to resolve the influence of the element containing ρ, the numerical integration needs to be performed more carefully. This is because the size of the element ($O(\kappa)$) is much larger compared to the thickness of the particle as $\rho \to 1$. The element $d\rho$ is divided into subelements ($d\xi$) of using a geometric progression in the following manner:

$$d\xi_{k+1} = \beta^k d\xi_1 \tag{3.23}$$

where $d\xi_1 = \frac{\kappa l(\rho)}{1000}$ and is the first subelement adjacent to ρ. The size of the last node is adjusted to make sure its end lies at $\rho + d\rho/2$. It should be noted here that in the limit $\rho \to \rho'$, the integrands in 4.51 and 4.52 are singular for all α. Analytical integration is performed to remove the singularities in this limit. The details of the analytical integration are given in the appendix A.2.

For N elements, the total number of unknown stress variables is $2N$, two unknown stress variables for each element. The number of equations is also $2N$. The $2N$ linear equations are then solved for the $2N$ stress variables by matrix inversion. The resultant torque acting on the particle is calculated from the f_1 and f_2 stress variables using the following equation:

$$\begin{aligned} G_A &= \int_S dS\,(y f_1 - \rho \cos^2\theta f_2) \\ &= 2\sum_{i=1}^{N} \rho_i ds_i (2\pi y_i f_{1i} - \pi \rho_i f_{2i}) \end{aligned} \tag{3.24}$$

where f_{1i} and f_{2i} are the stresses in 3.17 acting over the element i. The factor of 2 in the above equation accounts for the torque acting on the $-y$ half of the particle which by the antisymmetry of the flow about the $x-z$ plane and the fore-aft symmetry of the particle is equal in magnitude and direction to the torque acting in the $+y$ half of the particle.

3.4 Asymptotic Analysis for small κ

In the introduction, we showed using a simple scaling argument that the non-dimensionalized torque acting on a thin disk when its axis is parallel to the flow direction is $O(1)$. Using this argument, the scaling of the effective aspect ratio reduces to 3.11. When the particle is oriented with its axis in the gradient direction, we found that simple scaling arguments do not yield the correct order of the torque. In this section, we analytically solve for the stresses acting on the surface of the particle when its axis of symmetry is in the gradient direction (orientation A). Using these stresses, we determine the torque acting on the particle.

The integral representation of Stokes flow is used as the starting point of the analysis. In the limit $\kappa \to 0$, the surface of the disk can be divided into two regions: (i) The outer region where the surface is almost flat and the distance from the edge is greater than the local thickness, that is $1-\rho > O(\kappa(1-\rho^2)^\alpha)$. In this region, the problem can be treated as a regular perturbation problem. (ii) The inner region (boundary layer) exists close to the edge of the surface where the distance from the edge is of the same order as the thickness of the particle, that is $1-\rho \sim O(\kappa(1-\rho^2)^\alpha)$. The thickness of the boundary layer is $1-\rho \sim O(\kappa^{\frac{1}{1-\alpha}})$.

Based on the geometry of the particle, the inner region corresponds to the region where the slope of the particle is $O(1)$, which occurs only for shapes with $\alpha < 1$.

The rest of the analysis is divided into three parts. In the first part, we present analytical expressions for f_x and f_y stresses to the leading order and show that the torque due to the leading order stresses is zero. Then we obtain an integral equation for stresses in the outer region at the next order yielding the leading order contribution of the outer region to the torque. In the second part, we determine the size of the boundary layer and scaling of the leading order stresses acting in the boundary layer. Finally, the torque due to the stresses acting in the matching region between the inner and outer regions is calculated.

3.4.1 Torque from the outer region

In this sub-section, the leading order torque acting on the particle in the outer region is determined by solving for the stress acting on the particle . The torque from the leading order stresses ($O(1)$ for f_x and $O(\kappa)$ for f_y) turns out to be zero for thin axisymmetric particles and so we retain stresses up to ($O(\kappa)$ for f_x and $O(\kappa^2)$ for f_y) that are responsible for the first non-zero torque on the particle.

In the limit $\kappa \to 0$, the asymptotic expansion of the stresses acting on the surface of the particle and the overall torque in the vorticity direction can be represented by the following series:

$$\begin{aligned} f_x(\boldsymbol{\rho}) &= f_x^{(0)}(\boldsymbol{\rho}) + f_x^{(1)}(\boldsymbol{\rho})\kappa + \ldots\ldots \\ f_y(\boldsymbol{\rho}) &= f_y^{(1)}(\boldsymbol{\rho})\kappa + f_y^{(2)}(\boldsymbol{\rho})\kappa^2 + \ldots\ldots \\ G_A &= G_A^{(1)}\kappa + G_A^{(2)}\kappa^2 + \ldots\ldots, \end{aligned} \tag{3.25}$$

where the superscripts represent the order of the force with respect to κ. We note here that when the disk is infinitely thin, the disturbance flow is negligible and with the original flow in the $x-$ direction, a force-density in the $x-$ direction is sufficient to satisfy the no-slip boundary condition on the surface of the particle. As a result, the leading order force in the $y-$direction can only be $O(\kappa)$. Since the moment arm for f_x is $O(\kappa)$ smaller than the moment arm for f_y, the contributions to the torque by f_x and f_y are of the same order. The stress in the z direction, f_z to the leading order is less than $O(\kappa)$ (appendix A.1); f_z at $O(\kappa^2)$ could drive a stress in the x and y direction at $O(\kappa^3)$, since we will restrict ourselves to f_x at $O(\kappa)$ and f_y at $O(\kappa^2)$ hence we do not need to consider f_z for our analysis.

Beginning with the velocity field in the x-direction ($i = x$) and the boundary condition $v_x = 0$ on the surface, 3.16 reduces to:

$$-\kappa l(\rho) = I_{xx} + I_{xy} \tag{3.26}$$

To obtain the leading order solution for the stress, the above equation needs to be solved to $O(\kappa)$ since the driving term on the left hand side is $O(\kappa)$. The integrals I_{xx} and I_{xy} are the disturbance velocity fields in the x direction due to f_x and f_y stresses respectively. Here I_{xx} is the disturbance field due to a distribution of force dipoles per unit area where each force dipole consists of two forces of equal magnitude and opposite direction separated by the thickness of the particle with one force acting on the $+y$ half of the surface and the other acting on the $-y$ half of the surface. I_{xx} can be written as:

$$I_{xx} = \int_S dS' [J_{xx}(\boldsymbol{\rho} - \boldsymbol{\rho'} + \boldsymbol{e_y}\kappa(l(\rho) - l(\rho'))) - J_{xx}(\boldsymbol{\rho} - \boldsymbol{\rho'} + \boldsymbol{e_y}\kappa(l(\rho) + l(\rho')))] f_x(\boldsymbol{\rho'}) \tag{3.27}$$

The above integral has a singularity at $\boldsymbol{\rho} = \boldsymbol{\rho'}$. In the limit $\kappa \to 0$, the integrals can be divided into two parts: $|\boldsymbol{\rho} - \boldsymbol{\rho'}| \sim O(\kappa)$ and $|\boldsymbol{\rho} - \boldsymbol{\rho'}| > O(\kappa)$. In the region

where $|\boldsymbol{\rho} - \boldsymbol{\rho'}| \sim O(\kappa)$, the radial distance between the points ρ and ρ' is of the same order as the thickness of the particle. In the second region where $|\boldsymbol{\rho} - \boldsymbol{\rho'}| > O(\kappa)$, the thickness of the particle is smaller than the distance between the two points on the particle in the $x-z$ plane. In the region, where $|\boldsymbol{\rho} - \boldsymbol{\rho'}| = \rho'' \sim O(\kappa)$, one can write to the leading order $l(\rho) = l(\rho')$ and $f_x(\boldsymbol{\rho'}) = f_x(\boldsymbol{\rho})$. Rewriting I_{xx} as:

$$\begin{aligned} I_{xx} &= \int_S dS' \{[J_{xx}(\boldsymbol{\rho} - \boldsymbol{\rho'} + \boldsymbol{e_y}\kappa(l(\rho) - l(\rho'))) - J_{xx}(\boldsymbol{\rho} - \boldsymbol{\rho'} + \boldsymbol{e_y}\kappa(l(\rho) + l(\rho')))] f_x(\boldsymbol{\rho'}) \\ &\quad - [J_{xx}(\boldsymbol{\rho} - \boldsymbol{\rho'}) - J_{xx}(\boldsymbol{\rho} - \boldsymbol{\rho'} + \boldsymbol{e_y} 2\kappa l(\rho))] f_x(\boldsymbol{\rho})\} \\ &\quad + \int_S dS' [J_{xx}(\boldsymbol{\rho} - \boldsymbol{\rho'}) - J_{xx}(\boldsymbol{\rho} - \boldsymbol{\rho'} + \boldsymbol{e_y} 2\kappa l(\rho))] f_x(\boldsymbol{\rho}) \\ &\quad = I^*_{xx} + I^{**}_{xx} \end{aligned} \tag{3.28}$$

yields an integral, I^*_{xx}, whose dominant contribution comes from $|\boldsymbol{\rho} - \boldsymbol{\rho'}| > O(\kappa)$ and another integral, I^{**}_{xx}, whose dominant contribution comes from $|\boldsymbol{\rho} - \boldsymbol{\rho'}| \sim O(\kappa)$. For $|\boldsymbol{\rho} - \boldsymbol{\rho'}| = \rho'' > O(\kappa)$, one can Taylor expand the Green function involved in I_{xx} as:

$$J_{xx}(\boldsymbol{\rho} - \boldsymbol{\rho'} + \boldsymbol{e_y}\kappa(l(\rho) - l(\rho'))) = J_{xx}(\boldsymbol{\rho} - \boldsymbol{\rho'}) + \kappa(l(\rho') - l(\rho)) \frac{\partial J_{xx}(\boldsymbol{\rho} - \boldsymbol{\rho'})}{\partial y} + O(\kappa^2) \tag{3.29}$$

Using the Taylor series expansion of the Green's function in I^*_{xx} to $O(\kappa)$, when $|\boldsymbol{\rho} - \boldsymbol{\rho'}| \sim O(1)$, we get

$$\begin{aligned} I^*_{xx} &= \int_S dS' \left(\left[-2\kappa l(\rho) \frac{\partial J_{xx}(\boldsymbol{\rho} - \boldsymbol{\rho'})}{\partial y} \right] (f_x(\rho') - f_x(\rho)) \right) + O(\kappa^2) \\ &= \int_S dS' \left(\left[-2\kappa l(\rho) \cancel{\left(-\frac{y}{\rho''^3} - \frac{3x^2 y}{\rho''^5} \right)_{y=0}} \right]^0 (f_x(\rho') - f_x(\rho)) \right) + O(\kappa^2) \\ &= O(\kappa^2) \end{aligned} \tag{3.30}$$

We now account for the $\rho'' \sim O(\kappa)$ contribution in the integral I^{**}_{xx}. When $\rho'' \sim O(\kappa)$, we move the center of the coordinate system to the point of interest ρ. A differential area, with ρ being the center of the coordinate system, can be written

as $dS' = \rho'' d\rho'' d\theta''$. Here we neglect the slope of the particle when defining the arc length, $ds'' = d\rho''[1 + (\kappa \frac{dl(\rho'')}{d\rho''})^2]^{1/2} = d\rho'' + O(\kappa^2)$, i.e. to $O(\kappa)$, the arc length is equal to the distance between the two points in the $x-z$ plane. Scaling the distance in this coordinate system with κ and defining another variable as $\rho^* = \frac{\rho''}{\kappa}$, we can write I^{**}_{xx} as:

$$I^{**}_{xx} = \frac{\kappa f_x(\boldsymbol{\rho})}{8\pi} \int_0^\infty \rho^* d\rho^* \int_0^{2\pi} \Big[\frac{1}{\rho^*} - \frac{1}{(\rho^{*2} + 4l^2(\rho))^{1/2}} + \frac{\rho^{*2} \cos^2\theta''}{\rho^{*3}} - \frac{\rho^{*2} \cos^2\theta''}{(\rho^{*2} + 4l^2(\rho))^{3/2}} \Big] d\theta'' + O(\kappa^2) \tag{3.31}$$

In terms of the scaled variable ρ^*, the distance from the center of the coordinate system to the edge of the disk is $O(\frac{1}{\kappa}) \to \infty$, so that the upper limit of the above integral in ρ^* variable can be set to ∞. The integrand in 3.31 has an integrable singularity. Angular integration of 3.31 gives:

$$\begin{aligned} I^{**}_{xx} &= \frac{\kappa f_x(\boldsymbol{\rho})}{4} \int_0^\infty \rho^* d\rho^* \left[\frac{3}{2\rho^*} - \frac{1}{(\rho^{*2} + 4l^2(\rho))^{1/2}} - \frac{\rho^{*2}}{2(\rho^{*2} + 4l^2(\rho))^{3/2}} \right] + O(\kappa^2) \\ &= f_x(\boldsymbol{\rho})(\kappa l(\rho) + O(\kappa^2)) \end{aligned} \tag{3.32}$$

Adding contributions to I_{xx} from the two regions, $\rho'' > O(\kappa)$ and $\rho'' \sim O(\kappa)$, we get from 3.30 and 3.32:

$$I_{xx} = f_x(\boldsymbol{\rho})(\kappa l(\rho) + O(\kappa^2)) \tag{3.33}$$

It should be noted here that only the region $\rho'' \sim O(\kappa)$ contributes to I_{xx} at $O(\kappa)$. Thus, the leading order disturbance field generated in the x direction due to f_x surface stress is a resultant of forces acting in a small region of $O(\kappa)$ around the point of interest, ρ.

Now, we do a similar analysis for the I_{xy} integral. Unlike I_{xx}, I_{xy} represents a disturbance field due to two stresses of equal magnitude acting in the same

direction, where one stress is acting on the $+y$ half of the surface and the other stress is acting on the $-y$ half of the surface. I_{xy} can be written as:

$$I_{xy} = \int_S dS'[J_{xy}(\boldsymbol{\rho} - \boldsymbol{\rho'} + \boldsymbol{e_y}\kappa(l(\rho) - l(\rho'))) + J_{xy}(\boldsymbol{\rho} - \boldsymbol{\rho'} + \boldsymbol{e_y}\kappa(l(\rho) + l(\rho')))]f_y(\boldsymbol{\rho'}) \tag{3.34}$$

In the limit when $\kappa \to 0$, it is once again useful to divide the integral into two parts:

$$\begin{aligned} I_{xy} &= \int_S dS'([J_{xy}(\boldsymbol{\rho} - \boldsymbol{\rho'} + \boldsymbol{e_y}\kappa(l(\rho) - l(\rho'))) + J_{xy}(\boldsymbol{\rho} - \boldsymbol{\rho'} + \boldsymbol{e_y}\kappa(l(\rho) + l(\rho')))]f_y(\boldsymbol{\rho'}) \\ &\quad - [J_{xy}(\boldsymbol{\rho} - \boldsymbol{\rho'}) + J_{xy}(\boldsymbol{\rho} - \boldsymbol{\rho'} + \boldsymbol{e_y}2\kappa(l(\rho)))]f_y(\boldsymbol{\rho})) \\ &\quad + \int_S dS'[J_{xy}(\boldsymbol{\rho} - \boldsymbol{\rho'}) + J_{xy}(\boldsymbol{\rho} - \boldsymbol{\rho'} + \boldsymbol{e_y}2\kappa(l(\rho)))]f_y(\boldsymbol{\rho}) \\ &= I^*_{xy} + I^{**}_{xy} \end{aligned} \tag{3.35}$$

where the dominant contribution to I^*_{xy} comes from $|\boldsymbol{\rho} - \boldsymbol{\rho'}| > O(\kappa)$ and the dominant contribution to I^{**}_{xy} comes from $|\boldsymbol{\rho} - \boldsymbol{\rho'}| \sim O(\kappa)$. For $|\boldsymbol{\rho} - \boldsymbol{\rho'}| > O(\kappa)$, one can Taylor expand the Green function involved in I_{xy} as:

$$J_{xy}(\boldsymbol{\rho} - \boldsymbol{\rho'} + \boldsymbol{e_y}\kappa(l(\rho) - l(\rho'))) = \cancelto{0}{J_{xy}(\boldsymbol{\rho} - \boldsymbol{\rho'})} + \kappa(l(\rho) - l(\rho'))\frac{\partial J_{xy}(\boldsymbol{\rho} - \boldsymbol{\rho'})}{\partial y} + O(\kappa^2) \tag{3.36}$$

where, $J_{xy}(\boldsymbol{\rho} - \boldsymbol{\rho'}) = \frac{\rho' \cos\theta' y}{\rho''^3}|_{y=0} = 0$. Using the Taylor series expansion of the Green's function, J_{xy}, in I^*_{xy} when $|\boldsymbol{\rho} - \boldsymbol{\rho'}| = \rho'' \sim O(1)$, we get

$$\begin{aligned} I^*_{xy} &= \int_S dS'[2\kappa l(\rho)\frac{\partial J_{xy}(\boldsymbol{\rho} - \boldsymbol{\rho'})}{\partial y}f_y(\rho') - 2\kappa l(\rho)\frac{\partial J_{xy}(\boldsymbol{\rho} - \boldsymbol{\rho'})}{\partial y}f_y(\rho)] \\ &= \int_S dS' 2\kappa l(\rho) f_y(\rho')\left[\frac{\cos\theta''}{8\pi\rho''^2} + O(\kappa)\right] - f_y(\rho)\int \rho'' d\rho'' 2\kappa l(\rho)\int_0^{2\pi} d\theta''\left[\frac{\cos\theta''}{8\pi\rho''^2} + O(\kappa)\right] \\ &= \int_S dS' 2\kappa l(\rho) f_y(\rho')\left[\frac{\cos\theta''}{8\pi\rho''^2}\right] + O(\kappa^3) \end{aligned} \tag{3.37}$$

Using $|\boldsymbol{\rho} - \boldsymbol{\rho'}| = \rho'' \sim O(\kappa)$ in I^{**}_{xy}, we get

$$\begin{aligned} I^{**}_{xy} &= \int_S dS' 2\kappa l(\rho) f_y(\boldsymbol{\rho}) \left(\frac{\rho'' \cos\theta''}{\rho''^3} - \frac{\rho'' \cos\theta'' y^2}{\rho''^5}\right)\Big|_{y=0} \\ &= 2\kappa l(\rho) f_y(\boldsymbol{\rho}) \int_\rho^{\rho-1} \rho'' d\rho'' \frac{\rho''}{\rho''^3} \int_0^{2\pi} d\theta'' \cos\theta'' + O(\kappa^3) \\ &= O(\kappa^3) \end{aligned} \tag{3.38}$$

Combining results from 3.37 and 3.38, the complete I_{xy} is given by:

$$I_{xy} = \int_S dS' 2\kappa l(\rho) f_y(\boldsymbol{\rho'}) \frac{\cos\theta''}{8\pi\rho''^2} + O(\kappa^3) \tag{3.39}$$

Combining 3.26, 3.33, and 3.39, one can write the velocity field balance in the x direction as:

$$-\kappa l(\rho) = f_x(\boldsymbol{\rho})(\kappa l(\rho) + O(\kappa^2)) + \int_S dS' 2\kappa l(\rho) f_y(\boldsymbol{\rho'}) \frac{\cos\theta''}{8\pi\rho''^2} + O(\kappa^3) \tag{3.40}$$

We now use the velocity boundary condition in the y direction. To solve for the leading order force in the y direction, we again start with 3.16 for $i = y$ with the boundary condition $v_y = 0$ on the surface of the particle. 3.16 can then be written as:

$$v_y = 0 = I_{yx} + I_{yy} \tag{3.41}$$

The integrals I_{yx} and I_{yy} are the disturbance velocity fields in the y direction due to f_x and f_y stresses respectively. Like I_{xx}, I_{yx} is a disturbance field induced by a distribution of stress dipole terms whereas I_{yy} like I_{xy} is induced by a pair of stress distributions acting in the same direction. The undisturbed external velocity field in the y direction on the surface of the particle is zero, hence unlike the integral equation in x direction there is no external driving term here to drive a surface stress in the y direction. The driving term for the f_y stress comes

from the disturbance fields in the y direction, which are induced by the f_x stress (I_{yx} term). As we have seen earlier, f_x stress is originally driven by the externally imposed simple shear flow. The disturbance field, I_{yy}, due to the stress f_y then cancels the disturbance field, I_{yx}, due to f_x, to satisfy the no slip boundary condition in the y direction.

The disturbance field due to the stress f_x, I_{yx} is given by:

$$I_{yx} = \int_S dS' [J_{yx}(\boldsymbol{\rho} - \boldsymbol{\rho'} + \boldsymbol{e_y}\kappa(l(\rho) - l(\rho'))) - J_{yx}(\boldsymbol{\rho} - \boldsymbol{\rho'} + \boldsymbol{e_y}\kappa(l(\rho) + l(\rho')))] f_x(\boldsymbol{\rho'}) \tag{3.42}$$

Again we divide the integral into two parts dominated by $|\boldsymbol{\rho} - \boldsymbol{\rho'}| \sim O(\kappa)$ and $|\boldsymbol{\rho} - \boldsymbol{\rho'}| > O(\kappa)$. In the region, where $|\boldsymbol{\rho} - \boldsymbol{\rho'}| = \rho'' \sim O(\kappa)$, one can write to the leading order $l(\rho) = l(\rho')$ and $f_x(\boldsymbol{\rho'}) = f_x(\boldsymbol{\rho})$. Rewriting I_{yx} to take account of these two regions, we have

$$\begin{aligned} I_{yx} = & \int_S dS' ([J_{yx}(\boldsymbol{\rho} - \boldsymbol{\rho'} + \boldsymbol{e_y}\kappa(l(\rho) - l(\rho'))) - J_{yx}(\boldsymbol{\rho} - \boldsymbol{\rho'} + \boldsymbol{e_y}\kappa(l(\rho) + l(\rho')))] f_x(\boldsymbol{\rho'}) \\ & - [J_{yx}(\boldsymbol{\rho} - \boldsymbol{\rho'}) - J_{yx}(\boldsymbol{\rho} - \boldsymbol{\rho'} + \boldsymbol{e_y} 2\kappa l(\rho))] f_x(\boldsymbol{\rho})) \\ & + \int_S dS' [J_{yx}(\boldsymbol{\rho} - \boldsymbol{\rho'}) - J_{yx}(\boldsymbol{\rho} - \boldsymbol{\rho'} + \boldsymbol{e_y} 2\kappa l(\rho))] f_x(\boldsymbol{\rho}) \\ & = I^*_{yx} + I^{**}_{yx} \end{aligned} \tag{3.43}$$

Here the integral I^*_{yx} captures the behavior of the integral in the region $\rho'' > O(\kappa)$ and the integral I^{**}_{yx} captures the behavior in the region $\rho'' \sim O(\kappa)$. When $\kappa \to 0$ and $|\rho - \rho'| > O(\kappa)$, the Taylor series expansion of the Green's function J_{yx} is given as:

$$J_{yx}(\boldsymbol{\rho} - \boldsymbol{\rho'} + \boldsymbol{e_y}\kappa(l(\rho) - l(\rho'))) = 0 + \kappa(l(\rho) - l(\rho')) \frac{\partial J_{yx}(\boldsymbol{\rho} - \boldsymbol{\rho'})}{\partial y} + O(\kappa^2) \tag{3.44}$$

Using the above Taylor series expanion for I^*_{yx}, we get

$$\begin{aligned} I^*_{yx} &= \int_S dS'(-2\kappa l(\rho')\frac{\partial J_{yx}(\boldsymbol{\rho}-\boldsymbol{\rho'})}{\partial y}f_x(\rho') + 2\kappa l(\rho)\frac{\partial J_{yx}(\boldsymbol{\rho}-\boldsymbol{\rho'})}{\partial y}f_x(\rho)) \\ &= -\int_S dS' 2\kappa(l(\rho')f_x(\rho') - l(\rho)f_x(\rho))\frac{\rho''\cos\theta''}{\rho''^3} \\ &= -\int_S dS' 2\kappa l(\rho')f_x(\boldsymbol{\rho'})\frac{\partial}{\partial x'}(\frac{1}{\rho''}) \end{aligned} \tag{3.45}$$

The integral, I^*_{yx} has a singularity of type $\frac{1}{\rho-\rho'}$, which is integrable in the Cauchy principal value sense for generalized functions [100] . Here the Oseen tensor is a Green's function and is driven by the delta function and both are generalized functions. Using integration by parts, we get:

$$I^*_{yx} = 2\kappa\int_S \frac{dS'}{\rho''}\frac{\partial}{\partial x'}[l(\rho')f_x(\boldsymbol{\rho'})] \tag{3.46}$$

When $\rho'' \sim O(\kappa)$, the other integral I^{**}_{yx} can be written as:

$$I^{**}_{yx} = f_x(\boldsymbol{\rho})\int_S dS'\left[\left(\frac{\rho''\cos\theta''\kappa(l(\rho)-l(\rho'))}{(\rho''^2+\kappa(l(\rho)-l(\rho'))^2)^{\frac{3}{2}}}\right) - (\frac{\rho''\cos\theta''\kappa(l(\rho)+l(\rho'))}{(\rho''^2+\kappa(l(\rho)+l(\rho'))^2)^{\frac{3}{2}}})\right] \tag{3.47}$$

Substituting the Taylor series expansion of $l(\rho) - l(\rho') = \frac{dl(\rho)}{d\rho}\boldsymbol{\rho''}.\boldsymbol{e_\rho}$ to $O(\kappa)$ where $\boldsymbol{e_\rho}$ is a unit vector in the radial direction, the above expression becomes,

$$\begin{aligned} I^{**}_{yx} = \int_0^\infty\int_0^{2\pi}\kappa^2\rho^* d\rho^* d\theta''\Big[&\frac{\kappa^2\rho^*\cos\theta''(dl/d\rho)\boldsymbol{\rho''}.\boldsymbol{e_\rho}}{\kappa^3\rho^{*3}} \\ &- \frac{\kappa^2\rho^*\cos\theta''[2l(\rho)+(dl/d\rho)\boldsymbol{\rho''}.\boldsymbol{e_\rho}]}{\kappa^3(\rho^{*2}+4l(\rho)^2)^{\frac{3}{2}}}\Big]f_x(\boldsymbol{\rho}) \end{aligned} \tag{3.48}$$

Writing the above integral as a sum of two separate integrals:

$$\begin{aligned} I^{**}_{yx} = &\int_0^\infty\int_0^{2\pi}\kappa\rho^* d\rho^* d\theta''\frac{\rho^*\cos\theta''(dl/d\rho)\boldsymbol{\rho''}.\boldsymbol{e_\rho}[(\rho^{*2}+4l(\rho)^2)^{\frac{3}{2}} - \rho^{*3}]f_x(\boldsymbol{\rho})}{\rho^{*3}(\rho^{*2}+4l(\rho)^2)^{\frac{3}{2}}} \\ &- \int_0^\infty\int_0^{2\pi}\kappa\rho^* d\rho^* d\theta''\frac{\rho^*\cos\theta''2l(\rho)f_x(\boldsymbol{\rho})}{(\rho^{*2}+4l(\rho)^2)^{\frac{3}{2}}} \quad \rightarrow 0 \end{aligned} \tag{3.49}$$

The second integral above goes to zero, because $\int_0^{2\pi} d\theta''\cos\theta'' = 0$. Using $\boldsymbol{\rho''}.\boldsymbol{e_\rho} =$

$\kappa\rho^*(\cos\theta''\cos\theta + \sin\theta''\sin\theta)$, the remaining integral can now be written as:

$$I^{**}_{yx} = f_x(\boldsymbol{\rho})\kappa^2\frac{dl}{d\rho}\int_0^\infty \rho^* d\rho^* \frac{[(\rho^{*2} + 4l(\rho)^2)^{\frac{3}{2}} - \rho^{*3}]}{\rho^*[\rho^{*2} + 4l(\rho)^2]^{\frac{3}{2}}}\int_0^{2\pi} d\theta''(\cos^2\theta''\cos\theta + \frac{\sin 2\theta''}{2}\sin\theta)$$
$$= 4\pi\kappa^2\cos\theta l(\rho) f_x(\boldsymbol{\rho})\frac{dl(\rho)}{d\rho} \tag{3.50}$$

Thus, combining the integrals from 3.46 and 3.50, the velocity disturbance field in the y direction due to the f_x stress can be written as:

$$\begin{aligned} I_{yx} &= I^*_{yx}|_{\rho''>O(\kappa)} + I^*_{yx}|_{\rho''\sim O(\kappa)} + I^{**}_{yx}|_{\rho''>O(\kappa)} + I^{**}_{yx}|_{\rho''\sim O(\kappa)} \\ &= 2\kappa\int_S \frac{dS'}{\rho''}\frac{\partial}{\partial x}[l(\rho')f_x(\boldsymbol{\rho'})] + 4\pi\kappa^2\cos\theta l(\rho)f_x(\boldsymbol{\rho})\frac{dl(\rho)}{d\rho} \end{aligned} \tag{3.51}$$

Now writing the velocity disturbance field, I_{yy} in the y direction due to f_y, we get:

$$\begin{aligned} I_{yy} &= \int_S dS'[J_{yy}(\boldsymbol{\rho} - \boldsymbol{\rho'} + \boldsymbol{e_y}\kappa(l(\rho) - l(\rho'))) + J_{yy}(\boldsymbol{\rho} - \boldsymbol{\rho'} + \boldsymbol{e_y}\kappa(l(\rho) + l(\rho')))]f_y(\boldsymbol{\rho'}) \\ &= \int dS'\frac{2f_y(\boldsymbol{\rho'})}{\rho''} + O(\kappa^3) \end{aligned} \tag{3.52}$$

Combining 3.51 and 3.52 we get,

$$\int_S dS'\frac{1}{\rho''}2f_y(\boldsymbol{\rho'}) + O(\kappa^3) = -4\pi\kappa^2\cos\theta l(\rho)f_x(\boldsymbol{\rho})\frac{dl(\rho)}{d\rho} - 2\kappa\int_S\frac{dS'}{\rho''}\frac{\partial}{\partial x'}[l(\rho')f_x(\boldsymbol{\rho'})] \tag{3.53}$$

The above equation suggests that for f_x of $O(1)$, the driving term for f_y will be $O(\kappa)$. Hence the leading order f_y must be $O(\kappa)$ to satisfy the above equation, thus validating the expansion shown in 3.25 in the beginning of this section.

We have so far solved the momentum balance equations in the x and y direction to $O(\kappa^2)$. The obtained results are shown in 3.40 for the x momentum balance and 3.53 for the y momentum balance. These are the governing equations which are analyzed to $O(\kappa)$ in the next subsection. In subsection A2, using

physical arguments we show why the torque is zero to $O(\kappa)$ for thin disks irrespective of the shape of the particle. In subsection A3, we solve for the next order stresses to calculate torque at $O(\kappa^2)$.

Leading order forces in the outer region:

To calculate the first approximation to the stresses in the outer region, we solve 3.40 and 3.53 to the leading order after inserting the stress expansion from 3.25. Rewriting 3.40 to $O(\kappa)$ using the expansions for f_x and f_y, we get:

$$\begin{aligned} -\kappa l(\rho) &= f_x^{(0)}(\boldsymbol{\rho})\kappa l(\rho) \\ f_x^{(0)}(\boldsymbol{\rho}) &= -1 \end{aligned} \tag{3.54}$$

As expected the leading order force in the x direction is $O(1)$. The magnitude of the force is equal to what one would expect from the undisturbed simple shear flow on a flat surface and is independent of the exact shape of the particle in the outer region. It should be noted here that this is the force that a thin stationary particle exerts on the fluid, the force exerted by the fluid on the particle is equal in magnitude and opposite in sign.

Now to extract the leading order surface stress in the y direction, we rewrite 3.53 to $O(\kappa)$ using the expansion for f_y:

$$\begin{aligned} \kappa \int_S dS' \frac{1}{\rho''} 2 f_y^1(\boldsymbol{\rho}') &= -2\kappa \int_S \frac{dS'}{\rho''} \frac{\partial}{\partial x}[l(\rho') f_x^0(\boldsymbol{\rho}')] \\ f_y^1(\boldsymbol{\rho}) &= -\cos\theta \frac{\partial}{\partial \rho}(f_x^0(\boldsymbol{\rho}) l(\rho)) \end{aligned} \tag{3.55}$$

Although f_x to the leading order is $O(1)$ and f_y is $O(\kappa)$, the torques due to both f_x and f_y are of the same order since the moment arm for f_x is $O(\kappa)$ and the

moment arm for f_y is $O(1)$. The torque due to these leading order stresses can then be given as:

$$\begin{aligned} G_A^{(1)} &= \int dS\,(f_x^{(0)}(\rho)l(\rho) - f_y^{(1)}(\rho)x) \\ G_A^{(1)} &= \int dS\left[f_x^{(0)}(\rho)l(\rho) + \frac{dl(\rho)f_x^{(0)}(\rho)}{d\rho}\rho\cos^2\theta\right] \\ &= \pi\int_0^1 \rho d\rho\left[2l(\rho)f_x^{(0)}(\rho) + \rho\frac{dl(\rho)f_x^{(0)}(\rho)}{d\rho}\right] \end{aligned}$$

where $G_A^{(1)}$ is the $O(\kappa)$ contribution to the torque. Performing integration by parts, the above integral gives:

$$\begin{aligned} G_A^{(1)} &= \pi\int_0^1 \rho d\rho\left[2l(\rho)f_x^{(0)}(\rho) - 2l(\rho)f_x^{(0)}(\rho)\right] + \left[\pi\rho^2 l(\rho)f_x^{(0)}(\rho)\right]_{\rho=0}^{\rho=1} \\ &= 0 \end{aligned} \tag{3.56}$$

Thus, there is no torque originating from the leading order stresses in the outer region for any axisymmetric shape with fore-aft symmetry and $l(1) = 0$. Clearly, shapes described by 3.7 fall in this class and hence the torque acting on them to $O(\kappa)$ from the stresses on the outer region is zero. To get a non-zero torque, we need to now solve for the next order stresses. But before we do that, let us first examine why the torques in the vorticity direction due to the leading order stresses in the x and y direction cancel each other.

Physical reason for no net torque due to the leading order stresses

It is interesting to note that the torque due to the leading order stresses turns out to be zero (3.56) irrespective of the shape for thin particles. Here, we give a simple physical argument to explain why the torque due to $f_x^{(0)}$ cancels the torque due to $f_y^{(1)}$. When a thin particle with fore-aft symmetry is placed in simple

shear flow with its axis of symmetry in the gradient direction, the most obvious surface stresses acting on a unit element of the stationary particle would be equal and opposite stresses on the surface in the $+y$ and $-y$ half of the surface in the x direction separated by the thickness of the particle. Such a distribution of stress cancels the externally imposed simple shear flow and satisfies the no slip boundary condition in the x direction.We note again that while $f_x^{(0)}$ acting on a local region of $O(\kappa)$ around a point creates a velocity disturbance that cancels the mean shear flow at that point and satisfies the no slip boundary condition (3.32), the velocity disturbance in the y direction to the leading order is caused by $f_x^{(0)}$ acting over the entire disk, $\rho - \rho' > O(\kappa)$ (3.46). This $f_x^{(0)}$ stress acting on the top and bottom surface of the disk can be decomposed into a stresslet (symmetric force dipole) and a rotlet (antisymmetric force dipole). This decomposition is illustrated in figure 3.5 along with the fluid velocity field produced by the stresslet and rotlet. While the stresslet's fluid velocity field is nearly zero at the disk surface with a very small difference of velocity above and below the disk to balance the simple shear velocity disturbance, the rotlet velocity disturbance creates a large y-velocity at the disk surface that violates the no slip boundary condition. In order to satisfy the no slip boundary condition at the particle surface, the surface element must experience equal and opposite y forces on the two edges as well as equal and opposite x forces on the two faces leading to no net rotlet and but only a stresslet as illustrated in figure 3.5 (b). The y forces from neighboring elements cancel exactly leading to no net y stress when the surface is flat. When the thickness of the disk and the force per unit area varies with position, the y-stresses of neighboring elements do not exactly cancel and there is a net y-stress.

The form of the force f_y needed to cancel the disturbance flow can be argued

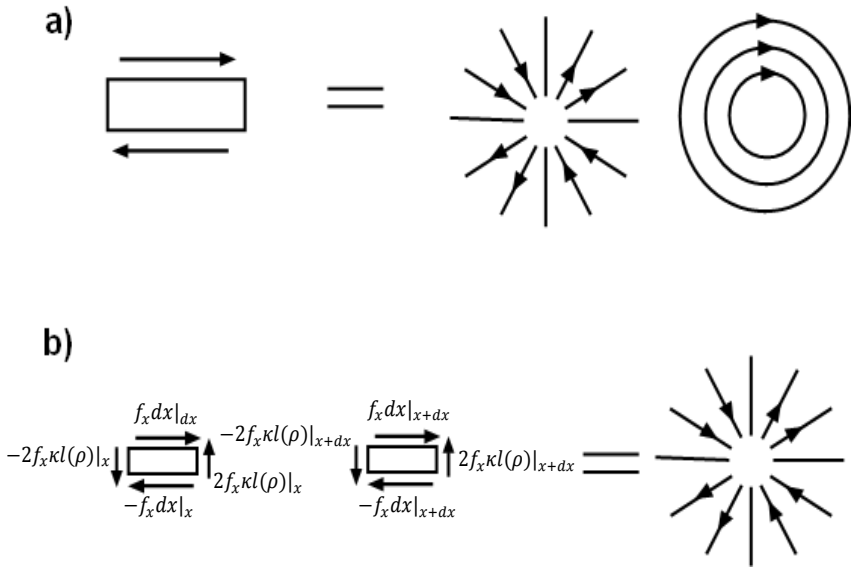

Figure 3.5: a) The forces on a disk in the x-direction illustrated on the left can be decomposed into a stresslet per unit area and a rotlet per unit area. The figures on the right illustrate the streamlines due to the stresslet, which cancels the simple shear velocity field at the disk surface, and the rotlet which leads to a y-velocity at the disk surface. B) Schematic of forces acting on two adjacent elements of size dx on the disk. A force in the y-direction of strength $2f_y(\rho)dx = -2f_x\kappa l(\rho)|_{x+dx} + 2f_x\kappa l(\rho)|_x$ balances the forces on the edge of the element leading to a stresslet with no rotlet and satisfies the no slip boundary condition in the y-direction.

in the following manner. On a surface element of size dS, the $x-$force is $f_x dS$ and the force dipole due to a pair of forces separated by $2\kappa l(\rho)$ is $2f_x\kappa l(\rho)dS$. To cancel the y disturbance field we need an equivalent f_y force dipole. The separation between the f_y stress acting on a small unit element of size dS is dx (where $dx >> \kappa$). The direction of f_y is the same on the $+y$ and $-y$ half of the particle surface, hence the strength of the force dipole due to the stress, f_y is given by $2f_y dxdS$. The balance between the two force dipoles can then be written as:

$$dS\,[2f_x(\boldsymbol{\rho})\kappa l(\rho)|_{x-\frac{dx}{2}} - 2f_x(\boldsymbol{\rho})\kappa l(\rho)|_{x+\frac{dx}{2}}] + 2f_y(\boldsymbol{\rho})dxdS = 0$$
$$-\frac{d}{dx}[f_x(\boldsymbol{\rho})\kappa l(\rho)] = f_y \tag{3.57}$$

With the above distribution of stresses in the y direction, the boundary condition $v_y = 0$ is satisfied to $O(\kappa)$. This distribution of stress along with leading order f_x stress results in no torque at $O(\kappa)$.

The case of the torque on a thin disk aligned with its long axes in the flow-vorticity plane described above can be compared with that of the torque on a long slender fiber with its long axis aligned in the flow direction. As noted in the introduction a naive estimate based on the assumption that stresses of $O(\mu\gamma)$ act on the particle and lead to a torque suggests that the torque in both cases is $O(\mu\gamma d^2 L)$. We have just seen that this estimate is too large for a disk because the nearly parallel flat surfaces of the disk yield a stresslet per unit area rather than a rotlet per unit area. Similarly, for a fiber with pointed ends, the naive estimate of $O(\mu\gamma d^2 L)$ torque when the fiber is aligned in the direction of flow is too large. The leading order torque on a slender fiber is $O(\mu\gamma d^2 L/ln\kappa)$ [34]. For a blunt slender fiber (for instance a cylindrical fiber), the leading order estimate of $O(\mu\gamma d^2 L)$ is correct but in this case torque originates from a force of $O(\mu\gamma d^2)$

at the end. We will see later that for sufficiently blunt disks the torque from the end also dominates over that from the outer region.

Next order stresses in the outer region:

In order to obtain a non-zero torque, we now calculate the stresses to the next order. The leading order $f_x^{(0)}$ as shown in the previous section is driven by the undisturbed shear flow velocity. The leading order $f_y^{(1)}$ is then driven by the disturbance field produced by $f_x^{(0)}$. Now, at the next order, from 3.40 one can conclude that is $f_x^{(1)}$ is driven by $f_x^{(0)}$ and $f_y^{(1)}$. Similarly, $f_y^{(2)}$ is driven by $O(\kappa^2)$ contribution of $f_x^{(0)}$ and $f_x^{(1)}$ in 3.53.

To get a non-zero torque at the next order, it turns out that one only needs to solve for $f_y^{(2)}$. As we will see later in this analysis, the contribution of the $f_x^{(1)}$ term to $f_y^{(2)}$ is of the same form as the contribution of the $f_x^{(0)}$ term to $f_y^{(1)}$ which did not result in any net torque and this result was found to be independent of the actual form of $f_x^{(0)}$ (3.56). Thus, to calculate the torque at $O(\kappa^2)$, we do not need to solve for the exact form of $f_x^{(1)}$.

Inserting the force expansion from 3.25 in the $y-$momentum balance 3.53 to $O(\kappa^2)$, one gets:

$$\int_S dS' \frac{1}{\rho''} 2 f_y^{(2)}(\boldsymbol{\rho'}) = -4\pi \cos\theta l(\rho) f_x^0(\boldsymbol{\rho}) \frac{dl(\rho)}{d\rho} - 2\int_S \frac{dS'}{\rho''} \frac{\partial}{\partial x'} [l(\rho') f_x^1(\boldsymbol{\rho'})] \tag{3.58}$$

Rewriting the above equation by combining the integrals,

$$-4\pi \cos\theta l(\rho) f_x^{(0)}(\boldsymbol{\rho}) \frac{dl(\rho)}{d\rho} = \int \frac{dS'}{\rho''} (f_y^{(2)}(\rho') + \cos\theta' \frac{d}{d\rho'} [l(\rho') f_x^{(1)}(\boldsymbol{\rho'})]) \tag{3.59}$$

In 3.59, the first order stress in the x direction, $f_x^{(1)}$ drives a component of $f_y^{(2)}$ in the same way as f_x^0 drives $f_y^{(1)}$. But in addition to $f_x^{(1)}$ driving a disturbance field in the $y-$ direction at $O(\kappa^2)$, $f_x^{(0)}$ also drives a term at $O(\kappa^2)$, the resultant stress term, $f_y^{(2)}$ is then driven by a combination of these two disturbance fields at $O(\kappa^2)$. The torque originating from the next order stresses, $f_x^{(1)}$ and $f_y^{(2)}$ in the outer region at $O(\kappa^2)$ can be written as:

$$\begin{aligned} G_A^{(2)} &= \int_S dS\,(f_x^{(1)}(\boldsymbol{\rho})l(\rho) - f_y^{(2)}(\boldsymbol{\rho})x) \\ &= \int_S dS\,(f_x^{(1)}(\boldsymbol{\rho})l(\rho) + \cos\theta\frac{d}{d\rho}[l(\rho)f_x^{(1)}(\boldsymbol{\rho})]x - \cos\theta\frac{d}{d\rho'}[l(\rho')f_x^{(1)}(\boldsymbol{\rho})]x - f_y^{(2)}(\boldsymbol{\rho})x). \end{aligned} \tag{3.60}$$

Integrating by parts, the first two terms in the above equation cancel and we are left with,

$$G_A^{(2)} = \int_S dS\,(-\cos\theta\frac{d}{d\rho'}[l(\rho')f_x^{(1)}(\boldsymbol{\rho})]x - f_y^{(2)}(\boldsymbol{\rho})x) = \int_S dS\,(-f_y^*(\boldsymbol{\rho})x), \tag{3.61}$$

where we define a new stress variable, $f_y^*(\boldsymbol{\rho}) = f_y^{(2)}(\boldsymbol{\rho}) + \cos\theta\frac{d}{d\rho}[l(\rho)f_x^{(1)}(\boldsymbol{\rho})]$. Thus, from the outer region there is a torque at $O(\kappa^2)$ which can be expressed completely in terms of $f_y^*(\boldsymbol{\rho})$ where $f_y^*(\boldsymbol{\rho})$ is given by the solution of the following equation,

$$-4\pi\cos\theta l(\rho)f_x^{(0)}(\rho)\frac{dl(\rho)}{d\rho} = \int\frac{dS'}{\rho''}f_y^*(\boldsymbol{\rho'}). \tag{3.62}$$

The only unknown in the above equation is f_y^*. The velocity disturbance field created by $f_x^{(0)}$ is responsible for driving a net f_y^*. Using $f_x^{(0)}(\rho) = -1$ in the outer region from 3.54, the dependence of the driving force of 3.62 on ρ can be written as $l(\rho)\frac{dl(\rho)}{d\rho} = -2\alpha\rho(1-\rho^2)^{2\alpha-1}$. This term has a singularity when $\rho \to 1$ for $\alpha < \frac{1}{2}$. Thus, the driving term for f_y^* in 3.62 is no longer $O(1)$ close to the edge of the particle for $\alpha < \frac{1}{2}$. Due to this, for $\alpha < \frac{1}{2}$ in addition to the $O(1)$ driving term for f_y^* from the outer region there is another term in the matching region driving f_y^*.

To calculate f_y^*, one needs to solve 3.62 numerically. Being an integral equation, the procedure used to solve 3.62 is very similar to the procedure used to implement the boundary element method. Again using the θ dependence of $f_y^*(\boldsymbol{\rho})$ from 3.17, one can write 3.62 as:

$$\int_0^1 \int_0^{2\pi} \frac{\rho' d\rho' d\theta'}{(\rho^2 + \rho'^2 - 2\rho\rho' \cos\theta'')^{\frac{1}{2}}} \cos\theta' f_2^*(\rho') = -4\pi \cos\theta l(\rho) f_x^{(0)}(\rho) \frac{dl(\rho)}{d\rho}, \quad (3.63)$$

where $f_y^* = f_2^* \cos\theta$. Integrating in the azimuthal direction and expressing the results in terms of complete elliptic integrals, the above equation can be written as:

$$\int_0^1 \rho' d\rho' S_2(\rho, \rho') f_2^* = 4\pi l(\rho) f_x^{(0)}(\rho) \frac{dl(\rho)}{d\rho}, \quad (3.64)$$

where S_2 is defined in the appendix A.2. As in the BEM simulations, the surface of the particle is discretized and f_2^* is assumed constant over each element on the surface. For $\alpha \geq \frac{1}{2}$, when there is no singularity at the edge, the surface of the particle is discretized in the radial coordinates with the size of all the elements kept constant and equal to 0.001.

For $\alpha < \frac{1}{2}$, the driving term for f_y^* in 3.62 diverges. To avoid the singularity, for these shapes the driving term is regularized by re-parameterizing the singular integrand. In this regularized form, the shape can be written as, $l(\rho) = (1 - \rho^2 + \epsilon)^\alpha$. A small but finite value of ϵ removes the singularity from 3.62. Here, ϵ plays the role of a boundary layer thickness. By varying ϵ, the effect of the qualitative effect of the singular driving force is captured by determining the scaling of the torque on ϵ. The regularized 3.62 can then be written as:

$$-4\pi\kappa^2 \cos\theta l(\rho) f_x^{(0)}(\rho) \left[\frac{-2\alpha\rho}{(1 - \rho^2 + \epsilon)^{1-2\alpha}} \right] = \int \frac{dS'}{\rho''} f_2^*(\boldsymbol{\rho}') \quad (3.65)$$

The regularized equation can now be solved for calculating f_2^* and the resultant torques for $\alpha < \frac{1}{2}$ for different values of ϵ. The values of ϵ used in the sim-

ulations, range from $10^{-3} - 10^{-7}$. The resultant torque obtained will then be a function of ϵ. The following discretization is used along the radial coordinates:

$$d\rho_{i+1} = \frac{1}{\frac{1}{\rho_l} + \frac{1}{(\rho_s \beta^i)}} \tag{3.66}$$

where ρ_i is the ith element on the surface, $\rho_l = 10^{-3}$, $\rho_s = 10^{-12}$, and $\beta = 1.002$. On the discretized surface, 3.64 can then be written as a system of linear equations:

$$\sum_{i=1}^{i=N} \rho_i d\rho_i S_2(\rho_i, \rho_j) f_2^*|_i = 4\pi l(\rho_j) f_x^{(0)}(\rho_j) \frac{dl(\rho)}{d\rho}|_{\rho_j} \; \forall j = 1 \text{ to } N \tag{3.67}$$

where $f_2^*|_i$ is the unknown stress acting on element i. There are N variables and N linear equations which are solved using matrix inversion to obtain f_2^*. For $\alpha > \frac{1}{2}$, since there is no singular term at the edge, the obtained results for f_2^* can be used to calculate the torque at $O(\kappa^2)$ from the outer region. On the other hand, for $\alpha < \frac{1}{2}$, ϵ has a strong influence on the torque . The torque obtained from the solution of regularized equation for f_2^* has two terms, an $O(\kappa^2)$ term and a larger term that has an inverse power law dependence on ϵ. In subsection C we will analyze the full integral equations and determine the effect of singularity at the edge on the scaling of the torque with respect to aspect ratio. We will then see that the dependence of the torque on the boundary layer thickness in the full integral equations is consistent with the dependence of the torque on ϵ obtained from the regularized outer region analysis based on the solution of 3.62.

3.4.2 Boundary layer

The calculations in the outer region analysis presented in subsection A assumed a flat surface with the distance from the edge greater than the thickness of the

particle. Close to the edge of the particle, the thickness of the particles is of the same order as the distance from the edge of the particle. In this region, the integral equations can be made independent of κ by rescaling the distance from the edge with a suitable function of κ. The $O(1)$ f_x stress no longer induces an $O(\kappa)$ stress in the y direction, but instead leads to an $O(1)$ stress in the $y-$ direction. Using a scaling of the form κ^β, where β is an unknown, a boundary layer coordinate can be defined as $\hat{\rho} = \frac{1-\rho}{\kappa^\beta}$, where $1-\rho$ is the distance from the edge. Now equating the distance from the edge to the thickness of the particle, one gets,

$$\begin{aligned} 1-\rho &\sim \kappa(1-\rho^2)^\alpha \\ \kappa^\beta\hat{\rho} &\sim \kappa^{1+\beta\alpha}2^\alpha\hat{\rho}^\alpha \\ \beta &= \frac{1}{1-\alpha} \end{aligned} \tag{3.68}$$

The above scaling also corresponds to the condition when the slope of the particle becomes $O(1)$. Using the above scaling for the boundary layer coordinate, the shape of the particle close to the edge can be written as:

$$\kappa l(\rho) = \kappa(\hat{\rho}\kappa^\beta)^\alpha(2-\alpha\kappa^\beta\hat{\rho})^\alpha = \kappa^\beta\hat{\rho}^\alpha 2^\alpha(1+O(\kappa^\beta)) \tag{3.69}$$

The radial distance between the two points, ρ and ρ' is given by:

$$\rho - \rho' = \kappa^\beta(\hat{\rho} - \hat{\rho'}) \tag{3.70}$$

Using 3.69 and 3.70, the integral 3.16 can then be written in terms of the boundary layer coordinate in the limit $\rho \to 1$:

$$
\begin{aligned}
0 = 2^{\alpha}\hat{\rho}^{\alpha}\delta_{ix} + \int d\hat{\rho}'(1+(2\alpha\hat{\rho}')^2)^{\frac{1}{2}}\Big[&\frac{\delta_{ix}}{((\hat{\rho}-\hat{\rho}')^2+2(\hat{\rho}^{\alpha}-\hat{\rho}'^{\alpha})^2)^{1/2}} \\
&+ \frac{(\hat{\rho}_i-\hat{\rho}'_i)(\hat{\rho}_x-\hat{\rho}'_x)}{((\hat{\rho}-\hat{\rho}')^2+2(\hat{\rho}^{\alpha}-\hat{\rho}'^{\alpha})^2)^{3/2}} - \frac{\delta_{ix}}{((\hat{\rho}-\hat{\rho}')^2+2(\hat{\rho}^{\alpha}+\hat{\rho}'^{\alpha})^2)^{1/2}} \\
&- \frac{(\hat{\rho}_i-\hat{\rho}'_i)(\hat{\rho}_x-\hat{\rho}'_x)}{((\hat{\rho}-\hat{\rho}')^2-2(\hat{\rho}^{\alpha}+\hat{\rho}'^{\alpha})^2)^{3/2}}\Big] f_x(\hat{\rho}') \\
+ \int d\hat{\rho}'(1+(2\alpha\hat{\rho}')^2)^{\frac{1}{2}}\Big[&\frac{\delta_{iy}}{((\hat{\rho}-\hat{\rho}')^2+2(\hat{\rho}^{\alpha}-\hat{\rho}'^{\alpha})^2)^{1/2}} + \frac{(\hat{\rho}_i-\hat{\rho}'_i)(\hat{\rho}_y-\hat{\rho}'_y)}{((\hat{\rho}-\hat{\rho}')^2+2(\hat{\rho}^{\alpha}-\hat{\rho}'^{\alpha})^2)^{3/2}} \\
&+ \frac{\delta_{iy}}{((\hat{\rho}-\hat{\rho}')^2+2(\hat{\rho}^{\alpha}+\hat{\rho}'^{\alpha})^2)^{1/2}} + \frac{(\hat{\rho}_i-\hat{\rho}'_i)(\hat{\rho}_y-\hat{\rho}'_y)}{((\hat{\rho}-\hat{\rho}')^2-2(\hat{\rho}^{\alpha}+\hat{\rho}'^{\alpha})^2)^{3/2}}\Big] f_y(\hat{\rho}') + O(\kappa^{\frac{1}{1-\alpha}})
\end{aligned}
\tag{3.71}
$$

The leading order terms in 3.71 are $O(1)$ and independent of κ. Hence, both f_x and f_y stresses are $O(1)$ in the boundary layer. One would then expect that the resultant leading order torque due to the $O(1)$ f_y stress acting on a area of size $O(\kappa^{\frac{1}{1-\alpha}})$ and moment arm of $O(1)$ will be of the $O(\kappa^{\frac{1}{1-\alpha}})$. However, it should be noted that any stresses in the boundary layer will create a fluid flow that will impinge upon the large no slip surface of the face of the disk. To maintain the no slip boundary condition, the flow will induce stresses opposite in sign to the boundary layer stress on the flat surface. The stresses on the flat surface and the boundary layer result in a force dipole per unit circumference as illustrated in figure 3.6 (d). The net torque from the boundary layer will thus depend on the force dipole rather than just the $O(1)$ boundary layer stress. In the next subsection, we discuss the stress in the flat region (matching region) due to the boundary layer stress and the resulting scaling of the torque.

3.4.3 Matching region solution driven by the outer region and the boundary layer

The analysis in subsections A and B indicates the need for a matching region analysis, where the matching region is defined as: $\hat{\rho} \to \infty$ in the boundary layer variable and $\rho \to 1$ in the outer variable. The $O(1)$ stress in the boundary layer creates a velocity disturbance field in the matching region which is the flat region close to the boundary layer and extends to infinity in the boundary layer coordinates. This velocity disturbance field induces stresses in the matching region to satisfy the no slip boundary condition. The forces in the boundary layer together with the forces in the matching region give rise to a force dipole which contributes to the torque from the boundary layer forcing. Also, from 3.62, we find that for $\alpha < \frac{1}{2}$ (figure 3.3), the driving term in the outer region for the f_y^* stress which is responsible for the leading order torque in the outer region is singular as $\rho \to 1$. As we be seen later in this section, this singular driving force leads to a stress field in the matching region which gives a torque contribution in addition to the torque at $O(\kappa^2)$ from the outer region. Thus, the matching region of the particle has two contributions to the stress: the first due to the $O(1)$ forcing in the $O(\kappa^{\frac{1}{1-\alpha}})$ boundary layer thickness and the other due to the singularity of the driving force term in 3.62 in the matching region . In this section, we derive the scaling of the stress and the resultant torques from both these contributions.

We will first write a single governing equation that accounts for both the contributions from the matching region discussed above. As noted earlier, in the boundary layer, stresses in both the x and y directions are of $O(1)$. Since the moment arm for the $x-$ direction stress is $O(\kappa)$ less than the moment arm for the

$y-$ direction stress, we expect the boundary layer forcing to modify the leading order torque via the y component of the disturbance field. Now considering the velocity field in the y-direction, in the limit when $\rho \to 1$ the driving term for f_y in the matching region is the $O(1)$ y-direction stress in the boundary layer. One can then recast 3.62 to account for both the $O(1)$ boundary layer driving force and the singular outer region forcing at the edge:

$$g(\hat{\rho}) - 4\pi\kappa^2 \cos\theta l(\rho) f_x^{(0)}(\rho) \frac{dl(\rho)}{d\rho} = \frac{1}{4\pi} \int \frac{d\boldsymbol{\rho}'}{|\boldsymbol{\rho}' - \boldsymbol{\rho}|} f_y(\boldsymbol{\rho}') \tag{3.72}$$

Here, the first term on the left hand side, $g(\hat{\rho})$ is an $O(1)$ function in the boundary layer which decays rapidly as $\hat{\rho} \to \infty$. In particular, we will assume that $g(\hat{\rho})$ decays faster than $1/\hat{\rho}$ as $\hat{\rho} \to \infty$. The second term is the outer region singular term forcing in the matching region as $\rho \to 1$. The unknown in the 3.72 is f_y.

3.72 can be interpreted as an integral representation of the Laplace equation where the right hand side is the single layer potential term for the Green's function in three dimensions. There is no double layer potential term in 3.72 as its contribution is zero across the rigid interface. The Laplace equation for a potential, Ψ is given by,

$$\nabla^2 \Psi = 0 \tag{3.73}$$

with boundary conditions

$$\Psi = g(\hat{\rho}) - 4\pi\kappa^2 \cos\theta l(\rho) f_x^{(0)}(\rho) \frac{dl(\rho)}{d\rho} \tag{3.74}$$

on the surface of a flat circular disk with the stress given by $f_y = \mathbf{e}_y \cdot \nabla\Psi$.

In the matching region, $1 - \rho \ll 1$ and $\hat{\rho} \gg 1$, we can approximate the flat disk as a semi-infinite planar surface because the circumference of the disk is very large compared with the distance from the end (see figure 3.6(b)). The

boundary condition 3.74 in the matching region reduces to

$$\Psi = \frac{C\kappa^2}{{\rho_h}^{1-2\alpha}} \text{ at } \theta_h = \pm\pi \tag{3.75}$$

where $\rho_h = 1-\rho$ and θ_h are polar coordinates in a plane perpendicular to the disk with an origin at the edge of the disk and C is a constant that can be determined from the outer solution. In addition to the driving term in 3.75, there is an $O(1)$ driving term that is localized in the boundary layer, a region much smaller than the matching region (see figure 3.6(a)).

We will now use linear superposition to find two contributions to the stress and torque from the $O(1)$ forcing term in the boundary layer and the outer region singular term in the matching region. The force density that balances the force on the edge of the disk satisfies a homogeneous boundary condition for the potential:

$$\Psi = 0 \text{ at } \theta = \pm\pi. \tag{3.76}$$

The solution of the potential field in polar coordinates with the above boundary conditions can then be used to calculate the force density in the matching region. The general solution is [96]:

$$\Psi = a_1 \frac{1}{\rho_h^{\frac{1}{2}}} \cos\frac{\theta_h}{2} + a_2 \frac{1}{\rho_h^{\frac{3}{2}}} \cos\frac{3\theta_h}{2} + ... \tag{3.77}$$

For the leading order stress on the surface, one only needs to consider the slowest decaying term in the above solution. Thus, using the first term of the general solution, the potential field is given by:

$$\Psi \sim a_1 \frac{1}{\rho_h^{\frac{1}{2}}} \cos\frac{\theta_h}{2} \tag{3.78}$$

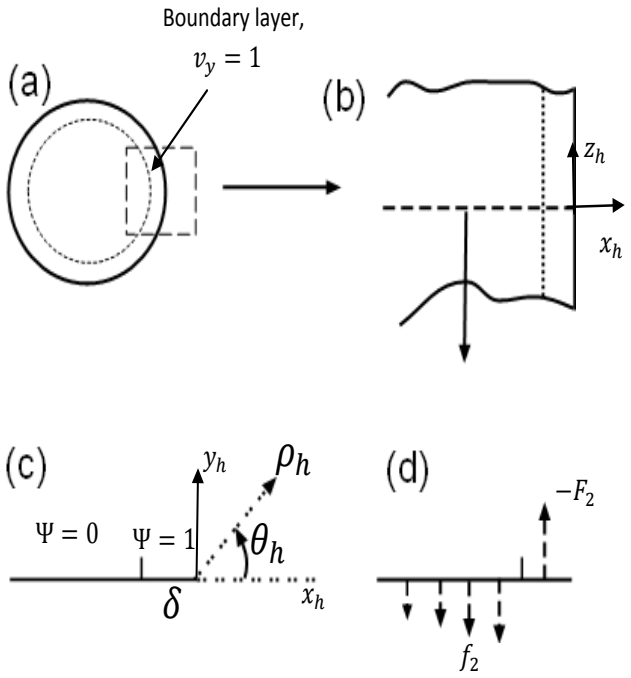

Figure 3.6: Schematic of the simplified boundary layer problem on the disk. (a) An $O(1)$ driving term on the edge of the disk (top view). (b) In the limit when size of the boundary layer and thickness of the disk are much smaller than the radius, close to the end the disk can be assumed to be a semi-infinite plane. (c) The semi-infinite plane could be further simplified to a semi-infinite line. The polar coordinate system is defined in a plane perpendicular to the disk. (d) The resulting force dipole due to the boundary layer forcing.

The force per unit area on the surface of the particle is then given by:

$$f_2 = \frac{1}{\rho_h}\frac{\partial \Psi}{\partial \theta_h}|_{\theta_h=\pi} - \frac{1}{\rho_h}\frac{\partial \Psi}{\partial \theta_h}|_{\theta_h=-\pi}$$
$$\sim \frac{a_1}{2\rho_h^{\frac{3}{2}}} \tag{3.79}$$

where $f_2 cos\theta = f_y$. The net force acting on the matching region should be equal and opposite to the force $-F_2 = O(\delta) = O(\kappa^{\frac{1}{1-\alpha}})$ arising from the boundary layer (by divergence theorem the net flux over the boundary is zero) itself so that

$$F_2 = \kappa^{\frac{1}{1-\alpha}} = \int_{\rho_m}^{\rho_{out}} f_2 d\rho_h = \frac{-2a_1}{3\pi\rho_m^{\frac{1}{2}}} \tag{3.80}$$

Here, ρ_m is a minimum radial distance for the matching region which is of the order of the boundary layer thickness $\delta = O(\kappa^{\frac{1}{1-\alpha}})$ and $\rho_{out} = O(1)$ is an upper limit to the radial extent of the matching region. We can solve 3.80 to find the coefficient a_1 of the potential field in the matching region,

$$a_1 = \kappa^{\frac{3}{2(1-\alpha)}}. \tag{3.81}$$

The magnitude of the torque G_{BL} due to the boundary layer force and the counter balancing matching layer force is proportional to the first moment of the force distribution in the matching region:

$$G_{\mathrm{BL}} = \int_{\rho_m}^{\rho_{out}} f_2 \rho_h d\rho_h \sim O(\delta^{\frac{3}{2}}) \sim O(\kappa^{\frac{3}{2(1-\alpha)}}) \tag{3.82}$$

Now we consider the second torque arising in the matching region, the one driven by the singular driving term in the matching region given by 3.75. The slowest decaying form of the potential field that includes a homogeneous solution along with the particular solution due to $O(\kappa^2)$ driving term contribution from the matching region is:

$$\Psi = \frac{A\cos(\theta/2)}{\rho_h^{\frac{1}{2}}} + C\kappa^2 \left(\frac{\rho_{out}}{\rho_h}\right)^{1-2\alpha} \frac{\cos[(1-2\alpha)\theta]}{\cos[(1-2\alpha)\pi]} \tag{3.83}$$

Here, A and C are unknown constants. The above solution is not valid for the case of $\alpha = \frac{1}{4}$ because at $\theta_h = \pm\pi$ the second term is singular over the entire space. We make use of the BEM numerics to solve for the special case of $\alpha = \frac{1}{4}$ and present the results in section V. The stress for a potential given by 3.83 is:

$$f_2 = \frac{A\sin(\pi/2)}{\rho_h^{\frac{3}{2}}} + \frac{2C(1-2\alpha)\kappa^2\rho_{out}^{1-2\alpha}\tan[(1-2\alpha)\pi]}{\rho_h^{2-2\alpha}} \tag{3.84}$$

The net force obtained by integrating this second solution over the matching region should be zero since the first term has already balanced the boundary layer stress. Hence:

$$F_2|_{match} = \int_{\rho_m}^{\rho_{out}} f_y d\rho_h = 0 \tag{3.85}$$

Substituting 3.84 in the above equation, we get:

$$\begin{aligned} 0 &= \frac{2A}{3}\left(\frac{1}{\rho_m^{\frac{1}{2}}} - \frac{1}{r_{out}^{\frac{1}{2}}}\right) + 2C\kappa^2\rho_{out}^{1-2\alpha}\tan[(1-2\alpha)\pi]\left(\frac{1}{\rho_m^{1-2\alpha}} - \frac{1}{\rho_{out}^{1-2\alpha}}\right) \\ A &= \frac{-3C\kappa^2\rho_{out}^{1-2\alpha}\tan[(1-2\alpha)\pi]}{\rho_m^{\frac{1}{2}-2\alpha}} \end{aligned} \tag{3.86}$$

Substituting the value of A from the above expression in 3.84, we get:

$$\begin{aligned} f_2 &= C\rho_{out}^{1-2\alpha}\tan[(1-2\alpha)\pi]\kappa^2\left[\frac{-3}{\rho_h^{\frac{3}{2}}\rho_m^{-2\alpha+\frac{1}{2}}} + \frac{2(1-2\alpha)}{\rho_h^{2-2\alpha}}\right] \\ &= D\kappa^2\left[\frac{-3}{\rho_h^{\frac{3}{2}}\rho_m^{-2\alpha+\frac{1}{2}}} + \frac{2(1-2\alpha)}{\rho_h^{2-2\alpha}}\right] \end{aligned} \tag{3.87}$$

where $D = C\rho_{out}^{1-2\alpha}\tan[(1-2\alpha)\pi]$. The torque G_{sing} due to the singular forcing in the outer region is then given by:

$$\begin{aligned} G_{\text{sing}} &= \int_{\rho_m}^{\rho_{out}} f_2\rho_h d\rho_h \\ &= D\kappa^2\left[\frac{-6}{\rho_m^{-2\alpha+\frac{1}{2}}}(\rho_{out}^{\frac{1}{2}} - \rho_m^{\frac{1}{2}}) + \frac{2(1-2\alpha)}{2\alpha}(\rho_{out}^{2\alpha} - \rho_m^{2\alpha})\right] \end{aligned} \tag{3.88}$$

3.88 can also be used to understand the role of the small parameter ϵ used to regularize the singular 3.62. The small parameter ϵ in the regularized equation is equivalent to the boundary layer size, ρ_m in the above equation. Thus, one can expect the torque dependence on ϵ to be $O(\epsilon^{2\alpha-\frac{1}{2}})$ for the regularized 3.65. We verify this scaling in the results section using the solution of 3.62. Substituting $\rho_m = O(\kappa^{\frac{1}{1-\alpha}})$ and $\rho_{out} = O(1)$ in 3.88,

$$G_{\text{sing}} = O(\kappa^{\frac{3}{2(1-\alpha)}}) + O(\kappa^2) \tag{3.89}$$

Here, the $O(\kappa^{\frac{3}{2(1-\alpha)}})$ term is the contribution of the singular term in the matching region and the $O(\kappa^2)$ torque is of the same order as the torque in the outer region. We have seen that the localized force density in the boundary layer and the counterbalancing force density in the matching region leads to a torque of $O(\kappa^{\frac{3}{2(1-\alpha)}})$ and that the singular driving term in the matching region leads to a torque of the same order. It should be noted however that the contribution from the singular term is only present for $\alpha < \frac{1}{2}$ whereas the contribution from the boundary layer is for $\alpha < 1$. Now, combining 3.82 and 3.89, the overall torque scaling for $\alpha < 1$ is :

$$G_{\text{net}} = O(\kappa^{\frac{3}{2(1-\alpha)}}) + O(\kappa^2) \tag{3.90}$$

3.5 Results

In this section, we present results obtained from the numerical simulations and compare them with the asymptotic analysis presented in the previous section. The asymptotic analysis in section IV revealed the scaling of the stresses and torques in the boundary layer and the matching region with respect to the particle aspect ratio κ. We also obtained the $O(\kappa)$ and $O(\kappa^2)$ solutions for f_x and f_y

as functions of ρ in the outer region and the corresponding predictions for the torque contribution from the outer region. We divide this section into four parts based on the distinct rotational behavior of the particle due to its shape. We begin the discussion in subsection A by comparing our numerical simulation results and the analytical results with the known analytical results for a spheroid. In subsection B, we discuss results for the case of $\alpha > \frac{1}{2}$, which corresponds to particles that have edges sharper than spheroidal particles. For $\alpha > 1$, there is no boundary layer and the outer solution applies for all radial positions. For $\frac{1}{2} < \alpha < 1$, there is a boundary layer of size $O(\kappa^{\frac{1}{1-\alpha}})$ which is less than $O(\kappa^2)$ and the resultant torque contribution from the boundary layer is always less than $O(\kappa^3)$. For these shapes, since the driving term for f_y^* is not singular at the edge, the first two contributions to the torque are $O(\kappa^2)$ and $O(\kappa^3)$ and both arise from the outer region. Thus for all the cases with $\alpha > 1/2$, treated in subsection B the outer solution provides a good approximation for the torque on a thin disk.

From the analysis for $\alpha < \frac{1}{2}$, the first two contributions to the torque come from the outer region and the boundary layer. From the outer region, there is an $O(\kappa^2)$ torque from the x and y stresses. There are two contributions to the torque from the edge. One from the singular driving force for f_y^* (3.62) and the other from the $O(1)$ stress in the boundary layer of $O(\kappa^{\frac{1}{1-\alpha}})$ close to the edge of the particle. Both these contributions to the torque are at $O(\kappa^{\frac{3}{2(1-\alpha)}})$. For $\frac{1}{4} < \alpha < \frac{1}{2}$, the $O(\kappa^2)$ contribution from the outer region is greater than the contribution from the singular driving force at the edge and the boundary layer stress contribution and is the leading order contribution. We discuss these shapes in subsection C, and as will be shown therein, the effective aspect ratio remains equal to the actual aspect ratio at the leading order. In subsection D, we discuss shapes represented by $0 < \alpha \leq \frac{1}{4}$. For this range of α, the leading order torque is $O(\kappa^{\frac{3}{2(1-\alpha)}})$

and comes from the boundary layer and matching regions, and as a result, the effective aspect ratio becomes asymptotically large compared to the actual aspect ratio in the limit of small κ. For these shapes, the second order contribution to the torque is $O(\kappa^2)$ and comes from the outer region . The special case of $\alpha = \frac{1}{4}$ for which we could not identify the scaling of torque from the boundary layer analysis in section IV is also discussed in subsection D using BEM simulations.

3.5.1 Torque on spheroids

Before presenting the simulation results for arbitrary α, it is helpful to present the results for the case of a spheroid, for which $\alpha = 1/2$. Although a spheroid is a special case where the effective aspect ratio is always equal to the aspect ratio of the particle at all aspect ratios, it can still be used as a basis to understand the behavior of the stresses in the outer and boundary layer regions as one can calculate the stresses acting on a spheroidal particle using the complete analytical results [37] in closed form. Dabade [37] analyzed the effects of inertia on the orientational dynamics of both prolate and oblate spheroidal particles in simple shear flow using the generalized reciprocal theorem and Stokes flow solutions obtained using a vector spheroidal harmonics formalism. The work allowed analytical results to be obtained for Stokes flow quantities over the entire range of aspect ratios. For the purpose of this work, Dabade's results are readily used to obtain the stresses and the torque acting on a stationary oblate spheroid. We use these exact analytical results to compare with the BEM results and the analytical results from the asymptotic analysis performed in section IV. Results for the stresses from the asymptotic analysis and the numerical simulations are verified with the complete analytical results for a stationary spheroid in both the outer

and boundary layer regions. As another test of accuracy of our numerical simulations, we compare the overall torque acting on the particle as predicted from the numerical simulations with the analytical results for the torque obtained by Perrin [116] for spheroidal particles. Edwardes [41] used ellipsoidal harmonics to solve for the general rotational motion of an ellipsoidal particle in an otherwise quiescent fluid. Perrin used Edwardes' results for ellipsoids to derive the friction coefficients of rotation of a spheroidal particle about its major and minor axes. Here the friction coefficient of rotation is the proportionality constant between the angular velocity of the particle and the external torque acting on it. We use Perrin's results along with Jeffery's results for the angular velocity to obtain the torque acting on a particle with fixed orientation A.

We first compare the surface stresses on the particle in both the boundary layer and the outer region. We use the complete analytical results for the stresses acting on the particle and expand them in terms of κ to obtain f_x to $O(\kappa)$ and f_y to $O(\kappa^2)$ in the outer region. The two stresses [37] to the second order are given by:

$$\begin{aligned} f_x &= -1 - \frac{3\pi}{4}\kappa + O(\kappa^2) \\ f_y &= -\frac{\kappa \cos\theta\rho}{(1-\rho^2)^{1/2}} + \left(\frac{8}{\pi} - \frac{3\pi}{4}\right)\frac{\kappa^2 \cos\theta\rho}{(1-\rho^2)^{1/2}} + O(\kappa^3) \end{aligned} \tag{3.91}$$

The leading order stresses, $f_x^{(0)}$ and $f_y^{(1)}$ from Dabade's complete analytical results are in agreement with the leading order stress obtained from our analysis in 3.54 and 3.55 for $\alpha = \frac{1}{2}$ and follow the relationship $f_y^1(\boldsymbol{\rho}) = -\kappa \cos\theta \frac{\partial}{\partial\rho}(f_x^0(\boldsymbol{\rho})l(\rho))$. As shown in the analysis such a relation between the x and y direction stresses results in zero net torque on the particle at $O(\kappa)$. The leading order torque then originates from the next order stresses, $f_x^{(1)}$ and $f_y^{(2)}$. The torque originating from these two stresses at $O(\kappa^2)$ can be represented in terms of a single stress,

$f_y^*(\boldsymbol{\rho}) = f_y^{(2)}(\boldsymbol{\rho}) - \cos\theta \frac{d}{d\rho}[l(\rho) f_x^{(1)}(\boldsymbol{\rho})]$, as shown in 3.61. Using Dabade's results we can write f_y^* for a spheroid as:

$$f_y^* = \left(\frac{8}{\pi} - \frac{3\pi}{4}\right) \frac{\cos\theta\rho}{(1-\rho^2)^{1/2}} - \cos\theta \frac{d}{d\rho}[l(\rho)\frac{3\pi}{4}]$$
$$f_y^* = \frac{8\cos\theta\rho}{\pi(1-\rho^2)^{1/2}} \tag{3.92}$$

The above exact analytical result for f_y^* is compared with the regularized outer solution for f_y^* from 3.63. The results are found to be in good agreement and are shown in figure 3.7 for $\kappa = 10^{-2}$.

We also compare our numerical results for f_y^* from BEM with Dabade's analytical results. Since f_y^* is responsible for the leading order torque from the outer region, we omit the comparison of the $x-$ direction and the $y-$ direction stresses individually with the BEM results and compare f_y^* with Dabade's complete analytical results as an indicator of the correct implementation of BEM numerical scheme. Since BEM simulations solve for the complete stresses f_y and f_x, f_y^* is extracted from f_y and f_x by using the following relationship:

$$f_y^*(\boldsymbol{\rho}) = (f_y(\boldsymbol{\rho}) + \kappa\cos\theta \frac{d}{d\rho}[f_x(\rho) l(\rho)])/\kappa^2 \tag{3.93}$$

In figure 3.7, f_y^* from the BEM simulations and the complete analytical results at $O(\kappa^2)$ are also presented. We find that the numerical and the analytical results are in good agreement.

Now we compare the stresses in the boundary layer from BEM simulations with the exact analytical results. In section IV, we showed that when one moves close to the edge of the particle and the thickness of the particle is of the same order as the distance from the edge of the particle, the governing integral equations can be made independent of κ to the leading order by applying a suitable scaling to the distance of the radial coordinate from the edge. This scaling is

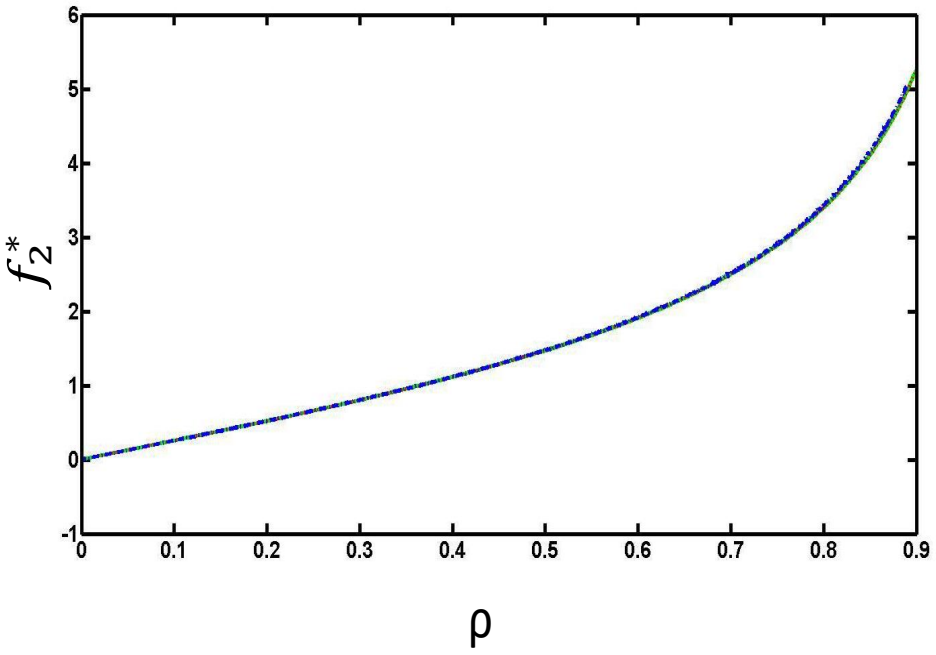

Figure 3.7: Comparison of $f_2^*(f_y^* = f_2^* cos\theta)$ from Dabade's analytical results (-, red curve), analytical-numerical results (:, green curve) from the present work, and BEM simulations (-., blue curve) from the present work for $\kappa = 10^{-2}$ in the outer region for a spheroid. Jeffery's analytical results and the analytical numerical results from the present work are indistinguishable on this plot.

identified to be $\kappa^{\frac{1}{1-\alpha}}$ and the rescaled boundary layer coordinate is defined as $\hat{\rho} = \frac{1-\rho}{\kappa^{\frac{1}{1-\alpha}}}$. The surface stresses when plotted as a function of the boundary layer coordinate are then expected to be independent of κ and should collapse into a single curve for all κ to the leading order. In figure 3.8, the two stress components, f_x and f_y, obtained from the BEM simulations as a function of the boundary layer coordinates are presented. The curves do not exactly collapse into a single curve indicating the presence of higher order stresses which depend on κ. Since the curves get closer to each other with decreasing κ, we conclude that, at the leading order, the stresses are indeed independent of κ. We compare stresses in the boundary layer from the BEM simulations with Dabade's exact analytical solutions in figure 3.9. The numerical results are in good agreement with the complete analytical results for the values of κ ($10^{-3} \leq \kappa \leq 8X10^{-2}$) used for the numerical simulations.To the relevant order, the analytical results for f_x and f_y in the boundary layer are given by [37] :

$$
\begin{aligned}
f_x &= -\frac{(2\hat{\rho})^{1/2}}{(2\hat{\rho}+1)^{1/2}} - \pi\kappa\frac{3\hat{\rho}^{1/2}}{2^{3/2}(1+2\hat{\rho})^{1/2}} \\
f_y &= \frac{-1}{(1+2\hat{\rho})^{1/2}} + \frac{(32-3\pi^2)\kappa}{4\pi(1+2\hat{\rho})^{\frac{1}{2}}} + \kappa^2\frac{(80-9\pi^2+12\hat{\rho})}{16(1+2\hat{\rho})^{\frac{1}{2}}} + O(\kappa^3\hat{\rho}^2/\hat{\rho}^{3/2})
\end{aligned}
\tag{3.94}
$$

In the matching region, i.e. $\hat{\rho} \to \infty$ and $\rho \to 1$, analytical results from the outer region (3.91) match analytical boundary layer force densities (3.94) to $O(\kappa)$.

We also compare the overall torques calculated from the BEM simulations with the analytical results from Perrin [116, 84] . Perrin's original results for oblate spheroids contained some algebraic errors; we use the following corrected results obtained by Koenig[84] :

$$
\begin{aligned}
C_2 &= \frac{32\pi(1-\kappa^4)}{3(2\kappa - S(2\kappa^2-1))} \\
S &= 2(1-\kappa^2)^{-1/2} tan^{-1}\left(\frac{1-\kappa^2}{\kappa^2}\right)^{1/2}
\end{aligned}
\tag{3.95}
$$

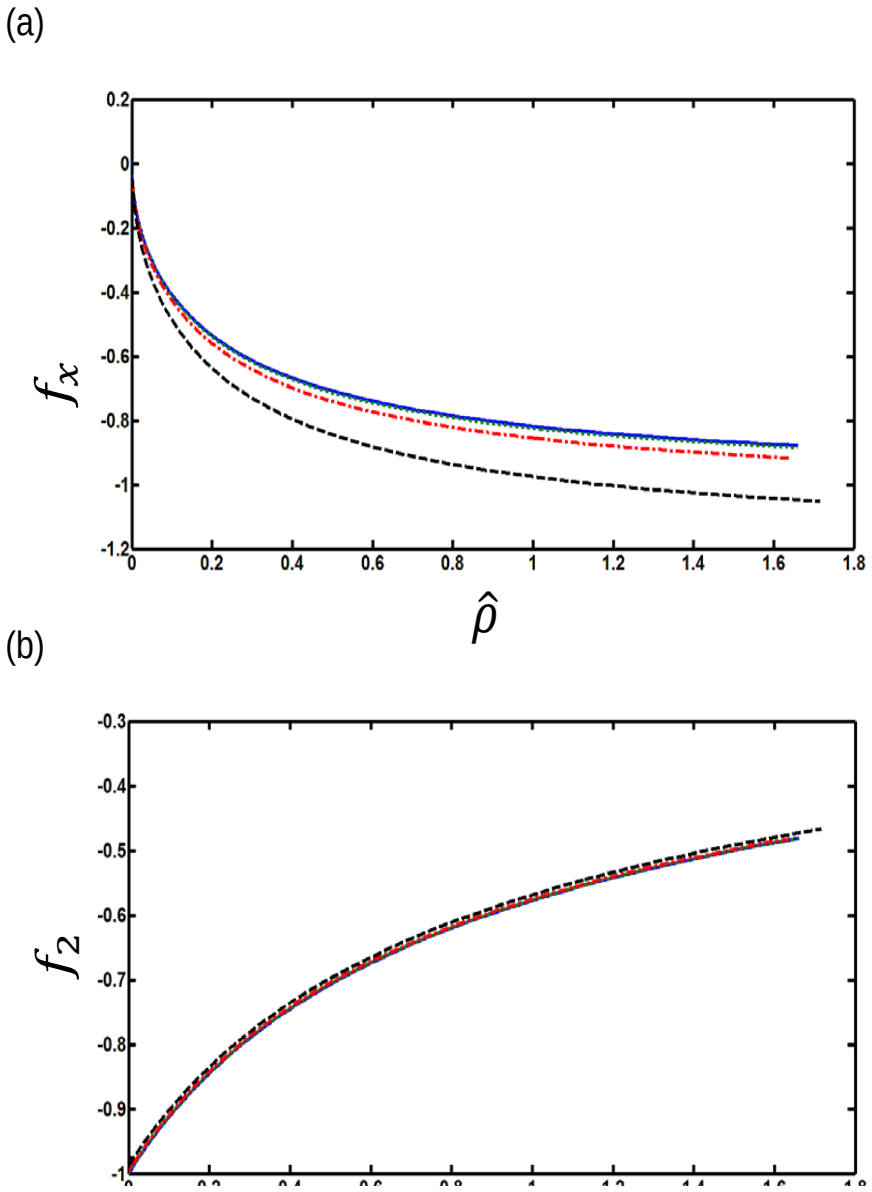

Figure 3.8: Force densities, (a) f_x and (b) f_2 ($f_y = f_2 \cos\theta$) for spheroids obtained from BEM simulations in the boundary layer as a function of the boundary layer coordinates for $\kappa = 0.001$ (-, blue), $\kappa = 0.004$ (:, green), $\kappa = 0.02$ (-., red), and $\kappa = 0.08$ (–, black).

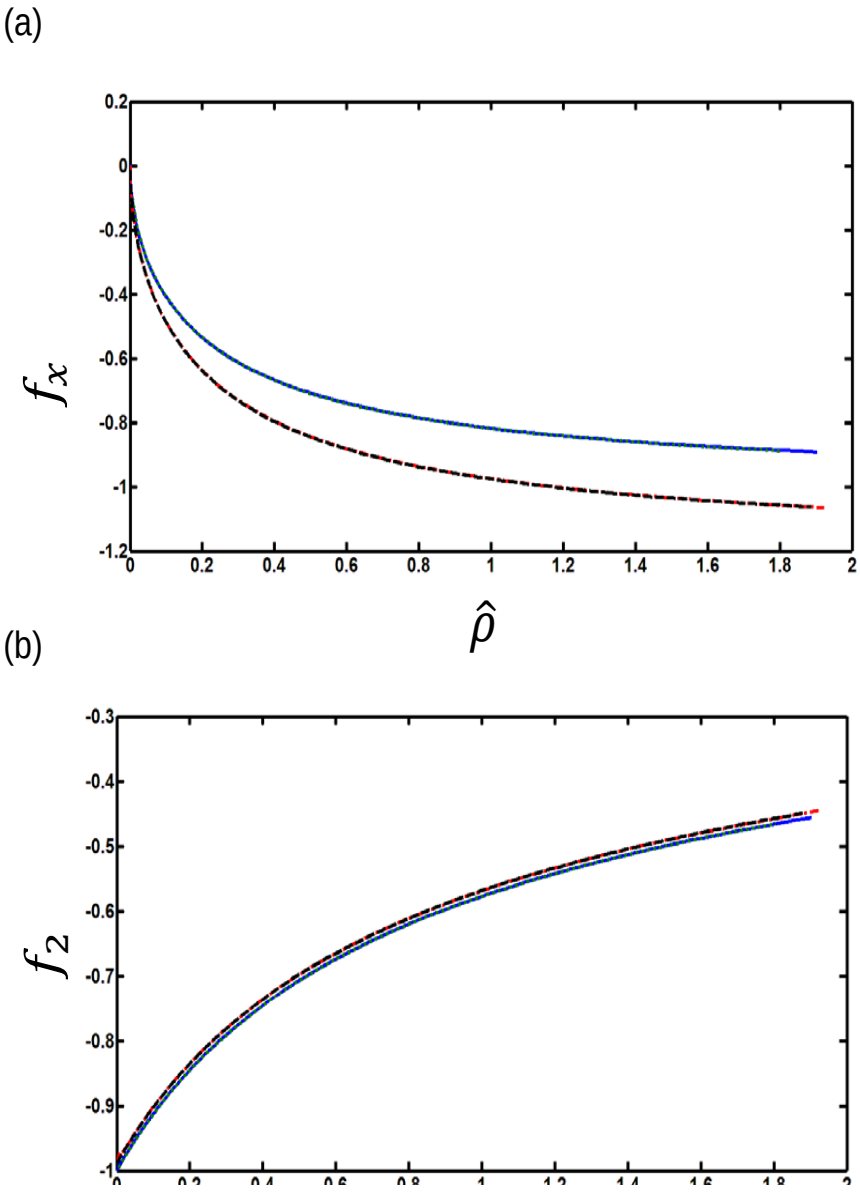

Figure 3.9: Comparison of force densities, (a) f_x and (b) f_2 ($f_y = f_2 \cos\theta$) in the boundary layer for spheroidal particles, obtained from BEM simulations and Dabade's analytical results. Comparison is made for two extreme aspect ratios used in the simulations, $\kappa = 0.001$(solid blue curve for BEM and dot green curve for Dabade) and $\kappa = 0.08$ (dash-dot red curve for BEM and dash-dash black curve for Dabade).

where C_2 is the friction coefficient of rotation around one of the major axis of the particle and S is a constant. In the limit when $\kappa \to 0$, we get $C_2 = \frac{32}{3} + O(\kappa^2)$ from 3.95. Combining Perrin's results for the friction coefficient with Jeffery's results for the angular velocity of a spheroid when the particle's axis is in the gradient direction, the torque acting on the particle is given by:

$$G_A|_{Perrin} = C_2 \frac{\kappa^2}{1+\kappa^2} \sim \frac{32\kappa^2}{3} + O(\kappa^4) \tag{3.96}$$

This value is the same as that obtained from the complete analytical results [37] calculated using the results for f_y^* from 3.92. Results from the BEM simulations are compared with Perrin's analytical results in figure 3.10. The numerical results are found to have errors smaller than 0.1% for $10^{-3} \leq \kappa \leq 8X10^{-2}$. The good comparison of the torques is consistent with the coincidence of the forces from the numerical simulations with the forces from the complete analytical results [37].

Perrin's results can also be used to determine the leading order torque acting on a thin disk in orientation B. For a spheroid, the torque is given by:

$$G_B|_{Perrin} = C_2 \frac{1}{1+\kappa^2} \sim \frac{32}{3} + O(\kappa^2) \tag{3.97}$$

where the leading order term corresponds to the torque on a plane surface and is independent of the shape of the particle. For a thin particle in general, at second order there will be two contributions to torque: an $O(\kappa)$ torque from the $O(1)$ leading order force density acting at positions perturbed by $O(\kappa)$ on the surface of the particle and another $O(\kappa)$ torque from an $O(\kappa)$ correction to the force density acting at $O(1)$ positions. Thus, we can conclude that in the limit $\kappa \to 0$ for all thin disks,

$$G_B = -\frac{32}{3} + O(\kappa) \tag{3.98}$$

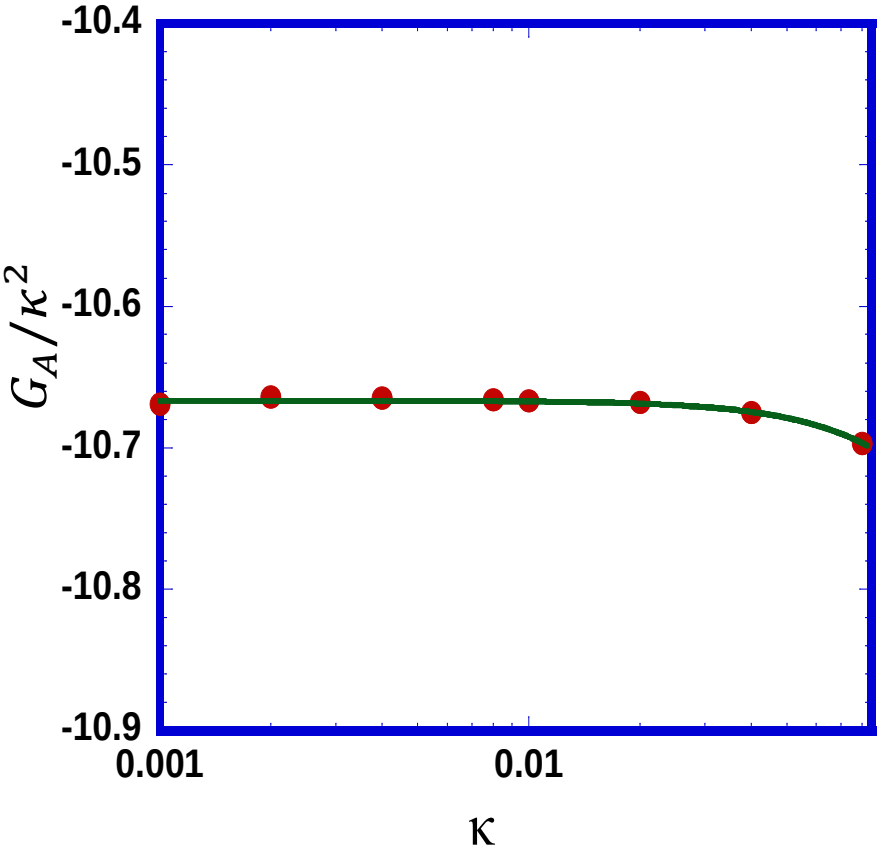

Figure 3.10: Comparison of the scaled analytical torque obtained from Perrin (curve) with the scaled torque obtained from the BEM simulations (circles) for spheroidal particles of different aspect ratio.

We will use the above result for the torque on a thin disk in orientation B, which is independent of the shape of the particle to leading order, along with G_A, to determine the effective aspect ratio of particles with different α. We have independently calculated the effective aspect ratio by solving for the angular velocity of torque-free particles (mobility problem) as was done by Singh et al. [129] and verified that there are no corrections to G_B that are larger than $O(\kappa)$.

3.5.2 Effective aspect ratio for $\alpha > \frac{1}{2}$

For $\alpha > \frac{1}{2}$, the slope of the particle close to the edge ($\rho \to 1$) is lower than that of a spheroid i.e. the particles are less blunt than a spheroid at the edge. For $\frac{1}{2} < \alpha < 1$, the slope is $O(1)$ in a region $1 - \rho = O(\kappa^{\frac{1}{1-\alpha}})$ whereas for $\alpha > 1$, the slope over the entire surface is $O(\kappa)$ and hence there is no boundary layer. In the boundary layer region for $\frac{1}{2} < \alpha < 1$, the leading order stresses are $O(1)$. The velocity disturbance caused by these stresses induce stresses over the flatter portion of the disk so that an overall force dipole leads to an $O(\kappa^{\frac{3}{2(1-\alpha)}})$ torque. This torque contribution is less than the second torque contribution from the outer region, which is $O(\kappa^3)$. Thus for these shapes we can ignore the torque contribution from the boundary layer region. From BEM simulations we verified that the stress distribution in the boundary layer to the leading order is $O(1)$ (not shown) and that the stress collapses into a single curve when plotted as a function of the boundary layer coordinate.

For $\alpha > \frac{1}{2}$, the driving term for f_y^* is not singular in the limit $\rho \to 1$, so the torque from the outer region can be calculated from stresses that are the solution to 3.62. From the asymptotic analysis, f_y^* is predicted to drive the leading order

torque in the outer region. Figure 3.11 shows a plot of f_y^* for different values of κ from the full BEM calculations along with f_y^* obtained by solving the integral 3.62 for $\alpha = 2/3$ and $\alpha = 2$. The BEM numerical results are in good agreement with the outer solution. For $\alpha = 2/3$ (and in general for $1/2 < \alpha < 1$), f_y^* obtained from the complete BEM solution and numerical solution of 3.63 diverges close to the edge (not shown) due to the $O(1)$ forcing from the boundary layer. The numerical solution of 3.63 does not capture this divergence because it does not include a boundary layer forcing. On the other hand, for $\alpha = 2$ (and in general for $\alpha > 1$), there is no divergence of f_y^* from BEM solution or from the solution of 3.63 as there is no boundary layer for $\alpha > 1$ particles.

The torque obtained from the BEM simulations is compared with the torque prediction from the numerical solution of 3.62 for $\alpha = \frac{2}{3}$ and $\alpha = 2$ in figure 3.12. The results are in good agreement, indicating that there is no contribution from the boundary layer region to the leading order for these shapes. The regularized outer results also help in predicting the coefficient of the torque scaling at $O(\kappa^2)$. The values of κ_e/κ (1 for $\alpha = \frac{1}{2}$, 0.81 for $\alpha = \frac{2}{3}$, and 0.44 for $\alpha = 2$ from figure 12) indicate that the rotation rate slows down as α increases or the particle becomes less blunt even though the rotation rate of the aligned disk remains proportional to κ^2.

3.5.3 Effective aspect ratio for $\frac{1}{4} < \alpha < \frac{1}{2}$

For the shapes with $\frac{1}{4} < \alpha < \frac{1}{2}$, the leading order contribution to the torque remains $O(\kappa^2)$ and comes from the outer region. This leading order contribution can be calculated based on the stress, f_y^*. For $\alpha < \frac{1}{2}$, the driving term for f_y^* in 3.62

(a)

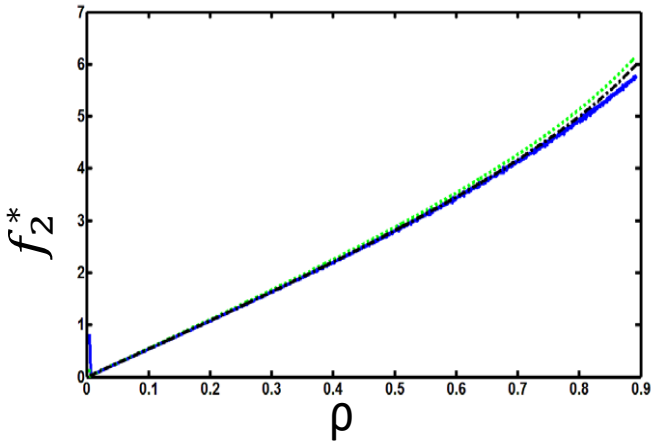

(b)

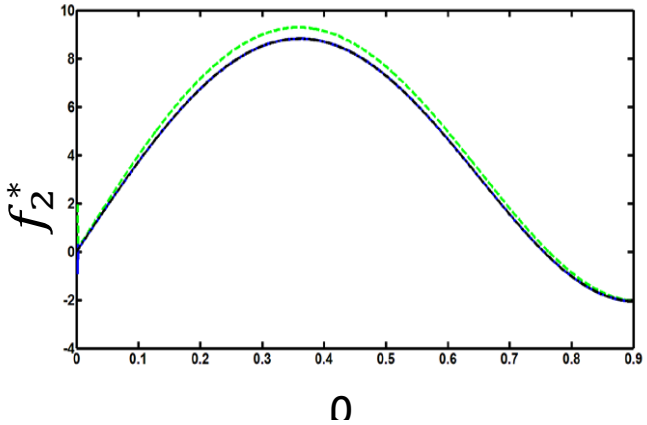

Figure 3.11: Comparison of f_2^* ($f_y^* = f_2^* \cos\theta$) for $\alpha = 2/3$ (a) and $\alpha = 2$ (b) for different values of κ obtained from the complete BEM simulations with f_2^* obtained from the analytical-numerical results of 3.63. (a) $\kappa = 0.001$ (solid blue curve), $\kappa = 0.08$ (dotted green curve), and f_2^* (dot-dashed black curve) from the analytical-numerical results. (b) $\kappa = 0.001$ (solid blue curve), $\kappa = 0.08$ (dotted green curve) and f_2^* (dot-dashed black curve) from the analytical-numerical results. Results for $\kappa = 0.001$ and analytical results are almost indistinguishable.

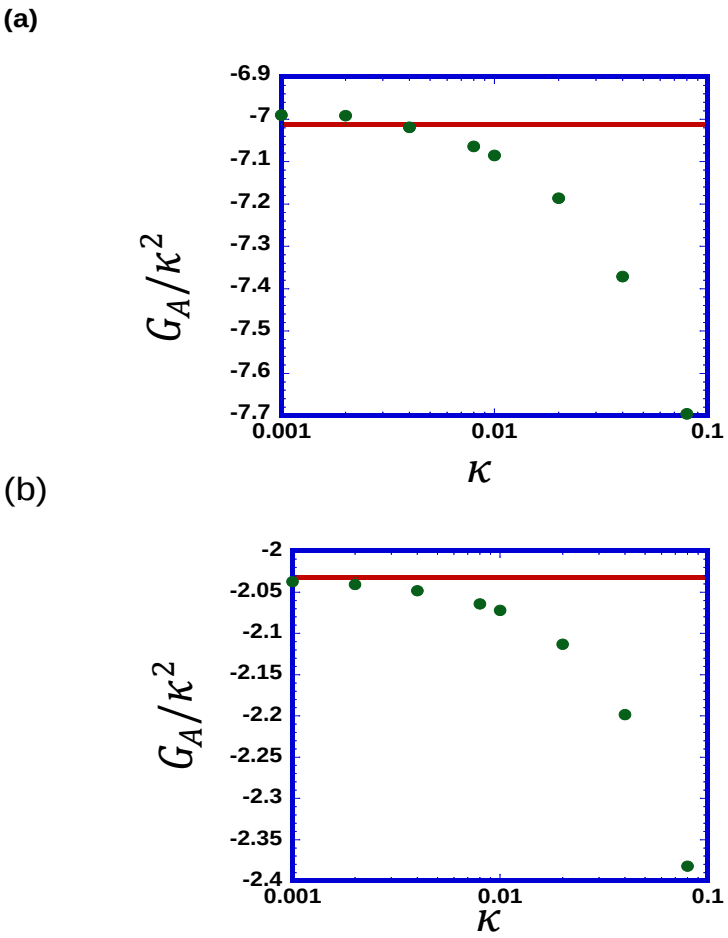

Figure 3.12: Comparison of the torque obtained from the BEM simulations (circles) with the torque from the numerical solution (straight line) for f_y^* from 3.63 for $\alpha = 2/3$ (a) and $\alpha = 2$ (b). Using $G_B = -32/3$, the corresponding effective aspect ratio from the numerical solution of f_y^* is $\frac{\kappa_e}{\kappa} = 0.81$ for $\alpha = 2/3$ and $\frac{\kappa_e}{\kappa} = 0.44$ for $\alpha = 2$.

is singular close to the edge of the particle; to remove the singularity the driving term is regularized by using a small parameter ϵ. 3.65 represents the regularized equation for the driving term where the small parameter ϵ plays the role of the boundary layer thickness. In section IV C, the regularization is shown to lead to an additional term, besides the leading order contribution of $O(\kappa^2)$ to f_y^*, that scales as $O(\kappa^2\epsilon^{2\alpha-\frac{1}{2}})$ (3.88). In figure 3.13, we present the dependence of torque on ϵ from the solution for f_y^* for $\alpha = \frac{3}{8}$ and use a fitting curve given by:

$$G_A = C_1 + C_2\epsilon^{1/4} \tag{3.99}$$

Numerical results are found to agree with the analytical predictions. The constant term in 3.99 corresponds to the $O(\kappa^2)$ torque contribution from the outer region while the second term of $O(\epsilon^{1/4})$ corresponds to the next order contribution of $O(\kappa^{3/2(1-\alpha)})$.

As before, the stresses in the boundary layer region are predicted to be $O(1)$ with a boundary layer size of $O(\kappa^{\frac{1}{1-\alpha}})$ for $\alpha < 1$. Figure 3.14 shows a plot of force densities, f_x and f_y in the boundary layer region as a function of the boundary layer coordinates for $\alpha = \frac{3}{8}$. Again at the leading order, the stresses are $O(1)$ and independent of κ. These $O(1)$ force densities in the boundary layer drive stresses over the flat matching region resulting in a force dipole which again contributes to a torque at $O(\kappa^{\frac{3}{2(1-\alpha)}})$. This boundary layer contribution is included in the BEM simulations.

For $\frac{1}{4} < \alpha < \frac{1}{2}$, the leading order torque contribution at $O(\kappa^2)$ comes from the outer region. At the second order, the torque is caused by the force densities driven by the singular driving force at the edge and the $O(1)$ stress in the boundary layer at $O(\kappa^{\frac{3}{2(1-\alpha)}})$. The leading order scaling of κ^2 and the next order scaling of $\kappa^{\frac{3}{2(1-\alpha)}}$ are close to each other in magnitude for the range of the aspect

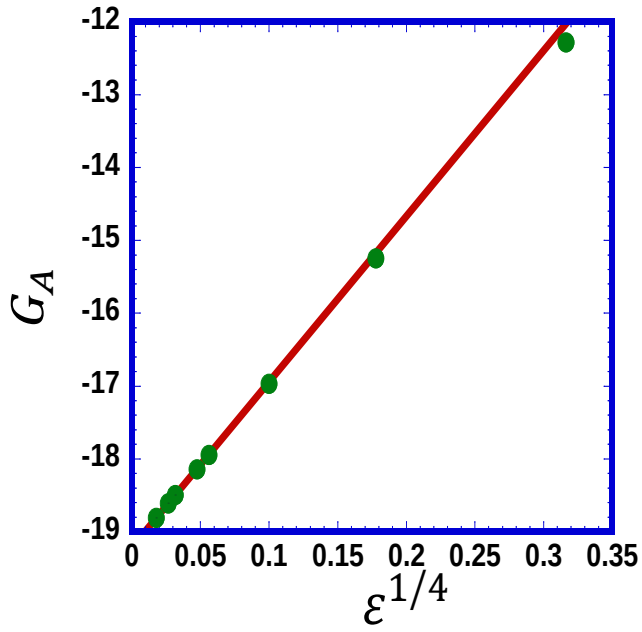

Figure 3.13: Scaling of the torque with respect to the small parameter, ϵ obtained from the numerical solution of the regularized 3.70 for $\alpha = 3/8$. Equation of the fitting line is $-19.21 + 22.73\epsilon(1/4)$.

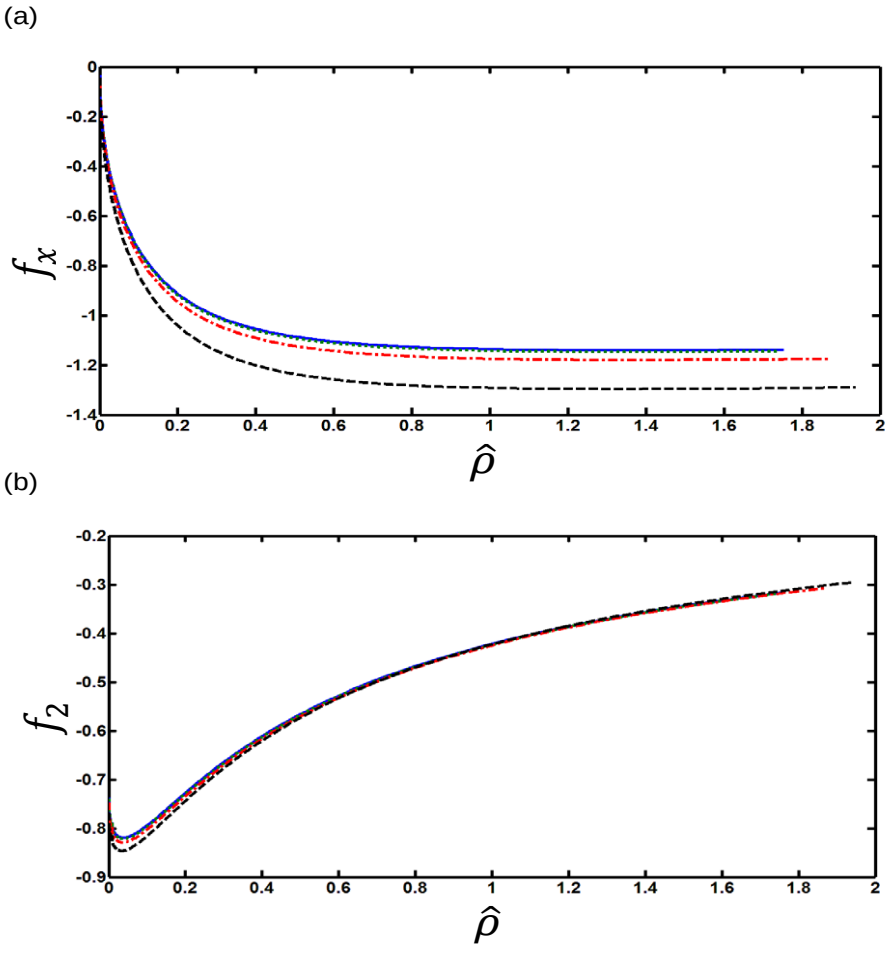

Figure 3.14: Force densities, (a) f_x and (b) f_2 ($f_y = f_2 \cos\theta$) for $\alpha = 3/8$ obtained from BEM simulations in the boundary layer as a function of the boundary layer coordinates for $\kappa = 0.001$(solid blue), $\kappa = 0.004$ (dotted green), $\kappa = 0.02$ (dot-dashed red), $\kappa = 0.08$ (dashed black).

ratio used in this study. Thus, we present the net torque obtained from the BEM simulations as a sum of an $O(\kappa^{\frac{3}{2(1-\alpha)}})$ term and an $O(\kappa^2)$ term. Writing the torque to the second order as a linear sum of these two terms, we get:

$$\begin{aligned} G_A &= H_1\kappa^{\frac{3}{2(1-\alpha)}} + H_2\kappa^2 \\ \frac{G_A}{\kappa^2} &= H_1\kappa^{\frac{4\alpha-1}{2(1-\alpha)}} + H_2 \end{aligned} \tag{3.100}$$

where H_1 and H_2 depend on α.In figure 3.15, we present the torque obtained from the BEM simulations for various values of α and fit 3.100 to the results to obtain H_1 and H_2 and also report the corresponding effective aspect ratio. From the regularized outer solution of 3.62, we already have the quantitative prediction of torque contribution at $O(\kappa^2)$ from the outer region, and this matches well with the result obtained from the the BEM simulations. For $\alpha = \frac{3}{8}$, the regularized integral equation predict a torque of $-19.21\kappa^2$ (figure 3.13) and the BEM simulations predict a torque of $-19.05\kappa^2$ (figure 3.15). We note here that the coefficient of the $O(\kappa^{\frac{12}{5}})$ contribution predicted from the regularized outer solution is different from the BEM prediction because the regularized outer solution of 3.62 does not account for the effect of the $O(1)$ boundary layer force density which also contributes at $O(\kappa^{\frac{12}{5}})$. For $\alpha = 3/8$, the torque fit given by $G_A/\kappa = -19.05 + 14.97\kappa^{2/5}$ can accurately predict the torque with less than 5% error for $\kappa \leq 0.08$ and the leading order term can estimate the torque to that accuracy for $\kappa \leq 0.001$.

Using the leading order toque on the particle in orientation B (3.98) and 3.100, the effective aspect ratio of the particle is given by:

$$\frac{\kappa_e}{\kappa} = \left[\frac{3H_2}{32}\right]^{\frac{1}{2}} \left(1 + \frac{H_1\kappa^{\frac{4\alpha-1}{2(1-\alpha)}}}{H_2}\right)^{\frac{1}{2}} \tag{3.101}$$

For $\alpha = 3/8$, the effective aspect ratio is given by, $\kappa_e/\kappa = 1.34(1 - 0.79\kappa^{2/5})^{1/2}$. As α decreases from 1/2 to 1/4 and the particle becomes more blunt, the rotation rate

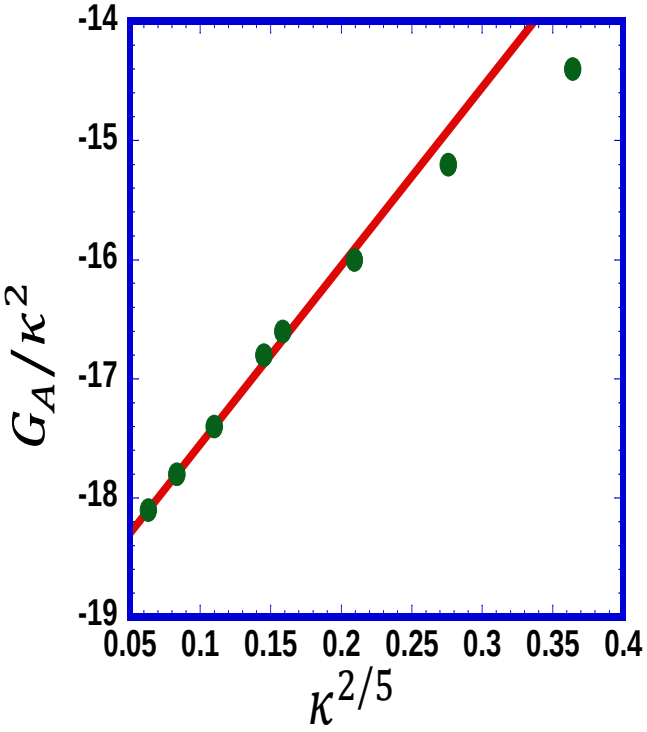

Figure 3.15: Torque acting on the particle obtained from BEM simulations for $\alpha = 3/8$. Here the linear fit is obtained using the three smallest aspect ratios used in the plot ($\kappa = 0.001$, 0.002, and 0.004). Equation of the fitting line is: $G_A/\kappa^2 = -19.045 + 14.973\kappa^{2/5}$. Using $G_B = -32/3$, the corresponding effective aspect ratio is $\frac{\kappa_e}{\kappa} = 1.34(1 - 0.79\kappa^{2/5})^{1/2}$ for $\alpha = 3/8$.

continues to increase even though the rotation rate of the aligned disk remains proportional to κ^2.

3.5.4 Effective aspect ratio for $0 \leq \alpha \leq \frac{1}{4}$

Particles with $0 \leq \alpha < \frac{1}{4}$ have edges that are sufficiently blunt so as to yield a strong singularity of the driving term for the stresses that dominates the torque on the particle. In this case the leading contributions to the torque are $O(\kappa^{\frac{3}{2(1-\alpha)}})$ and arise due to the influence of the singular forcing term on the stresses in the matching region and the force dipole arising due to the large stresses in the boundary layer. The next contribution to the torque is $O(\kappa^2)$ and comes from the outer region. The torque is again expressed as a sum of these two torque contributions using 3.100.

In the analysis for $0 \leq \alpha < \frac{1}{4}$ in section IV, we showed that the driving term for f_y^* in 3.62 is singular close to the edge. The influence of this singular forcing at the edge on the torque can be evaluated using the regularized numerical solution of 3.62. In figure 3.16, we show the dependence on ϵ, of the torque obtained from the regularized numerical solution for $\alpha = \frac{1}{8}$ and $\alpha = \frac{1}{16}$. For both values of α, we find the torque to be proportional to $\epsilon^{-\frac{1}{2}+2\alpha}$ as predicted by the analysis. The rapid increase in torque with decreasing ϵ indicates that the torque is now dominated by the singularity in the boundary layer.

From the analysis, the stresses are predicted to be $O(1)$ in a boundary layer of $O(\kappa^{\frac{1}{1-\alpha}})$ thickness for $\alpha < 1$. Figure 3.17 shows a plot of the force densities, f_x and f_y in the boundary layer region as a function of the boundary layer coordinate for $\alpha = \frac{1}{8}$. Again, to the leading order, the stresses are $O(1)$ and independent of

(a)

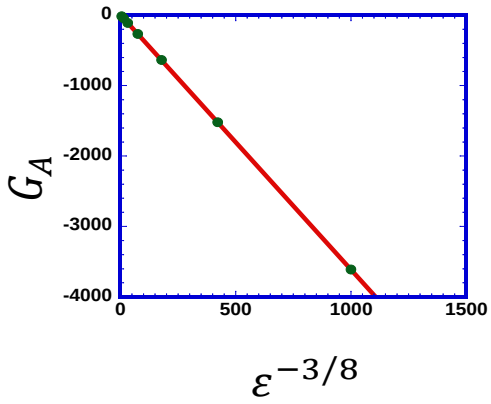

(b)

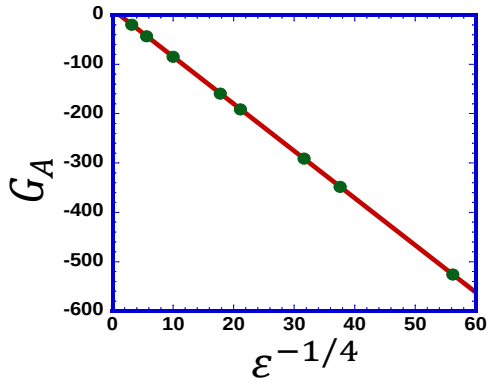

Figure 3.16: Scaling of the torque with respect to the small parameter ϵ obtained from the numerical solution of the regularized 3.70. (a) Scaling of the torque for $\alpha = 1/16$. Equation of the line is $5.45 - 3.62\epsilon^{-3/8}$. (b) Scaling of torque for $\alpha = 1/8$. Equation of the line is $10.96 - 9.55\epsilon^{-1/4}$. The curves are obtained by fitting a straight line for the three smallest values of ϵ.

κ.

In figure 3.18, we present the torque obtained from the BEM simulations for various values of α and fit the results with 3.100 to obtain H_1 and H_2 and report the corresponding effective aspect ratios. For $\alpha < 1/4$, the coefficients of the leading order torque at $O(\kappa^{\frac{3}{2(1-\alpha)}})$ cannot be predicted from the dependence of torque on ϵ obtained from the numerical results of 3.65. This is due to the fact that we do not have any analytical or numerically aided analytical estimate of the torque from the boundary layer region which also contributes to the torque at $O(\kappa^{\frac{3}{2(1-\alpha)}})$. The results that we obtain from the full BEM are a combination of both torques from the boundary layer region and torque from the singularity at the edge to the leading order at $O(\kappa^{\frac{3}{2(1-\alpha)}})$. Fitting the data with 3.100, the torque can be accurately predicted for $\alpha = 0$ with less than 6% error for $\kappa \leq 0.08$. The leading order term alone can estimate the torque to within 6% for $\kappa \leq 0.04$. For $\alpha = 1/8$, there is an error of less than 8% for $\kappa \leq 0.08$ with both the leading order terms and an error of $\leq 10\%$ for $\kappa \leq 0.002$ using the leading order term . For the special case of a circular disk, $\alpha = 0$, we find that $\kappa_e/\kappa = 1.12\kappa^{-1/4}(1 + +0.21\kappa^{1/2})^{1/2}$. For $\alpha = 1/8$, we find $\kappa_e/\kappa = 1.31\kappa^{-1/7}(1 - 0.55\kappa^{2/7})^{1/2}$. In figure 3.19, we compare our prediction of effective aspect ratio with previous reported data for $\alpha = 0$ disk [57, 104, 128]. For almost all the aspect ratios, the present study indicates a larger effective aspect ratio than both the previous simulation studies [104, 128] . Meng and Higdon [104] use a planar array of spheres to represent the disk, due to this their disk has rounded edges which leads to lower effective aspect ratios; the effect of rounding of the edges on the torque has been shown by Singh et al. [128]. The difference between Singh et al. [128] predictions and the present study is more modest. This difference could be due to the limited grid resolution of Singh et al.'s finite element computations.

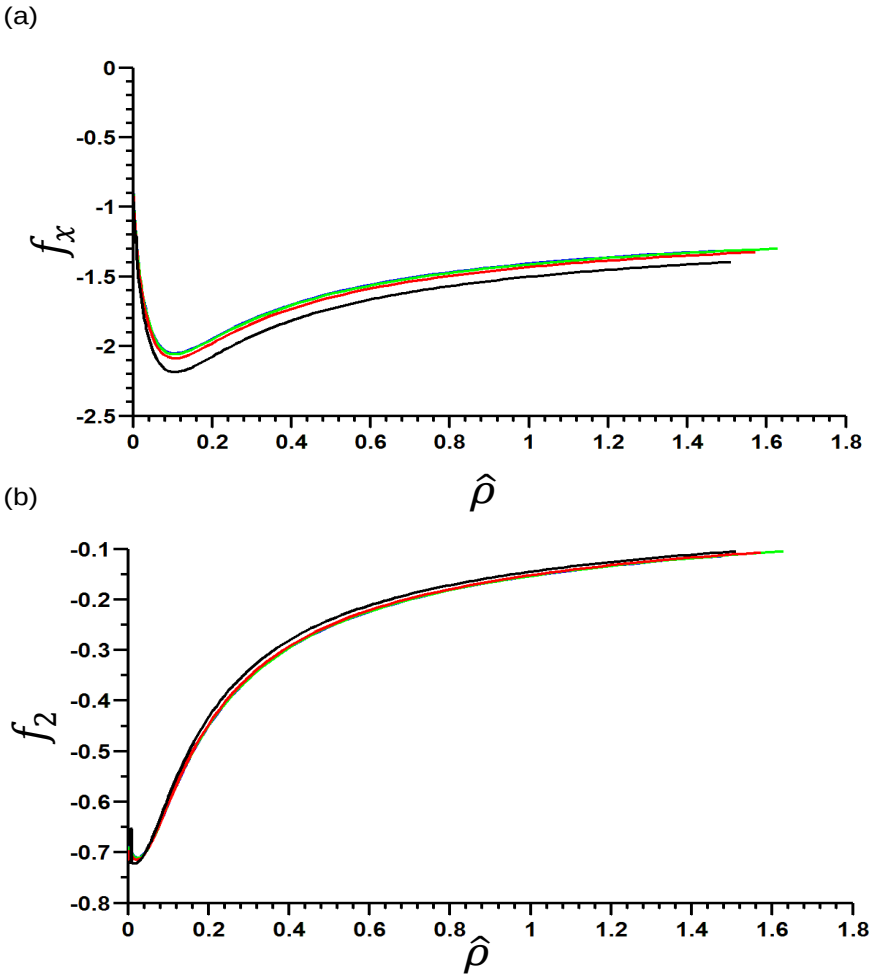

Figure 3.17: Stresses in the inner region for $\kappa = 0.001$ (blue), 0.004 (green), 0.02 (red), and 0.08 (black) as a function of the boundary layer coordinate for $\alpha = 1/8$.

(a)

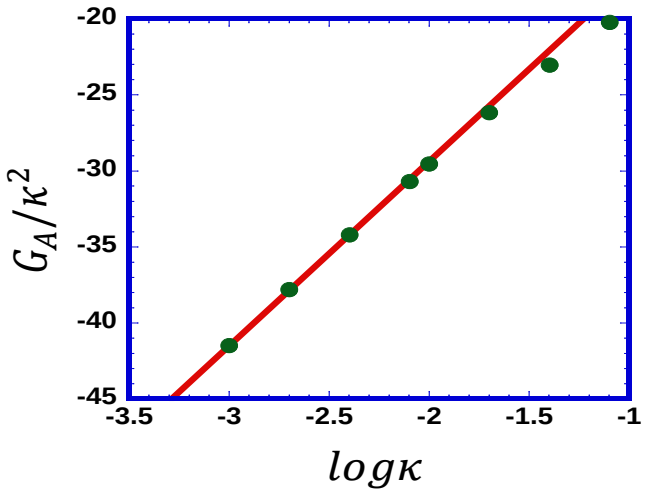
-20
-25
-30
-35
-40
-45
-3.5
-3
-2.5
-2
-1.5
-1
G_A/κ^2
$log\kappa$

(b)

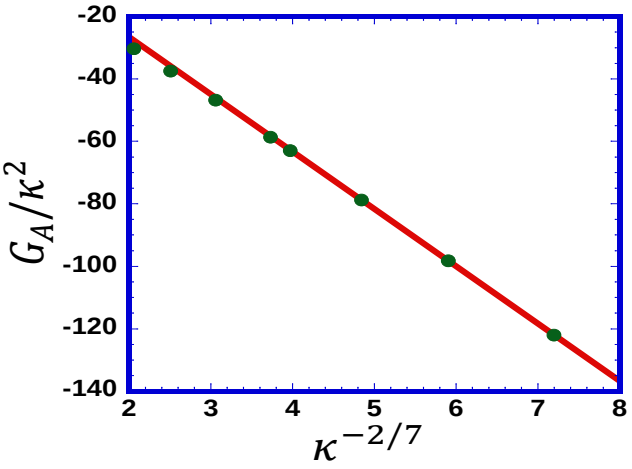
-20
-40
-60
-80
-100
-120
-140
2
3
4
5
6
7
8
G_A/κ^2
$\kappa^{-2/7}$

(c)

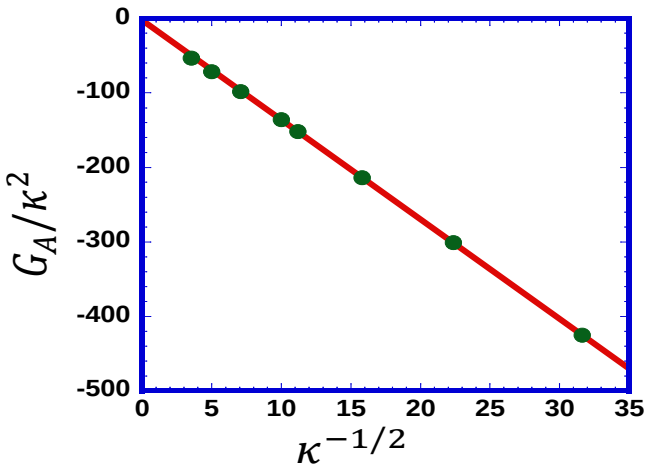

Figure 3.18: Variation of the torque with respect to the aspect ratio for $\alpha = 1/4$ (a), $1/8$ (b) and 0 (c). Here the linear fit is obtained using the three smallest aspect ratios in the plot ($\kappa = 0.001$, 0.002, and 0.004). Equation of the fitting line is: $G_A/\kappa^2 = -5.11 + 12.13 \log \kappa$ for $\alpha = 1/4$, $G_A/\kappa^2 = 10.12 - 18.36\kappa^{-2/7}$ for $\alpha = 1/8$, and : $G_A/\kappa^2 = -2.80 - 13.35\kappa^{-1/2}$ for $\kappa = 0$. Using $G_B = -32/3$, the corresponding effective aspect ratio is $\frac{\kappa_e}{\kappa} = 1.07(\log \frac{1}{\kappa})^{1/2}\left(1 - \frac{0.42}{\log \kappa}\right)^{1/2}$ for $\alpha = 1/4$, $\frac{\kappa_e}{\kappa} = 1.31\kappa^{-1/7}(1 - 0.55\kappa^{2/7})^{1/2}$ for $\alpha = 1/8$, and $\frac{\kappa_e}{\kappa} = 1.12\kappa^{-1/4}(1 + 0.21\kappa^{1/2})^{1/2}$ for $\alpha = 0$.

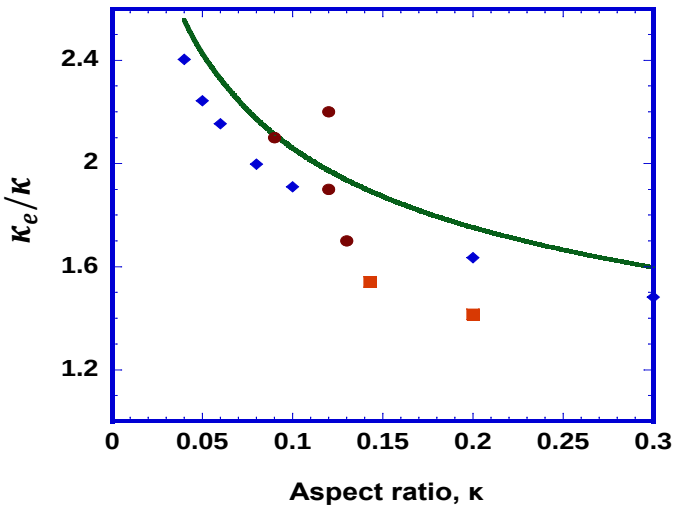

Figure 3.19: Ratio of the effective aspect ratio to the actual aspect ratio for thin disks ($\alpha = 0$) obtained from the present work (continuous curve, $\frac{\kappa_e}{\kappa} = 1.12\kappa^{\frac{-1}{4}}(1 + 0.21\kappa^{1/2})^{1/2}$) compared with the FEM simulations of Singh et al. (diamond), Meng and Higdon (square) results for the disk approximated by planar arrays of spheres, and the experimental results of Goldsmith and Mason (circle).

In the asymptotic analysis for force density in the matching region, we found that $\alpha = \frac{1}{4}$ is a special case because the general solution for Laplace's equation used for the potential function failed to satisfy the boundary condition. Thus, it was not possible to predict the scaling of the torque contribution from the edge with κ for this case using the asymptotic analysis and we instead obtain this scaling by using the regularized numerical solution of 3.62. We find that the torque is proportional to $\ln \epsilon$ (figure 3.20), indicating that the singularity in the integral for the torque is $log\rho_m$ for $\alpha < \frac{1}{4}$ whereas it is $\rho_m^{-\frac{1}{2}+2\alpha}$ for $\alpha < \frac{1}{4}$. Since $\rho_m = O(\kappa^{\frac{4}{3}})$, the leading order torque contribution from the matching region for $\alpha = \frac{1}{4}$ is $\kappa^2 log\kappa$. There is still an $O(\kappa^{\frac{3}{2(1-\alpha)}})$ contribution to torque from the $O(1)$ force densities in the boundary layer of the particle. This torque contribution for $\alpha = \frac{1}{4}$ is $O(\kappa^2)$ which is thus of the same order as the contribution to the torque from the outer region. For $\alpha = \frac{1}{4}$, a linear combination of $O(\kappa^2 log\kappa)$ and $O(\kappa^2)$ is used to fit the numerical results:

$$\frac{G_A}{\kappa^2} = H_1 log\kappa + H_2 \tag{3.102}$$

Unlike $\alpha < 1/4$ case, the value of H_1 can be predicted using the regularized outer solution for $\alpha = \frac{1}{4}$ since only the singular term at the edge contributes to it. H_1 from the analytical numerical results is $\frac{9.21}{1-\alpha} = 12.28$ and H_1 from the BEM results is 12.13. With the torque fit of $G_A/\kappa^2 = -5.11 + 12.13 \log \kappa$, there is $\leq 4\%$ error in torque predictions for $\alpha = 1/4$. The corresponding effective aspect ratio for $\alpha = 1/4$ is given by $1.07(\log(1/\kappa))^{1/2}(1 - 0.42/\log \kappa)^{1/2}$.

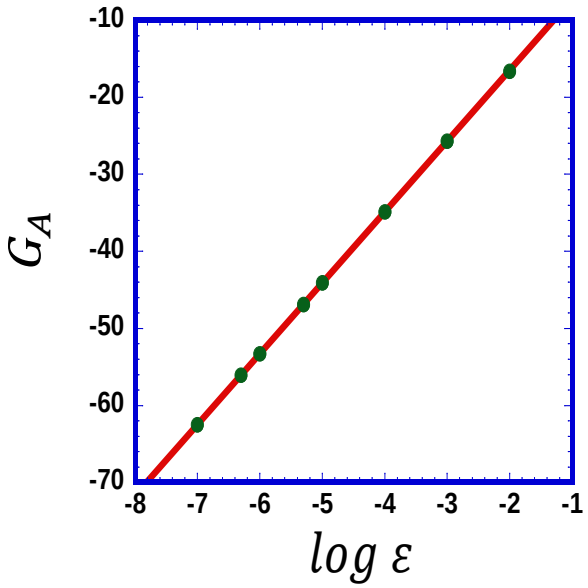

Figure 3.20: Scaling of the torque with respect to the small parameter ϵ obtained from the numerical solution of the regularized equation for $\alpha = 1/4$. Equation of the line is $2 + 9.21 \log \epsilon$, obtained by fitting a line to the smallest three values of ϵ used in the simulations.

3.6 Conclusion

We have studied the rotational motion of rigid thin axisymmetric particles in simple shear flow at low Reynolds number. An axisymmetric particle undergoes rotational motion in one of an infinite set of orbits in simple shear flow. This rotational motion is completely determined by a single parameter called the effective aspect ratio of the particle. One can tune the shape of the particle to change its effective aspect ratio and thus its rotational motion in simple shear flow. We have extended previously known results for the effective aspect ratio to small aspect ratio for a one-parameter family of shapes whose thickness is $\kappa(1-\rho^2)^\alpha$. This family of shapes allows a full range of power law dependence of the thickness of the particle on the radial distance $1-\rho$ from the particle edge as $\rho \to 1$ spanning the range from blunt objects $\alpha = 0$ with a non-zero thickness at the edge to $\alpha \leq 1$ for the thickness goes smoothly to zero but has an infinite slope at the edge, to sharp particles with a finite non-zero slope ($\alpha = 1$) or zero slope $\alpha > 1$ at the edge.

Here is a brief summary of our findings. The effective aspect ratio of a particle can be calculated from the torque acting on the particle when it is oriented with its axis of symmetry in the gradient direction. Based on the order of magnitude of surface stresses, the surface of the particle can be divided into two regions, an outer region where the thickness of the particle is much smaller than the distance from the edge and a boundary layer region (present when $\alpha < 1$) of $O(\kappa^{\frac{1}{1-\alpha}})$ width where the thickness is of the same order as the distance from the edge. The order of magnitude of the torque contribution from the inner region depends on the shape of the particle close to the edge whereas that from outer region is independent of the shape of the particle. For a whole range of particle

shapes ($\alpha \leq 1/4$), the motion of the particle is dictated by the edge contribution. This is similar to the case of a slender fiber where, as shown originally by Cox [34], blunt ends increase the effective aspect ratio by $O((\ln \kappa)^{1/2})$ in the limit of large κ, so that a slender cylindrical fiber completes a single Jeffery orbit in a time of $O(\kappa(\ln \kappa)^{1/2})$ in contrast to a fiber with pointed ends which takes a time of $O(\kappa)$. The sensitivity of effective aspect ratio to the shape of the edge is considerably amplified for disk shaped particles compared to large aspect ratio particles. The effective aspect ratio of sufficiently blunt-ended ($\alpha < 1/4$) disk-shaped particles becomes algebraically larger by a factor of $O(\kappa^{\frac{1-4\alpha}{4(1-\alpha)}})$.

For all particle shapes of small thickness, the leading order stresses in the x and y direction contribute to no net torque at $O(\kappa)$ (3.56). For $\alpha > \frac{1}{4}$, the leading order torque contribution comes from the outer region at $O(\kappa^2)$. Thus, the effective aspect ratio, κ_e for these particles scales as their aspect ratio, κ. For $1/4 < \alpha < 1/2$, the leading order effective aspect ratio still scales as $O(\kappa)$ but the first correction to this scaling is large ($O(\kappa^{\frac{3}{4(1-\alpha)}})$). For $\alpha < \frac{1}{4}$, the leading order torque contribution comes from the edge and is $O(\kappa^{\frac{3}{2(1-\alpha)}})$. The scaling of the effective aspect ratio for these particles is $O(\kappa^{\frac{3}{4(1-\alpha)}})$. For $\alpha = \frac{1}{4}$, we find that the torque contribution from the edge scales as $\kappa^2 \log \kappa$ and thus the effective aspect ratio scales as $\kappa(\log \kappa)^{\frac{1}{2}}$. Figure 3.21 shows the exponent, ζ of the leading order term in the relation $\kappa_e = a\kappa^{\zeta}$ for the whole range of $0 \leq \alpha < \infty$. In table 3.1, we summarize the dependence of the effective aspect ratio on aspect ratio for different α considered in this work.

The rotational motion of non-spherical particles plays an important role in determining the bulk properties of a suspension. In this work, we find that blunt (small α) particles tend to rotate faster. This source of variation in rota-

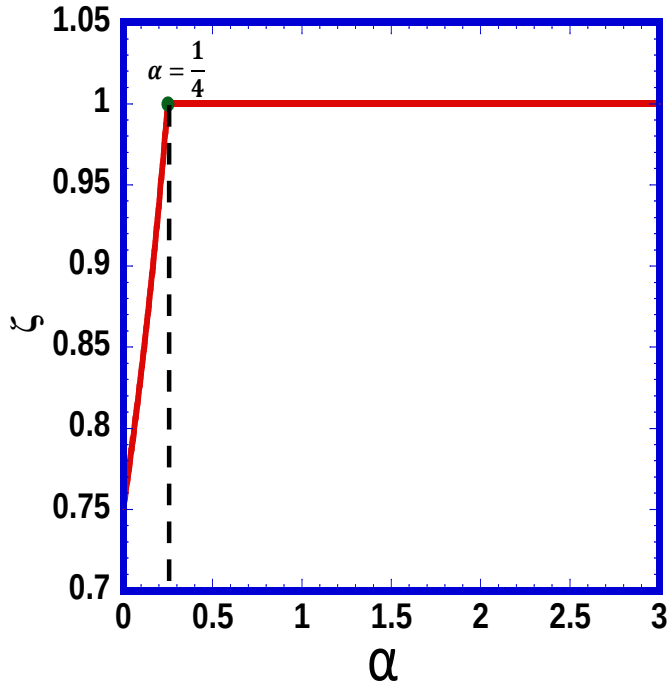

Figure 3.21: To leading order, $\kappa_e = a\kappa^{\zeta}$ ($\alpha \neq 1/4$) when the particle shape is given by, $y(\rho) = \kappa(1 - \rho^2)$. The exponent ζ is plotted as a function of α. The scaling of 1 extends to $\alpha \to \infty$. For $\alpha = 1/4$, the effective aspect ratio scales as $\kappa_e = a(\kappa(\log \kappa)^{1/2})$

α	κ_e/κ
0	$1.12\kappa^{\frac{-1}{4}}\left(1+0.21\kappa^{\frac{1}{2}}\right)^{\frac{1}{2}}$
1/8	$1.31\kappa^{\frac{-1}{7}}\left(1-0.55\kappa^{\frac{2}{7}}\right)^{\frac{1}{2}}$
1/4	$1.07\left(\log\frac{1}{\kappa}\right)^{\frac{1}{2}}\ \left(1-\frac{0.42}{log\kappa}\right)^{\frac{1}{2}}$
3/8	$1.34\left(1-0.79\kappa^{\frac{2}{5}}\right)^{\frac{1}{2}}$
1/2	1
2/3	0.81
2	0.44

Table 3.1: The effective aspect ratio with respect to the aspect ratio as a function of different values of α considered in this work when the particle shape is given by, $y(\rho) = \kappa(1-\rho^2)^\alpha$

tional motion is purely due to the shape of the particles and can be useful in different applications. For example, one can use a suspension of large α particles for preparing materials used as a gas barrier. For such materials, alignment of particles is important, large α particles have a slow rotation rate when oriented near the flow-gradient plane and thus a larger tendency to flow align. On the other hand, for suspensions in which particles are added to increase the viscosity of the suspension, blunt (small α) particles would be preferred. In an imposed simple shearing motion of the ambient fluid, the increased rate of dissipation which occurs due to the presence of a non-spherical particle is highly dependent upon its orientation, so the viscosity of a dilute suspension depends on the probability distribution of orientations among all the suspension particles. According to Jeffery's analysis, each axisymmetric particle rotates in one of an infinite set of orbits. In the absence of particle interactions and Brownian motion, a particle will remain indefinitely in the same orbit. Hence, one might conclude that the distribution of particle orbits is completely determined by the initial distribution of orientations in the suspension. Such an initial condition leads to a time-dependent orientation distribution of the suspension and hence leads to an effective viscosity of the suspension which is periodic in time [45] . Jeffery's solution completely neglects such effects as fluid and particle inertia [76, 136, 137], Brownian motion and particle-particle interactions [123, 134], all of which will be present in a suspension. Hence, an alternative view might be that these (presumably) small departures from undisturbed creeping flow will lead to a slow change in the orbit of a particle so that eventually a steady-state distribution of orbits may be established which is independent of the initial orientations of the particles. For small particles, one can use Leal and Hinch's [97] analysis for the orbit distribution of weakly Brownian particles undergoing

rotational motion in simple shear flow. Leal and Hinch used the following expression from Jeffery to calculate the effective viscosity of a dilute suspension of spheroids

$$\frac{\mu_{\text{eff}} - \mu}{\mu n} = \left[K_1 < \sin^4\theta \sin^2 2\phi > + K_2 < \cos^2\theta > + K_3 < \sin^2\theta >\right] \tag{3.103}$$

where μ_{eff} is the effective viscosity of the suspension, n is the number of particles per unit volume and the angle brackets (<>) indicate an average over the particle orientation distribution. For spheroids [72, 97], in the limit $\kappa << 1$, $K_1 = 5d^3/18$, $K_2 = 4d^3/9$ and $K_3 = V_s$, where $V_s = \frac{\pi d^3 \kappa}{6}$ is the volume of the spheroid. From their solution for the distribution of particles among the Jeffery orbits due to weak Brownian motion, Leal and Hinch determined the orientational moments to be $< \sin^4\theta \sin^2 2\phi >= 1.248\kappa_e$ and $< \cos^2\theta >= 1.792\kappa_e$ in the limit $\kappa_e \ll 1$. These orientational results are applicable to any small aspect ratio axisymmetric tumbling particle. For a spheroid with $\kappa_e = \kappa$ these results yield,

$$\frac{\mu_{\text{eff}} - \mu}{\mu\Phi} = 3.183 + O(\kappa) \tag{3.104}$$

where, Φ = volume fraction of the solid particles.

For any particle shape, the constants K_1, K_2, and K_3 can be determined by considering the stresslet acting on the particle whose axis of symmetry is oriented along the extensional axis of the extensional component of the shear flow (orientation C: $\theta = \pi/2$ and $\phi = \pi/4$), in the vorticity direction (orientation D: $\theta = 0$) and in the gradient direction (orientation A: $\theta = \pi/2$ and $\phi = \pi/2$), respectively. In orientations C and D, the imposed fluid velocity at the particle surface is $O(\gamma d)$ and the resulting $O(\mu\gamma d^3)$ stresslet is to leading order that of a planar circular disk and is independent of the detailed particle shape for $\kappa \ll 1$. Thus, for all thin disk particles, to the leading order, $K_1 = 5d^3/18$ and $K_2 = 4d^3/9$. The

stresslet for particles in orientation A can be determined using the leading order force distribution derived in section IV A. The leading order contributions to the stresslet in orientation A are given by:

$$S_{xy} = -\frac{1}{2}\int_S (f_y \rho \cos\theta + f_x \kappa l(\rho)) dS \tag{3.105}$$

where $-f_x$ and $-f_y$ are the forces exerted by the fluid on the particle. Using the leading order f_x (3.54) and f_y (3.55) forces we have,

$$\begin{aligned} S_{xy} &= -\frac{2\kappa}{2}\int_0^1 \int_0^{2\pi} (\rho \cos^2\theta \frac{\partial l(\rho)}{\partial \rho} - l(\rho)) \rho d\rho d\theta \\ &= \frac{2\pi\kappa}{(1+\alpha)} \mu\gamma d^3 \\ &= 8V\mu\gamma \end{aligned} \tag{3.106}$$

where V ($= \frac{\pi d^3 \kappa}{4(\alpha+1)}$) is the volume of the particle. It should be noted here that the leading order forces lead to a stresslet at $O(\kappa)$ although the torque at $O(\kappa)$ is zero. The contribution to the stresslet from the boundary layer is $O(\kappa^{3/2(1-\alpha)})$ which is less than the leading order $O(\kappa)$ contribution and hence can be neglected. The contribution to the stress for a particle number density, n is then given by $nS_{xy} = 8nV\mu\gamma$ and the coefficient, $K_3 = \frac{8nV\mu\gamma}{2\mu\gamma n} = 4V$. Using this result in 3.103, for a thin disk effective viscosity is given by,

$$\begin{aligned} \frac{\mu_{eff} - \mu}{\mu n} &= \frac{5d^3}{18} < \sin^4\phi \sin^2 2\phi > + \frac{4d^3}{9} < \cos^2\theta > + 4V < \sin^2\theta >) \\ &= 1.15 d^3 \kappa_e + 4V \end{aligned} \tag{3.107}$$

In the case of cylindrical disks ($\alpha = 0$), using $\kappa_e/\kappa = 1.12\kappa^{-1/4}(1 + +0.21\kappa^{1/2})^{1/2}$, the effective viscosity is given by,

$$\frac{\mu_{\text{eff}} - \mu}{\mu\Phi} = 1.64\kappa^{-1/4}(1 + 0.21\kappa^{1/2})^{1/2} + 4. \tag{3.108}$$

Thus, the intrinsic viscosity of cylindrical disks unlike that of spheroidal disks will grow as $\kappa^{-1/4}$ with decreasing aspect ratio. Previous experimental work by

Jogun and Zukoski [73] and Kasperski et al. [78] has reported viscosity of suspension containing kaolinite clay particles. Kasperski et al. has shown that for volume fraction of Na-kaolinite particles between 4.510^{-3} to 0.035, the ratio $\frac{\mu_{\text{eff}}-\mu}{\mu\Phi_d}$ varies between 4.2 to 7.6. Where ϕ_d is the volume fraction of particles calculated based on dry weight and for Na-kaolinite it is expected to be equal to the actual volume fraction (ϕ) in the suspension due to its non-swelling behavior. Unfortunately, Kasperski et al. did not report the aspect ratio of their particles. Our prediction of viscosity of the suspension in 3.108 corresponds to $\frac{\mu_{\text{eff}}-\mu}{\mu\Phi_d} = 7$ for an aspect ratio of 0.1. Jogun and Zukoski [73] has reported the viscosity of dispersions of kaolin clay particles of aspect ratio $1/10 - 1/12$ for only one volume fraction in the dilute limit. For a volume fraction of 0.05, the viscosity of the suspension of kaolin clay particles is found to be 1.9 mPa.s. Assuming the continuous phase viscosity of their aqueous buffer solution as 1 mPa.s (which is not reported by Jogun and Zukoski [73]), 3.108 predicts a suspension viscosity of 1.35 mPa.s. Meng and Higdon [104] numerically calculated viscosity for their disk particle suspension where the particles are formed by a planar assembly of small spherical particles. For a volume fraction of 0.01 of aspect ratio 1/7 particles, they found the relative viscosity of the suspension to be 1.039. 3.108 predicts a relative viscosity of 1.068. It seems that a more controlled study of rheological behavior of thin disk suspension in the dilute regime is needed to verify the effective viscosity predictions here.

The family of shapes considered in this work, $y = \kappa(1-\rho^2)^\alpha$, allows for any power law dependence $(1-\rho)^\alpha$ of the particle thickness with respect to the distance $1-\rho$ from the edge of the particle in the limit as $\rho \to 1$. Since our analysis shows that scaling of the thickness with respect to distance from the edge controls the order of magnitude of the stresses, we can extrapolate our results to

suggest the scaling of the effective aspect ratio for all low aspect ratio convex, axisymmetric shapes with fore-aft symmetry whose surface is continuous and differentiable. As noted earlier, the leading order torque at $O(\kappa)$ is zero (3.56) for all flat, thin particle irrespective of the exact shape as long as $l(1) = 0$. Particles with a finite slope at the edge $\alpha > 1$ have no singular stresses near the edge and we can expect $\kappa_e \sim \kappa$. Particles whose slope approaches infinity near the edge exhibit a boundary layer wherein the stresses in the y direction are $O(1)$. However, the torque from this boundary layer remains smaller than that from the outer region when the thickness is less singular than $(1-\rho)^{1/4}$ and again $\kappa_e \sim \kappa$. For blunter shapes whose thickness scales as $(1-\rho)^{\alpha}$ with $\alpha < 1/4$ as $\rho \to 1$, the boundary layer and matching region near the edge of the particle dominate the torque and $\kappa_e/\kappa \sim \kappa^{\frac{\alpha-\frac{1}{4}}{1-\alpha}}$. Any particle shape in which the particle thickness reaches an $O(\kappa)$ value within an $O(\kappa)$ distance from the edge can be expected to yield an $O(\kappa)$ boundary layer thickness and an effective aspect ratio $\kappa_e \sim \kappa$ similar to the cylindrical disk. In this work, we have not optimized the shape of the particle to identify the slowest or the fastest rotating particle. Singh et al. [129] have identified ring shape particles which stop rotating in simple shear flow but shape of the fastest rotating thin particle remains unknown.

3.7 Appendix

This section is divided into two parts. In the first part, we show that the stress in the z direction, f_z does not influence the integral equations for the velocity field in the x and y direction to $O(\kappa^2)$. In the second part, the elliptic integral formulations of the integral equations used for the BEM simulations is shown.

3.7.1 Contribution of f_z to velocity disturbance fields in x and y directions

The matched asymptotic analysis performed in section IV, assumed that the contribution of the surface stress, f_z to the velocity disturbance field in the x and y direction is less than $O(\kappa^2)$. Here, we show that to be true by first determining that the scaling of the leading order non-zero f_z is $O(\kappa^2)$ and then showing that the contribution of the leading order f_z stress to the disturbance field in the x and y direction is $O(\kappa^3)$. It should be noted here that by the symmetry of the problem, f_z by itself cannot induce a torque on the particle. The torque contribution can only come from the velocity disturbance field caused by f_z in the x and y direction which in turn can drive f_x and f_y stresses.

We start with the integral equation 3.12 for the velocity field in the z direction and using the boundary condition, $v_z = 0$ on the surface of the particle, we get:

$$\begin{aligned}
0 = &\int_S dS'[J_{zx}(\boldsymbol{\rho} - \boldsymbol{\rho'} + \boldsymbol{e_y}\kappa(l(\rho) - l(\rho'))) - J_{zx}(\boldsymbol{\rho} - \boldsymbol{\rho'} + \boldsymbol{e_y}\kappa(l(\rho) + l(\rho')))]f_x(\boldsymbol{\rho'}) \\
&+ \int_S dS'[J_{zy}(\boldsymbol{\rho} - \boldsymbol{\rho'} + \boldsymbol{e_y}\kappa(l(\rho) - l(\rho'))) + J_{zy}(\boldsymbol{\rho} - \boldsymbol{\rho'} + \boldsymbol{e_y}\kappa(l(\rho) + l(\rho')))]f_y(\boldsymbol{\rho'}) \\
&+ \int_S dS'[J_{zz}(\boldsymbol{\rho} - \boldsymbol{\rho'} + \boldsymbol{e_y}\kappa(l(\rho) - l(\rho'))) - J_{zz}(\boldsymbol{\rho} - \boldsymbol{\rho'} + \boldsymbol{e_y}\kappa(l(\rho) + l(\rho')))]f_z(\boldsymbol{\rho'}) \\
&= I_{zx} + I_{zy} + I_{zz} \qquad (3.109)
\end{aligned}$$

Here I_{zx} and I_{zy} are the disturbance fields in the z direction due to f_x and f_y stresses. Starting with the disturbance field due to f_x stress, one can divide the integral I_{zx} into two parts that contribute in $|\boldsymbol{\rho} - \boldsymbol{\rho'}| > O(\kappa)$ and $|\boldsymbol{\rho} - \boldsymbol{\rho'}| \sim O(\kappa)$.

Rewriting I_{zx}:

$$\begin{aligned} I_{zx} &= \int_S dS'([J_{zx}(\boldsymbol{\rho}-\boldsymbol{\rho'}+\boldsymbol{e_y}\kappa(l(\rho)-l(\rho'))) - J_{zx}(\boldsymbol{\rho}-\boldsymbol{\rho'}+\boldsymbol{e_y}\kappa(l(\rho)+l(\rho')))]f_x(\boldsymbol{\rho'}) \\ &- [J_{zx}(\boldsymbol{\rho}-\boldsymbol{\rho'}) - J_{zx}(\boldsymbol{\rho}-\boldsymbol{\rho'}+\boldsymbol{e_y}2\kappa l(\rho))]f_x(\boldsymbol{\rho})) \\ &+ \int_S dS'[J_{zx}(\boldsymbol{\rho}-\boldsymbol{\rho'}) - J_{zx}(\boldsymbol{\rho}-\boldsymbol{\rho'}+\boldsymbol{e_y}2\kappa l(\rho))]f_x(\boldsymbol{\rho}) \\ &= I^*_{zx} + I^{**}_{zx} \end{aligned} \tag{3.110}$$

where the integral I^*_{zx} is evaluated for $|\boldsymbol{\rho}-\boldsymbol{\rho'}| > O(\kappa)$ with no contribution from the singularity at $\boldsymbol{\rho}$. Using the Taylor series expansion for J_{zx} for small κ, we get

$$\begin{aligned} I^*_{zx} &= \int dS'([-2\kappa^2 l(\rho)l(\rho')\frac{\partial^2 J_{zx}(\boldsymbol{\rho}-\boldsymbol{\rho'})}{\partial y}|_{y=0}]f_x(\boldsymbol{\rho'}) \\ &- [-2\kappa^2 l^2(\rho)\frac{\partial^2 J_{zx}(\boldsymbol{\rho}-\boldsymbol{\rho'})}{\partial y}|_{y=0}]f_x(\boldsymbol{\rho})) + O(\kappa^3) \\ &= O(\kappa^2) \end{aligned} \tag{3.111}$$

In determining the above scaling we use the already known result, $f_x(\boldsymbol{\rho}) = -1 + O(\kappa)$. We now account for the contribution of the singular part of I_{zx} to the disturbance field. When $\rho'' \sim O(\kappa)$, we move the center of the coordinate system to the point of interest ρ. A unit area, with ρ being the center of the coordinate system, can be written as $dS' = \rho'' d\rho'' d\theta''$. We can write I^*_{zx} as:

$$I^{**}_{zx} = \int_\rho^{1-\rho}\int_0^{2\pi} \rho'' d\rho'' d\theta''(\frac{\rho''\cos\theta''\rho''\sin\theta''}{\rho''^3} - \frac{\rho''\cos\theta''\rho''\sin\theta''}{(\rho''^2+4\kappa^2 l^2(\rho))^3}) \tag{3.112}$$

Integrating over θ'' we get,

$$I^{**}_{zx} = 0 + O(\kappa^3) \tag{3.113}$$

Thus, combining 3.111 and 3.113, we can write the contribution of the f_x stress dipole to the disturbance field in the z direction as:

$$I_{zx} = \int_S dS'(-2\kappa^2 l(\rho)\frac{\partial^2 J_{zx}(\boldsymbol{\rho}-\boldsymbol{\rho'})}{\partial y^2}|_{y=0})(l(\rho')f_x(\rho') - l(\rho)f_x(\rho)) + O(\kappa^3) \tag{3.114}$$

We now calculate the disturbance field due to f_y stresses. Writing the integral I_{zy} as a sum of terms contributing when $\rho'' > O(\kappa)$ and $\rho'' \sim O(\kappa)$, we get

$$\begin{aligned} I_{zy} &= \int_S dS'[J_{zy}(\boldsymbol{\rho} - \boldsymbol{\rho'} + \boldsymbol{e_y}\kappa(l(\rho) - l(\rho'))) + J_{zy}(\boldsymbol{\rho} - \boldsymbol{\rho'} + \boldsymbol{e_y}\kappa(l(\rho) + l(\rho')))]f_y(\boldsymbol{\rho'}) \\ &- \int_S dS'[J_{zy}(\boldsymbol{\rho} - \boldsymbol{\rho'}) + J_{zy}(\boldsymbol{\rho} - \boldsymbol{\rho'} + \boldsymbol{e_y}2\kappa l(\rho))]f_y(\boldsymbol{\rho}) \\ &+ \int_S dS'[J_{zy}(\boldsymbol{\rho} - \boldsymbol{\rho'}) + J_{zy}(\boldsymbol{\rho} - \boldsymbol{\rho'} + \boldsymbol{e_y}2\kappa l(\rho))]f_y(\boldsymbol{\rho}) \\ &= I^*_{zy} + I^{**}_{zy} \end{aligned} \tag{3.115}$$

The integral I^*_{zy} has a singularity of type $\frac{1}{\rho'}$ and is evaluated as a Cauchy principal value. Using the Taylor series expansion for J_{zy}, we get:

$$\begin{aligned} I^*_{zy} &= \int_S dS'(2\kappa l(\rho)f_y(\boldsymbol{\rho'})\frac{\partial J_{zy}(\boldsymbol{\rho} - \boldsymbol{\rho'})}{\partial y} - 2\kappa l(\rho)f_y(\boldsymbol{\rho})\frac{\partial J_{zy}(\boldsymbol{\rho} - \boldsymbol{\rho'})}{\partial y}) + O(\kappa^3) \\ &= \int_S dS' 2\kappa l(\rho)f_y(\boldsymbol{\rho'})\frac{\partial J_{zy}(\boldsymbol{\rho} - \boldsymbol{\rho'})}{\partial y} + O(\kappa^3) \end{aligned} \tag{3.116}$$

We now account for the singular ($\rho \to \rho'$) contribution to the integral I_{zy}.

$$I^{**}_{zy} = \int_S dS'(\frac{2\kappa l(\rho)\rho'' \sin\theta''}{(\rho''^2 + 4\kappa^2 l^2(\rho))}) \tag{3.117}$$

Substituting $\rho'' = \kappa\rho^*$, we get

$$\begin{aligned} I^{**}_{zy} &= \kappa f_y(\boldsymbol{\rho}) \int_0^\infty \rho^* d\rho^* \int_0^{2\pi} \frac{\rho^* \sin\theta'' d\theta''}{(\rho^{*2} + 4l^2(\rho))^{\frac{3}{2}}} \\ &= 0 + O(\kappa^3) \end{aligned} \tag{3.118}$$

Combining 3.116 and 3.118, we can write the contribution of f_y stress to the disturbance field in z direction as:

$$I_{zy} = \int_S dS'(2\kappa l(\rho)\frac{\partial J_{zy}(\boldsymbol{\rho} - \boldsymbol{\rho'})}{\partial y})f_y(\boldsymbol{\rho'}) + O(\kappa^3) \tag{3.119}$$

Now substituting 3.114 and 3.119 in 3.109, one can write:

$$\begin{aligned}
-I_{zz} &= \int_S dS'(-2\kappa^2 l(\rho)\frac{\partial^2 J_{zx}(\boldsymbol{\rho}-\boldsymbol{\rho'})}{\partial y}|_{y=0})(l(\rho')f_x(\rho') - l(\rho)f_x(\rho)) \\
&+ \int_S dS'(2\kappa l(\rho)\frac{\partial J_{zy}(\boldsymbol{\rho}-\boldsymbol{\rho'})}{\partial y})(f_y(\boldsymbol{\rho'}) - f_y(\boldsymbol{\rho})) + O(\kappa^3) \\
&= \int_S dS' 2\kappa l(\rho)\left[-\kappa(\frac{-3x'z'}{\rho''^5})(f_x(\boldsymbol{\rho'})l(\rho') - f_x(\boldsymbol{\rho})l(\rho)) + \frac{z'}{\rho''^3}f_y(\boldsymbol{\rho'})\right] + O(\kappa^3) \\
&= \int_S dS' 2\kappa l(\rho)\left[-\kappa(\frac{\partial}{\partial x'}\frac{z'}{\rho''^3})(f_x(\boldsymbol{\rho'})l(\rho') - f_x(\boldsymbol{\rho})l(\rho)) + \frac{z'}{\rho''^3}f_y(\boldsymbol{\rho'})\right] + O(\kappa^3)
\end{aligned} \tag{3.120}$$

Using integration by parts now:

$$\begin{aligned}
I_{zz} &= \int_S dS' 2\kappa l(\rho)\Big[-\frac{z'}{\rho''^3}(\frac{\partial}{\partial x'}\kappa f_x(\boldsymbol{\rho'})l(\rho')) \\
&+ \frac{z'}{\rho''^3}f_y(\boldsymbol{\rho'})\Big] + O(\kappa^3) \\
&= \int_S dS' 2\kappa^2 l(\rho)(\frac{z'}{\rho''})[f_y(\rho') - f_y(\rho')] \\
&+ O(\kappa^3) \\
&= O(\kappa^3)
\end{aligned} \tag{3.121}$$

Thus, leading order disturbance field in the z direction due to f_x and f_y stresses is of $O(\kappa^3)$. Now we determine the leading order stress f_z required to cancel the $O(\kappa^3)$ disturbance field due to f_x and f_y to maintain the no slip boundary condition. Dividing I_{zz} into two parts:

$$\begin{aligned}
I_{zz} &= \int_S dS'[J_{zz}(\boldsymbol{\rho}-\boldsymbol{\rho'} + \boldsymbol{e_y}\kappa(l(\rho) - l(\rho'))) - J_{zz}(\boldsymbol{\rho}-\boldsymbol{\rho'} + \boldsymbol{e_y}\kappa(l(\rho) + l(\rho')))]f_z(\boldsymbol{\rho'}) \\
&- \int_S dS'[J_{zz}(\boldsymbol{\rho}-\boldsymbol{\rho'}) - J_{zz}(\boldsymbol{\rho}-\boldsymbol{\rho'} + \boldsymbol{e_y}2\kappa l(\rho))]f_z(\boldsymbol{\rho}) \\
&+ \int_S dS'[J_{zz}(\boldsymbol{\rho}-\boldsymbol{\rho'}) - J_{zz}(\boldsymbol{\rho}-\boldsymbol{\rho'} + \boldsymbol{e_y}2\kappa l(\rho))]f_z(\boldsymbol{\rho}) \\
&= I^*_{zz} + I^{**}_{zz}
\end{aligned} \tag{3.122}$$

Here the integral I^*_{zz} captures the behavior for $\rho'' \sim O(\kappa)$ and I^{**}_{zz} takes into account the contribution of the singularity as $\boldsymbol{\rho'} \to \boldsymbol{\rho}$. In the region $\rho'' > O(\kappa)$,

using a Taylor series expansion for J_{zz}, I^*_{zz} can be written as:

$$I^*_{zz} = \int_S dS' \left[-2\kappa l(\rho) f_z(\boldsymbol{\rho'}) \frac{\partial J_{zz}(\boldsymbol{\rho} - \boldsymbol{\rho'})}{\partial y} - (-2\kappa l(\rho) f_z(\boldsymbol{\rho}) \frac{\partial J_{zz}(\boldsymbol{\rho} - \boldsymbol{\rho'})}{\partial y}) + O(\kappa^2) f_z(\boldsymbol{\rho}) \right]$$
$$= 0 - 0 + O(\kappa^2) f_z(\boldsymbol{\rho}) \tag{3.123}$$

Now we determine the contribution of the singular part of I_{zz} to the disturbance field:

$$I^{**}_{zz} = \int_S dS' \left(\frac{1}{\rho''} + \frac{\rho''^2 \sin^2\theta''}{\rho''^3} - \frac{1}{(\rho''^2 + 4l(\rho))^{\frac{1}{2}}} - \frac{\rho''^2 \sin^2\theta''}{(\rho''^2 + 4l^2(\rho))^{\frac{3}{2}}} f_z(\boldsymbol{\rho}) \right) \tag{3.124}$$

Moving the center of the coordinate system to $\boldsymbol{\rho}$ and defining a new variable $\rho^* = \frac{\rho''}{\kappa}$, I^{**}_{zz} reduces to:

$$I^{**}_{zz} = \kappa f_z(\boldsymbol{\rho}) \int_0^\infty \rho^* d\rho^* d\theta'' \left(\frac{1}{\rho^*} + \frac{\sin^2\theta''}{\rho^*} - \frac{1}{(\rho^{*2} + 4l^2(\rho))^{\frac{1}{2}}} - \frac{\rho^{*2} \sin^2\theta''}{(\rho^{*2} + 4l^2(\rho))^{\frac{3}{2}}} \right)$$
$$= f_z(\boldsymbol{\rho}) O(\kappa) \tag{3.125}$$

Combining the I_{zz} disturbance field from 3.123 and 3.125, we get

$$I_{zz} = f_z(\boldsymbol{\rho}) O(\kappa^2) + f_z(\boldsymbol{\rho}) O(\kappa) \tag{3.126}$$

We already know from 3.121 that the leading order disturbance field is $O(\kappa^3)$ in the z direction. The leading order stress f_z is then given by:

$$O(\kappa^3) = f_z(\boldsymbol{\rho}) O(\kappa^2) + f_z(\boldsymbol{\rho}) O(\kappa)$$
$$f_z(\boldsymbol{\rho}) = O(\kappa^2) \tag{3.127}$$

The leading order stress in the z direction is $O(\kappa^2)$. $f_z(\boldsymbol{\rho})$ is a stress dipole with a pair of equal and opposite forces separated by a thickness of $2\kappa l(\rho)$. The disturbance field due to this pair of stresses to the leading order can then be given by $f_z(\boldsymbol{\rho})\kappa l(\rho) \sim O(\kappa^3)$. Thus, the contribution of the f_z stress is always going to be less than $O(\kappa^2)$ in the x and y direction.

3.7.2 Elliptic integral formulations

Here, the integrals in 4.51 and 4.52 are integrated in the azimuthal direction (θ) and expressed in terms of complete elliptic integrals. In this section, first we express 4.51 and 4.52 in terms of elliptic integrals and then present the asymptotic expansions of the integral to deal with the singularity in the integrand. Rewriting 4.51 and 4.52 we get,

$$\begin{aligned}(v_x - \gamma y)8\pi &= I_{xx} + I_{xy} \\ v_y 8\pi &= I_{yx} + I_{yy}\end{aligned} \tag{3.128}$$

where the integrals on the right hand side can be defined as:

$$\begin{aligned}I_{xx} &= \int \rho' ds' f_1(\rho')[I_1 + \rho^2 \cos^2\theta I_3 + \rho'^2 I_5 - 2\rho\rho' \cos\theta I_4 \\ &\quad - I_1' - \rho^2 \cos^2\theta I_3' - \rho'^2 I_5' + 2\rho\rho' \cos\theta I_4'] \\ I_{xy} &= \int \rho' ds' f_2(\rho')[\rho \cos\theta(y - y')I_4 + \rho \cos\theta(y + y') \\ &\quad - \rho'(y - y')I_5 - \rho'(y + y')I_5'] \\ I_{yx} &= \int \rho' ds' f_1(\rho')(\rho \cos\theta(y - y')I_3 - \rho'(y - y')I_4 - \rho \cos\theta(y - y')I_3' + \rho'(y - y')I_4') \\ I_{yy} &= \int \rho' ds' f_2(\rho')(I_2 + (y - y')^2 I_3 + I_2' + (y + y')^2 I_3')\end{aligned} \tag{3.129}$$

where the integrals $I_1 - I_5$ can be defined as:

$$I_1 = S_1, \quad I_2 = \cos\theta S_2, \quad I_3 = S_3, \quad I_4 = \cos\theta S_4, \quad I_5 = \cos(2\theta)S_5 + \sin^2\theta S_3, \tag{3.130}$$

Since the above expressions are valid for all values of θ, we use $\theta = 0$ for our simulations. The terms $S_1 - S_5$ are defined as:

$$
\begin{aligned}
S_1 &= \int_0^{2\pi} \frac{d\psi}{(A_1^2 - B^2\cos\psi)^{\frac{1}{2}}} = \frac{4}{C_1}K(D_1) \\
S_2 &= \int_0^{2\pi} \frac{\cos\psi d\psi}{(A_1^2 - B^2\cos\psi)^{\frac{1}{2}}} = \frac{4}{C_1 B^2}(A_2^2 K(D_1) - C_2^2 E(D_2)) \\
S_3 &= \int_0^{2\pi} \frac{d\psi}{(A_1^2 - B^2\cos\psi)^{\frac{3}{2}}} = \frac{4}{C_1^3}\frac{E(D_1)}{1 - D_1^2} \\
S_4 &= \int_0^{2\pi} \frac{\cos\psi d\psi}{(A_1^2 - B^2\cos\psi)^{\frac{3}{2}}} = \frac{4}{C_1^3 B^2}(A_1^4 \frac{E(D_1)}{1 - D_1^2}) \\
S_5 &= \int_0^{2\pi} \frac{\cos^2\psi d\psi}{(A_1^2 - B^2\cos\psi)^{\frac{3}{2}}} \\
&= \frac{4}{C_1^3}\left(\frac{8(D_1^2 - 2)(D_1^2 - 1)K(D_1) - 2(D_1^4 - 8D_1^2 + 8)E(D_1)}{2D_1^4(D_1^2 - 1)}\right)
\end{aligned}
\tag{3.131}
$$

Here $A_1 = (\rho^2 + \rho'^2 + (y - y')^2)^{\frac{1}{2}}$, $B = (2\rho\rho')^{\frac{1}{2}}$, and $D_1 = \left(\frac{2B^2}{A_1^2 + B^2}\right)^{\frac{1}{2}}$. K and E are complete elliptic integrals given by:

$$
\begin{aligned}
K &= \int_0^{\frac{\pi}{2}} \frac{d\psi}{(1 - D_1^2\sin^2\psi)^{\frac{1}{2}}} \\
E &= \int_0^{\frac{\pi}{2}} (1 - D_1^2\sin^2\psi)^{\frac{1}{2}} d\psi
\end{aligned}
\tag{3.132}
$$

In the limit $D_1 \to 1$, all the formulas in 4.59 become singular. Physically it is equivalent to ρ' approaching ρ, i.e. calculating the disturbance field very close to a ring of forces. The singularity of the integrand is a weak *log* singularity and hence integrable. To handle this singularity numerically, the integrals are analytically simplified first. For that purpose the following asymptotic expansions of the elliptic functions are used [98]:

$$
\begin{aligned}
K(D_1) &= log\frac{4}{D_1'} + \frac{1}{2}\left(log\frac{4}{D_1'} - 1\right)D_1'^2 + \frac{9}{64}\left(log\frac{4}{D_1'} - \frac{7}{6}\right)D_1'^4 \\
E(D_1) &= 1 + \frac{1}{2}\left(log\frac{4}{D_1'} - \frac{1}{2}\right)D_1'^2 + \frac{3}{16}\left(log\frac{4}{D_1'} - \frac{13}{12}\right)D_1'^4
\end{aligned}
\tag{3.133}
$$

where $D_1' = (1 - D_1^2)^{\frac{1}{2}}$. In the simulations, for $D_1' \leq 10^{-6}$, the above analytical formulaes were used for integration instead of the numerical results.

All the integrals from $I_1' - I_5'$ are evaluated in a manner similar to the integrals $I_1 - I_5$ except A_1 is replaced by $A_2 = (\rho^2 + \rho'^2 + (y + y')^2)^{\frac{1}{2}}$ and D_1 is replaced by $D_2 = \left(\frac{B^2}{A_2^2 + B^2}\right)^{\frac{1}{2}}$. The integral $I_1' - I_5'$ are not expected to have a singularity because even when $\rho' \to \rho$ the distance between the two points is proportional to $2y$.

3.8 Acknowledgement

The authors thank Vivek Dabade for providing original Mathematica files to reproduce analytical results for spheroids in simple shear flow. We acknowledge support from the Corning Foundation in the form of a graduate fellowship for V.S. and grants from the NYSTAR J.D. Watson Investigator Program, and the National Science Foundation (CTS-0529042).

CHAPTER 4

RIGID RING SHAPED PARTICLES THAT ALIGN IN SIMPLE SHEAR FLOW

Most rigid, torque-free, low-Reynolds number, axisymmetric particles undergo a time periodic tumbling motion in a simple shear flow, with their axes of symmetry following a set of closed Jeffery orbits. We have identified a class of rigid, ring-like particles whose axes of symmetry instead reach a permanent alignment near the velocity gradient direction with the plane of the particle aligning near the flow-vorticity plane. An asymptotic analysis for small particle aspect ratio (ratio of length parallel to the axis of symmetry to diameter perpendicular to the axis) shows that an appropriate asymmetry of the ring cross-section with a thinner outer edge and thicker inner edge leads to a tendency to rotate in a direction opposite to the vorticity; this tendency can balance the usual rotation rate associated with the finite thickness of the particle. Boundary integral computations for finite particle aspect ratios are used to determine the conditions of aspect ratio and degree of asymmetry that lead to the aligning behavior and the final orientation of the axis of symmetry of the aligned particles. The aligning particle follows an equation of motion similar to the Leslie-Erickson equation for the director of a small molecule nematic liquid crystal. However, whereas the alignment of the director arises from intermolecular interactions, the ring-like particle aligns solely due to its intrinsic rotational motion in a low Reynolds number flow.

4.1 Introduction

It is well known that most rigid particles rotate continuously in simple shear flow of a Newtonian fluid in the absence of inertial effects. A natural question to ask is whether there are any exceptional particle shapes which can allow the particle to stop rotating and reach a permanent alignment. This question was first raised in Bretherton's classical paper [20] on the rotation of axisymmetric particles. Bretherton argued that a dumbbell consisting of asymmetrical beads could stop rotating but he concluded that the aspect ratio of the connecting rod required to achieve this behavior was unrealistically large so that a rigid particle of this shape could not be created in practice. Inspired by Bretherton's work, we show that moderate aspect ratio ring-shaped particles with a local cross-sectional shape that is thinner on the outer edge than on the inner edge can align in a simple shear flow. The asymmetry of the shape leads to a force per unit circumference that opposes the usual rotation of a finite aspect ratio particle with the fluid vorticity.

Understanding the motion of a single particle in flow is a fundamental problem of fluid mechanics with implications in a wide variety of fields like engineering, geophysics, and physiology [13, 42, 95, 51, 56, 29]. Stokes (1851) was the first to analyze the translational motion of a rigid sphere in an unbounded quiescent fluid at low Reynolds number. Einstein [43] later studied the behavior of a single spherical particle in simple shear flow to estimate the effective viscosity of a dilute suspension of spherical particles. The behavior of particles with non-spherical shapes in simple shear flow at low Reynolds number was first studied by Jeffery [72]. Jeffery showed that in the absence of inertial effects, a spheroidal (ellipsoid with two equal semi-diameters) particle's center

translates with the velocity of the fluid and the axis of symmetry rotates in a periodic motion with a period that depends on the aspect ratio (κ) of the particle where κ is defined as the ratio of length (L) parallel to the axis of symmetry to diameter (d) perpendicular to the axis. In this Jeffery rotational motion, the time period of particle rotation increases as the aspect ratio becomes large or small and the particle spends more time aligned with its longer axis in the flow direction. However, to date, it has been thought that there is no shape for which a rigid particle completely stops rotating in simple shear flow at finite aspect ratio.

While no previous studies have revealed a rigid particle that stops rotating in unbounded simple shear flow of a low Reynolds number Newtonian fluid, there are a number of other conditions in which particles can align in simple shear flow. Deformable particles like vesicles with fluid or solid inclusions [39, 75, 88], droplets [142], and the swimming micro-organism chlamydomonas [122] can align in simple shear flow. Particles can also align in simple shear flow due to inertial effects as shown by Subramanian and Koch [136] . A fiber has also been observed to align in a viscoelastic fluid [67]. Interactions with the wall can also stop a particle from tumbling at separations smaller than a critical value as revealed for oblate spheroidal particles by the simulations of Mody and King [106].

Rigid particles in low Reynolds number flows can also align in linear flows other than simple shear flow. In particular, a two-dimensional linear flow in which the magnitude of the extension rate exceeds the magnitude of the rotation rate by a sufficient (aspect ratio dependent) factor will cause a particle to stop rotating [53]. In a pure extensional flow, a particle aligns with its long axis along

the axis of extension. For the case of simple shear flow where the magnitudes of the extensional and rotational flows are equal no such alignment has been achieved. Linear flows are of particular interest because suspended particles are often much smaller than the scale of the fluid flow. Under these circumstances, one can Taylor expand the fluid velocity near the particle. The leading order uniform flow causes only a translational motion of a neutrally buoyant particle, while the linear flow is the first component to cause particle rotation. Simple shear flow is the linear flow of greatest interest because it represents the local linear flow for a unidirectional fluid flow. In a steady unidirectional fluid flow, the velocity gradient is independent of time along the particle's trajectory so that the particle can experience the shear long enough to reach its final oscillatory or aligning behavior. While one can observe a steady two-dimensional fluid flow (for instance, extensional flow) in the particle frame by controlling its position to remain at the stagnation point of a four-roll mill flow, the local linear flow in the particle reference frame will generally be unsteady in other non-unidirectional fluid flows.

The original work of Jeffery described the motion of spheroidal particles in terms of the aspect ratio of the particle. Bretherton [20] later showed that all axisymmetric particles follow Jeffery's equation of motion for spheroidal particles in simple shear flow as long as a tumbling parameter (λ) or an effective aspect ratio (κ_e) is used in the equation for the rotation rate. At low Reynolds number, Bretherton [72, 20] showed that the rotational motion of an axisymmetric particle in linear flow is given by:

$$\dot{\mathbf{p}} = \mathbf{p}.\Omega + \lambda(\mathbf{p}.\mathbf{E} - \mathbf{ppp} : \mathbf{E}), \tag{4.1}$$

where $\mathbf{p}$ is the orientation of the axis of symmetry of the particle, $\dot{\mathbf{p}}$ is the rate of change of the orientation, and λ is a constant which depends on the shape of

the particle. Motion of the normal director vector of a liquid crystal in a linear flow can also be described using (4.1) when the deviation from equilibrium is small as is most often the case for small molecule liquid crystals [90, 28]. In such systems, molecular interactions lead to the alignment and either $\lambda > 1$ (flow aligning liquid crystals) or $\lambda < 1$ (tumbling liquid crystals) can be achieved depending on the intermolecular potentials. For the case of liquid crystals, λ is called the tumbling parameter and $\mathbf{p}$ is the orientation of the normal director vector of the liquid crystal. In this work also we will refer to λ as the tumbling parameter where $\mathbf{p}$ will be the orientation of the particle's axis of symmetry. For a spheroid, $\lambda = \frac{\kappa^2-1}{\kappa^2+1}$ where κ is the actual aspect ratio of the particle. For the other shapes that are known to date $|\lambda| \leq 1$ and one can replace κ by an effective aspect ratio, κ_e, which will in general be different from the actual particle aspect ratio [20]. In (4.1), $\mathbf{\Omega}$ is the vorticity tensor and $\mathbf{E}$ is the strain tensor, given by:

$$\mathbf{E} = \frac{1}{2}(\nabla \mathbf{v} + \nabla \mathbf{v}^T) \tag{4.2}$$

$$\mathbf{\Omega} = \frac{1}{2}(\nabla \mathbf{v} - \nabla \mathbf{v}^T) \tag{4.3}$$

For simple shear flow, the time period of rotation, T of a particle with $-1 \leq \lambda \leq 1$ is given by:

$$T = \frac{2\pi}{\gamma(1-\lambda^2)}, \tag{4.4}$$

where γ is the shear rate. For $-1 < \lambda < 1$, the period of rotation of the particle is finite, and κ lies between 0 and ∞. In the asymptotic limit, the particle aligns with its longer axis in the flow direction for $\lambda = 1$ or $\lambda = -1$, which corresponds to an aspect ratio of $\kappa = \infty$ (infinitesimally thin rod) or $\kappa = 0$ (infinitesimally thin disk) respectively for a spheroid. Both these shapes, a line and a plane, are obviously only mathematical possibilities. It should be noted that in the micro-hydrodynamics literature where particles encountered generally have $|\lambda| < 1$, κ_e

is generally used to describe the behavior of a particle but for a value of $|\lambda| \geq 1$, κ_e corresponds to an imaginary value. Since in this work we encounter particle shapes for which $|\lambda| > 1$, we use the tumbling parameter to describe the behavior of the particles studied here.

The forces which act to rotate a typical particle such as a spheroid in simple shear flow are shown in figure 1 (a). The net torque due to the combination of these forces rotates the particle in the vorticity direction. Although the forces in the y-direction retard the rotation of the particle they always lead to a smaller torque than the forces in the x direction for spheroidal particles. Cox [34] and Singh et al. [130] have performed asymptotic analyses to calculate the rotation rates for a variety of shapes at high and low aspect ratio, respectively, in simple shear flow and found that for the classes of shapes studied, the rotational motion does not cease until the aspect ratio is ∞ or 0.

Bretherton [20] in his classic paper describing the motion of axisymmetric particles, presented one possible particle shape with $\lambda \geq 1$, such that it would stop rotating in simple shear flow. Bretherton's shape (figure 1(b)) included two almost spherical particles connected by a thin rod of length, L and diameter, d. The shape of the almost spherical particles is given by:

$$h(\beta) = g(1 + \alpha P_3(\cos\beta)). \tag{4.5}$$

Here h is the distance of the surface from the center of the deformed sphere, g is the radius of the undeformed sphere, β is the angle between the radial vector on the surface and the rod connecting the two deformed spheres, P_3 is the third Legendre polynomial, and α is a small parameter. On this assembly of particles, there are three type of torques acting: (i) A torque acting in the vorticity direction on the particle when the almost spherical particles at the end are not

Figure 1.

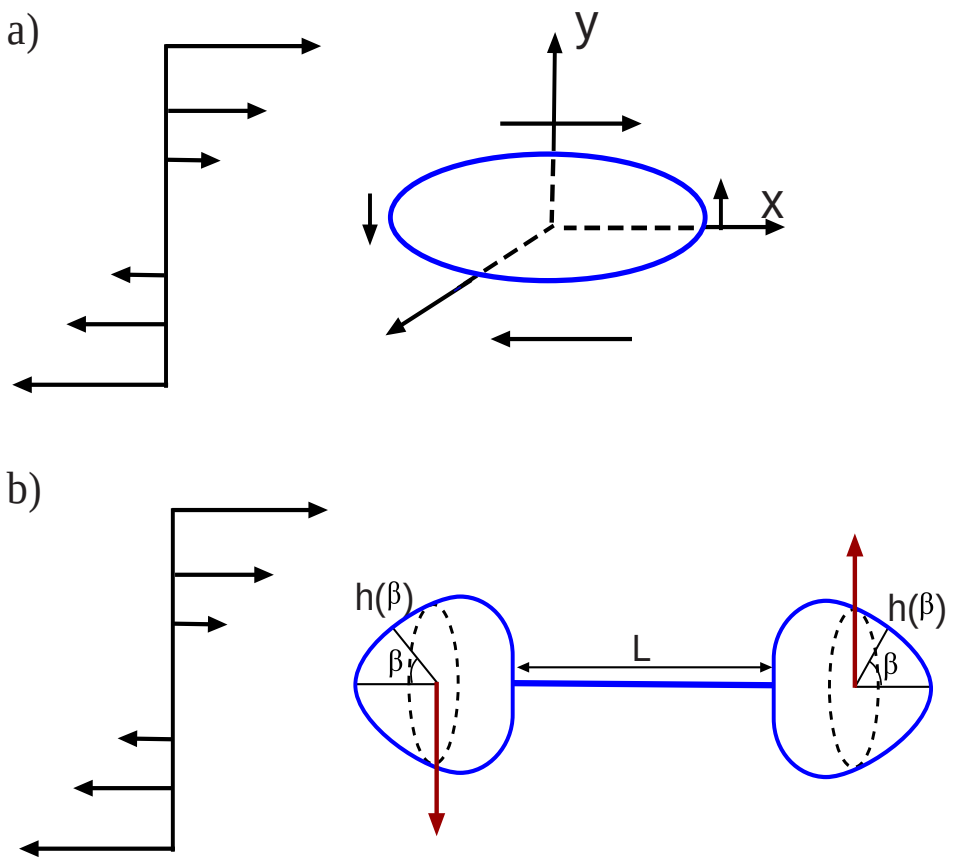

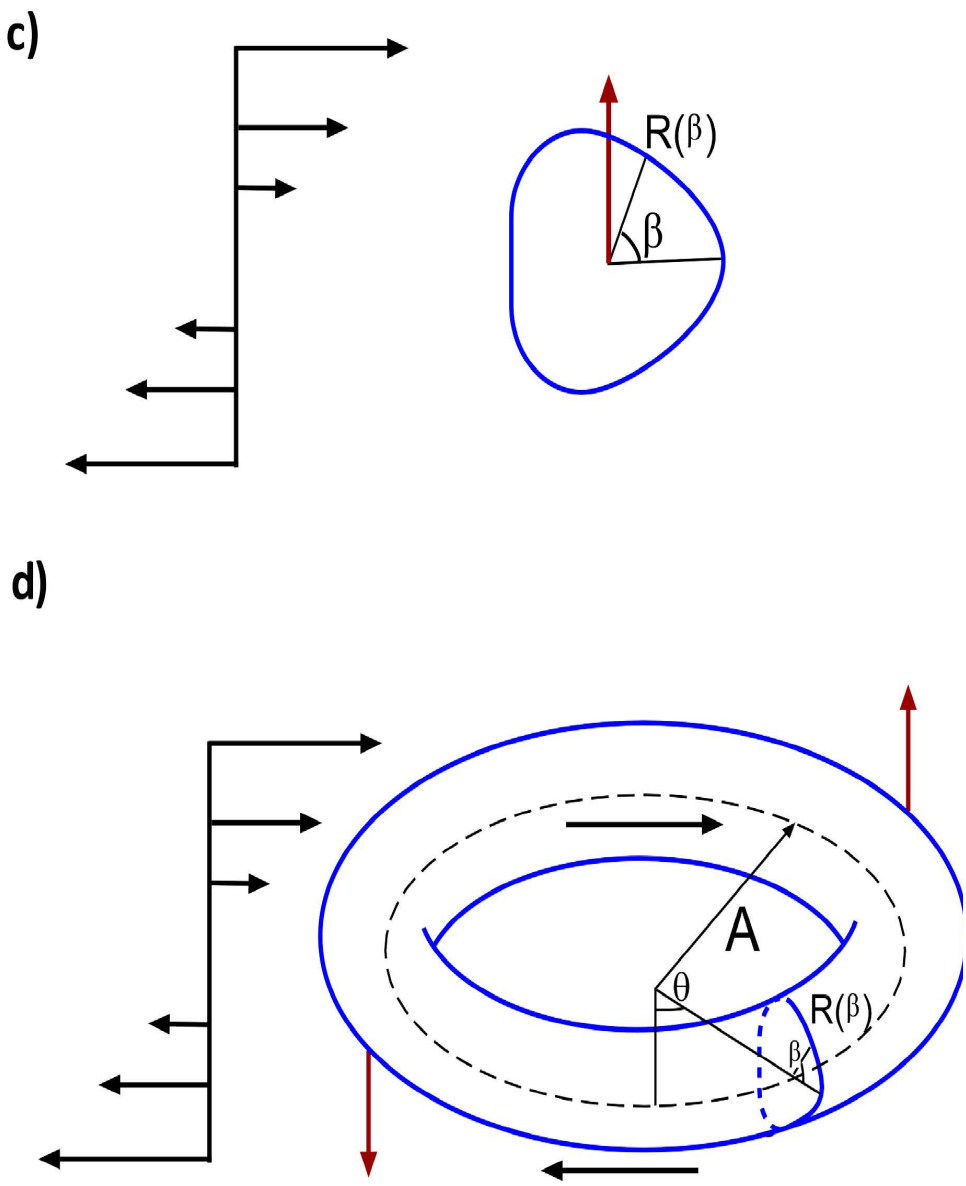

Figure 4.1: Schematic representation of forces acting on non-spherical rigid particles in simple shear flow. (a) Typical forces acting on a spheroid in simple shear flow causing it to rotate. (b) Bretherton's proposal for a particle shape that could align in simple shear flow. The axis of symmetry of the particle aligns near the flow direction. (c) Schematic of a lateral force acting on a perturbed circle. (d) Schematic of forces acting on a ring. Forces due to asymmetry in the shape generate a torque in the direction opposite to the vorticity.

allowed to rotate due to the connecting rod, (ii) another torque in the vorticity direction on the thin connecting rod, and (iii) a torque in a direction opposite to vorticity which originates from lateral forces (figure 1 (b)) acting on particles due to their lack of spherical symmetry. Here, the first two torques are the typical torques that act on particles in simple shear flow. The opposing torque acting on the fore-aft asymmetric particles is less familiar, although a number of authors [110, 16] have noted the existence of lateral forces on non-for-aft symmetric particles in other contexts. Solving Stokes equation around the almost spherical particles, Bretherton calculated that in the limit when the torque acting on the rod connecting the particles is infinitesimal (i.e. neglecting torque (ii)), a distance, $L = \frac{28g}{3\alpha}$ between the two almost spherical particles will stop the entire assembly of the particles from rotating. Bretherton estimated that the torque on the thin rod can be neglected if $\frac{1}{\ln(L/d)} << \alpha$. For a value of $\alpha = 0.1$, this would mean that the aspect ratio ($\kappa = \frac{L}{d}$) of the rod should be much greater than e^{10}. Since the resistance of an elastic beam to bending decreases rapidly with increasing aspect ratio, from a practical stand point a rigid particle with such an aspect ratio would not be possible. [48] suggested that in order for a fiber to avoid bending due to viscous stresses in shear flow, its elastic modulus should be larger than $2\mu\gamma\kappa^4/(ln(2\kappa) - 1.75)$, and this, for a fluid of viscosity, $\mu = 1$ cp, shear rate, $\gamma = 1$ s^{-1}, and $\kappa = e^{10}$ turns out to be $5.3X10^4$ GPa which is about 50 times larger than the elastic modulus of diamond. Bretherton referred to these shapes as extreme and concluded by saying that "in the private guess of the author the thickness of the thin rod must be too small to be consistent with rigidity".

Since Bretherton's work, we know of no report of a particle shape that aligns in simple shear flow, although the problem has been mentioned in some clas-

sical texts [81, 91] . The particular challenge in determining the shape of the particle for which $|\lambda| \geq 1$ is that there is no explicit relation between the shape of a particle and λ, even though λ depends only on the particle shape and is independent of the flow. For a general particle shape, an appropriate Stokes flow problem needs to be solved to relate the angular velocity of the particle with the strain rate (4.1) to determine the unknown parameter λ [6, 34] . We note one attempt by Willis [148] to develop a model in which the rotational motion of the particle can be described explicitly based on the shape of the body without solving the full fluid mechanics problem. Willis' model is based on the *ad hoc* assumption that the torque on a particle is proportional to the integral over the particle volume of the cross product of the position relative to the particle center and the relative velocity between the particle and the undisturbed fluid velocity. In Willis' model, the three principal moments of inertia (without the density factors) of the body could be used to calculate the value of λ. Despite the non-rigorous assumptions in Willis' model, it was very successful in describing the rotation rate of a variety of shapes. This model predicted that there cannot be any axisymmetric particle shape for which $|\lambda| \geq 1$, so the model would be qualitatively inaccurate for particles that can align in simple shear flow.

In this work, we present finite-aspect-ratio ring shaped rigid particles (figure 1(d)) which can stop tumbling in simple shear flow at low Reynolds number. The non-tumbling ring shapes can be obtained by revolving a two dimensional shape lacking fore-aft symmetry (figure 1 (c)) about an axis as shown in figure 1 (d). The asymmetric shape of the cross-section is a circular shape perturbed with a third Fourier mode analogous to Bretherton's nearly spherical shape. Unlike Bretherton's non-tumbling particle shape where the torque acting on the connecting rod in the vorticity direction was large enough to rotate the parti-

cle, the ring shapes introduced here do not require a connecting rod and hence there is no additional torque in the vorticity direction due to it. Instead the ring shape provides the necessary connectivity and the asymmetric shape creates a lateral force per unit circumference at all angular positions opposing rotation with vorticity. In the next section, we discuss the motion that a particle with $|\lambda| \geq 1$ follows before aligning as well as determining the final orientation as a function of λ. In section 3, we present an asymptotic analysis for the rotation of a thin ring-shaped particle with an asymmetric cross-section. We show how certain types of asymmetry in cross-sectional shape can give rise to rotational motion in a direction opposite to the direction of vorticity. We discuss some of the basic characteristics of the shape that can lead to the non-tumbling behavior of the particle. We show that lack of fore-aft symmetry in the local cross-section of the ring is a necessary but not sufficient condition for the alignment of the ring shaped particles. In section 4, we describe the boundary element method and the details of the method pertinent to the present problem. We then present boundary element simulation predictions at finite aspect ratio. We determine the largest aspect ratio at which the asymmetric ring can remain aligned for different degrees of asymmetry. We also estimate the angle with respect to the flow at which the particle will align as a function of its shape. Finally, we discuss some of the implications of alignment on the properties of suspensions of these particles.

4.2 Motion of a particle with $|\lambda| \geq 1$

Bretherton [20] described the motion that a particle with $|\lambda| \geq 1$ would undergo before it stops rotating; we reproduce his results in this section using a slightly

different notation that is closer to that of Jeffery. Unlike Jeffery's rotating particles ($|\lambda| \leq 1$), which rotate in a periodic motion in one of an infinite set of orbits, particles with $|\lambda| \geq 1$ align in one of the two stable equilibrium directions (figure 2). The equations for the rotational motion can be obtained by solving (4.1) and are given by:

$$\tan\phi = \begin{cases} p' \tanh\xi & \text{for } C_1 < 0 \\ \frac{p'}{\tanh\xi} & \text{for } C_1 > 0 \end{cases} \tag{4.6}$$

$$\tan\theta = \begin{cases} C((p'^2+1)\cosh 2\xi - p'^2 + 1)^{\frac{1}{2}} & \text{for } C_1 < 0 \\ C((p'^2+1)\cosh 2\xi + p'^2 - 1)^{\frac{1}{2}} & \text{for } C_1 > 0 \end{cases} \tag{4.7}$$

where $p' = (\frac{\lambda+1}{\lambda-1})^{\frac{1}{2}}$ $(= -i\kappa_e)$, $\xi = \frac{p't}{p'^2-1} - \frac{1}{2}\ln|C_1|$, ϕ_0 and θ_0 are the orientation angles of the particle at $t = 0$, $C_1 = \frac{\tan\phi_0 - p'}{\tan\phi_0 + p'}$ is a constant that depends on the initial orientation (ϕ_0), and C is the orbit constant of the particle trajectory which is also determined by the initial orientation of the particle (ϕ_0, θ_0). Here we have followed Jeffery's convention and adopted a spherical coordinate system with θ as the angle of the particle orientation relative to the vorticity (z-axis) direction and ϕ as the angle of the projection of the particle orientation into the flow-gradient plane relative to the gradient (y-axis) direction. The orbit constant, C is analogous to the orbit constant used to describe Jeffery's rotational motion. The other constant of integration, C_1 depends only on the projection of the initial orientation into the flow-gradient plane.

As $\gamma t \to \infty$, irrespective of the initial orientation (except for the four unstable equilibrium points), the orientation of the particle approaches one of the two

Figure 2.

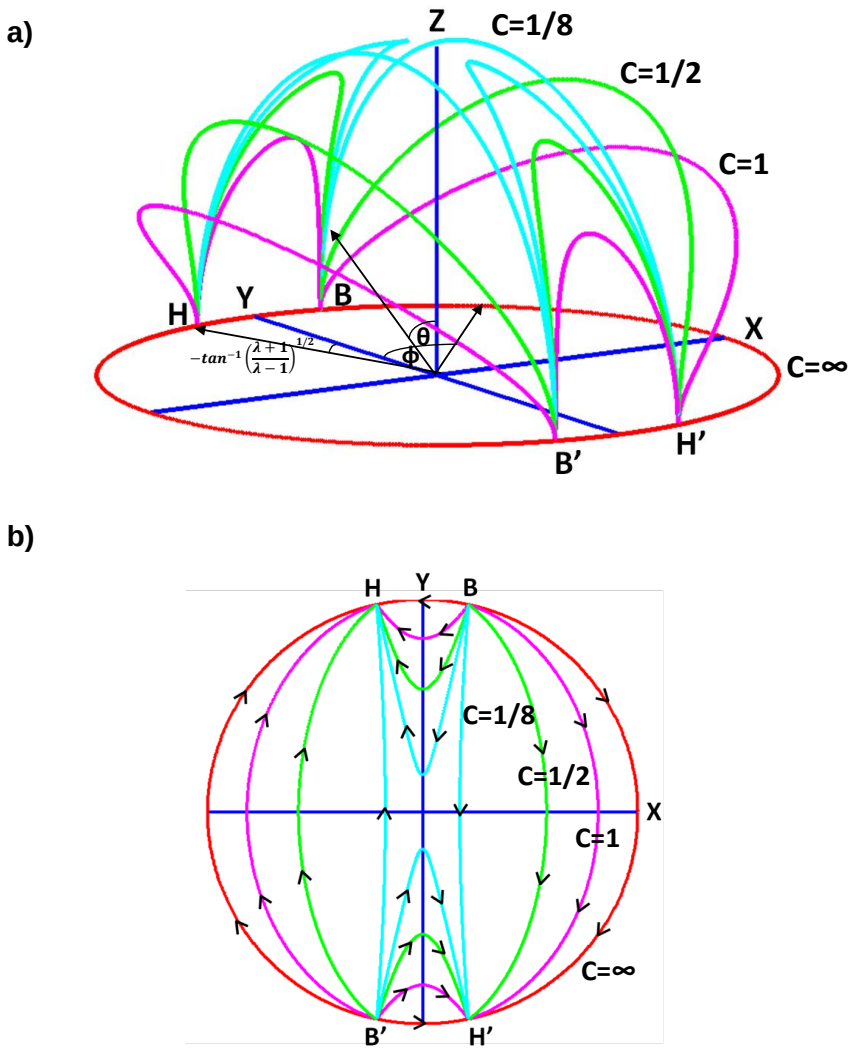

Figure 4.2: Motion of particles that align in simple shear flow. (a) Trajectories of a particle with different initial conditions in simple shear flow for $\lambda = -1.1$. b) Projections of the same trajectories in the $x - y$ plane. The trajectories represented here are for $C = \infty$ (red), $C = 1$ (magenta). $C = \frac{1}{2}$ (green), and $C = \frac{1}{8}$ (cyan). Here, H and H′ correspond to stable equilibrium positions and B and B′ to unstable equilibrium positions.

stable orientations, given by $\theta = \pi/2$ and

$$\tan\phi = \begin{cases} p' & \text{for } \lambda \geq 1 \\ -p' & \text{for } \lambda \leq -1 \end{cases}$$

For $\lambda = 1$, $p' = \infty$ and for $\lambda = -1$, $p' = 0$ so that in both these cases the long axis of the particle is aligned in the flow direction. As the magnitude of λ increases, the inclination of the long axis of the particle to the flow-vorticity plane approaches a limiting value of $\frac{\pi}{4}$ which is the principle direction of the extensional component of the flow. This maximum inclination of the long axis to the flow direction is achieved when $\lambda \to \pm\infty$. When $|\lambda + 1| \ll 1$, the angle of the stable orientation of the particle to the shear gradient direction is given by $-\left(\frac{1+\lambda}{-2}\right)^{\frac{1}{2}}$. Figure 2 (a) shows trajectories of the particle's axis of symmetry for different values of the orbit constant for $\lambda = -1.1$. Figure 2 (b) shows projections of the trajectories of the particle in the flow gradient plane. Points H and H′ are the points of stable equilibrium where the typical torque due to the shear flow cancels the torque due to the asymmetric shape. Apart from the two stable orientations in the flow-gradient plane there are also two unstable orientations in this plane given by points B and B′ in figure 2. A small perturbation from these two unstable equilibrium positions will move the particle towards one of the two stable equilibrium positions. There are two additional unstable equilibrium positions in which the particle can stay aligned, along the $\pm z$ (vorticity) direction. In these orientations, in the absence of any perturbations, the particle could continue rotating about its axis without ever aligning. Again, a small perturbation out of the vorticity direction would cause the particle to drift towards the stable orientations H or H′. In the case considered here where the particle has a mirror symmetry about the plane perpendicular to the axis of symmetry (example- in figure 1(d)), the two stable equilibria H and H′ are indistinguishable. Simi-

larly, there are two indistinguishable pairs of unstable equilibria (B and B′ and $\pm z$). We note here that the aligning behavior of the particle is consistent with Stokes flow reversibility. To see that this is true, we simply reverse the sign of the undisturbed simple shear flow at infinity. If the particle is initially aligned in the stable (H or H′) or unstable (B or B′) equilibrium directions, in the reverse flow also it will stay aligned except now it will be in the unstable (B or B′) or stable (H or H′) equilibrium directions. If the particle is initially flipping, in the reverse flow its angular velocity will simply reverse its sign while the particle will stay in the same orbit. Typically, a particle will approach a stable orientation during the forward shear flow. When the flow is reversed, this fixed point becomes unstable and the particle will undergo a flip to align with the newly stable fixed point which was the unstable fixed point of the forward shear flow.

In general, when a particle undergoes rotational motion in simple shear flow, the minimum angular velocity acting on the particle is observed when the long axis of the particle is aligned in the flow direction. In this case, the long axis of the particle is along the axis of symmetry for $\lambda > 0$ and perpendicular to the axis of symmetry for $\lambda < 0$. At the point of transition from tumbling to the non-tumbling state ($|\lambda| = 1$), the angular velocity of the particle is 0 with the long axis in the flow direction. A very simple test of the ability of a particle shape to avoid tumbling is thus that the angular velocity of the particle when oriented with its long axis along the flow direction is either 0 or in the direction opposite to the vorticity. Based on this simple idea, in the next section we use asymptotic analysis to introduce a particle shape which can stop rotating in simple shear flow. We establish that the particle stops tumbling by showing that the angular velocity of the particle with its long axis aligned in the flow direction becomes 0 which corresponds to $\lambda = -1$ for the shape considered here.

4.3 Asymptotic analysis for a thin ring with a slightly asymmetric cross-section

Like any incompressible linear flow, simple shear flow can be decomposed into an extensional flow and a rotational flow. In simple shear flow, the tendency of a particle to undergo rotational motion in the vorticity direction can be attributed to the rotational component of the shear flow. The rotational component of the flow tends to rotate the particle in the vorticity direction while the extensional component tends to align the long axis of the particle along the extensional axis. A rigid particle rotates with the rotational velocity of the fluid since the rotational component of the flow does not try to deform the particle. On the other hand, the response of a particle to the extensional flow component depends on its shape; for an axisymmetric particle the response can be completely described using λ, the tumbling parameter. In simple shear flow the strengths of the rotational and extensional components of the flow are equal and the response of the particle to the flow is dominated by the rotational component for $|\lambda| < 1$ and by the extensional component for $|\lambda| > 1$. As a result, the particle continues to rotate for $|\lambda| < 1$ and aligns for $|\lambda| \geq 1$.

In a linear flow at low Reynolds number in the absence of external forces, the center of a particle with fore-aft symmetry translates with the fluid velocity. However, a particle without fore-aft symmetry can undergo a cross-stream migration due to the extensional component of the flow in the direction of shear. This phenomena has been discussed in a number of studies [20, 16, 110] for three dimensional asymmetric particles of different shapes. Since the velocity of the particle must be a linear function of the rate of strain tensor and can also depend

on the orientation vector, it must take the form

$$\mathbf{U} = \eta_1 \mathbf{E} \cdot \mathbf{p} + \eta_2 \mathbf{pp} \cdot \mathbf{E} \cdot \mathbf{p} \tag{4.8}$$

where η_1 and η_2 are constants that depend on the particle shape. For a particle with fore-aft symmetry, the velocity of the particle when it is oriented in $\mathbf{p}$ and $-\mathbf{p}$ should be same, i.e $\mathbf{U}(\mathbf{p}) = \mathbf{U}(-\mathbf{p})$. Hence, the coefficients $\eta_1 = \eta_2 = 0$ for such a particle and the particle translates with the fluid velocity . For a particle without fore-aft symmetry η_1 and η_2 can be non-zero. We will consider a particle with $\mathbf{p} = \mathbf{e}_x$ in a simple shear flow with $E_{xy} = E_{yx}$ as the only non-zero components of rate of strain tensor. Here $\mathbf{e}_x$ is the unit vector in the x-direction. In this case $U_x = 0$ and $U_y = \eta_1 E_{xy}$ and we will obtain a cross-stream drift velocity in the y-direction.

In this work, we show that a two dimensional particle without fore-aft can also undergo such a cross-stream migration in simple shear flow (figure 1 (c)). To the best of our knowledge, cross-stream migration of two dimensional particles has not been discussed in the literature. Using such asymmetric shapes, we postulate that a three dimensional axisymmetric shape (figure 1(d)) formed by revolving the two dimensional cross-section (figure 1(c)) can align in simple shear flow. Using asymptotic analysis, we calculate the angular velocity generated by the local cross-sectional shape of the ring in terms of the degree of asymmetry (α) and aspect ratio of the particle. The condition of alignment is then obtained by balancing the angular velocity due to asymmetry with the angular velocity of the particle in the vorticity direction due to finite aspect ratio.

The cross-stream motion of the two-dimensional particle can be obtained through one of two approaches. First, one may directly pose the mobility problem of determining the relative velocity of the particle and fluid when the par-

ticle is force-free. Second, taking a resistivity approach, one may first compute the force acting on a particle held stationary in a simple shear flow and then compute the velocity of a particle relative to the fluid driven by this force. In addition to being more direct, the first, force-free approach has the advantage of avoiding Stokes paradox, which states a Stokes fluid velocity cannot be determined in an unbounded two-dimensional flow with a net force acting on a particle. For this reason we adopt the first approach in our quantitative treatment of the cross-stream velocity of the two-dimensional particle and the resulting rotational velocity of the three-dimensional ring-shaped particle in section 3.2. However, the resistitivity formulation has the advantage that one can more easily visualize the stresses driving the particle motion and for this reason we use this approach in section 3.1 to provide a physical understanding of the cross-stream driving forces.

4.3.1 Physical origin of the cross-stream force on an asymmetric two dimensional particle

In this subsection we adopt a resistivity formulation and consider the forces per unit area acting on an axisymmetric ring-shaped particle that is held fixed in the xz-plane and on a two-dimensional particle that constitutes the local cross-section of this ring-shaped particle. We will be particularly interested in the net torque that would tend to drive the axisymmetric particles to rotate with or against the vorticity and the net force per unit area on the local cross-section that contributes to this torque.

The forces acting on a typical particle such as a spheroid held stationary in

simple shear flow are shown in figure 1(a). The surface forces per unit area f_x in the x-direction create a fluid velocity disturbance that cancels the externally imposed simple shear flow at the particle surface. These x-forces also create a disturbance velocity in the y direction which gives rise to a surface force in the y direction on the surface of the particle to satisfy the no slip boundary condition. The net torque due to the combination of these forces rotates the particle in the direction of vorticity. For a particle with fore-aft symmetry the net force acting is 0. But a particle without fore-aft symmetry in simple shear flow can have a cross-stream force acting on it due to the extensional component of the flow. We present one such shape (figure 1(c)) which, when force free, can undergo drift in a direction perpendicular to the direction of flow.

Let us consider a ring (figure 1 (d)) of perturbed circular cross-section. If the radius of the unperturbed circular cross-section is c and the radius of the perturbed cross-section is scaled with c, the shape of the perturbed cross-section is given by:

$$R(\beta) = 1 + \alpha \cos(3\beta), \tag{4.9}$$

where R is the radius of the perturbed cross section as a function of β, α is again the asymmetry parameter, and β is the angular coordinate in the local polar coordinate system measured relative to the line connecting the center of the ring to the center of the cross-section. Note here that the coordinate β is differently defined from the β used by Bretherton in the local spherical coordinate system of his aligning particle shape. Let the radius of the ring non-dimensionalized with c be A, measured from the center of the global coordinate system whose origin is at the center of the ring to the center of the cross section as shown in figure 1 (d). We define the aspect ratio of the ring as the ratio of the radius of the circular cross-section to the radius of the ring, i.e. $\kappa = \frac{1}{A}$.

For $A \gg 1$, one can locally approximate the ring as a straight infinite cylinder. Thus, a small part of the ring of thickness ($Ad\theta$) can be modeled as an infinitely long cylinder held at an angle θ to the simple shear flow (figure 3 (a)), where θ is the azimuthal angle measured from the vorticity direction in the flow-vorticity plane. Using linear superposition of Stokes flow solutions, the flow over an infinitely long cylinder inclined at an angle (θ) can be divided into two parts: (i) Flow parallel to a long cylinder (figure 3(b)) with a $\cos\theta$ component of the shear flow acting over it and (ii) flow perpendicular to a long cylinder with a $\sin\theta$ component of the flow acting (figure 3 (c)).

The problem is now reduced to the solution of the force acting on an infinite cylinder aligned with its axis in the flow direction as shown in figure 3 (b) and an infinite cylinder aligned with its axis in the vorticity direction as shown in figure 3 (c). The undisturbed flow fields for the two problems in the new coordinate systems are now given by:

$$v_{x^*} = 0, \quad v_y = 0, \quad v_{z^*} = -y\cos\theta \tag{4.10}$$

$$v_{x^*} = y\sin\theta, \quad v_y = 0, \quad v_{z^*} = 0; \tag{4.11}$$

where all the length scales are non-dimensionalized using the radius (c) of the undeformed ring cross-section, and the velocity gradients are non-dimensionalized using the shear rate, γ of the simple shear flow. In the following discussion stresses are non-dimensionalized with $\mu\gamma$. The above flows are simple shear flows with $\cos\theta$ and $\sin\theta$ as the new non-dimensionalized shear rates. z^* is the local coordinate along the axis of the ring and r is the local radial coordinate.

For case (i), in which the cylinder is aligned in the direction of flow, one can neglect the end effects of the cylinder on the disturbance field in the limit when

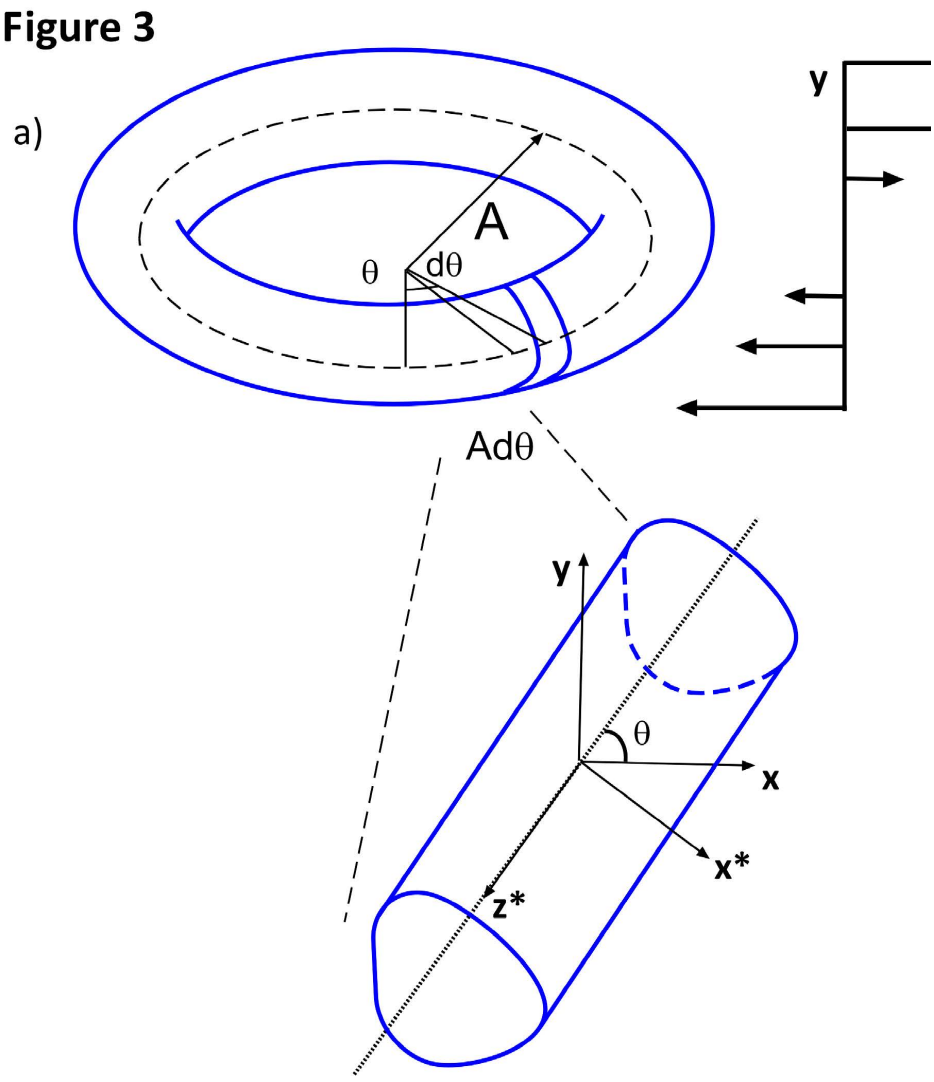

Figure 4.3: In the limit when $A \gg 1$, a small cross section of a ring (a) inclined at an angle θ to the flow gradient plane can be divided into two parts: An infinitely long cylinder aligned parallel (b) to the flow direction and an infinitely long cylinder perpendicular (c) to the flow gradient plane.

the cylinder is infinitely long. This assumption implies that the flow is everywhere parallel to the axis of the cylinder i.e., $v_{x^*}, v_y = 0$ with $v_{z^*}(r,\beta)$ the only non-zero component of the velocity. With flow parallel to the axis one can say that the pressure, $p = 0$ since only variation in x^* and y are allowed and the velocity is perpendicular to these directions. The momentum balance equation then reduces to $\nabla^2 v_{z^*} = 0$. The flow applies a shear stress along the axis of particle but no forces in the $x^* - y$ plane. There is no net force per unit length in the z^* direction but rather a torque per unit length acting in the vorticity direction due to a force dipole as illustrated in figure 3 (b).

In case (ii) (figure 3 (c)), the imposed velocity in the x^*-direction induces stresses and a pressure variation in the x^*y plane and a net force per unit length in the y-direction. If we further decompose the shear in the x^*y-plane into an extensional and rotational component, we may note that the rotational fluid flow cannot induce a force. For a general three-dimensional particle, a fluid rotation far from the particle characterized by the vorticity $\boldsymbol{\omega}$ can induce a force

$$\mathbf{F} = \mathbf{H}.\boldsymbol{\omega} \tag{4.12}$$

where the resistance tensor $\mathbf{H}$ must be a pseudo-tensor. Since $\mathbf{H}$ depends only on the shape of the particle, this implies that the particle shape must be chiral. However, one cannot have a chiral two-dimensional particle so we conclude that the force due to fluid rotation in zero.

Thus, we will consider the fluid velocity and the force per unit length on the particle cross-section due to the extensional component of the shear flow. A complete treatment of this problem would require a slender body theory with a quasi-two-dimensional inner solution matched to an outer solution in which the particle is treated as a ring of forces. The matching condition on the inner

solution can be written in terms of the force per unit length F that the particle exerts on the fluid and a velocity of the fluid V relative to the ring produced by the deviation of the velocity disturbance of the ring of forces from that of an infinite line of forces as

$$\begin{aligned} v_r &= \sin\theta\left[r\sin\beta\cos\beta + V\sin\beta + \frac{F}{2\pi}(\sin\beta - \sin\beta\ln r)\right], \\ v_\beta &= \sin\theta\left[\frac{r}{2}(\cos^2\beta - \sin^2\beta) + V\cos\beta - \frac{F\cos\beta}{2\pi}\ln r\right] \quad \text{as} \quad r \to \infty \end{aligned} \tag{4.13}$$

The no slip boundary condition on the inner solution at the cylinder surface is

$$v_r = 0, \quad v_\beta = 0 \quad \text{at} \quad r = R \tag{4.14}$$

The inner solution is obtained by applying these boundary conditions to the general two-dimensional solution to Stokes equation written in terms of the stream function in a manner similar to that outlined for the mobility problem in section 3.2. In a full slender-body treatment, the relationship between V and F which depends on the particle aspect ratio would be obtained by matching the inner solution to an outer solution. However, for illustrative purposes we will examine the qualitative variation of the force on the particle surface for the inner solution in the case $V = 0$. In section 3.2, we will see that the quantitative cross-stream migration rate can be obtained from the inner solution in a mobility formulation without the need to match to an outer solution.

Before considering the forces acting on an infinitely long cylinder with the asymmetric cross-section given by (4.9), let us first consider a cylinder with circular cross-section. The forces on the surface of the cylinder in pure extensional flow are shown in figure 4 (a). Due to the symmetry of the shape, the forces on the circle in opposite quadrants cancel each other. When the cross-sectional

shape is not fore-aft symmetric, the forces on the particle in opposite quadrants no longer cancel each other. Figure 4 (b) shows the forces acting on the rod when the shape of the cross-section is given by (4.9). The net force in the x^*-direction is still zero but there is a net force in the $y-$direction. This effect can be seen more clearly in figure 4 (c) which represents the difference between the y-components of the forces on the asymmetric and the circular cross-sections.

Now let us consider the physical mechanisms leading to a net positive y-component of the force on the asymmetric particle. In figure 4 (c), we have highlighted 3 regions of the first quadrant of the particle where the asymmetry increases the force per unit area in the y-direction, f_y. We will explain the origin of the extra force in these regions; the mechanisms leading to extra f_y in the other quadrants are similar. We can write f_y in terms of the components of the stress tensor as:

$$f_y = \sigma_{yy} n_y + \sigma_{yx^*} n_{x^*}, \tag{4.15}$$

The primary contribution to the yy-stress, σ_{yy}, comes from the pressure, while the primary contribution to σ_{yx^*} is from the viscous stress. n_{x^*} and n_y are the components of the normal vector to the surface in the x^* and y directions. In region 1, the asymmetric particle extends radially outward further into the flow than the circle increasing the velocity gradient and the viscous stress contribution to σ_{yx^*}. The lift force in region 2 arises primarily from the first term in (4.15). However, we found that the pressure and σ_{yy} do not change substantially. Instead it is the variation of the y-component of the unit normal with particle shape, given to $O(\alpha)$ by

$$n_y = \cos(\beta) + 3\alpha \cos\beta \sin 3\beta, \tag{4.16}$$

that accounts for the increased pressure-induced y-force. Similarly, in region 3, an increase in n_{x^*}, leads to a larger viscous stress contribution to the y-force. This

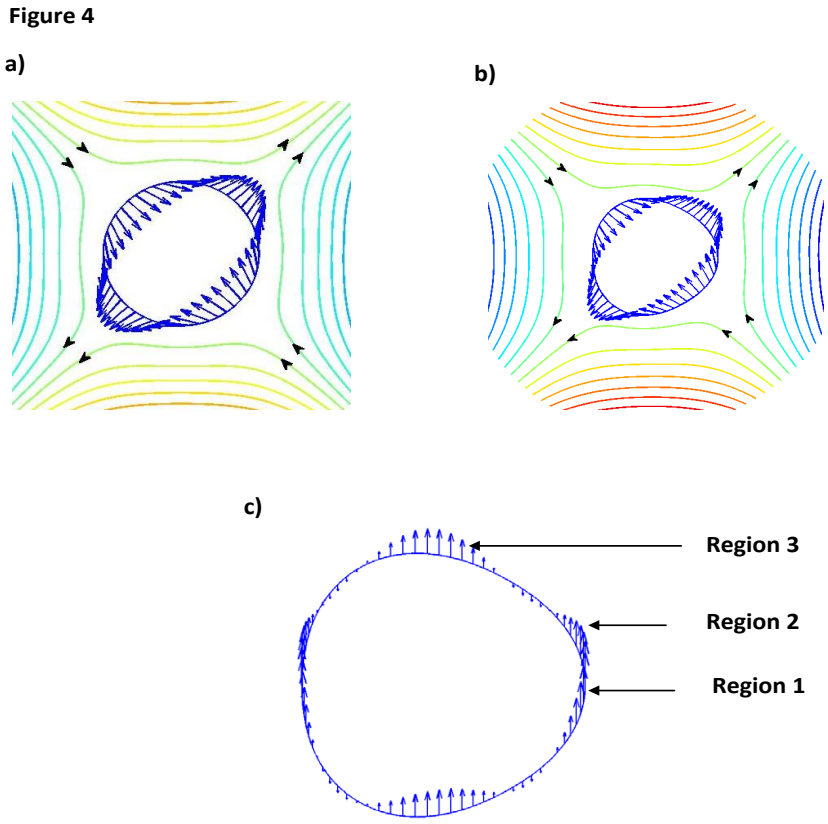

Figure 4.4: Comparison of forces on circular and non-circular cross-sections in extensional flow. (a) Forces acting on a long cylinder with circular cross-section in extensional flow. The surface of the cross-section and the forces are in blue color; the other colored lines indicate streamlines. (b) Forces acting on a long cylinder with non-circular cross-section $(1 + 0.1\cos 3\beta)$ in extensional flow. The surface of the cross-section and the forces are in blue; the other colored lines indicate streamlines. (c) Difference of forces in the lateral direction between a circular and a non-circular cross-section cylinder. The three regions in a quadrant where net lateral forces are acting.

can be seen by noting that n_{x^*} is given by

$$n_{x^*} = \cos(\beta) - 3\alpha \sin\beta \sin 3\beta \tag{4.17}$$

and region 3 corresponds to $\beta > \frac{\pi}{3}$ and $\sin 3\beta < 0$ as well as being a region with a high shear stress.

4.3.2 Derivation of the cross-stream velocity

In this subsection, we will perform a detailed asymptotic analysis to determine the drift velocity of an asymmetric two-dimensional particle and the resulting rotation rate of a ring with an asymmetric cross-section. Particles are known to migrate across streamlines in unidirectional flows due to asymmetry [110, 16], deformability [113, 57], inertia [65, 145], and non-Newtonian behavior of the fluid [66]. The migration of the particle due to inertia, deformability and the non-Newtonian behavior of the fluid require a combination of linear and quadratic flow or particle-wall hydrodynamic interactions in a bounded simple shear flow. However, an asymmetric particle can migrate in an unbounded simple shear flow. This migration is dependent on the orientation of the particle relative to the shear flow. Nir and Acrivos [110] considered a freely suspended asymmetric particle and found that it underwent a time periodic cross-stream migration with no net migration averaged over the particle's period of rotation. Brenner [16] considered a resistivity problem for an asymmetric particle and showed that either rotation of the particle or an imposed extensional flow can cause a cross-stream force. In our case, the two dimensional particle is the cross-section of a ring and the connectedness of the ring can prevent its rotation. To determine the rotation rate in a mobility formulation for the entire ring when

the ring is aligned in the xz-plane, we will be interested in the cross-stream y velocity on a two-dimensional particle aligned in the x^*-direction. If the stresses created by the component of shear flow perpendicular to the local axis of the ring (4.11) lead to a particle rotation rate (torque) that exceeds that created by the component of the shear flow parallel to the local axis (4.10), the particle will tend to rotate against the vorticity when it is in the xz-plane and will achieve a fixed orientation upstream of the xz-plane.

Here, we first calculate the drift velocity of a particle lacking fore-aft symmetry across streamlines in two-dimensional flow. We find that the drift velocity of the two-dimensional fore-aft asymmetric cross-section is distributed over the ring such that it creates a rigid body rotation in a direction opposite to the vorticity direction. This rigid body rotation, in the asymptotic limits of $A >> 1$ and $\alpha << 1$, allows us to simply superimpose the angular velocity due to the fore-aft symmetry on the Jeffery type angular velocity of the ring in simple shear. In the next subsection, we use the balance between the two angular velocities to obtain the condition for alignment of the particle.

The shape of the cross-section is represented using Fourier modes with the coefficient of the mode (α) being small. We derive the leading order drift velocity of the cross-section by expanding in a regular perturbation expansion in α. To keep the discussion general, let the shape of the cross-section be given by:

$$R(\beta) = 1 + \alpha \cos((2m+1)\beta) \qquad \text{for } m \geq 1, \tag{4.18}$$

where α is a small parameter. Only odd Fourier modes are considered here as even modes are fore-aft symmetric and cannot lead to a cross-stream drift. We solve for the drift velocity of a force-free non-rotating particle in the undisturbed flow field given by (4.11).

Let the unknown drift velocity of the particle be v_1 in $+y$ direction. We use the stream function approach to solve the Stokes flow problem in two dimensions. The general solution for the stream function [96] is used along with the boundary conditions that, far from the particle, the fluid velocity is given by simple shear and, on the surface of the particle, the fluid velocity is equal to v_1 in $+y$ direction. Writing the undisturbed velocity field at $r \to \infty$ in polar coordinates:

$$v_r = r \sin\theta \sin\beta \cos\beta, \quad v_\beta = -r \sin\theta \sin^2\beta \tag{4.19}$$

In polar coordinates, the velocity field is related to the stream function as:

$$v_r = \frac{1}{r}\frac{d\psi}{d\beta}, \quad v_\beta = -\frac{d\psi}{dr} \tag{4.20}$$

so the boundary condition (4.20) expressed in terms of the stream function is:

$$\psi|_{r\to\infty} = \sin\theta \frac{r^2(1-\cos(2\beta))}{4} + c_1 \tag{4.21}$$

Using the general solution [96] for the stream function in polar coordinates, the stream function may be expressed as:

$$\begin{aligned}\psi = \sin\theta \frac{r^2(1-\cos(2\beta))}{4} + c_1 + c_2 \ln(r) + d_1 \frac{\cos(\beta)}{r} + d_2 \frac{\cos(2\beta)}{r^2} + \hat{d}_2 \frac{\cos(2\beta)}{r^0} \\ + d_3 \frac{\cos(3\beta)}{r^3} + \hat{d}_3 \frac{\cos(3\beta)}{r^1} + d_4 \frac{\cos(4\beta)}{r^4} + \hat{d}_4 \frac{\cos(4\beta)}{r^2} \\ + d_5 \frac{\cos(5\beta)}{r^5} + \hat{d}_5 \frac{\cos(5\beta)}{r^3} + \ldots d_n \frac{\cos(n\beta)}{r^n} + \hat{d}_n \frac{\cos(n\beta)}{r^{n-2}} + \ldots .\end{aligned} \tag{4.22}$$

Here we have included only those terms in the stream function corresponding to the imposed simple shear flow (4.21) and a velocity disturbance due to the particle that is required to decay as $r \to \infty$. In addition we have omitted terms that involve sine functions owing to the symmetry of the particle and flow about the x^*z^* plane.

To find the unknown constants in (4.22), the no-slip boundary condition at the surface of the particle is used:

$$\begin{aligned} v_r &= v_1 \sin(\beta) = \frac{1}{r}\frac{d\psi}{d\beta}, \\ v_\beta &= v_1 \cos(\beta) = -\frac{d\psi}{dr} \quad \text{at } r = 1 + \alpha\cos((2m+1)\beta). \end{aligned} \tag{4.23}$$

Using (4.22), these conditions can be written as:

$$\begin{aligned} v_1 \sin(\beta)|_{r=R} =& \frac{\sin\theta}{2} R\sin(2\beta) + 0 + -\frac{d_1\sin(\beta)}{R^2} - \frac{2d_2\sin(2\beta)}{R^3} \\ & - \frac{2\hat{d}_2\sin(2\beta)}{R} + \ldots - \frac{nd_n\sin(n\beta)}{R^{n+1}} - \frac{n\hat{d}_n\sin(n\beta)}{R^{n-1}} + \ldots \end{aligned} \tag{4.24}$$

$$\begin{aligned} v_1 \cos(\beta)|_{r=R} =& -\frac{\sin\theta}{2} R(1-\cos(2\beta)) - \frac{c_2}{R} + \frac{d_1\cos(\beta)}{R^2} \\ & \frac{2d_2\cos(2\beta)}{R^3} + 0 + \ldots + \frac{nd_n\cos n\beta}{R^{n+1}} + \frac{(n-2)\hat{d}_n\cos n\beta}{R^{n-1}} + \ldots \end{aligned} \tag{4.25}$$

Using the above boundary conditions on the surface of the particle, we calculate the drift velocity v_1 as well as the unknown coefficients c_2, d_1, d_2, $\hat{d}_2 \ldots$ used to describe stream function in (4.22). The process involves expressing terms in (4.24) and (4.25) in terms of sine and cosine Fourier modes respectively and using orthogonality of Fourier series to solve for the unknown coefficients.

First, we consider a circular cylinder so that $\alpha = 0$ and $R = 1$. Using the surface boundary conditions (4.23) with $\alpha = 0$, we get [21] :

$$\psi = \sin\theta\left[\frac{r^2(1-\cos(2\beta))}{4} - \frac{\ln(r)}{2} - \frac{\cos(2\beta)}{4r^2} + \frac{\cos(2\beta)}{2r^0}\right] \tag{4.26}$$

The only non-zero Fourier mode is the second mode driven by the $\cos(2\beta)$ term of the simple shear flow stream-function when the surface of the particle is circular. In this case, there is no drift velocity, i.e., $v_1 = 0$. The solution for the stream function around an infinitely long circular cylinder rotating in a simple shear flow was first given by Bretherton [21]; the above relation (4.26) is a special case of that solution when angular velocity of the cylinder is 0.

Next we consider the first perturbation to the stream function due to finite asymmetry. When $\alpha \neq 0$, the $O(\alpha^0)$ terms in the solution for the stream function in the presence of a circle are the terms that drive other modes of the stream function at $O(\alpha)$. In particular the perturbed flow is driven by the interaction of the $(2m+1)$ mode of the perturbed surface and the $O(1)\cos(2\beta)$ terms and the $\ln(r)$ term in the (4.26). To the leading order any term in (4.24) and (4.25) can be written as:

$$\begin{aligned} R^a \sin 2\beta &= (1 + a\alpha\cos((2m+1)\beta))\sin 2\beta = \sin 2\beta + a\alpha(\sin((2m+3)\beta) - \sin((2m-1)\beta)) \\ R^a &= 1 + a\alpha\cos((2m+1)\beta) \\ R^a \cos 2\beta &= \cos 2\beta + a\alpha(\cos((2m+3)\beta) + \cos((2m-1)\beta)). \end{aligned} \tag{4.27}$$

where the first equality gives the type of term needed in (4.24) and the second and third equality the types of terms needed in (4.25). It should be noted here that in both (4.24) and (4.25), the same Fourier modes appear, except in one case all terms are expressed in terms of sine functions and in the other in terms of cosine functions. The other difference is the $\frac{1}{r}$ (from $\ln r$ term) term which appears only in (4.25) and drives the $2m+1$ mode. Thus, to the leading order it turns out that only $2m-1$, $2m+1$, and $2m+3$ Fourier modes terms are non-zero in the general stream function solution (4.22). All other modes are higher order in α.

Since we are interested in shapes for which $v_1 \neq 0$, it is valuable to note that the only term that can drive the v_1 term to first order is the first Fourier mode, which is non-zero for $m = 1$. Hence, amongst the family of shapes represented by (4.18), the only shape with a non-zero drift velocity is that with the third Fourier mode (4.9) perturbation. The solution of the stream function for such a

shape is given by:

$$\begin{aligned}\psi &= \sin\theta\Big[\frac{r^2(1-\cos(2\beta))}{4} - \frac{\ln(r)}{2} - \frac{\cos(2\beta)}{4r^2} - \frac{\alpha\cos(\beta)}{2r} + \frac{\cos(2\beta)}{2r^0} \\ &\quad + \frac{\alpha\cos(3\beta)}{2r^3} - \frac{\alpha\cos(3\beta)}{2r^1} - \frac{\alpha\cos(5\beta)}{2r^5} + \frac{\alpha\cos(5\beta)}{2r^3}\Big],\end{aligned} \tag{4.28}$$

and the drift velocity in this case is:

$$v_1 = \frac{\alpha\sin\theta}{2} \tag{4.29}$$

4.3.3 Condition for alignment

The drift velocity, v_1 to the leading order is proportional to α, a measure of the degree of asymmetry of the cross-section. When this cross-section becomes part of the ring, one can calculate an angular velocity originating from this drift velocity. The $\sin\theta$ dependence of the drift velocity for a cross-section corresponds to a solid-body rotation of the ring. The corresponding rigid body rotation rate of the ring in the vorticity direction when its axis of symmetry is in the gradient direction is given by:

$$\begin{aligned}-\omega_{as} A sin\theta &= v_1 \\ \omega_{as} &= -\tfrac{\alpha}{2A}\end{aligned} \tag{4.30}$$

The angular velocity of the ring in (4.30) arises from the asymmetry of the cross-section and is opposite to the direction of vorticity. Apart from this angular velocity, a finite aspect ratio ring will undergo rotation in the vorticity direction due to the torque per unit length exerted by the shear flow. In the limit when $\alpha \ll 1$, the leading order angular velocity of the ring is the same as the angular velocity of a ring with circular cross-section in simple shear flow. The torque

per unit length arises from a local interaction of the flow with the ring cross-section and is independent of A and this leads to a total torque proportional to the circumference $2\pi A$. The resistance to rotation is proportional to $\ln A/A^3$ so the rotation rate induced by the torque is proportional to $(\ln A)/A^2$. Thus the angular velocity in the vorticity direction is given by:

$$\omega_{cc} = 0.815\frac{\ln A}{A^2} + O(\alpha\frac{lnA}{A^2}) \tag{4.31}$$

where the prefactor of the leading order term in (4.31) was obtained using the BEM simulations presented in section 5.

The net angular velocity of a ring in the vorticity direction, in the limits $A \gg 1$ and $\alpha \ll 1$ can be calculated using linear superposition of angular velocities calculated in (4.30) and (4.31), is then given by:

$$\omega = \frac{1+\lambda}{2} = 0.815\frac{\ln A}{A^2} - \frac{\alpha}{2A} + O(\alpha\frac{lnA}{A^2}) \tag{4.32}$$

Here, the tumbling parameter, λ is written in terms of the angular velocity of the particle using (4.1) and the knowledge that the particle is oriented in the gradient direction. It should be noted here that there are two $O(\alpha)$ terms in (4.32), however the $O(\alpha\frac{lnA}{A^2})$ can be neglected compared to $\frac{\alpha}{2A}$ term when $A \gg 1$.

The particle will reach a steady alignment if the tumbling parameter is less than or equal to -1. This occurs when the rotation rate of a particle in the flow-gradient plane is less than or equal to zero which corresponds to the angular velocity due to the asymmetry of the particle being greater than or equal to the angular velocity of the particle with the circular cross-section. This condition is given by:

$$\begin{aligned} \frac{\alpha}{2A} &\geq 0.815\frac{\ln A}{A^2} \\ \alpha &\geq 1.63\frac{\ln A}{A} \end{aligned} \tag{4.33}$$

The equal to sign in the above equation corresponds to a critical radius of the ring at which the particle first aligns and has a permanent orientation within the flow-vorticity plane. A radius above this critical value leads to alignment of the axis of symmetry of the particle as noted earlier at an angle ϕ to the gradient direction given by $\tan\phi = -\left(\frac{\lambda+1}{\lambda-1}\right)^{\frac{1}{2}}$. It should be noted here that unlike Bretherton's [20] shape, the ring shape presented here can align at a moderate aspect ratio. A challenge to achieve alignment with Bretherton's shape is the need for the asymmetric beads to overcome the torque on the connecting rod. In our shape there is no need for a connector and the entire circumference of the ring is providing a cross-stream force that contributes to the torque that is opposite to the vorticity direction. Another distinction is that the non-tumbling shapes studied in this work have $\lambda \leq -1$ where as for Bretherton's shape $\lambda \geq 1$. Both our particle shape and Bretherton's are able to achieve alignment without an external body force or torque.

Thus far, we have described the cross-stream migration of a two-dimensional circular particle perturbed by the third Fourier mode and its role in creating a flow-aligning ring-shaped particle. We now discuss other perturbed shapes. Based on tensor symmetries discussed at the beginning of section 3, it is clear that fore-aft asymmetry is required to create cross-stream migration. However, it is interesting to note that not all fore-aft asymmetries could give rise to a lateral migration. It will be shown in Appendix A.1 that any perturbed shape of the form:

$$R = 1 + \alpha\cos((2m+1)\beta) \text{ for } m > 1, \tag{4.34}$$

corresponding to modes higher than third order gives no migration velocity to any order in α. Thus, a ring with the cross-sectional shapes represented by (4.34) can align in simple shear flow only for $m = 1$.

Although shapes represented by (4.34) do not drift in the gradient direction, we find that combinations of perturbations involving higher order modes could give rise to a lateral force at higher orders in α. For example, a combination of Fourier modes of the form

$$R = 1 + \alpha_1 \cos((2m_1 + 1)\beta) + \alpha_2 \cos((2m_2 + 1)\beta) \tag{4.35}$$

can give a drift velocity for $m_1 = 2$ and $m_2 = 3$ as shown in appendix A.1.

4.4 Boundary Element Method

The asymptotic solutions obtained above are valid only in the limits $A \gg 1$ and $\alpha \ll 1$; at finite A and α the problem needs to be solved using a numerical scheme. Both the resistivity and mobility problems discussed are ideally suited to be solved using the boundary element method [151, 81, 121], which solves an integral representation of the creeping-flow problem on the two dimensional surface of the particle instead of solving the Stokes equations in the three dimensional domain. The starting point for the boundary element method is an integral equation for the velocity field written in terms of the stresses acting on the boundary convoluted with the Green's function. The general integral representation of the creeping-flow problem was obtained by Ladyzhenskaya [89]. For the case of flow around rigid boundaries, the simplified integral equations [81] for the creeping-flow problem can be written as:

$$\mathbf{v}(\mathbf{r}) = \mathbf{u}(\mathbf{r}) + \int_S \mathbf{J}(\mathbf{r} - \mathbf{r}').\mathbf{f}(\mathbf{r}')dS' \tag{4.36}$$

where $\mathbf{r}$ and $\mathbf{r}'$ are position vectors, $\mathbf{v}$ is the velocity on the boundary, $\mathbf{u}$ is the undisturbed fluid velocity (simple shear flow here) in the absence of the boundary, $\mathbf{f}$ is the unknown stress, S represents the boundary of the flow domain, dS'

indicates integration over S with respect to the point $\boldsymbol{r'}$, and $\mathbf{J}$ is the Green's function. The integral term on the right hand side represents the disturbance field created by the stresses at $\mathbf{r}'$ on the velocity at $\mathbf{r}$. For the Stokes problem, $\mathbf{J}$ is given by:

$$J_{ij} = \frac{1}{8\pi}\left(\frac{\delta_{ij}}{r} + \frac{r_i r_j}{r^3}\right). \tag{4.37}$$

Based on the symmetry of the particle studied here about the $x-z$ plane and the anti-symmetry of the flow about the $x-z$ plane, we can further simplify the problem by identifying the following relationship between stresses acting on the surface of the particle:

$$f_x(\boldsymbol{\rho}, +y) = -f_x(\boldsymbol{\rho}, -y), \quad f_y(\boldsymbol{\rho}, +y) = f_y(\boldsymbol{\rho}, -y), \quad f_z(\boldsymbol{\rho}, +y) = -f_z(\boldsymbol{\rho}, -y), \tag{4.38}$$

where $\boldsymbol{\rho}$ is the radial vector in polar coordinates in the $x-z$ plane. Using the above relations, the boundary integral formulation for the problem is then reduced to:

$$\begin{aligned} v_i(\mathbf{r}) - \Gamma_{ij} r_j = \int_S dS'(&f_y(\boldsymbol{\rho'}, y')[J_{iy}(\boldsymbol{\rho} - \boldsymbol{\rho'} + \mathbf{e}_y(y - y')) + J_{iy}(\boldsymbol{\rho} - \boldsymbol{\rho'} + \mathbf{e}_y(y + y'))] \\ &+ f_x(\boldsymbol{\rho'}, y')[J_{ix}(\boldsymbol{\rho} - \boldsymbol{\rho'} + \mathbf{e}_y(y - y')) - J_{ix}(\boldsymbol{\rho} - \boldsymbol{\rho'} + \mathbf{e}_y(y + y'))] \\ &+ f_z(\boldsymbol{\rho'}, y')[J_{iz}(\boldsymbol{\rho} - \boldsymbol{\rho'} + \mathbf{e}_y(y - y')) - J_{iz}(\boldsymbol{\rho} - \boldsymbol{\rho'} + \mathbf{e}_y(y + y'))]) \end{aligned} \tag{4.39}$$

where $\boldsymbol{\Gamma}$ is the non-dimensional imposed velocity gradient tensor. The integration is now performed on the surface of the particle in the $+y$ direction.

Given the axisymmetry of the particle, the unidirectional nature of the imposed flow and the orientation of the particle with respect to the external flow, one can expect a simple dependence of stresses on the θ direction. Using the finite element software package Comsol, we have determined the following func-

tional dependence of the stresses on the azimuthal (θ) direction:

$$\begin{aligned} f_x(\boldsymbol{\rho}, +y) &= f_1(\rho, +y)\cos(2\theta) + f_2(\rho, +y) \\ f_y(\boldsymbol{\rho}, +y) &= f_3(\rho, +y)\cos\theta \\ f_z(\boldsymbol{\rho}, +y) &= f_4(\rho, +y)\sin(2\theta) \end{aligned} \tag{4.40}$$

These finite element Comsol simulations have been performed in a manner similar to the ones described in Singh et al. [128] for determining effective aspect ratio of cylindrical disks. Using the above dependence of stresses on the azimuthal direction in 4.39, we analytically integrate along the azimuthal direction. These results are shown in Appendix A.2. The remaining problem is then reduced to numerical integration along the radial direction and requires discretization only over the cross-section of the ring. It should be noted here that in the limit $\boldsymbol{\rho} \to \boldsymbol{\rho}'$, the Green's functions in equation (4.39) are singular. Analytical integration is performed to remove the singularities in this limit. The details of the analytical integration are also given in Appendix A.2.

For the simulations, the ring cross-section is discretized into N elements. Each element subtends an equal angle $d\beta$ at the center of the ring cross-section and the entire cross-section is at a constant value of θ from the vorticity direction. The stresses over the individual elements are considered to be constant. Each element itself is locally divided into N_{small} elements to integrate the Green's function. For the results presented in this work, we have taken $N = 500$ and $N_{small} = 20$.

In the present work, we solve two types of problems: 1) determine the angular velocity of a torque-free particle (mobility problem); and 2) determine the torque acting on a stationary particle (resistivity problem). For solving the resistivity problem (type 2), the surface velocity of 0 is used in the integral equa-

tion and the problem is solved for the stresses (f_1, f_2, f_3, f_4) acting on the particle which corresponds to $4N$ variables. Momentum balances in three directions yield $3N$ linear equations for N elements for a single constant value of θ. An additional N number of equations are obtained by applying the momentum balance in the $x-$ direction (4.51) for another value of θ. The two constant values of θ used in the simulations are: $\pi/4$ for momentum balances in all three directions and 0 for momentum balance in $x-$ direction. The resultant torque is calculated from the stresses using the following equation:

$$\begin{aligned} T_z &= 2 \int_S dS\,(y f_x - \rho \cos\theta f_y) \\ &= 2 \int_S dS\,(y(f_1 \cos 2\theta + f_2) - \rho \cos^2\theta f_3) \end{aligned} \tag{4.41}$$

The factor of 2 in the above equation accounts for the torque acting on the $-y$ half of the particle which by symmetry of the flow about $x-z$ plane and fore-aft symmetry of the particle is equal in magnitude and direction to the torque acting in the $+y$ half of the particle.

For the solution of the mobility problem (type 1), an unknown angular velocity, ω, along the vorticity direction is assumed. The velocity boundary conditions on the surface of the particle for this case are then given by:

$$\begin{aligned} v_x &= \omega y \\ v_y &= -\omega \rho \cos\theta \end{aligned} \tag{4.42}$$

In the simulations for this case, there are $4N+1$ unknowns, with angular velocity, ω of the ring being an additional unknown. The condition of no net torque, $T_z = 0$, is applied to (4.41) to solve for the additional unknown.

4.5 Numerical and Analytical Predictions

In this section we present the results of the boundary element simulations and compare these results with the analytical predictions derived in section 3. We first validate our implementation of the boundary element method by comparing with analytical predictions for the torque on a circular ring rotating in a quiescent fluid. The analytical results are then compared with the simulation results in the limit when $\alpha \ll 1$ and $A \gg 1$. Finally, BEM results for finite aspect ratios and finite α values for the ring particles with cross-section given by (4.9) are presented. We determine the critical α-dependent radius of the ring, A at which the ring will transition from rotating continuously to reaching a steady alignment. The resistance formulation is used for the validation of the torque results in sub-section 5.1, while all the other results involve calculation of the angular velocity for a freely rotating ring using the mobility formulation.

4.5.1 Circular cross section ring

When $\alpha = 0$, the particle's cross-section is circular and the ring has the shape of a circular torus. The torque and the rotation rate of such a ring with its axis of symmetry in the gradient direction of a simple shear flow satisfy the relationship:

$$T_z - 8\pi g_z (A+1)^3 \left(\omega - \frac{1+\lambda}{2}\right) = 0. \tag{4.43}$$

Here, two parameters, the tumbling parameter, λ and the torque coefficient, g_z allow one to calculate the torque on a particle rotating with any angular velocity ω in simple shear flow. We calculated the tumbling parameter, λ of the particle by solving for the angular velocity of the particle when the particle is torque

free ($T_z = 0$) from the BEM simulations of the mobility problem. The torque coefficient is then calculated based on the BEM simulations of the resistivity problem ($\omega = 0$). Our results for the torque coefficient can be compared with previous theoretical work while we obtain new predictions for the tumbling parameter of a circular torus.

Circular-torus shaped particles have been extensively studied in the past [139, 115, 149, 74, 59, 140] particularly because of interest in ring polymers. We will compare our simulation results with the complete solutions of Goren and O'Neill [59] and the asymptotic solutions of Johnsont and Wu [74]. Goren and O' Neill [59] have determined the torque and force on rotating and translating circular-torus particles in a fluid that is at rest at infinity. They obtained analytical results even for finite aspect ratio particles by solving the equations of motion for the fluid in toroidal coordinates. In particular, we will consider their analytical results for the torque coefficient calculated for a torus rotating about one of its long axes.

The scaling of the torque coefficient at high aspect ratio is obtained from the results of Johnson and Wu[74] who used the singularity solution for Stokes flow to solve for the flow past a slender ring with circular cross-section. Johnson and Wu calculated the force per unit length and the torque per unit length acting on the ring cross-section, we present two leading terms for the torque coefficient of the particle at large A which are generated by the force per unit length term. In the limit $A \gg 1$, the force per unit length is given by: $(= -8\pi\left(\frac{((1+\lambda)/2)A}{2(\ln 8A-\frac{3}{2})}\right)\sin\theta + O(\frac{1}{A^2}))$ for rings rotating about one of their longer axes where θ is the angle relative to the axis of rotation. The torque acting on the

particle due to this force can then be written as:

$$T_z = \int_0^{2\pi} 8\pi \left(\frac{((1+\lambda)/2)A}{2(\ln 8A - \frac{3}{2})} \right) \sin^2\theta A^2 d\theta$$
$$= 8\pi^2 \left(\frac{((1+\lambda)/2)A^3}{2(\ln 8A - \frac{3}{2})} \right) \tag{4.44}$$

Using (4.43) and (4.44), the torque coefficient is given by:

$$g_z = \frac{\pi}{(2\ln 8A - 3)} \left(1 - \frac{3}{A}\right) + O(\frac{1}{A^2}) \tag{4.45}$$

Figure 5 presents a comparison of the complete analytical solution of torque coefficients obtained from table 1 of Goren and O'Neill [59], torque coefficients obtained from Johnson and Wu [74] in (4.45) and results from the BEM simulations. Our numerical predictions (□) are in very good agreement with the analytical predictions (⋄) of Goren and O'Neill [59] at all values of the ring radius. Johnson and Wu 's [74] predictions (continuous curve) at small aspect ratio are in good agreement with the exact results when the non-dimensional radius of the ring is larger than 20.

The angular velocity ω_{cc} of a torque-free circular-torus in the xz-plane of a simple shear flow is plotted in figure 6 for A ranging from 1.5 to 250. The scaling analysis outlined in (4.31) indicating that the rotation rate is proportional to $\frac{\ln(A)}{A^2}$ is quantitatively accurate at small aspect ratios and remains a good approximation for A as small as 3. The tumbling parameter can be calculated from ω_{cc} using (4.43). The effective aspect ratio of the ring shaped particle to the leading order is then given by:

$$\kappa_e = \left(\frac{1+\lambda}{2}\right)^{\frac{1}{2}} = \left(\frac{0.815 \ln A}{A^2}\right)^{\frac{1}{2}} = 0.903\kappa(ln(1/\kappa))^{\frac{1}{2}} \tag{4.46}$$

It is interesting to note that slender circular rings like long cylindrical fibers rotate logarithmically faster than spheroids of the same aspect ratio [34] (Singh

Figure 5

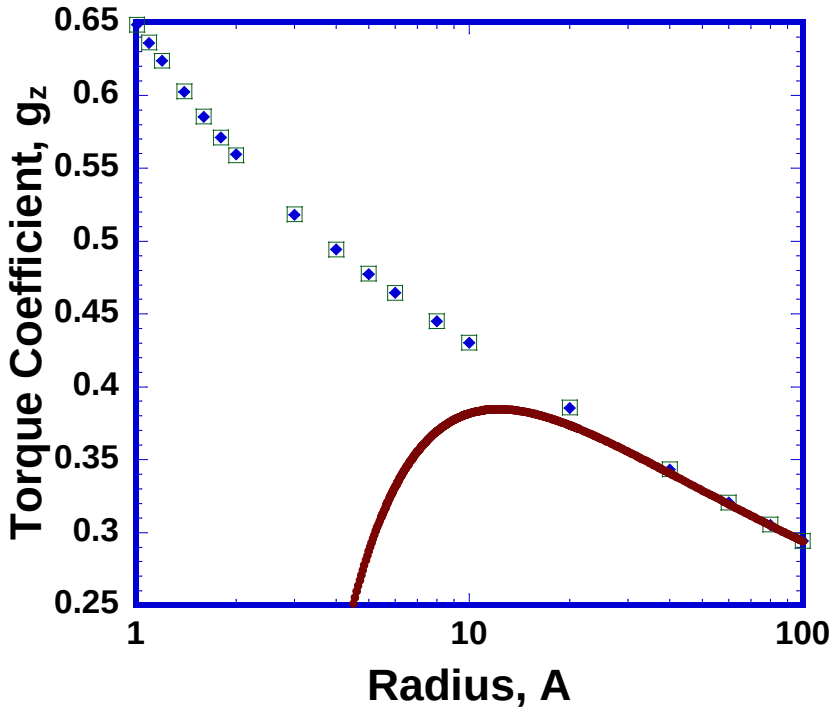

Figure 4.5: Comparison of torque coefficient, g_z between complete analytical results [59] (⋄), BEM simulations (□), and asymptotic analysis (continuous curve, (4.45)) [74] for a circular cross-section ring ($\alpha = 0$).

et al. [128] incorrectly listed Cox's asymptotic effective aspect ratio of cylinders for $\kappa >> 1$ as $\frac{1.24\kappa}{ln(\kappa)}$ rather than $\frac{1.24\kappa}{(ln(\kappa))^{1/2}}$ in equation 9. However, the correct formula was used in figure 5 of Singh et al. [128]). In contrast, the effective aspect ratio of low aspect ratio circular disks [130] is larger than the particle aspect ratio by an algebraic factor.

4.5.2 Comparison of asymptotic analysis with simulation for large A and small α

Here, we compare our predictions from the asymptotic analysis of a thin ring in the limit when $A \gg 1$ and $\alpha \ll 1$ with the BEM simulations. A ring with a circular cross-section undergoes Jeffery's rotational motion in the vorticity direction in simple shear flow with an angular velocity, ω_{cc} (4.31). When the shape of the cross-section is slightly non-circular as given by (4.9), the angular velocity of the particle is a combination of this Jeffery's rotational velocity and an angular velocity due to the asymmetry of the cross-section of the ring. From the asymptotic analysis in section 3, we have shown that in the limit when $\alpha \ll 1$ and $A \gg 1$, the angular velocity, ω_{as} of the particle due to the asymmetric cross-section is given by (4.30). As noted earlier, the net angular velocity, ω is given by:

$$2\omega = 1 + \lambda = 1.63\frac{\ln A}{A^2} - \frac{\alpha}{A} + O(\alpha\frac{lnA}{A^2}) \qquad ((4.32))$$

It should be noted here that the angular velocity, ω_{cc} also changes due to the change in the cross-section but is a factor of A^{-1} less than ω_{as} and can be neglected in the leading order analysis. Figure 7 shows twice the angular velocity of the particle as a function of α for $A = 50,\ 100, \text{and } 200$. The straight

Figure 6

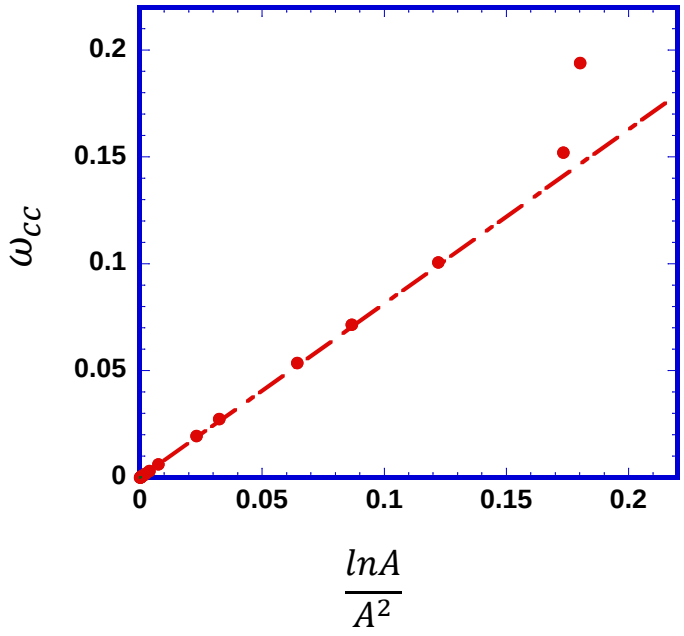

Figure 4.6: Angular velocity of a ring with circular cross-section for $A \geq 1.5$. The straight line fit is plotted using data for $A \geq 100$ and is given by $\omega_{cc} = 0.815\frac{\ln A}{A^2}$.

lines are fits to the simulations for values of $\alpha < 0.02$. The slope of these lines for $A = 200$ and $A = 100$ are found to be within 1.5% of the predicted slope of $\frac{1}{A}$ from the analysis in (4.32). The slope of the line for $A = 50$ is about 3% less than the predicted slope. The intercept of the lines on the y-axis corresponds to twice the angular velocity of the particle with circular cross-section. The linear dependence of the rotation rate on α provides a good approximation to the computational results up to $\alpha \approx 0.08$. At higher α, the rotation rate decreases more slowly with α suggesting that backward rotation of the ring due to the asymmetry saturates at finite α.

4.5.3 Finite aspect ratio calculations

As the non-dimensional radius, A of the ring becomes smaller and the deviation of the cross-section from a circular shape becomes more significant, the asymptotic approximations used in section 3 are no longer accurate. To explore the rotation rate of particles in this regime we perform a series of boundary element simulations for a range of A and α. Using (4.32), the tumbling parameter is calculated by solving for the torque free angular velocity of the ring in the BEM. For practical purposes it is of interest to find the minimum radius (maximum aspect ratio) of the the particle at which it will reach a steady alignment. Since the transition from tumbling to aligning motion occurs when the tumbling parameter λ is equal to -1, we plot $1 + \lambda$ as a function of the radius of the ring, A, for $\alpha = 0$, 0.1, 0.4 and 0.55 in figure 8. As A increases, $1 + \lambda$ decreases and crosses 0 which is the point of transition from tumbling to non tumbling. For the particles that stop rotating, the value of $1 + \lambda$ after reaching a minimum starts increasing with increasing A although it does not cross 0 again. This behavior is consistent

Figure 7.

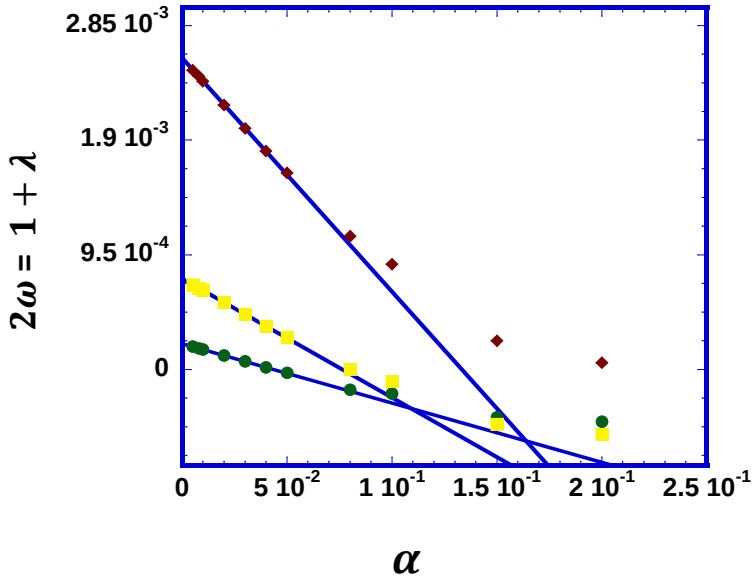

Figure 4.7: Angular velocity of the ring shaped particles with axis of symmetry oriented in the gradient direction as a function of α for $A = 50$ ($\diamond$), $A = 100$ ($\square$), and $A = 200$ ($\circ$) in the limit of small α. Equations of the lines for the three cases are: $2\omega = 2.58X10^{-3} - 1.94X10^{-2}\alpha$ for $A = 50$, $2\omega = 7.51X10^{-4} - 9.86X10^{-3}\alpha$ for $A = 100$, and $2\omega = 2.14X10^{-4} - 4.93X10^{-3}\alpha$ for $A = 200$.

with the asymptotic analysis (4.32) which indicates that $1 + \lambda$ scales like $O(\frac{\alpha}{A})$ for $A \gg 1$ and $\alpha \ll 1$.

For $\lambda + 1 < 0$, a particle's axis of symmetry reaches a fixed orientation in the xy-plane. The angle between the particle's axis of symmetry and the gradient direction is given by $-\tan^{-1}\left(\frac{\lambda+1}{\lambda-1}\right)^{\frac{1}{2}}$ (figure 2) which, for $\lambda \sim -1$, can be simplified to just $-(\frac{1+\lambda}{-2})^{\frac{1}{2}}$. The maximum absolute value of the angle of inclination from figure 8 is 0.032, obtained for $\alpha = 0.55$ and $A = 70$. It should be noted here that small values of the inclination angle imply that the stability of the particle against perturbations is small. Any perturbation that is large enough to rotate the particle by an angle of $2(\frac{1+\lambda}{-2})^{\frac{1}{2}}$ will result in the particle rotating by an angle of π, from one stable equilibrium orientation (near the +y axis) to the other stable equilibrium orientation (near the -y axis).

Typical rigid particle shapes like cylinders, disks, spheroids, and rings with circular cross-section undergoing Jeffery's rotational motion have a period of rotation that increases as the particle becomes thinner, i.e., $\lambda \to \pm 1$ when the particle aspect ratio approaches 0 or ∞. Like ring shapes with circular cross-section, it is the natural tendency of the ring particles with cross-section given by (4.9) to rotate slowly and have small absolute values of $1 + \lambda$ as the aspect ratio is decreased. However, due to the presence of a non-circular cross-section these particles actually stop rotating ($\lambda = -1$) at finite values of the aspect ratio. The transition of the particle from Jeffery like periodic rotational motion to the aligned state as a function of the particle radius and α is shown in figure 9. Above the curve, particles tumble and below the curve particles do not tumble in the simple shear flow. For the values of α shown in figure 9, the minimum integral value of the radius for which a particle can align is $A = 30$ which occurs

Figure 8

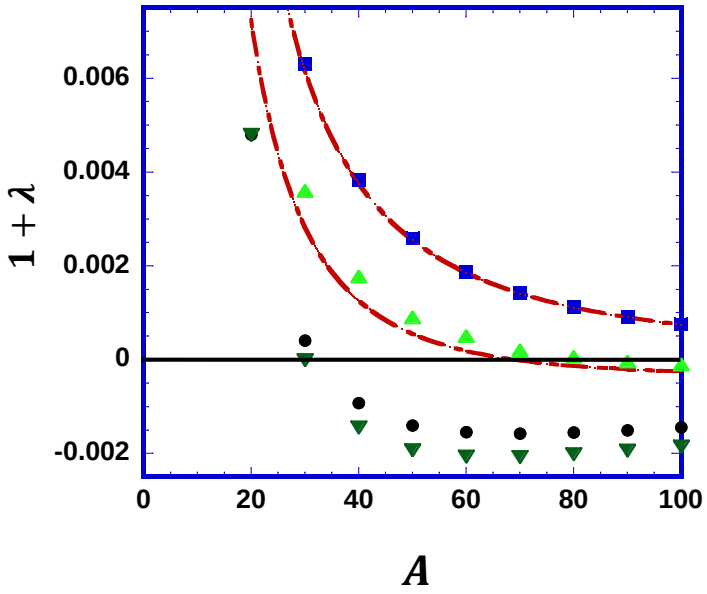

Figure 4.8: Change in the parameter, $1 + \lambda$ (4.32) as a function of non-dimensionalized radius of the ring, A for $\alpha = 0$ ($\square$), $\alpha = 0.1$ ($\triangle$), $\alpha = 0.4$ ($\circ$), and $\alpha = 0.55$ ($\triangledown$). Value of $1 + \lambda$ less than 0 denotes the region where particle aligns in simple shear flow. The continuous curves for $\alpha = 0$ and 0.1 represent the results from the asymptotic analysis for small α and large A.

for $\alpha \sim 0.55$. The dependence of the maximum flow aligning aspect ratio on the asymmetry parameter is weak over a broad range $\alpha = 0.4$ to 0.9 for which the minimum A remains between 30 and 33. This minimum value of the flow aligning radius is obtained for the cross-sectional shapes studied in this work but likely does not represent the global minimum of the radius (or maximum of the aspect ratio) for all the rigid particle shapes that can align in simple shear flow. For more practical applications of suspensions of these particles, aspect ratio closer to 1 ($A \sim 1$) would be very useful. In this work, we have not attempted to optimize the shape of the cross-section to increase the angular velocity of the particle due to asymmetry. Some of the questions that remain to be answered are: What is the optimum shape of the cross-section which induces maximum angular velocity of the ring due to asymmetry? Are ring shaped particles the only particles which could align in simple shear flow? If not, then what is the global optimum shape that maximizes the aspect ratio of the non-tumbling particles?

4.6 Conclusion

In this work, we have presented particle shapes that can stop rotating in simple shear flow. Particles in simple shear flow tumble due to the rotational component of the simple shear flow. We have used an asymmetry between the inner and outer portions of a ring's cross-section to induce a lateral force per unit length on the cross-section of the particle. The torque due to this force cancels the torque trying to rotate the particle in the vorticity direction at appropriate aspect ratios. The particular shape that we have studied is a ring with the cross-section given by $R = 1 + \alpha \cos 3\beta$ and the radius given by A. Unlike Bretherton's

Figure 9.

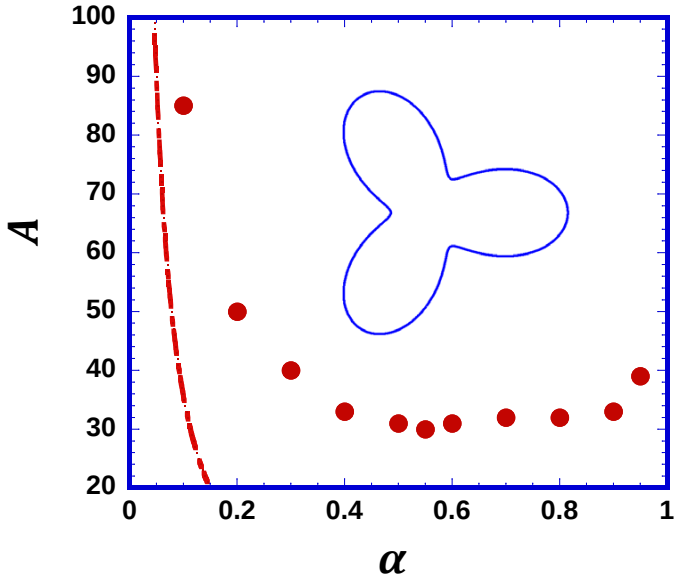

Figure 4.9: State diagram showing the non-dimensionalized radius of the particle at which the particle transitions from a continuously tumbling state to the non-tumbling state for various values of α. The points here represent the smallest integer value of A for which the particle stops tumbling. The cross-sectional shape ($\alpha = 0.55$) of the particle that aligns at a radius of 30 is shown in the graph. The continuous curve represents the transition predicted from the asymptotic analysis in (4.33). The shape of the cross-section for $\alpha = 0.55$ is shown.

proposed non-tumbling particle shape, the ring shaped non-tumbling particles do not require a connector and can stop tumbling at finite aspect ratios while maintaining rigidity. To leading order in α, the angular velocity of the particle due to asymmetry is given by $\frac{\alpha}{2A}$. We have shown that lack of fore-aft symmetry of the cross-section is a necessary but not a sufficient condition to induce a lateral force per unit circumference on the particle which is necessary for alignment.

The tumbling parameter for the non-tumbling particle shapes presented in this work lie in the range $\lambda \leq -1$ which corresponds to the alignment of axis of symmetry close to the gradient direction whereas the tumbling parameter of the shape presented by Bretherton [20] lies in the range $\lambda \geq 1$ which corresponds to the alignment of axis of symmetry close to the flow direction. Values of the tumbling parameter for the shapes studied in this work are calculated for different values of A and α. The equilibrium orientation of the axis of symmetry of the particle is found to be close to the gradient direction (figure 8) due to which the stability of the particles to perturbations is not very high. We found that the minimum radius of the ring for which the particle stops rotating is about 30 which is obtained for $\alpha \sim 0.55$.

In light of the small $1 + \lambda$ values obtained for the non-rotating particle shapes studied here, it is important to examine the practicality of our findings when applied to actual engineering systems. Since most engineering systems would involve Poisseuille flows, it is of interest to determine the effect of quadratic flows on the rotational behavior of the aligning particles. In unbounded quadratic flows, it has been shown that the rotational motion of particles also follow the equation of motion as given by Jeffery [31]. Thus even in pipe flow the parti-

cles discussed in this work will not undergo rotational motion. In the case of bounded quadratic flow, interactions with the wall also play a role in determining the motion of the particle. There is precedent from the fiber literature which shows that interactions with the wall decreases the rate of rotation of the fibers [133]. Mody and King [106] have shown that spheroidal disks with $\kappa = 0.25$ when placed beyond a critical distance (1.2 times radius) undergo a retarded Jeffery's rotational motion and at a distance of about 0.7 times the radius completely stop rotating. Thus, for the case of non-rotating rings, it seems likely that wall interactions will not disturb the non-tumbling nature of the particles.

It is possible that hydrodynamic interactions among the particles could lead to tumbling if the asymmetric rings were dispersed in a fluid at finite concentrations rather than as a single particle as considered here. It may be noted however that at very high concentrations steric interactions among Brownian fibers [27] or disks [73] can lead to highly aligned suspensions. It might be expected that steric effects also inhibit rotation at high concentrations in non-Brownian systems. Thus at high concentration and low concentrations, the non-rotating particles studied here should continue to stay aligned in the flow-vorticity plane. At moderate concentrations the hydrodynamic disturbance of one particle may induce rotation of neighboring particles. However, even in this case, it seems unlikely that a catastrophic deviation from flow aligning will occur in moderately concentrated suspensions. The velocity disturbance caused by the aligned particles is relatively modest. In addition, if one particle does begin to rotate it is likely to align again after rotating through an angle of π rather than flipping continuously.

Although we have been able to show that the ring shape particles can align at

moderate aspects ratios of about 30, the physical manifestation of such particles is still going to be challenging. For low Reynolds number and non-Brownian conditions, there is only a small size range, for aspect ratio of 30, in which the particle will continue to align for viscous fluids. The problem of fabrication is further complicated by the kind of shapes (Figure 9) needed for alignment at moderate aspect ratio. It seems that a technique like 3d printing can be used to fabricate these particles. For an aspect ratio of 30, one can fabricate a ring with a radius of 1 cm and a cross-section of mean radius $300\mu m$. For $\alpha = -0.55$, the characteristic length of asymmetry of the cross-section will be $150\mu m$. This critical dimension is achievable with emerging methods in 3-d printing [99]. For this size range the particle would not undergo Brownian motion of sufficient amplitude to flip the particle. To make low Re for this particle size, viscous fluids like glycerine or polybutene (10 Poise) should be used. It should be further noted that in this paper we study cross-sectional shapes with Fourier modes because of the ease of mathematical analysis on such shapes, but cross-sectional shapes like equilateral triangle and right angle triangle should also be able to align the particle at appropriate aspect ratios. These triangular shapes can be fabricated using more conventional fabrication technique such as lithographic patterning of photosensitive polymers on rigid substrates [4] . A large number of particles could be formed by replica molding based on one or a few master structures [46]. Finally, we note that we have discovered only a class of shape which can align, there are possibly other shapes of lower aspect ratio and simpler design which could align and could be fabricated with greater ease.

We will now discuss some broad implications of an aligning particle suspension. The non-rotating nature of the ring shaped particles discussed in this work can have important rheological consequences on suspensions. In a sus-

pension of rotating circular rings, an O(κ) fraction of the rings will be rotating at any given time. These rotating rings experience a force per unit circumference of order $\mu\gamma A^*$ leading to a stresslet, the first moment of the force distribution, of order $\mu\gamma A^{*3}$. Here A^* is the dimensional radius of the ring. The contribution of these rotating rings to the stress in the suspension is $O(n\kappa)$, the number density of flipping rings times their stresslet, yielding an enhancement of the effective viscosity μ_{eff} given by $(\mu_{\text{eff}} - \mu)/\mu = O(nA^{*2}c)$ where c is the radius of the ring's cross-section. In a suspension of rotating rings, like a suspension of rotating fibers, this contribution from tumbling particles dominates over the contributions from the $O(1)$ fraction of the particles that are near the flow-vorticity plane. In a suspension of non-rotating rings, the particles' contribution to the viscosity is purely due to rings aligned near the flow-vorticity plane which exert an $O(\mu\gamma c^2)$ stresslet per unit circumference on the fluid leading to a much smaller enhancement of the effective viscosity $(\mu_{\text{eff}} - \mu)/\mu = O(nA^*c^2)$ than that $(\mu_{\text{eff}} - \mu)/\mu = O(nA^{*2}c)$ obtained for rotating rings. Due to this lower resistance to shearing, a suspension of aligning particles could have benefits in terms of ease of processing.

Like the viscosity, the collision rate of ring particles can also be shown to change drastically if the particles do not tumble. For suspensions of tumbling particles with low and high aspect ratio, the leading order contribution to the collision rate comes from collisions of rotating particles with aligned particles. Following the arguments of Singh et al. [128] for circular cylinders, the leading order collision rate for a suspension of ring shaped particle with circular cross-section is given by $O(n^2A^{*2}c\gamma)$. Like thin disks, the contribution to the collision rate from the $O(1)$ fraction of the particles that are near the flow-gradient plane is lower. In a suspension of non-tumbling ring particles there are no particles

undergoing rotation, thus the leading order collision rate arises from collisions of pairs of aligned rings and is given by $O(n^2 A^* c^2 \gamma)$. This rate is $O(1/A)$ smaller than the collision rate of the rotating ring suspension. A smaller rate of collision would decrease the rate of cluster formation of particles thus improving the processing properties of the suspension.

Materials made from non-tumbling particulate suspensions using methods such as injection molding could have a high degree of anisotropy because particles will be aligned in a single plane at least when particle interactions are negligible. As a result the properties of the material such as the elastic modulus, thermal conductivity, magnetic and electric properties which depends on the orientation distribution of the constituent material would also be expected to have a high degree of anisotropy. For instance, a thin sheet of composite material containing aligned particles in the flow-vorticity plane during injection molding could have a high elastic modulus for extensional deformations in the plane of the sheet and a low resistance to shear deformation across the thickness of the part. Similarly, if the particles are highly conducting, the in-plane conductivity of the material could be high and the conductivity across the thickness small. The possibility of tuning material properties in this way motivates further work toward optimizing the shape leading to non-tumbling behavior and the development of experimental methods to form such non-rotating particles.

We acknowledge support for a graduate fellowship from the Corning Foundation (V.S.), the NYSTAR J.D. Watson Investigator Program, and the National Science Foundation (CTS-0529042).

4.7 Appendix

This appendix is divided into two parts. In the first, we solve Stokes flow around the two dimensional cross-sections of the ring in simple shear flow using the stream-function approach at higher orders in α. We show that not all cross-sectional shapes which lack fore-aft symmetries can lead to a drift velocity in the gradient direction even at higher order in α. Thus, while a lack of fore-aft symmetry is a necessary condition to induce a cross-stream velocity, it is not a sufficient condition. In the second part, we simplify the original integral equations by carrying out integrations in the azimuthal direction using complete elliptic integrals, thus transforming the surface integrals into line integrals. Analytical results for the singular integrands encountered in the BEM formulations are also presented.

4.7.1 Higher order drift velocity calculations for a two dimensional particle lacking fore-aft symmetry

In section 3 we showed that at leading order in α the cross-stream motion of a two-dimensional particle results only from the third Fourier mode perturbation in shape. However, we might have expected that other odd modes lacking fore-aft symmetry would yield drift at higher orders in α. It will be shown in this appendix, however that even at higher orders in α a cross-section described by (4.18) yields cross-stream drift only when $m = 1$. This implies that not all shapes lacking fore-aft symmetry can lead to a non-zero drift velocity. Interestingly, previous studies [16, 20] of asymmetric three-dimensional particles have

only considered the third Legendre polynomial and have not commented on the question of whether cross-stream drift occurs, even in the limit of small α, for higher order mode perturbations in shape.

The general solution for the stream function in simple shear flow around the particle is still given by (4.22) along with the velocity boundary conditions (4.24) and (4.25) on the particle surface. The strategy is again to express the right hand side terms in the first boundary condition equation (4.24) in terms of sine Fourier modes and the second boundary condition equation (4.25) in terms of cosine modes and then show that even at higher orders in α only certain modes of stream function are non-zero. Specifically, we show that shear flow acting on a particle given by (4.18), does not drive $\sin\beta$ or $\cos\beta$ terms in the stream function solution which must be non-zero for a non-zero drift velocity (v_1), unless $m = 1$.

The driving terms for the stream function from the imposed flow in (4.24) and (4.25) are: $R\sin 2\beta$, R, and $R\cos 2\beta$. Both the terms $R\sin 2\beta$ and $R\cos 2\beta$ drive the same terms in the stream function solution. Thus we limit our discussion to terms from (4.25) since it has an extra driving term of R from the simple shear flow. Let us now consider a general term from the multipole expansion of the velocity field in (4.25): $\frac{\cos(n\beta)}{r^{n+1}}$. On the surface of the particle, at higher orders in α this term can be written as :

$$\left.\frac{\cos(n\beta)}{r^{n+1}}\right|_{r=R} = \left(1 - \alpha(n+1)\cos(b\beta) + \alpha^2\frac{(n+1)n}{2}\cos^2(b\beta) - \ldots\ldots\right)\cos(n\beta) \quad (4.47)$$

where, $b = 2m + 1$. To express the above equation in terms of Fourier modes, the

product terms, $\cos^a(b\beta)\cos(n\beta)$ can be expressed as summations of cosine terms,

$$\cos(b\beta)\cos(n\beta) = \frac{1}{2}(\cos((b+n)\beta) + \cos((b-n)\beta))$$

$$\cos^2(b\beta)\cos(n\beta) = \frac{1}{4}(\cos(2b+n)\beta + 2\cos n\beta + \cos(2b-n)\beta)$$

$$\cos^a(b\beta)\cos(n\beta) \rightarrow \cos((ab+n)\beta),\ \cos(((a-2)b+n)\beta)\ldots\cos((2b+n)\beta),\ \cos(n\beta),$$
$$\cos((2b-n)\beta),\ldots\cos((ab-n)\beta);\ \forall\ \frac{a}{2} \in \mathbb{N}$$

$$\cos^a b\beta\cos n\beta \rightarrow \cos((ab+n)\beta),\ \cos(((a-2)b+n)\beta)\ldots\cos((b+n)\beta),\ \cos((b-n)\beta),$$
$$,\ldots\cos((ab-n)\beta);\ \forall\ \frac{a+1}{2} \in \mathbb{N} \tag{4.48}$$

In the last two results, terms on the left hand side of the symbol $\rightarrow$ can be written as the sum of the terms on the right hand side with some pre-factors. These two results can be shown easily using induction. Since a, b, and n are non-negative integers, the only terms that can give a $\cos\beta$ term (driving term for the drift velocity) are $\cos((b-n)\beta),\ \cos((2b-n)\beta),\ldots\cos((ab-n)\beta)$ for $n = b-1,\ b+1,\ 2b-1,\ 2b+1,\ldots\ ab-1,\ ab+1$. The Fourier modes in the general solution of the stream-function that could give rise to a drift velocity are shown in figure 10 (a).

Now in order to show that the drift velocity is 0 at higher orders in α, we need to show that all of the terms in figure 10(a) that can give rise to a non-zero drift velocity are zero themselves. This can be proven by showing that all the modes in the stream function driven by the original driving modes of the imposed flow (simple shear flow) are different from the Fourier modes of the general stream function solution (figure 10(a)) that can give a non-zero drift velocity. The original driving modes of simple shear flow in (4.25) are: $\cos(2\beta),\ \cos(b\beta),\ \cos((b-2)\beta)$ and $\cos((b+2)\beta)$. These original modes can drive

the following modes in the stream function solution:

$$\begin{aligned}
\cos^a(b\beta)\cos(2\beta) &\rightarrow \cos((ab\pm 2)\beta),\ \ \cos(((a-2)b\pm 2)\beta)\ldots\ldots \\
\cos^a(b\beta)\cos(b\beta) &\rightarrow \cos((ab\pm b)\beta),\ \ \cos(((a-2)b\pm b)\beta),\ldots\ldots \\
\cos^a(b\beta)\cos((b\pm 2)\beta) &\rightarrow \cos((ab\pm(b\pm 2))\beta),\ \ \cos(((a-2)b\pm(b\pm 2))\beta),\ldots\ldots
\end{aligned} \tag{4.49}$$

In these results again terms on the left hand side of the symbol $\rightarrow$ can be written as the sum of the terms on the right hand side with some pre-factors. The only Fourier modes in the stream function solution driven by the original modes of simple shear flow are $\pm 2, b,\ b\pm 2,\ 2b,\ 2b\pm 2,\ldots\ldots ab,\ ab\pm 2$. These modes are represented on the number line in figure 10 (b) alongside modes that can drive the first fourier mode. It is clear that there is no overlap between the two sets of modes for $b > 3$. Hence for the cross-sectional shapes given by (4.18), the only shape which will drift in the gradient direction is $m = 1$.

Although within the family of shapes represented by (4.18), only a single shape can undergo drift in the lateral direction, this does not mean that there is only one two dimensional shape lacking fore-aft symmetry that undergoes drift. Shapes could have a combination of perturbations like:

$$R(\beta) = 1 + \alpha_1\cos(b_1\beta) + \alpha_2\cos(b_2\beta) \qquad \text{for } b_1,\ b_2 > 3, \tag{4.50}$$

For these shapes, it can be shown that for a general term $(\frac{\cos(n\beta)}{r^{n+1}}|_R)$ to give a non zero value of v_1 (or drive the first Fourier mode in the stream function solution): $n = \ b_1\pm 1,\ b_2\pm 1,\ b_1\pm b_2\pm 1,\ 2b_1\pm 1,\ 2b_2\pm 1,\ 2b_1\pm b_2\pm 1,\ b_1\pm 2b_2\pm 1,\ldots\ldots..$ On the other hand Fourier modes of stream function solution driven by the shear flow are: $2, b_1,\ b_2,\ b_1\pm 2,\ b_2\pm 2, b_1\pm b_2\pm 2,\ 2b_1,\ 2b_2,\ldots$

For a non-zero v_1, there should be a Fourier mode driven by the shear flow

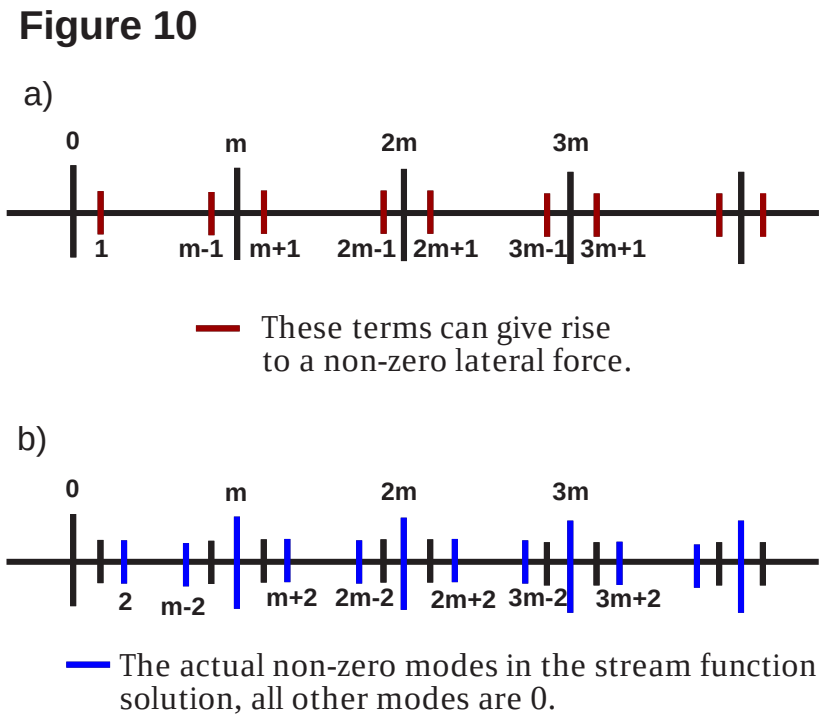

Figure 4.10: (a) Fourier modes in the stream function solution that could give rise to a non-zero drift. (b) Fourier modes in the stream function solution that are driven by the original shear flow including higher order terms in the expansion.

that could also drive the first Fourier mode. For $b_1 = 5$ and $b_2 = 7$, one of the Fourier modes of stream function driven by shear flow is $b_2+2 = 9$ and one of the Fourier modes which can drive the first Fourier modes is $2b_1 - 1 = 9$. Thus, this shape can undergo drift in the gradient direction even without the third Fourier mode perturbation in shape. The resultant contribution to the drift velocity is $O(\alpha_1^2\alpha_2)$. For this shape, similarly there is another contribution to drift velocity at $O(\alpha_2^2\alpha_1)$ and other higher order contributions.

4.7.2 Elliptic integral formulations

Using the azimuthal dependence of stresses from 4.40, the boundary integral equation 4.39 can be written as:

$$
\begin{aligned}
v_x - y = &\int_0^1 \rho' ds' d\theta' (f_1(\rho', y')\cos(2\theta') + f_2(\rho', y'))\Big[\frac{1}{(\rho''^2 + (y-y')^2)^{\frac{1}{2}}} \\
&+ \frac{(\rho\cos\theta - \rho'\cos\theta')^{\frac{1}{2}}}{(\rho''^2 + (y-y')^2)^{\frac{3}{2}}} - \frac{1}{(\rho''^2 + (y+y')^2)^{\frac{1}{2}}} - \frac{(\rho\cos\theta - \rho'\cos\theta')^{\frac{1}{2}}}{(\rho''^2 + (y+y')^2)^{\frac{3}{2}}}\Big] \\
&+ \int_0^1 \rho' ds' d\theta' f_3(\rho', y')\cos(\theta')\Big[\frac{(\rho\cos\theta - \rho'\cos\theta')(y-y')}{(\rho''^2 + (y-y')^2)^{\frac{3}{2}}} \\
&+ \frac{(\rho\cos\theta - \rho'\cos\theta')(y+y')}{(\rho''^2 + (y+y')^2)^{\frac{3}{2}}}\Big] \\
&+ \int_0^1 \rho' ds' d\theta' f_4(\rho', y')\sin(2\theta')\Big[\frac{(\rho\cos\theta - \rho'\cos\theta')(\rho\sin\theta - \rho'\sin\theta')}{(\rho''^2 + (y-y')^2)^{\frac{3}{2}}} \\
&- \frac{(\rho\cos\theta - \rho'\cos\theta')(\rho\sin\theta - \rho'\sin\theta')}{(\rho''^2 + (y+y')^2)^{\frac{3}{2}}}\Big]
\end{aligned}
\tag{4.51}
$$

$$
\begin{aligned}
v_y = &\int_0^1 \rho' ds' d\theta' (f_1(\rho', y')\cos(2\theta') + f_2(\rho', y'))\Big[\frac{(\rho\cos\theta - \rho'\cos\theta')(y - y')}{(\rho''^2 + (y-y')^2)^{\frac{3}{2}}} \\
&- \frac{(\rho\cos\theta - \rho'\cos\theta')(y + y')}{(\rho''^2 + (y+y')^2)^{\frac{3}{2}}}\Big] \\
&+ \int_0^1 \rho' ds' d\theta' f_3(\rho', y')\cos(\theta')\Big[\frac{1}{(\rho''^2 + (y-y')^2)^{\frac{1}{2}}} + \frac{(y-y')^2}{(\rho''^2 + (y-y')^2)^{\frac{3}{2}}} \\
&+ \frac{1}{(\rho''^2 + (y+y')^2)^{\frac{1}{2}}} + \frac{(y+y')^2}{(\rho''^2 + (y+y')^2)^{\frac{3}{2}}}\Big] \\
&+ \int_0^1 \rho' ds' d\theta' f_4(\rho', y')\sin(2\theta')\Big[\frac{(\rho\sin\theta - \rho'\sin\theta')(y - y')}{(\rho''^2 + (y-y')^2)^{\frac{3}{2}}} \\
&- \frac{(\rho\sin\theta - \rho'\sin\theta')(y + y')}{(\rho''^2 + (y+y')^2)^{\frac{3}{2}}}\Big]
\end{aligned} \tag{4.52}
$$

$$
\begin{aligned}
v_z = &\int_0^1 \rho' ds' d\theta' (f_1(\rho', y')\cos(2\theta') + f_2(\rho', y'))\Big[\frac{(\rho\cos\theta - \rho'\cos\theta')(\rho\sin\theta - \rho'\sin\theta')}{(\rho''^2 + (y-y')^2)^{\frac{3}{2}}} \\
&- \frac{(\rho\cos\theta - \rho'\cos\theta')(\rho\sin\theta - \rho'\sin\theta')}{(\rho''^2 + (y+y')^2)^{\frac{3}{2}}}\Big] \\
&+ \int_0^1 \rho' ds' d\theta' f_3(\rho', y')\cos(\theta')\Big[\frac{(\rho\sin\theta - \rho'\sin\theta')(y - y')}{(\rho''^2 + (y-y')^2)^{\frac{3}{2}}} \\
&+ \frac{(\rho\sin\theta - \rho'\sin\theta')(y + y')}{(\rho''^2 + (y+y')^2)^{\frac{3}{2}}}\Big] \\
&+ \int_0^1 \rho' ds' d\theta' f_4(\rho', y')\sin(2\theta')\Big[\frac{1}{(\rho''^2 + (y-y')^2)^{\frac{1}{2}}} + \frac{(\rho\sin\theta - \rho'\sin\theta')^2}{(\rho''^2 + (y-y')^2)^{\frac{3}{2}}} \\
&- \frac{1}{(\rho''^2 + (y+y')^2)^{\frac{1}{2}}} - \frac{(\rho\sin\theta - \rho'\sin\theta')^2}{(\rho''^2 + (y+y')^2)^{\frac{3}{2}}}\Big]
\end{aligned} \tag{4.53}
$$

where $\rho'' = (\rho^2 + \rho'^2 - 2\rho\rho'\cos\theta'')^{\frac{1}{2}}$ is the distance between the two points $\boldsymbol{\rho}$ and $\boldsymbol{\rho'}$ in the $\rho - \theta$ plane, $\theta'' = \theta - \theta'$, and $ds' = d\rho'\left(1 + \left(\frac{dy'}{d\rho'}\right)^2\right)^{\frac{1}{2}}$ is the arc-length. Since the unknowns (f_1, f_2, f_3, f_4) in the above equations 4.53, 4.51, and 4.52 are now independent of θ, these equations can now be integrated analytically along the azimuthal direction and expressed in terms of complete elliptic functions.

Applying the no slip boundary condition to the velocity field arising from

the boundary element formulation led to equations 4.51, 4.52, and 4.53. Integration of these equations in the azimuthal direction (θ) direction can be expressed in terms of complete elliptic integrals. In this subsection, first we express 4.51, 4.52, and 4.53 in terms of elliptic integrals and then present the asymptotic expansions of the integral to deal with the singularity in the integrand. Rewriting equations 4.51, 4.52, and 4.53 we get,

$$\begin{aligned}
(v_x - y)8\pi &= I_{xx1} + I_{xx2} + I_{xy} + I_{xz} \\
v_y 8\pi &= I_{yx1} + I_{yx2} + I_{yy} + I_{yz} \\
v_z 8\pi &= I_{zx1} + I_{zx2} + I_{zy} + I_{zz}, \qquad (4.54)
\end{aligned}$$

where the integrals on the right hand side can be defined as:

$$\begin{aligned}
I_{xx1} &= \int \rho' ds' f_1(\rho')(I_6 + \rho^2 \cos^2\theta I_5 + \rho'^2 I_8 - 2\rho\rho' \cos\theta I_7 - I'_6 - \rho^2 \cos^2\theta I'_3 - \rho'^2 I'_5 + 2\rho\rho' \cos\theta I'_7) \\
I_{xx2} &= \int \rho' ds' f_2(\rho')(I_1 + \rho^2 \cos^2\theta I_3 + \rho'^2 I_5 - 2\rho\rho' \cos\theta I_4 - I'_1 - \rho^2 \cos^2\theta I'_3 - \rho'^2 I'_5 + 2\rho\rho' \cos\theta I'_4) \\
I_{xy} &= \int \rho' ds' f_3(\rho')(\rho \cos\theta (y - y') I_4 + \rho \cos\theta (y + y') - \rho'(y - y') I_5 - \rho'(y + y') I'_5) \\
I_{xz} &= \int \rho' ds' f_4(\rho')(2\rho^2 \sin\theta \cos\theta I_9 - 2\rho\rho' \sin\theta I_{10} - 2\rho'\rho \cos\theta (I_4 - I_7) + 2\rho'^2 (I_5 - I_8) \\
&- 2\rho^2 \sin\theta \cos\theta I'_9 + 2\rho\rho' \sin\theta I'_{10} + 2\rho'\rho \cos\theta (I'_4 - I'_7) - 2\rho'^2 (I'_5 - I'_8)) \\
I_{yx1} &= \int \rho' ds' f_1(\rho')(\rho \cos\theta (y - y') I_5 - \rho'(y - y') I_7 - \rho \cos\theta (y + y') I'_5 + \rho'(y + y') I'_7) \\
I_{yx2} &= \int \rho' ds' f_2(\rho')(\rho \cos\theta (y - y') I_3 - \rho'(y - y') I_4 - \rho \cos\theta (y - y') I'_3 + \rho'(y - y') I'_4) \\
I_{yy} &= \int \rho' ds' f_3(\rho')(I_2 + (y - y')^2 I_3 + I'_2 + (y + y')^2 I'_3) \\
I_{yz} &= \int \rho' ds' f_4(\rho')(2\rho \sin\theta (y - y') I_9 - 2\rho \sin\theta (y + y') I'_9 - 2\rho'(y - y')(I_4 - I_7) + 2\rho'(y + y')(I'_4 - I'_7)) \\
I_{zx1} &= \int \rho' ds' f_1(\rho')(\rho^2 \sin\theta \cos\theta I_5 - \rho\rho' \cos\theta I_{10} - \rho'\rho \sin\theta I_7 + \rho'^2 I_{11} \\
&- \rho^2 \sin\theta \cos\theta I'_5 + \rho\rho' \cos\theta I'_{10} + \rho'\rho \sin\theta I_7 + \rho'^2 I'_{11}) \qquad (4.55)
\end{aligned}$$

$$
\begin{aligned}
I_{zx2} &= \int \rho' ds' f_2(\rho')(\rho^2 \cos\theta \sin\theta I_3 - \rho\rho' \cos\theta I_{12} - \rho'\rho \sin\theta I_4 + \rho'^2 I_9 \\
&- \rho^2 \cos\theta \sin\theta I'_3 + \rho\rho' \cos\theta I'_{12} + \rho'\rho \sin\theta I'_4 - \rho'^2 I'_9) \\
I_{zy} &= \int \rho' ds' f_3(\rho')(\rho \sin\theta(y - y')I_4 - \rho'(y - y')I_9 + \rho \sin\theta(y + y')I'_4 - \rho'(y + y')I'_9) \\
I_{zz} &= \int \rho' ds' f_4(\rho')(2I_{13} + 2\rho^2 \sin^2\theta I_9 + 2\rho'^2(I_9 - I_{11}) - 4\rho\rho' \sin\theta(I_4 - I_7) \\
&- 2I_{13} - 2\rho^2 \sin^2\theta I'_9 - 2\rho'^2(I'_9 - I'_{11}) + 4\rho\rho' \sin\theta(I'_4 - I'_7))) \qquad (4.56)
\end{aligned}
$$

where $I_1 - I_{13}$ are:

$$
\begin{aligned}
I_1 &= S_1, \\
I_2 &= \cos\theta S_2, \\
I_3 &= S_3, \\
I_4 &= \cos\theta S_4, \\
I_5 &= \cos(2\theta)S_5 + \sin^2\theta S_3, \\
I_6 &= (2\cos^2\theta - 1)S_6 + \sin^2\theta S_1, \\
I_7 &= \frac{3}{4}(\cos\theta - \cos(3\theta))S_4 + \cos(3\theta)S_7, \\
I_8 &= (\frac{3}{8} - \frac{\cos(2\theta)}{2} + \frac{\cos(4\theta)}{8})S_3 + (\cos(2\theta) - \cos(4\theta))S_5 + \cos(4\theta)S_8, \\
I_9 &= \sin(2\theta)S_5 - \frac{\sin(2\theta)}{2}S_3, \\
I_{10} &= \sin(3\theta)S_7 + \sin\theta(1 - 3\cos^2\theta)S_4, \\
I_{11} &= \frac{3}{8}\sin(2\theta)(S_5 - S_3) + \frac{\sin\theta}{4}(4\cos(3\theta)S_8 - 3\cos(3\theta)S_5 + 3\cos\theta S_5), \\
I_{12} &= \sin\theta S_4, \\
I_{13} &= \sin(2\theta)S_6 - \frac{\sin(2\theta)}{2}S_1 \qquad (4.57)
\end{aligned}
$$

and $S_1 - S_8$ are defined as:

$$
\begin{aligned}
S_1 &= \int_0^{2\pi} \frac{d\theta'}{(A_1^2 - B^2\cos\theta')^{\frac{1}{2}}} = \frac{4}{C_1}K(D_1) \\
S_2 &= \int_0^{2\pi} \frac{\cos\theta' d\theta'}{(A_1^2 - B^2\cos\theta')^{\frac{1}{2}}} = \frac{4}{C_1 B^2}(A_2^2 K(D_1) - C_2^2 E(D_2)) \\
S_3 &= \int_0^{2\pi} \frac{d\theta'}{(A_1^2 - B^2\cos\theta')^{\frac{3}{2}}} = \frac{4}{C_1^3}\frac{E(D_1)}{1 - D_1^2} \\
S_4 &= \int_0^{2\pi} \frac{\cos\theta' d\theta'}{(A_1^2 - B^2\cos\theta')^{\frac{3}{2}}} = \frac{4}{C_1^3 B^2}(A_1^4 \frac{E(D_1)}{1 - D_1^2})
\end{aligned}
\tag{4.58}
$$

$$
\begin{aligned}
S_5 &= \int_0^{2\pi} \frac{\cos^2\theta' d\theta'}{(A_1^2 - B^2\cos\theta')^{\frac{3}{2}}} \\
&= \frac{4}{C_1^3}\left(\frac{8(D_1^2 - 2)(D_1^2 - 1)K(D_1) - 2(D_1^4 - 8D_1^2 + 8)E(D_1)}{2D_1^4(D_1^2 - 1)}\right) \\
S_6 &= \int_0^{2\pi} \frac{\cos^2\theta' d\theta'}{(A_1^2 - B^2\cos\theta')^{\frac{1}{2}}} \\
&= \frac{4}{C_1}(\frac{1}{3D_1^4}(4(D_1^2 - 2)E(D_1) + (3D_1^4 - 8D_1^2 + 8)K(D_1))) \\
S_7 &= \int_0^{2\pi} \frac{\cos^3\theta' d\theta'}{(A_1^2 - B^2\cos\theta')^{\frac{3}{2}}} \\
&= -\frac{4}{C_1^3}\left(\frac{4(9D_1^6 - 41D_1^4 + 64D_1^2 - 32)K(D_1) - 2(3D_1^6 - 38D_1^4 + 96D_1^2 - 64)E(D_1)}{6D_1^6(D_1^2 - 1)}\right) \\
S_8 &= \int_0^{2\pi} \frac{\cos^4\theta' d\theta'}{(A_1^2 - B^2\cos\theta')^{\frac{3}{2}}} \\
&= \frac{4}{C_1^3}\left(\frac{-2(5D_1^4 - 16D_1^2 + 16)((D_1^4 - 16D_1^2 + 16)E(D_1) - 8(D_1^4 - 3D_1^2 + 2)K(D_1))}{10D_1^8(D_1^2 - 1)}\right)
\end{aligned}
\tag{4.59}
$$

The first four integrals above are taken directly from Lee and Leal [98] and the rest are evaluated using the following generic transformation:

$$
\int_0^{2\pi} \frac{\cos^a\theta' d\theta'}{(A_1^2 - B^2\cos\theta')^{\frac{m}{2}}} = \frac{(-1)^a 4}{C_1^m}\int_0^{\pi/2} \frac{\cos^a 2\theta' d\theta'}{(1 - D_1^2\sin^2\theta')^{\frac{m}{2}}} \tag{4.60}
$$

The integral on the right hand side is then evaluated using Mathematica Integrator to give the results in (4.59). Here $A_1 = (\rho^2+\rho'^2+(y-y')^2)^{\frac{1}{2}}$, $B = (2\rho\rho')^{\frac{1}{2}}$, $C_1 = (A_1^2 + B^2)^{\frac{1}{2}}$ and $D_1 = \left(\frac{2B^2}{A_1^2+B^2}\right)^{\frac{1}{2}}$. K and E are complete elliptic integrals given by:

$$K = \int_0^{\frac{\pi}{2}} \frac{d\theta'}{(1 - D_1^2 \sin^2\theta')^{\frac{1}{2}}}$$
$$E = \int_0^{\frac{\pi}{2}} (1 - D_1^2 \sin^2\theta')^{\frac{1}{2}} d\theta' \tag{4.61}$$

In the limit $D_1 \to 1$, all the formulas in (4.59) become singular. This condition arises when ρ' approaches ρ and corresponds to calculating the velocity disturbance field very close to a ring of forces. This leads to a weak logarithmic singularity which is integrable. To handle this singularity in the simulations, the integration is performed analytically when $D_1 \to 1$ using the following asymptotic expansions of the elliptic functions [98]:

$$\begin{aligned} K(D_1) &= \ln\frac{4}{D_1'} + \frac{1}{2}\left(\ln\frac{4}{D_1'} - 1\right)D_1'^2 + \frac{9}{64}\left(\ln\frac{4}{D_1'} - \frac{7}{6}\right)D_1'^4 \\ E(D_1) &= 1 + \frac{1}{2}\left(\ln\frac{4}{D_1'} - \frac{1}{2}\right)D_1'^2 + \frac{3}{16}\left(\ln\frac{4}{D_1'} - \frac{13}{12}\right)D_1'^4 \end{aligned} \tag{4.62}$$

where $D_1' = (1 - D_1)^{\frac{1}{2}}$. The analytical integration is used when $D_1' \leq 10^{-6}$. For larger D_1' a numerical integration is performed using complete elliptic integrals.

All the integrals from $I_1' - I_{13}'$ are evaluated in a manner similar to the integrals $I_1 - I_{13}$ except A_1 is replaced by $A_2 = (\rho^2+\rho'^2+(y+y')^2)^{\frac{1}{2}}$, C_1 by $C_2 = (A_2^2+B^2)^{\frac{1}{2}}$, and D_1 by $D_2 = \left(\frac{2B^2}{A_2^2+B^2}\right)^{\frac{1}{2}}$. The integrals $I_1' - I_{13}'$ are not expected to have a singularity because even when $\rho' \to \rho$ the distance between the two points is proportional to the thickness, $2y$.

CHAPTER 5

COLLISION EFFICIENCY OF RED BLOOD CELL AGGREGATION

Red blood cells make up 35 – 50% by volume of blood and their interactions with the flow and with each other dictate the complex rheological properties of blood. In the presence of macromolecules(proteins, polymers etc.), red blood cells aggregate to form stacked coin like linear structures called rouleaux. The lower energy face to face aggregation here is not governed by the Brownian motion of the monomer unit but instead is dictated by the deformability of the cells. This non-Brownian type shape selective self assembly of red blood cells makes it an interesting system to understand assembly phenomena at the microscale. In this work we use red blood cell assembly as a model system to understand kinetics of aggregation of soft colloidal particles in shear flow. In particular, we determine the dependence of the collision efficiency of aggregation on the average shear rate in the flow.

5.1 Introduction

Aggregation of red blood cells (rbcs) is an important physiological phenomenon due to its effect on the viscosity of blood [30]. Red blood cell aggregation is unique in the sense that rbcs form well defined linear stack coin like structures (Figure 1) upon aggregation when rigid particle systems with size of the range of rbcs form flocs. The thermodynamically driven structures formed during rbc aggregation are not expected for particle size larger than few microns (meso scale) as they are too big to undergo significant Brownian motion which is generally used to search for the minimum energy state in an aggregate. For the

case of rbc aggregation, the high deformability [131] of the cells allow the cells to form minimum energy structures after collisions. Due to the weak Brownian motion of rbcs, the aggregation is thermodynamically irreversible and kinetically limited and thus hydrodynamics is required to drive aggregation of the cells. The objective of this paper is to understand kinetics of assembly of red blood cells in simple shear flow. We do experiments with horse red blood cells at different shear rate to understand the role of hydrodynamics in aggregation. The scaling of rate constant of rbc dimer formation with respect to shear rate is determined for different binding forces. Understanding of aggregation for deformable particle is also relevant in the context of self assembly. At sub-micron scale, Brownian forces could be used to direct the building block towards minimum energy state. As for meso scale particles, in the absence of Brownian forces it is always a challenge to form minimum energy structures. Thus at meso length scale in the absence of Brownian forces, one strategy to self assemble is using softness of the building blocks to direct them toward lower energy states.

Aggregation occurs when two or more particles collide or adhere. Except for a very dense suspension, simultaneous collisions between three or more particles can be assumed to be negligible. Using this assumption of binary particle collision leading to aggregation, kinetics of aggregation can be described using the following rate equation called Smoluchowski equation [146]:

$$\frac{dn_i}{dt} = \frac{1}{2}\sum_{m=1}^{\infty}\sum_{j=k} k_{jm}p_{jm}n_j n_m - \sum_{j=1}^{j=\infty} k_{ij}p_{ij}n_i n_j. \tag{5.1}$$

In the above expression, k_{ij} is the ideal collision frequency of particles of i and j number of monomers. p_{ij} is the collision efficiency of aggregates of size i and j. The overall rate constant of aggregation, K is given by the product of ideal

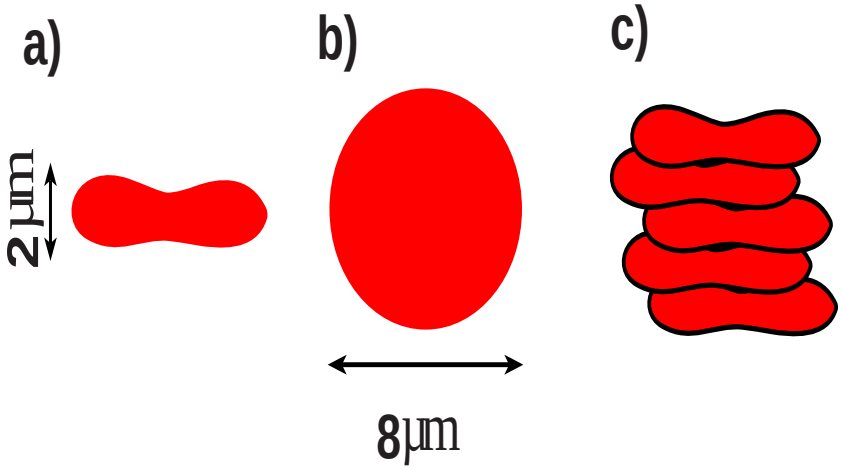

Figure 5.1: a) and b) schematic of a red blood cell and c) red blood cell aggregate in stacked coin like structure called rouleaux

collision rate and collision efficiency.

The ideal collision frequency, k is characteristic of the driving force that brings the particles together and its calculation assumes that there are no hydrodynamic and colloidal interactions. Some common mechanism used to drive aggregation are Brownian motion [118], shear flow [146], or differential settling. For a dilute suspension of spherical particles of radius b, k_{11} calculated by Smoluchowski [146] analytically is given by:

$$k = \frac{32}{3}\gamma b^3 \tag{5.2}$$

For non-spherical particles though rotation motion of the particle also becomes important and affect the collision rate. Singh et al. [128] have recently done simulations to estimate the ideal collision rate of cylindrical shaped particles taking into account the rotational motion of the particles.

Collision efficiency, p is the probability of aggregation of two particles that are predicted to collide when no interactions are considered. It depends on a number of factors like hydrodynamic interactions, surface interactions, local shear stresses trying to pull the aggregate apart etc. Since in most systems more than one of these factors is present and all these factors are dependent on the position of the surface, it makes it complicated to model p and is generally determined experimentally.

For the case of red blood cells, shear flow usually drives the collisions since cells do not undergo strong Brownian motion and differential settling rates ($\sim 1\mu m$) [25] of the cell are also very small. Individual motion of the cell in shear flow could be used to determine the ideal collision frequency of cells [72, 128]. Once the cells are in close proximity, a combination of colloidal, hydrodynamic and surface elastic forces determine whether the cells are going to aggregate or

not. The colloidal forces typically depend on the attractive van der Waal forces and repulsive electrostatic interactions which in turns depend on the charges on the surface of the cells and can be tuned by the ionic strength [70] of the solution. Additional attractive colloidal forces in the case of rbc aggregation originate from the presence of macromolecules in the suspension. For the case of rbc aggregation, the mechanism of the attractive potential generated by the macromolecules is not completely established. Two mechanisms of aggregation have been proposed to explain the aggregation of RBC in polymer solutions viz. cross bridging [71] and depletion interactions [3, 109]. For the purpose of this paper we are going to assume depletion attraction as the origin of the attractive potential but none of the explanation of our results changes if the mechanism was surface binding. In the presence of macromolecules, when the cells come in contact in the absence of fluid flow, if the energy of cell adhesion due to depletion interaction and van der Waal forces is greater than the electrostatic repulsion then adhesion of cells is favored. After initial contact between the cells the contact area between the cells increases leading to face to face aggregates [131] at equilibrium which corresponds to the minimum energy state.

In the presence of the fluid flow, which is the primary mechanism to bring the cells together, the mechanism of aggregation is more complicated. In a typical collision between a pair of cells in simple shear flow, the flow brings the cells together in the compressional quadrant of the flow. The rate at which a pair of cells collide is proportional to the shear rate of the flow (5.2). The cells when they are close together start undergoing adhesion involving increase in the surface area of interaction between the cells, at the same time due to the shear flow the cells are also undergoing rotational motion [72]. Once the cell pair is in extensional component of the flow there is hydrodynamic force try-

ing to pull the cells apart. The schematic of this behavior is shown in figure 2. The dependence of fluid flow on the overall rate constant of aggregation is not straightforward, the ideal collision rate increases linearly with increase in the shear rate but collision efficiency decreases with increase in the shear rate. Increase in the shear rate for the case of deformable particle aggregation not only increases the hydrodynamic forces trying to pull the cells apart in simple shear flow but at the same time increases the rate of rotation of cells when they are in contact, thus giving cells less time to undergo rearrangement to increase the contact area. Such behavior has been observed in the form of viscosity for blood cell sample where at high shear rates, aggregates are rapidly broken and cells are monodisperse. In the absence of shear, red cells collide only rarely, so aggregation proceeds very slowly. Low shear rates induce red cell aggregation, presumably by increasing the collision frequency without inducing sufficient mechanical forces to disaggregate the cells.

Experimental measurement of p_{ij} is complicated due to its dependence on both the size and the shape of the aggregate. The number of unknown p_{ij} in 5.1 is also large when aggregation is unrestricted. In this work, the simplest possible case of aggregation is studied that is in the limit of low concentration of mono dispersed cells colliding to form only dimers. The modified Smoluchowski equation in this limit is reduced to:

$$\frac{dn_1}{dt} = k_{11} p_{11} n_1^2 \tag{5.3}$$

In this limit there are only two unknowns k_{11} and p_{11}, out of which k_{11} can be determined using Singh et al. [128] results. So the only unknown left to be determined is p_{11}, in this work we experimentally determine p_{11} for a range of shear rate and polymer concentration. Understanding of collision efficiency in the limiting case of dimer formation can be considered as the first step towards

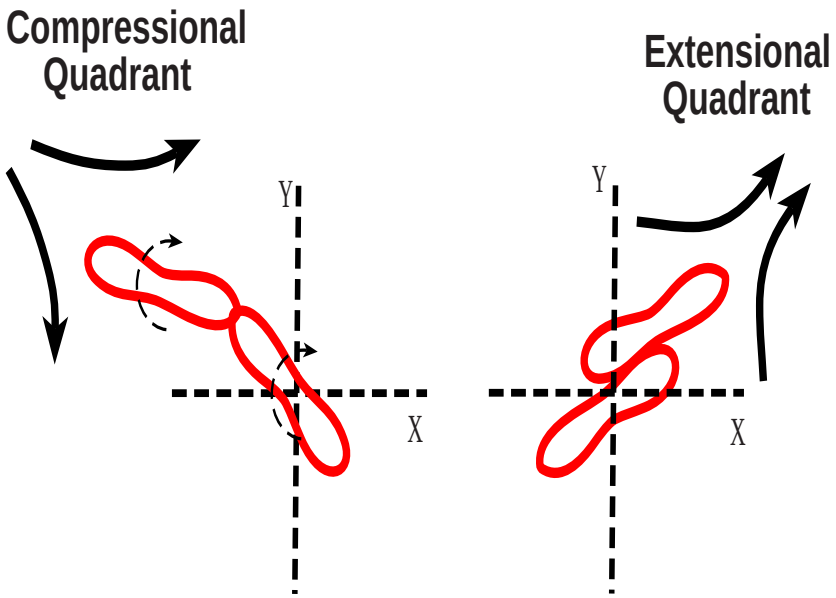

Figure 5.2: Schematic of a pair of red blood cell colliding in the compressional quadrant and then undergoing rotation as well as adhesion and rearrangement until it reaches the extensional quadrant where hydrodynamic and colloidal forces decide whether the aggregate will break or continue to exist.

understanding collision efficiency of deformable particles in shear flow. For the rest of the paper symbol k is used to denote k_{11} and symbol p is used for p_{11}.

5.2 Background

Smoluchowski 's in his analysis assumes that particles travel in straight trajectories along streamlines, i.e., streamlines are not disturbed by the presence of particles. However, due to van der Waals forces, electric double-layer and hydrodynamic interactions, particle trajectories deviate from a straight line as particles approach each other. By calculating the resultant trajectories, the collision efficiency can be calculated for doublet formation resulting from the collision of two primary particles. One of the earliest such calculations of collision efficiency was done by Van de ven and Mason [38, 35]. In this work, the following dependence of p on shear rate for spherical particles was calculated in the limit when only van der waal forces are acting,

$$p = f(\bar{\lambda})(\frac{A}{36\pi\mu\gamma b^3})^{0.18} \tag{5.4}$$

where, A = Hamaker constant, γ = shear rate, μ =viscosity, b =radius of the particle, λ = wavelength of dispersion interactions, and $\bar{\lambda} = \frac{\lambda}{2\pi b}$. Typical values of $f(\bar{\lambda})$ for $\lambda = 100nm$ are 0.79, 0.87, and 0.95 for particle radius of 2, 1, and 0.5 μm respectively.

Recently, Agarwal et al. [1] have studied collision efficiency for shear induced aggregation of spherical glass beads involving polymer bridging forces. The collision efficiency for bridging flocculation is expressed in terms of dimensionless parameters which show the relative magnitudes of electric double-layer repulsion, van der Waals attraction, steric interaction and hydrodynamic forces.

They also obtained a power law dependence of collision efficiency on shear rate. It was found that the power law scaling depends on the concentration of polymer adsorbed on the surface of the glass beads. For the range of polymer concentration studied in their work, the power law scaling for dependence on shear rate, γ was found to lie in between -0.69 to -0.81.

For the case of red blood cell aggregation, the authors are not aware of any experimental collision efficiency calculations. Murata and Secomb [108] have postulated a scaling of -1 for collision efficiency with respect to shear rate for aggregation of rbcs. They proposed that molecular bridges take certain amount of time to form when two rbcs collide and since two rbcs spend a time inversely proportional to the shear rate hence sticking probability should vary as inverse of shear rate. Rearrangement of cells upon collision to increase the surface area of interaction is another event which is time dependent could be the limiting time scale of aggregation. No work has been done so far that verifies the scaling of Murata and Secomb [108] though. In this work we calculate the scaling of collision efficiency with respect to shear rate without investigating whether it is the rearrangement of cells or molecular driving forces which limit the collision efficiency of cells.

Under physiological conditions i.e. high hematocrit conditions, rbc aggregation has been widely studied. Experimentally, Barshtein et al. [5] calculated the overall rate constant of aggregation of rouleaux formation for different hematocrit based on the model proposed by Samsel et al. [127]. The model proposed by Samsel et al. [127] assumes that there are three kind of different collisions that could lead to aggregation - single erythrocyte rouleaux collision, rouleaux-rouleaux collision and rouleaux rouleaux collision leading to forma-

tion of branches. Based on these three type of collisions, they assumed that there are three types of rate constant. They failed to do any collision efficiency calculations and its dependence on shear rate.

5.3 Materials and methods

Sample preparation: Fresh blood samples were drawn from horse blood and heparinized. The blood sample was used for the experiments on the same day. Erythrocytes were washed three times with a PBS solution with 0.5% BSA by weight in it and suspended in the same solution. BSA was added to keep the cells well suspended. Polymer solution was prepared separately in PBS solution with 0.5% BSA solution using *PEG*35000.

Experimental procedure: Erythrocytes and polymer solutions were filled in two separate syringes. The syringe with cell suspension also contained a small magnetic bar which along with a magnetic stirrer was used to avoid the settling of the cells in the syringe. Using a syringe pump, both cell solution and polymer solutions were then pumped in a microchannel through two separate inlets at a constant and equal flow rate. The microchannel itself was placed vertically on an inverted microscope which was flipped by 90 degrees. The vertical arrangement of the channel prevented the cells from settling in the microchannel along the shorter dimensions of the channel. Sedimentation velocities in the direction and opposite to the direction of flow were small compared to axial velocities and hence can be neglected. Sedimentation of cells in the tubing upstream of the microchannel was avoided by using very high input flow rates. In retrospect, the entire problem of sedimentation of rbcs in the buffer solution could have been avoided by preparing a neutrally buoyant suspension of cells as done by Ro-

man et al. [125]. The microchannel used for the experiments itself consisted of a number of components whose purpose is as explained below (Figure 3):

I. Staggered herringbone mixer [135] - A mixer was used in the beginning of the microfluidic channel to mix the polymer solution with the cell solution.

II. Narrow channel - The mixer was followed by a narrow channel which had very high shear rate. This was used as a disaggregator to dissociate cell aggregates formed during mixing.

III. Data collection channel - A rectangular channel of dimensions $500\mu m$ width by $110\mu m$ height was used following the mixer to study kinetics of aggregation. Due to the large width of the channel, gradients in velocity are assumed to be small along the breadth of the channel. All the data collection measurements were made in this part of the microfluidic device.

IV. Shunt- A shunt in parallel with the disaggregator and the data collection channel was used to allow higher flow rates upstream of the channel to avoid sedimentation.

Data collection: Images were taken at a magnification of 20X by stopping the flow using a valve. Images were taken at two separate points- one somewhere in the beginning of the data collection channel called point I and second image at some distance down the length of the data collection channel called point II.

Data analysis: Manual counting of the cells was done using imageJ to quantify the extent of dimerization. For each image, the number of monomers and dimers were counted. Data was separately collected for both upstream and downstream points. If a aggregate of size m larger than a dimer was observed then it was counted as $m-1$ number of dimers since to form an aggregate of size m, $m-1$ aggregation steps must have taken place. The number of aggregates larger than a dimer were very small ($< 10\%$).

Shear rate calculations: The average shear rate(γ) in a rectangular channel can be calculated based on the flow rate in the channel. Though in this case, it should be noted that due to the presence of the shunt parallel to the data collection microchannel, the flow rate in the channel is not equal to the flow rate set using the syringe pump. In theory the flow rate in the microchannel can be determined based on the ratio of the resistance of the shunt and the series resistance of the disaggregator and the data collection channel but since the resistance of the shunt is small, a very small fluctuation in this resistance can change the flow rate in the microchannel by a large magnitude. Hence to accurately measure the average shear rate in the data collection channel, before each data collection step, the speed (v_{max}) of the fastest moving cell in the channel was measured. The speed of the fastest flowing cell was determined by focusing the microscope at different heights in the data collection channel without disturbing the flow. The speed of the cells was later calculated by measuring the distance cells traveled and the number of frames it took to travel that distance. Data was taken for a number of cells to make sure that multiple number of cells moving at the highest velocity were observed. This measurement is particularly aided by the fact that velocity profile in a rectangular channel is parabolic with maximum velocity at the center of the channel and smaller gradients in that zone. Hence there is comparatively bigger region at the center of the channel where most cells are flowing at or close to the maximum velocity of the channel. Since in Poiseuille flow, velocity at the center is maximum and is equal to half the average velocity in the channel. The average shear rate can then be determined using the following equation:

$$\gamma = \frac{v_{max}}{2h}, \tag{5.5}$$

where h is the height of the channel.

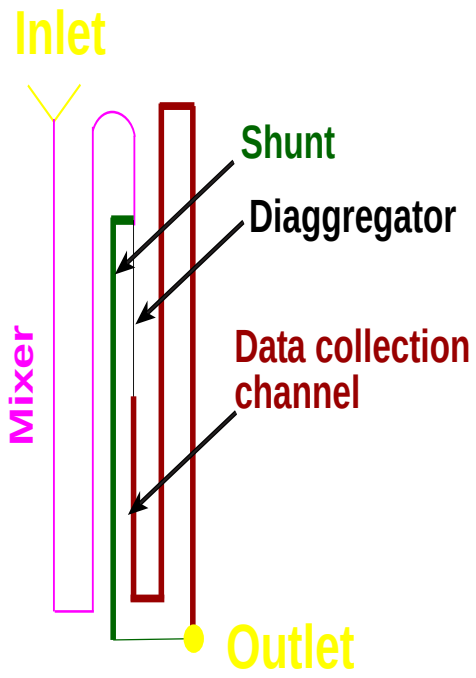

Figure 5.3: Schematic of the microfluidic channel used in the experiments.

5.4 Results and Discussion

In the limit when the concentration of monomers is low and collisions lead to the formation of only dimers, the modified Smoluchowski equation (5.3) can be integrated over the initial time, t_{init} to the final time, t to give:

$$\left(\frac{1}{n_t} - \frac{1}{n_{init}}\right) = k_{11} p_{11} (t_{init} - t) \tag{5.6}$$

where n_{init} is the initial number of monomers per unit volume at time t_{init} and n_t is the number of monomers per unit volume at time t. The above equation gives the extent of aggregation over a time $t - t_{init}$. The time $t - t_{init}$ can be calculated in the experiments based on the distance travelled by the cells and the average velocity of the cells in the channel. Average velocity in the channel is given by $v_{avg} = \frac{v_{max}}{2}$. Average shear rate is given by 5.5. Thus, if the distance between point I and point II is l then time over which aggregation occurs is given by $t - t_{init} = \frac{l}{\gamma h}$. 5.6 is then reduced to:

$$\left(\frac{1}{n_t} - \frac{1}{n_{init}}\right) \frac{\gamma}{k\bar{l}} = p \tag{5.7}$$

Here $\bar{l} = \frac{l}{h}$ is the non-dimensionalized length travelled by the cells from the initial point of observation to the final point of observation. The quantity n_{init} and n_t are calculated from the image analysis of the data at upstream and downstream of the channel. The only unknown in the above equation is p.

Dependence of p on shear rate is then calculated by running experiments with different known shear rates and collecting n_t and n_{init} for known values of $\bar{l}$. Figure 4. presents dependence of collision efficiency on shear rate for experiments done with different polymer concentration. Inspired by the previous work done in this field [38, 1], a power law dependence was assumed between

collision efficiency and shear rate:

$$p = \gamma^x \tag{5.8}$$

where x is the unknown scaling of collision efficiency dependence on shear rate. The value of x for experiments conducted at different polymer concentrations is found to be in the range -1 to -1.7. This dependence is much stronger than the dependence of collision efficiency on shear rate for the case of van der Waal interactions [38] and is stronger than the dependence of collision efficiency on shear rate for the case brdging interactions for hard sphere[1] .

The dependence of the overall rate constant of collision on shear rate is thus given by:

$$K = kp = O(\gamma^1)O(\gamma^{-1\sim-1.7}) = O(\gamma^{0\sim-0.7}) \tag{5.9}$$

The large negative scaling with respect to shear rate seems to concur with Murata and Secomb's [108] postulate about a specific time needed for bridging molecules to start making bonds. At the same time it does not rule out that the time scale associated with the rearrangement of the cells to form face to face aggregate might be important too. According to this hypothesis, after collision of two rbcs, cells may fail to stick together when they are unable to stay in contact for some specific time required for them to rearrange to form face to face aggregates. Since the amount of time cells spend together is of the order $\frac{1}{\gamma}$, hence collision efficiency can vary as inverse of shear rate.

Shifting of the curves with increase in polymer concentration implies that the collision efficiency increases with increase in colloidal forces. This is in accordance with both the bridging and the depletion interaction mechanism as increasing polymer concentration increases the attractive colloidal energy thus

increasing the probability that two cells when in contact will form a dimer. Ideally, one should be able to get exact dependence on colloidal forces from the intercept of the line. However, the data here is not clean enough to make any quantitative statements about that.

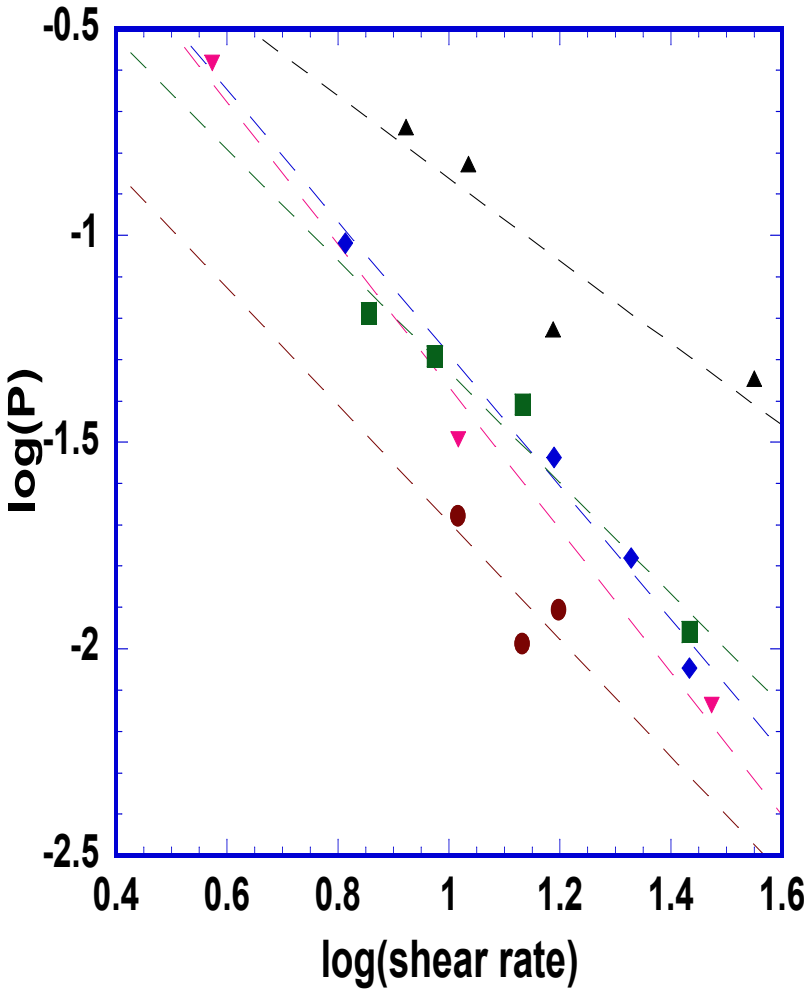

Figure 5.4: Variation of collision efficiency with shear rate at various polymer concentration. (a) PEG conc. = $1.25g/l$ (diamond), equation of the line is y =-1.35x+0.017, (b) PEG conc. = $1.25g/l$ (square), equation of the line is y =-1.42x - 0.28, (c) PEG conc. = $0.75g/l$ (circle), equation of the line is y =-1.60x+0.31, (d) PEG conc. = $1.5g/l$ ($\triangle$), equation of the line is y =-1.346x+0.017198, (e) PEG conc. = $1.25g/l$ ($\triangledown$), equation of the line is y =-1.346x+0.017198.

CHAPTER 6

MIGRATION OF A SOFT PARTICLE ON A CURVED RIGID SURFACE

Deformability of a particle is used to tune its motion on a curved surface. Migration of a vesicle on a curved surface is theoretically studied in the limit of strong adhesion ($\beta >> 1$), where β is the ratio of colloidal energy to bending energy. Interaction energy of the vesicle with the rigid surface is calculated as a function of the colloidal energy, elastic stretching energy, size of the vesicle, and curvature of the rigid surface. It is shown that the energy of the vesicle decreases with increase in the curvature of the rigid surface. This change in energy of the vesicle can be used to move it from low to high curvatures. For small angles of contact and $kR_o << 1$, the leading order migration rate of the vesicle is found to be $O(\frac{K_c R_o \zeta_o}{\nu} \frac{dk}{dx})$ over a surface with finite curvature (k) in one direction and zero in the other, where R_o is the size of the vesicle, K_c is the colloidal energy per unit area, ν is the viscosity of the surrounding fluid, and ζ_o is the colloidal length scale, and dk/dx is the rate of change of curvature over the surface.

6.1 Introduction

Vesicle composed of lipids can bind to surfaces in the presence of attractive colloidal interactions. In biology, adhesion of membranes is essential to a number of processes like red blood cell aggregation, phagocytosis, endocytosis, angiogenesis etc. Studying vesicle adhesion is also important to understand the interaction of soft particles employed in applications like drug delivery. In this work, we investigate the interaction of a vesicle with a rigid curved surface in the limit of strong adhesive forces. At strong adhesion limit, vesicle can undergo stretch-

ing to increase the area available for adhesion. We compare the contribution to energy from the increase in area due to the elastic stretching and from the extra area available for a deflated vesicle. The resulting rate of migration of the vesicle on the curved surface are estimated.

When certain amphiphilic molecules (for instance phospholipids) are introduced in an aqueous environment, they aggregate to form bilayer structures with the polar ends in contact with the aqueous phase and the hydrophobic ends facing each other and shielded from the aqueous phase. In general, these bilayer membranes form closed structures called vesicles to avoid the energy cost associated with the interaction of the hydrophobic ends with the aqueous phase. Most cellular membranes are made of such lipid bilayers with embedded proteins. Due to this vesicles are sometimes used as a model system to understand cell membranes. Vesicle suspensions are also employed in many important applications and products such as fabric softeners, drug delivery, and hair therapeutics. Although the building blocks (lipids) of a vesicle are few nanometers in size, the size of a vesicle can be few hundred micrometer. It is this relatively large size along with their mechanics that make vesicles an interesting system to study in the context of self assembly.

Self-assembly is the autonomous organization of components into patterns or structures without human intervention. A typical self assembly process has two components: 1) a sampling mechanism, which helps in sampling of the entire configuration space of the system and 2) presence of a binding mechanism, which determines the most favorable configuration of assembly. The building blocks for self assembly may comprise atoms, molecules, colloids and macroscopic objects. At sub micron scale strong Brownian forces serves the purpose

of a sampling mechanism and weak non covalent interactions like van der waal, electrostatic forces, hydrogen bonds act as binding mechanism. At meso and macroscale($> 1\mu m$), due to the absence of any natural sampling mechanism, self assembly is much more challenging [147]. Only a very careful control of interactions and external sampling mechanism can lead to self assembly. Directed fluidic assembly has shown some promise in assembly at mesoscale [86] but it requires highly controlled fluidic system to place building blocks at the desired positions. Krishnan et al [85, 87] have used electrostatic energy of charged particles along with device topography to trap particles and arrange them. In the current work, we study an example of non-Brownian type assembly where deformability of the particle is used to direct particles towards lower energy states. We use vesicle as a model system to study soft particle assembly. Here, the deformability of the particle acts as a sampling mechanism and colloidal interactions between the particle and the surface acts as a binding mechanism. The curvature driven assembly could be used to increase interfacial mass transport to valleys (large curvature regions). Valleys are regions in a flow where convective forces are weak and transport is limited. Using the curvature driven migration of a soft particle one can transport material to high curvature regions, not accessible otherwise.

For an isolated vesicle, shape is determined by the minimization of its bending energy along with a constraint on its area and volume. The area of a membrane is typically constant as lipid molecules optimally arrange themselves in a membrane and there is a large energy penalty for a lipid molecule to move out of the membrane and exist freely in an aqueous solution. Also, although the membrane of a vesicle is permeable to water, the volume of the vesicle is typically constant. This arises from the fact that in the presence of any solutes of

large ions, to which the membrane is impermeable, transfer of water can result in building of osmotic pressure. Thus, the volume of the vesicle is controlled by the osmotic pressure difference between the solution inside the vesicle and outside. A difference in osmotic pressure can lead to large changes in vesicle shape, for example, red blood cells bursting in hypertonic solutions.

Binding of two vesicles or a vesicle and a rigid substrate can involve specific and non-specific interactions. Specific adhesion interactions involve certain type of molecules on the two surface which lead to binding of the two surfaces. Nonspecific interactions on the other hand are general and not specific to the molecules on the surface, for instance, depletion interactions and van der Waals. In this work, we focus on non-specific forces acting between a vesicle and a non-deformable surface. The energy and shape of an adhered vesicle, in addition to the bending energy and the volume constraint, also depends on the adhesion energy strength between the two surfaces. Depending on the strength of the adhesion energy, the constant area constraint can be relaxed. When the adhesion energy is high, the membrane can stretch to increase the contact area and increase the attractive colloidal energy between the two surfaces. In this case, the increase in the colloidal energy is balanced by the tension in the membrane that limits the extent of the membrane stretch.

In the next section, we describe the model used to describe the vesicle adhering to a rigid surface. We take into account the colloidal energy, the bending energy, and the area extension energy to describe the energy of the vesicle. Then in section 3, we analytically and numerically calculate the energy and shape of the vesicle, first on a flat surface and then on a curved surface. We then use the energy of the vesicle as a function of curvature to estimate the force acting on

the vesicle due to the change in surface curvature and calculate its migration rate under Stokes condition.

6.2 Model

We consider a vesicle of volume ($V = 4\pi R_o^3/3$) equal to that of a sphere of radius R_o. The area of the isolated vesicle is also fixed and is given by:

$$A_o = 4\pi(1 + \epsilon)R_o^2 \tag{6.1}$$

where ϵ is a non-dimensional parameter that denotes the excess area of the vesicle compared to a sphere of radius, R_o. For $\epsilon = 0$, the isolated vesicle shape is that of a sphere of radius R_o.

The shape of the vesicle in the absence of any external forces (hydrodynamic, colloidal etc) is primarily determined by the bending resistance of the vesicle. In the model presented here, the vesicle is assumed to have a constant volume. In the plane of the bilayer, the vesicles have fluid like properties with very high resistance to elastic extension in area. But in the presence of strong adhesive energy, the membrane can stretch its area to increase its colloidal interaction energy. The area extension modulus of the membrane is assumed to be K_a. The molecular fluctuations of the lipid molecules are ignored here.

The bending energy, E_b of the vesicle is given by [61]:

$$E_b = \frac{K_b}{2}\int((2H + C_o)^2 + K_g\kappa)dS \tag{6.2}$$

where, $2H$ is the mean curvature of an element, C_o is the spontaneous curvature, κ is the gaussian curvature, K_g = bending moduli for change in gaussian curvature, and dS is a differential area.

When the adhesive energy is large, the vesicle can also increase its area of adhesive interaction at the cost of elastic energy. The increase in the energy of the vesicle due to a dA increase in the area is given by:

$$E_a = K_a \frac{dA^2}{A_o} \tag{6.3}$$

A vesicle close to a surface can experience a number of colloidal forces like van der Waals and depletion interactions. We here consider a simple form of the surface energy given by:

$$E_c = \begin{cases} 0 & \text{if } \zeta > \zeta_o; \\ -K_c A_c & \text{if } \zeta < \zeta_o; \end{cases} \tag{6.4}$$

where K_c is the colloidal energy per unit area, ζ_o is the length scale over which the surface colloidal forces are active (typically of the $O(nm)$). We define two non-dimensional parameters here, $\beta = K_c R^2/K_b$ as the ratio of the colloidal and the bending energy and $\alpha = K_c/K_a$ as the ratio of the colloidal energy per unit area and the area extension modulus. In this work we consider the limit when colloidal energy of interaction is much larger than the bending energy. In this limit, the extent of the area which is in contact with the surface is determined by the colloidal energy and the area extension modulus and the unattached part of the vesicle is always spherical in shape as it allows the vesicle to have maximum area of adhesive interactions for a given volume.

The entire problem of a vesicle moving over a curved surface can be divided into two parts: 1) statics of a vesicle adhesion on a flat surface (Figure. 1 (a)) and 2) dynamics of a vesicle moving over a curved surface (Figure. 1(b)). In the first part we solve for the equilibrium shape of a vesicle when its in contact with a flat surface. The solution will determine the energy of the vesicle when

it is in contact with a flat surface as a function of its bending modulus, area extension modulus, and surface colloidal forces. In the second part, energy of the vesicle over a curved surface as a function of curvature of the surface is calculated. Using this energy, the driving force for the migration of vesicle from low curvature to high curvature is estimated. This colloidal driving force is balanced by the drag force acting on the vesicle due to its motion. The drag force can be obtained by solving stokes equation using lubrication approximation in the region close to the surface. This expression of force is then combined with the lubrication problem of a vesicle sliding over a surface to estimate migration velocities.In the analysis we will now deal with the individual parts separately.

6.3 Asymptotic and numerical analysis for large β

6.3.1 Statics of a vesicle binding to a surface

In the limit when the colloidal interaction energy is much larger than the bending energy, i.e. $\beta >> 1$, the influence of the bending energy on the shape of the membrane can be ignored. In this case, the shape of the vesicle far away from the surface is spherical to maximize the area in contact with the surface. A balance between the elastic stretching forces and the colloidal forces determine the area in contact with the surface. The shape of the rim region joining the flat attached part of the surface with the spherical cap is determined by a balance between the adhesive energy and the bending energy. Since $\beta >> 1$, we can ignore the contribution of the rim region to the overall energy of the vesicle

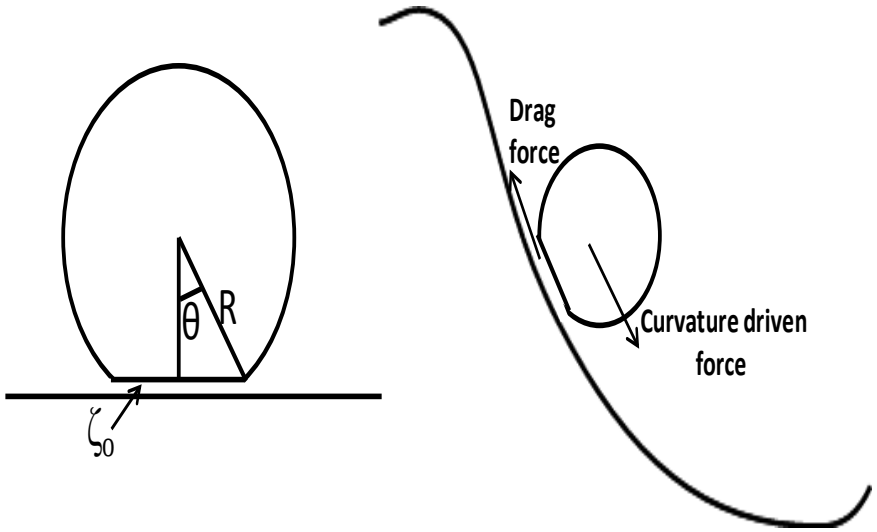

Figure 6.1: (a) Vesicle undergoing attractive colloidal interactions with a flat surface. (b) Vesicle moving on a surface due to its varying curvature.

which to the leading order is $O(\beta^{\frac{1}{2}})$ less than the colloidal energy. The energy of the vesicle adhered to a surface can be described in terms of the contact angle, θ (figure 1). To determine θ, we first determine the energy of the vesicle in the adhered state as a function of θ and then minimize the energy with respect to θ while satisfying the area and the volume constraint.

The volume of the vesicle when adhered to a surface can be written as a sum of the volume of the spherical cap (V_{cap}) and the volume of the cone (V_{cone}) which subtends an angle θ on the flat surface.

$$\begin{aligned} V_{cap} + V_{cone} &= \frac{\pi R^3}{3}(2(1+\cos\theta) + \sin^2\theta\cos\theta) \\ &= \frac{\pi R^3}{3}(1+\cos\theta)^2(2-\cos\theta) \end{aligned} \tag{6.5}$$

Applying the volume constraint and using $V = 4\pi R_o^3/3$ as the original volume of the vesicle, we have

$$\frac{R}{R_o} = \left(\frac{4}{(1+\cos\theta)^2(2-\cos\theta)}\right)^{\frac{1}{3}} \tag{6.6}$$

In the adhered state, the area of the vesicle can be written as a sum of the area of the spherical cap and the area of the surface in contact:

$$\begin{aligned} A_{cap} + A_c &= \pi R^2(2(1+\cos\theta) + \sin^2\theta) \\ &= \pi R^2(1+\cos\theta)(3-\cos\theta) \end{aligned} \tag{6.7}$$

Assuming that the vesicle in contact with the surface has its area stretched by an amount dA. The stretched area is then given by:

$$\begin{aligned} dA &= A_{cap} + A_c - 4\pi R_o^2(1+\epsilon) \\ \frac{dA}{4\pi R_o^2(1+\epsilon)} &= \left[\frac{(1+\cos\theta)(3-\cos\theta)}{4(1+\epsilon)}\left(\frac{R}{R_o}\right)^2 - 1\right] \end{aligned} \tag{6.8}$$

Using 6.6, we have

$$\frac{dA}{4\pi R_o^2(1+\epsilon)} = \left(\frac{3-\cos\theta}{4^{\frac{1}{3}}(1+\epsilon)(1+\cos\theta)^{\frac{1}{3}}(2-\cos\theta)^{\frac{2}{3}}} - 1\right) \tag{6.9}$$

In the limit when the bending modulus of the vesicle is small, the energy of the adhered vesicle has two contributions: from the colloidal energy of interaction with the flat surface and from the elastic stretching energy. The colloidal energy of interaction of the vesicle is given by:

$$\begin{aligned} U_c &= -K_c \pi R^2 \sin^2\theta \\ &= -K_c \pi R_o^2 \frac{4^{\frac{2}{3}}(1-\cos\theta)}{(1+\cos\theta)^{\frac{1}{3}}(2-\cos\theta)^{\frac{2}{3}}} \end{aligned} \tag{6.10}$$

The elastic stretching energy is given by:

$$\begin{aligned} U_a &= K_a \frac{dA^2}{A_o} \\ &= K_a 4\pi R_o^2 (1+\epsilon)\left(\frac{3-\cos\theta}{4^{\frac{1}{3}}(1+\epsilon)(1+\cos\theta)^{\frac{1}{3}}(2-\cos\theta)^{\frac{2}{3}}} - 1\right)^2 \end{aligned} \tag{6.11}$$

The total energy of the vesicle is given by:

$$U = U_a + U_c \tag{6.12}$$

The only unknown in the above equation is θ which can be determined by the minimization of total energy. Using $\frac{dU}{d\theta} = 0$, we get

$$\alpha = 2(1-\cos\theta)\left(\frac{3-\cos\theta}{4^{\frac{1}{3}}(1+\epsilon)(1+\cos\theta)^{\frac{1}{3}}(2-\cos\theta)^{\frac{2}{3}}} - 1\right) \tag{6.13}$$

6.13 is numerically solved to determine θ as a function of α and ϵ. In the limit of small contact angle, θ, the above expression can be simplified to,

$$\alpha = (-1 + 1/(1+\epsilon))\theta^2 + \frac{\epsilon\theta^4}{12(1+\epsilon)} + \frac{(45-2\epsilon)\theta^6}{720(1+\epsilon)} \tag{6.14}$$

In the limit when $\alpha = 0$, the contact angle can be completely determined from the area and the volume constraint. The contact area has no contribution from elastic stretching in this limit. 6.14 can be simplified to give,

$$\theta = 2\epsilon^{\frac{1}{4}} \tag{6.15}$$

In the limit when the excess area $\epsilon = 0$, all the contact area is available due to the elastic stretching of the membrane. The contact angle is given by

$$\theta = (16\alpha)^{\frac{1}{6}} \tag{6.16}$$

In figure 2, the contact angle of the vesicle is shown as a function of ϵ for different values of α. The values of α used are from a typical value of $K_a = 100mJ/m^2$ [124] and a range of colloidal energy, $K_c = 5X10^{-5} - 5X10^{-3}mJ/m^2$. It should be noted here that the contribution to interaction from the elastic stretching is small even for very small values of $\epsilon > 10^{-4} - 10^{-3}$.

One can also re-scale 6.14, using $\theta^* = \frac{\theta}{16\alpha^{\frac{1}{6}}}$ and $\epsilon^* = \frac{\epsilon}{\alpha^{2/3}}$ to obtain a relation between θ^* and ϵ^* independent of α,

$$\theta^{*6} - 16\epsilon^*\theta^{*2} = 16 \tag{6.17}$$

Figure 3 shows the non-dimensionalized θ^* as a function of ϵ^*.

The energy of the adhered vesicle using 6.12 and the numerical solution of 6.13 is shown in figure 4 as a function of ϵ. In the limit when, $\theta \to 0$, the energy of the adhered vesicle is dictated by the colloidal interaction energy to the leading order in θ:

$$\frac{U}{4\pi R_o^2(1+\epsilon)K_a} = -\alpha\frac{\theta^2}{4(1+\epsilon)} \tag{6.18}$$

6.3.2 Dynamics of a vesicle moving over a curved surface

The colloidal energy changes linearly with the area of interaction. We have seen above how the area of interaction (or contact angle) changes with α and ϵ on a

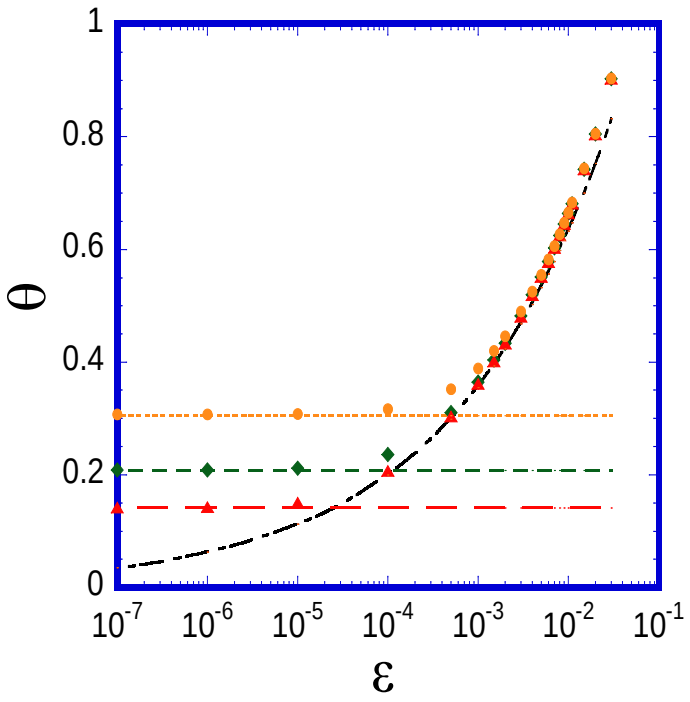

Figure 6.2: Contact angle as a function of ϵ for $\alpha = 1/20000$ (orange), = $1/200000$ (green), and $1/2000000$ (red). The continuous straight lines correspond to the asymptotic limit of $(16\alpha)^{\frac{1}{6}}$ for different values of α and the continuous curve (black) corresponds to $2\epsilon^{\frac{1}{4}}$.

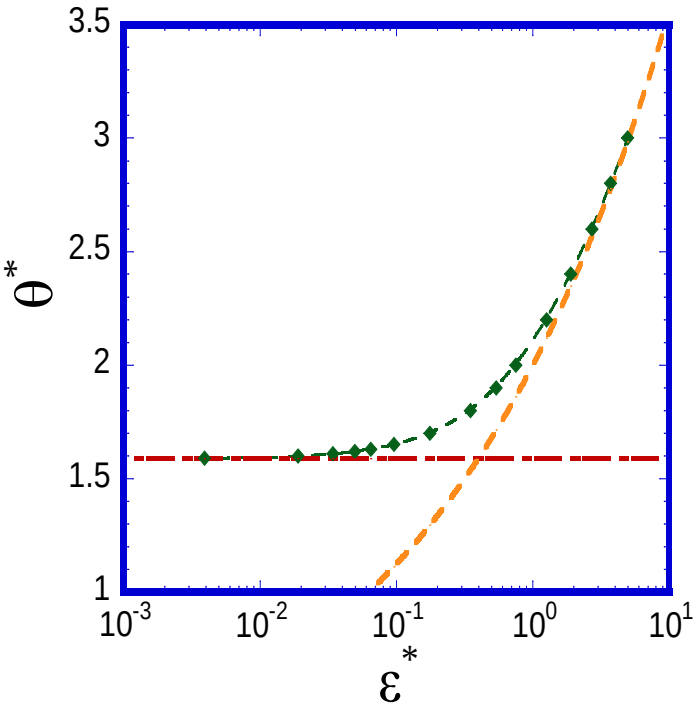

Figure 6.3: Scaled contact angle, θ^* as a function of ϵ^*. Here the continuous curves correspond to the scaled limit of $16^{1/6}$ (red) for $\epsilon = 0$ and $2\epsilon*^{1/4}$ (orange) for $\alpha = 0$.

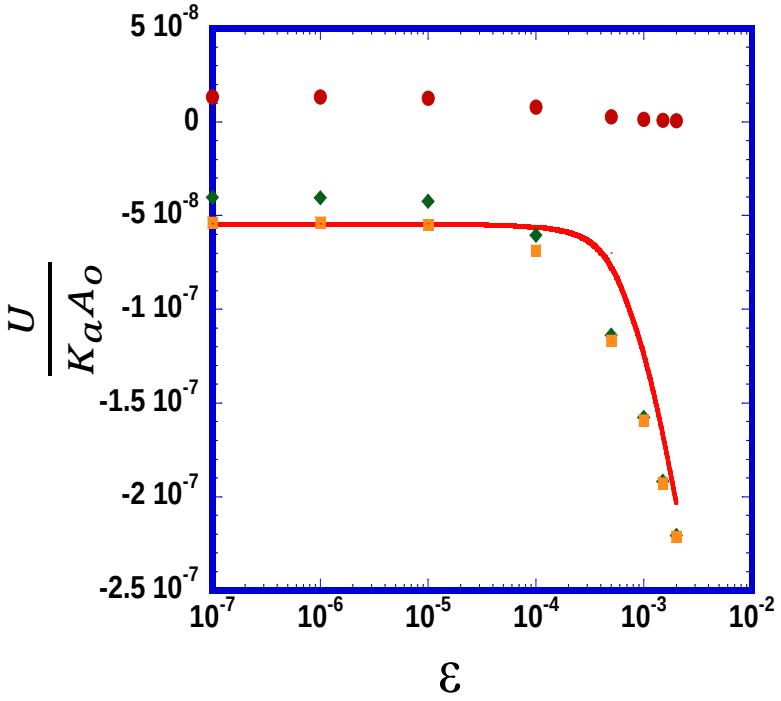

Figure 6.4: Energy (green diamond) of an adhered vesicle for $\alpha = 1/200000$ as a function of ϵ. Colloidal energy (orange square) and the elastic energy (red circle) are also shown here. The continuous curve (orange) corresponds to the colloidal energy of the vesicle in the limit $\theta \to 0$.

flat surface. One can also increase or decrease the area of interaction by changing the curvature of the surface. Compared to a flat surface, when the surface is concave the area of interaction increases and when the surface is convex the area decreases. In this subsection, we will show how the energy of interaction over a curved surface changes for a vesicle for small curvatures. Changing the spatial curvature of the surface can then be used to move the vesicle over it.

Let us place the center of the coordinate axis at the center of the contact area between the vesicle and the rigid surface. One can use a paraboloid to represent any curved surface locally, at the center of the coordinate axis the surface is given by:

$$z = k_1 x^2 + k_2 y^2 \tag{6.19}$$

where $2k_1$ and $2k_2$ are the local curvatures in the x and y directions. We will here do the analysis for the special case of a cylindrical parabola $k = k_1 >> k_2$ which has 0 curvature in one of the directions. Although not all surfaces can be locally described as a cylindrical parabola, the surface can still be used as a model system to show the effect of curvature on the area of interaction compared to a flat surface.

Interaction with a cylindrical parabola for small curvatures

Consider a vesicle placed on a surface which can locally be described as:

$$z = kx^2 \tag{6.20}$$

with $2k$ being the local curvature of the surface. We assume that the curvature of the surface is small, $kR_o << 1$ and remains constant in the contact region. The

part of the vesicle not in contact with the surface will still form a spherical cap to maximize its adhesive area of interaction. The equation of the spherical cap is given by:

$$x^2 + y^2 + (z - z_o)^2 = R^2 \tag{6.21}$$

where z_o is the distance between the center of the spherical cap to the center of the adhesive area (origin).

The curve of intersection of the cylindrical parabola with the spherical cap (6.21) is the curve circumscribing the area of the vesicle interacting with the surface. Using 6.20 and 6.21 to leading order in $O(kR_o)$, it is given by:

$$\frac{x^2}{\frac{R^2 - z_o^2}{1 - 2kz_o}} + \frac{y^2}{R^2 - z_o^2} = 1 \tag{6.22}$$

The above equation is that of an ellipse with major axis, $a = \left(\frac{(R^2 - z_o^2)}{1 - 2kz_o}\right)^{1/2}$ and minor axis, $b = (R^2 - z_o^2)^{\frac{1}{2}}$. The curve of intersection is no longer axisymmetric and hence the contact angle now is a function of the azimuthal angle (ϕ). We use $\theta_c(\phi)$ to denote the contact angle as a function of ϕ and θ for the contact angle in the x direction ($\phi = 0$) . Using 6.22, contact angle at any azimuthal angle, ϕ is given by:

$$\cos\theta_c(\phi) = \left(1 - \frac{a^2 \cos^2\phi + b^2 \sin^2\phi}{R^2}\right)^{\frac{1}{2}} \tag{6.23}$$

The volume of the spherical cap to the leading order in $O(kR_o)$ is now given by,

$$\begin{aligned} V_{cap} &= \frac{R^3}{3} \int_0^{2\pi} (1 + \cos\theta_c(\phi)) d\phi \\ &= \frac{\pi R^3}{3} (2 + 2\cos\theta + kR \sin^2\theta) \end{aligned} \tag{6.24}$$

The volume of the cone is given by,

$$V_{cone} = \frac{\pi a b z_o}{3} \tag{6.25}$$

Applying the volume constraint we get,

$$\begin{aligned} V =& V_{cap} + V_{cone} \\ \frac{R}{R_o} =& \left[\frac{4}{(1+\cos\theta)^2(2-\cos\theta)}\right]^{\frac{1}{3}} \left[\frac{1}{1+\frac{4^{1/3}2kR_o\sin^4\theta}{3(2-\cos\theta)^{4/3}(1+\cos\theta)^{8/3}}}\right] \end{aligned} \tag{6.26}$$

The area of the spherical cap is given by,

$$\begin{aligned} A_{cap} &= R^2\int_0^{2\pi}(1+\cos\theta_c(\phi))d\phi \\ &= \pi R^2(2+2\cos\theta+kR\sin^2\theta) \end{aligned} \tag{6.27}$$

Area of the elliptic base in contact with the curved surface is given by,

$$A_c = \pi ab = \pi R^2\sin^2\theta - k\pi R^3\cos\theta\sin^2\theta \tag{6.28}$$

Applying area conservation, the increase in the area due to the elastic stretching is given by,

$$dA = \pi R^2\sin^2\theta - k\pi R^3\cos\theta\sin^2\theta + \pi R^2(2+2\cos\theta+kR\sin^2\theta) - 4\pi R_o^2(1+\epsilon) \tag{6.29}$$

The energy of the vesicle due to the colloidal energy of interaction and due to elastic stretching is then given by,

$$\frac{U}{A_oK_a} = dA^2 - \frac{\alpha(\sin^2\theta - kR\cos\theta\sin^2\theta)}{4(1+\epsilon)} \tag{6.30}$$

The unknowns in the problem are θ, R, and dA which can be solved using 6.30, 6.29 and 6.26. We numerically solve for the equilibrium contact angle in the x direction, using $\frac{dU}{d\theta} = 0$. Figure 5 shows the change in contact angle in $x-$direction as a function of ϵ for $kR_o = 0.1$. In the limit when θ is small, the contact area and the energy to leading order in θ are given by:

$$A_c = \pi R_o^2(1-kR_o)\theta^2 \tag{6.31}$$

$$\frac{U}{A_oK_a} = -\frac{\alpha(1-kR_o)\theta^2}{4(1+\epsilon)} \tag{6.32}$$

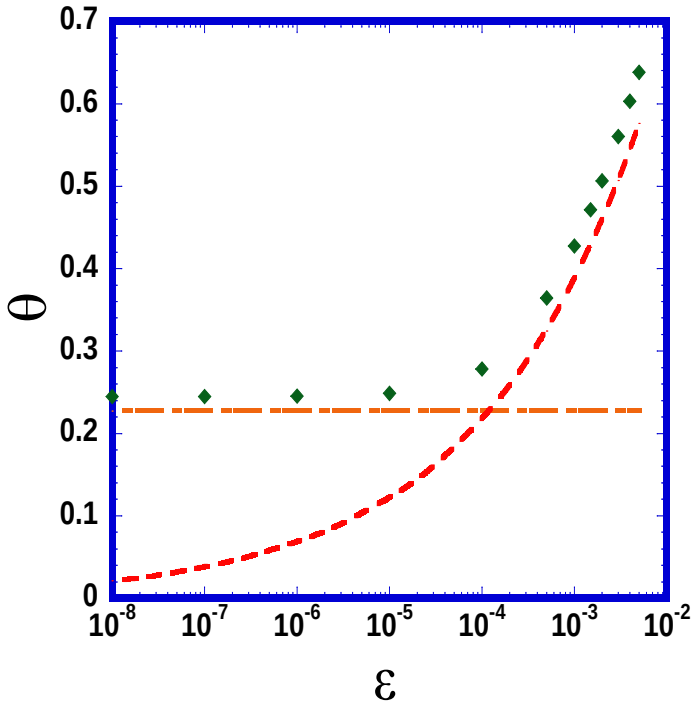

Figure 6.5: Contact angle, θ at $\phi = 0$ as a function of ϵ for $k = 0.1/R$ and $\alpha = 5X10^{-4}/100$. Here the continuous curves correspond to the asymptotic limits of $\epsilon = 0$ (red, —) and $\alpha = 0$ (orange, -.-.).

We analytically estimate the contact angle in the $x-$direction in two limits now: in the limit when θ is small and $\alpha = 0$ which corresponds to the case when the elastic energy of stretching of the membrane is infinitely large compared to the colloidal energy and the interaction of the vesicle is solely determined by the extra area (ϵ) available to the vesicle to undergo adhesion and the limit when $\alpha = 0$ which corresponds to the contact angle being solely determined by the competition between the elastic stretching and the colloidal interaction energy.

$$\theta|_{\alpha=0} = 2\epsilon^{1/4}(1 + \frac{5kR_o}{6}) \tag{6.33}$$

$$\theta|_{\epsilon=0} = (16\alpha)^{1/6}(1 + \frac{17kR_o}{18}) \tag{6.34}$$

In these two limits, the energy of the vesicle to the leading order in θ is given by:

$$U|_{\alpha=0} = -4\pi R_o^2 K_c \epsilon^{1/2}(1 + \frac{2}{3}kR_o) \tag{6.35}$$

$$U|_{\epsilon=0} = -\pi R_o^2 K_a (2\alpha)^{4/3}(1 + \frac{8}{9}kR_o) \tag{6.36}$$

Velocity of migration

As seen in the previous section, the energy of interaction is a function of the local curvature of the rigid surface. Thus, a force can act on the particle if its curvature changes with position. The magnitude of the force (F_x) for a cylindrical parabola is given by,

$$F_x = -\frac{dU}{dx} = -CR_o\frac{dk}{dx} \tag{6.37}$$

where C is a constant for a given R_o, α, and ϵ and independent of k. When $\alpha = 0$ and $\epsilon = 0$, one can analytically determine the constant C. Using 6.36, we have

$$F_x|_{\alpha=0} = \frac{8\pi R_o^2 K_c \epsilon^{1/2}}{3} \frac{R_o dk}{dx}$$
$$F_x|_{\epsilon=0} = \frac{8\pi R_o^2 K_a (2\alpha)^{4/3}}{9} \frac{R_o dk}{dx} \tag{6.38}$$

At steady state the force acting on the vesicle to move it, will be balanced by an equal and opposite viscous drag force. The largest contribution to this drag force will come from the lubrication film between the vesicle and the surface due to its very small thickness (~ nm) (figure 1 (b)). The lubrication drag force is given by

$$F_{drag} = \frac{\nu W}{\zeta_o} A_c \tag{6.39}$$

where W = migration velocity of the vesicle and ν is the viscosity of the ambient fluid. The above drag force expression is obtained by using a no slip boundary condition at the fluid membrane interface which will be violated if the membrane of the vesicle undergoes tank treading. Equating the drag force eq(6.39) with the horizontal force (eq.(6.37), we get

$$W = \frac{C R_o \zeta_o}{\gamma A_c} \frac{dk}{dx} \tag{6.40}$$

In the limiting case of $\epsilon = 0$ and $\alpha = 0$, the migration velocity is given by:

$$W|_{\epsilon=0} = \frac{2 K_c R_o \zeta_o}{3\nu} \frac{dk}{dx} \tag{6.41}$$
$$W_{\alpha=0} = \frac{8 K_c R_o \zeta_o}{9\nu} \frac{dk}{dx} \tag{6.42}$$

It is interesting to note here that the migration velocities are independent of ϵ and K_a, which are essential in determining the interaction area of the vesicle and the rigid surface. This is because the drag force resisting the motion of the vesicle is also proportional to the interaction area and cancels the interaction

area term in the force balance. Substituting $K_c = -5X10^{-4}\frac{J}{m^2}$ ([47]) ,$\zeta_o = 10^{-8}m$, $\nu = 10^{-3}\frac{Js}{m^3}$, $R_o = 100\mu m$ and a change in curvature by a factor of 10 from $kR_o = 0.01$ to $kR_o = 0.1$ over a length scale of $1000\mu m$ in the above expression we get,

$$W \sim 10^{-1}\mu m/s \tag{6.43}$$

6.4 Conclusion

In this work, we have determined the migration rate of a vesicle on a rigid surface with changing curvature. In the strong adhesion limit, the vesicle tries to maximize its area of interaction with the surface. The area available for the adhesion has two components, elastic stretching of the membrane and free available area for a deflated vesicle. It is shown that for typical values of K_c and K_a, the energy contribution even for a very small value of the free available area ($\epsilon \sim 10^{-3}$) dominates over the area available from elastic stretching. On a flat surface, in the limit of small contact angle, the contact area scales as $O(\alpha^{1/3})$ for $\epsilon = 0$ and as $O(\epsilon^{1/2})$ for $\alpha = 0$. It is shown that for a particular system, the area of interaction can be increased by increasing the curvature of the surface leading to lowering of energy. This lowering in energy at higher curvatures can displace the vesicle from low to high curvatures on the surface. The migration velocity is found to be of the $O(\frac{2K_cR_o\zeta_o}{3\nu}\frac{dk}{dx})$ in the limit of small contact angle.

Curvature driven movement of a soft particle can be used to increase interfacial mass transport to valleys (large curvature regions). Valleys are regions in a flow where convective forces are generally weak and hence transport is limited. Vesicles are also frequently used as carriers for drugs. The drug delivery efficiency of a vesicle is dictated by its permeability which in turn can be modified

by the adhesion characteristic of the vesicle to the substrate [12, 11] . The curved surface driven migration studied here shows a change in the adhesion energy of the vesicle as a function of the curvature. A drug delivery vesicle very sensitive to the adhesion can be used to deliver drugs to more specific parts of the body.

CHAPTER 7

CONCLUSIONS

In this thesis, the role of shape and deformability of the particle on its motion are studied. The work leaves out a number of questions unanswered which can be investigated in future research. A general criticism of the thesis is that the problems studied here are idealized and are not completely representative of the real systems. Nevertheless, the author thinks that the results obtained are instructive and should help in understanding realistic systems. Here is a brief summary of the work done and a discussion of some of the outstanding questions.

The ideal collision rate of cylindrical particles presented in chapter 2 extends the work done by Smoluchowski [146] for spherical particles to that of cylindrical particles. Here, the particles are assumed to follow the motion associated with simple shear flow without interacting with one another through hydrodynamic or colloidal interactions. Collision is detected when two particles geometrically overlap in their trajectories. For a more accurate estimation of the collision rate, inter-particle interactions need to be taken into account. The interparticle interactions can significantly alter the trajectories of the particles, thus influencing their collision rate. For instance, for the case of spherical particles, Batchelor and Green [10] have shown that lubrication forces are strong enough to prevent solid body contact in the absence of any colloidal interactions. For the case of fibers, Sundararajakumar and Koch [138] have shown that the lubrication forces are not strong enough to prevent solid body contact between fibers. It remains to be seen how cylindrical particles of finite aspect ratio behave when one accounts for interparticle interactions. A particular case of interest is the col-

lision of low aspect ratio particles. Do two colliding thin disks make solid body contact? Boundary element method simulations can be used to simulate the dynamics of suspensions of disks that interact via hydrodynamic disturbances. These simulations can also determine the effect of particle-particle interactions on the shear-induced structure and the effective shear viscosity of the suspension in the semi-dilute limit. Along similar lines, another problem of interest is the collision behavior of deformable particles like red blood cells. In chapter 6, in the presence of colloidal interactions, the effect of deformability of a particle on its motion on a curved surface is studied. But the work did not consider the pre-collision events which will involve the dynamics of the deformable particle in flow and the subsequent hydrodynamic interactions with another red blood cell or rigid surface. Inclusion of these interactions can set the stage for carrying further investigation of flow involving red blood cells in blood.

In chapter 3, the rotational behavior of a family of shapes is explored. Based on the effective aspect ratio of the particle, the effective viscosity of a dilute suspension of cylindrical thin disk is predicted. The predicted results though do not completely agree with the little experimental results available at dilute concentration. Further experimental work will be useful. The work shows that for cylindrical disks, to the leading order, edge of the particle dictates the rotational behavior and hence the rheological properties. Further experimental work with a well controlled edge geometry will be useful to verify the predictions and explain the discrepancy with the experimental data.

In chapter 4, a class of rigid ring shaped particles has been identified which can align at moderate aspect ratio of $1/30$ in simple shear flow. Its been argued that the aligning behavior of the particle can be useful in imparting anisotropic

properties to a material or a suspension. However, even at the moderate aspect ratio of 1/30, physical manifestation of this class of particles is going to be challenging and was not demonstrated in the work. As a next step, it will be nice to fabricate these particles using techniques like 3d printing or lithography and demonstrate their non-tumbling behavior experimentally. The work also did not attempt to optimize the shape of the particle to further increase the aspect ratio. Optimizing the present ring shape particle will involve finding a two dimensional shape with larger lateral migration velocity than the shape shown here in the presence of simple shear flow. This two dimensional shape can then be rotated to form a ring shape particle which can stop rotating at aspect ratio larger than 1/30. One can use the BEM simulation framework used in the current work to explore other two dimensional shapes by adding higher legendre polynomial modes which can stop tumbling at higher aspect ratio. A more rigorous approach will involve using variational calculus to find the two dimensional shape with maximum lateral migration velocity in simple shear flow. The variational calculus approach has been used in the past by Pironneau [119] to calculate the shape of the particle which will experience minimum drag when moving through a viscous fluid at low Reynolds number. Another aspect of research that needs to be addressed in terms of the practical applications of the aligning behavior of the particles is the effect of hydrodynamic interactions between these non-tumbling particles. The work shows that individual particles can align in simple shear flow but in the presence of other particles its not clear what degree of alignment, the suspension as a whole will achieve. To impart highly anisotropic properties to the suspension, a high degree of alignment of particles is needed.

There are also some open ended questions that the theoretical work on non-tumbling particle leaves unanswered, like: Are ring shaped particles the only particles which could align in simple shear flow? If not, then what is the global optimum shape that maximizes the aspect ratio of the non-tumbling particles? Bretherton [20] showed an asymmetric particle shape which can also stop tumbling. However, a small perturbation out of the equilibrium will cause Bretherton's asymmetric particles to rotate and move away from the equilibrium position. The present work did not explore asymmetric particle shapes which also have the potential to stop tumbling in flow. On a similar theme, another question that one can ask is, what is the shape of the fastest rotating particle? The family of shapes considered in chapter three showed a cylindrical disk to be the fastest rotating particle. But the question about the shape of the fastest rotating particle was not addressed.

In chapter 5, assembly of red blood cells (rbcs) is studied experimentally. Red blood cells are too large ($\sim 8\mu m$) to undergo Brownian motion. In the absence of Brownian motion, rigid particles are expected to form random structures. But rbcs in the presence of attractive colloidal interactions form stacked coin like linear structures called rouleaux. The work presents shear rate dependence of collision efficiency of face-face type assembly of two red blood cells. In disease like, hypertension, malaria and diabetes, the aggregation and disagreggation of RBC play an important role in the pathophysiologic behavior of blood circulation. The work however failed to investigate the dependence of collision efficiency on the bending rigidity of red blood cells, the physical property that primarily distinguishes red blood cell assembly from rigid particle assembly. The work also did not identify rules based on hydrodynamic forces, colloidal forces, and deformability of the particle which lead to aggregation or disaggregation.

Such rules will be useful for understanding both soft particle self-assembly and physiological reasons for red blood cell assembly.

In chapter 6, inspired by the face-face aggregation behavior of red blood cells, effect of deformability of particles on migration over a curved surface is studied. The work shows that one can tune the response of a deformable particle on a surface by tuning the geometry of the rigid surface. The study was though done in a variety of limiting conditions. More comprehensive solutions can be obtained for finite values of parameters using a numerical approach. In future, experimental work showing a soft particle moving over a surface will be useful. To be able to achieve motility for vesicle over long distances, the rigid surface needs to have a continuously changing curvature at length scales of $O(\mu m)$, achieving that is going to be challenging.

BIBLIOGRAPHY

[1] S. Agarwal, R. K. Gupta, and D. Doraiswamy. A model for the collision efficiency of shear- induced agglomeration involving polymer bridging. *Colloids and Surfaces A: Physicochemical and Engineering Aspects*, 345:224–230, 2009.

[2] E. Anczurowski and S. G. Mason. Particle motions in sheared suspension. xxiv. rotations of rigid spheroids and cylinders. *Transactions of the Society of Rheology*, 12:209–215, 1968.

[3] S. Asakura and F. Oosawa. On interaction between two bodies immersed in a solution of macromolecules. *Journal of Chemical Physics*, 22:1255–1256, 1954.

[4] S. Badaire, C Cottin-Bizonne, J. W. Woody, A. Yang, and A. D. Stroock. Shape selectivity in the assembly of lithographically designed colloidal particles. *J. Am. Chem. Soc.*, 2007.

[5] G. Barshtein, D. Wahnblum, and S. Yesgar. Kinetics of linear rouleaux formation studied by visual monitoring of red cell dynamic organization. *Biophysical Journal*, 78:2470–2474, 2000.

[6] G. K. Batchelor. Slender-body theory for particles of arbitrary crosssection in stokes flow. *Journal of Fluid Mechanics*, 44:419–440, 1970.

[7] G. K. Batchelor. The stress system in a suspension of force-free particles. *Journal of Fluid Mechanics*, 41(3):545–570, 1970.

[8] G. K. Batchelor. The stress generated in a non-dilute suspension of elongated particles by pure straining motion. *Journal of Fluid Mechanics*, 46, 1971.

[9] G. K. Batchelor and J. T. Green. The determination of the bulk stress in a suspension of spherical particles to order c^2. *Journal of Fluid Mechanics*, 56(3):401–427, 1972.

[10] G. K. Batchelor and J. T. Green. The hydrodynamic interaction of two small freely-moving spheres in a linear flow field. *Journal of Fluid Mechanics*, 56:375–400, 1972.

[11] A.-L. Bernard, M.-A. Guedeau-Boudeville, L. Jullien, and J.-M. di Meglio. Strong adhesion of giant vesicles on surfaces: Dynamics and permeability. *Langmuir*, 16:6809–6820, 2000.

[12] A.-L. Bernard, M.-A. Guedeau-Boudeville, O. Sandre, S. Palacin, J.-M. di Meglio, and L. Jullien. Permeation through lipid bilayers by adhesion of giant vesicles on decorated surfaces. *Langmuir*, 16:6801–6808, 2000.

[13] D. S. Bhattacharyya. Orientation of mineral lineation along the flow direction in rocks. *Tectonophysics*, 3:559–564, 1966.

[14] W. R. Blakeney. *The viscosity of fiber suspensions*. PhD thesis, Lawrence University, 1965.

[15] J. F. Brady and G. Bossis. Stokesian dynamics. *Annual Review of Fluid Mechanics*, 20:111–157, 1988.

[16] H. Brenner. The stokes resistance of an arbitrary particle. 3. shear fields. *Chemical Engineering Science*, 19:631–651, 1964.

[17] H. Brenner. The stokes resistance of an arbitrary particle ii - an extension. *Chemical Engineering Science*, 19:599–629, 1964.

[18] H. Brenner. Rheology of a dilute suspension of axisymmetric brownian particles. *International Journal of Multiphase Flow*, 1:195–341, 1974.

[19] H. Brenner and R. G. Cox. The resistance to a particle of arbitrary shape in translational shape motion at small reynolds number. *Journal of Fluid Mechanics*, 17(4):561–595, 1963.

[20] F. P. Bretherton. The motion of rigid particles in a shear flow at low reynolds number. *Journal of Fluid Mechanics*, 14:284–304, 1962.

[21] F. P. Bretherton. Slow viscous motion round a cylinder in a simple shear. *Journal of Fluid Mechanics*, 12:591–613, 1962.

[22] C. J. Brinker and G. W. Scherer. *Sol-gel science: The physics and chemistry of sol-gel processing*. Gulf Professional Publishing, 1990.

[23] A. B. D. Brown, S. M. Clarke, P. Convert, and A. R. Rennie. Orientational order in concentrated dispersions of plate-like kaolinite particles under shear. *Journal of rheology*, 44:221–233, 2000.

[24] B. K. Brunk, D. L. Koch, and L. W. Lion. Turbulent coagulation of colloidal particles. *Journal of Fluid Mechanics*, 364:81–113, 1998.

[25] Peter B. Canham, A. W. L. Jay, and Eva Tilsworth. The rate of sedimentation of individual human red blood cells. *Journal of Cell Physiology*, 78:319–332, 1971.

[26] M. Chaouche and D. L. Koch. Rheology of non-brownian rigid fiber suspensions with adhesive contacts. *Journal of Rheology*, 45(2), 2001.

[27] S. B. Chen and D. L. Koch. Isotropic-nematic phase transitions in aqueous

solutions of weakly charged, rodlike polyelectrolytes. *Journal of Chemical Physics*, 104(1):359–374, 1996.

[28] S. B. Chen and D. L. Koch. Rheology of highly aligned nematic liquid crystals. *Journal of non-Newtonian Fluid Mechanics*, 69:273, 1997.

[29] S. Chien. Red-cell deformability and its relevance to blood-flow. *Annual Review of Physiology*, 49:177–192, 1987.

[30] S. Chien, S. Usami, R. J. Dellenba, M. Gregerse, L. B. Nanninga, and M. M. Guest. Blood viscosity - influence of erythrocyte aggregation. *Science*, 157, 1967.

[31] A. T. Chwang. Hydrodynamics of low-reynolds-number flow. part 3. motion of a spheroidal particle in quadratic flows.1975. 72(1): p. 17-34. *Journal of Fluid Mechanics*, 72(1):17–34, 1975.

[32] I. L. Claeys and J. F. Brady. Suspensions of prolate spheroids in stokes flow. 1. dynamics of a finite number of particles in an unbounded fluid. *Journal of Fluid Mechanics*, 251:411–442, 1993.

[33] R. G. Cox. The motion of long slender bodies in a viscous fluid. part 1. general theory. *Journal of Fluid Mechanics*, 44:791, 1970.

[34] R. G. Cox. The motion of long slender bodies in a viscous fluid. part 2. shear flow. *Journal of Fluid Mechanics*, 45(4):625–657, 1971.

[35] A. S. G. Curtis and L. M. Hocking. Collision efficiency of equal spherical particles in a shear flow. the influence of london-van der waals forces. *Transactions of Faraday Society*, 66:1381–1390, 1970.

[36] E. L. Cussler, S. E. Hughes, W. J. Ward, and R. Aris. Barrier membranes. *Journal of Membrane Science*, 38:161–174, 1988.

[37] Vivekanand Dabade. Orientation dynamics of anisotropic particles in viscoelastic fluids. Master's thesis, JNCASR, April 2009.

[38] T. G. M. Van de ven and S. G. Mason. The microrheology of colloidal dispersions vii. orthokinetic doublet formation of spheres. *Colloid and Polymer Science*, 1977:468–479, 225.

[39] J. Deschamps, V. Kantsler, and V. Steinberg. Phase diagram of single vesicle dynamical states in shear flow. *Physical Review Letters*, 102(11), 2009.

[40] M. Djabourov, J. P. Lechaire, and F. Gaill. Structure and rheology of gelatin and collagen gels. *Biorheology*, 30(3-4):191–205, 1993.

[41] D. Edwardes. Steady motion of a viscous liquid in which an ellipsoid is constrained to rotate about a principal axis. *Quarterly Journal of Pure and Applied Mathematics*, 26:70–78, 1893.

[42] D. A. Edwards, J. Hanes, G. Caponetti, J. Hrkach, A. Ben-Jebria, M. L. Eskew, J. Mintzes, D. Deaver, N. Lotan, and R. Langer. Large porous particles for pulmonary drug delivery. *Science*, 276(5320):1868–1872, 1997.

[43] A. Einstein. *Ann. Phys. Leipzig*, 19:289, 1906.

[44] A. Einstein. *Ann. Phys. Leipzig*, 24:591, 1911.

[45] R. Eisenschitz. *Z. Physik. Chem.*, 158, 1932.

[46] Larken E. Euliss, Julie A. DuPont, Stephanie Gratton, and Joseph DeSimone. Imparting size, shape, and composition control of materials for nanomedicine. *Chemical Society Review*, 35:1095–1104, 2006.

[47] E. A. Evans. Detailed mechanics of membrane-membrane adhesion and separation. i. continuum of molecular cross-bridges. *Biophysical Journal*, 48:175–183, 1985.

[48] O. L. Forgacs and S. G. Mason. Particle motions in sheared suspensions ix. spin and deformation of threadlike particles. *Journal of Colloid Science*, 14:457–472, 1959.

[49] M. L. Gardel, J. H. Shin, F. C. MacKintosh, L. Mahadevan, P. Matsudaira, and D. A. Weitz. Elastic behavior of cross-linked and bundled actin networks. *Science*, 304(5675):1301–1305, 2004.

[50] F. J. Gauthier, H. L. Goldsmith, and S. G. Mason. Particle motion in non-newtonian media. *Rheologica Acta*, 10, 1971.

[51] N. C. Gay. The motion of rigid particles embedded in a viscous fluid during pure shear deformation of the fluid. *Tectonophysics*, 5(2):81–88, 1967.

[52] D. Geldart. Types of gas fluidization. *Powder Technology*, 7(5):285–292, 1973.

[53] S. K. Ghosh and H. Ramberg. Reorientation of inclusions by combination of combination of pure and simple shear. *Tectonophysics*, 34:1–70, 1976.

[54] P. J. Gierszewski and C. E. Chaffey. Rotation of an isolated triaxial ellipsoid suspended in slow viscous flow. *Canadian Journal of Physics*, 56(1):6–11, 1978.

[55] T. Gillespie. The effect of aggregation and particle size distribution on the viscosity of newtonian suspensions. *Journal of Colloid and Interface Science*, 94(1), 1983.

[56] H. L. Goldsmith. Poisseuli lecture: From papermaking fibers to human red blood cells. *Biorheology*, 30:165–190, 1993.

[57] H. L. Goldsmith and S. G. Mason. The flow of suspensions through tubes i. single spheres, rods, and discs. *Journal of Colloid Science*, 17:448–476, 1962.

[58] H. L. Goldsmith and S. G Mason. Particle motion in sheared suspensions. 13. the spin and rotation of disks. *Journal of Fluid Mechanics*, 12(1):88–96, 1962.

[59] S. L. Goren and Michael E. O'Neill. Asymmetric creeping motion of an open torus. *Journal of Fluid Mechanics*, 101:97–110, 1980.

[60] O. G. Harlen and D. L. Koch. Orientational drift of a fiber suspended in a dilute polymer solution during oscillatory flow. *Journal of Non Newtonian Fluid Mechanics*, 81:73–91, 1997.

[61] Helfrich. Elastic properties of lipid bilayers- theory and possible experiments. *Zeitschrift fr Naturforschung*, 28 c, 1973.

[62] B. Herzhaft, E. Guazzelli, M. B. Mackaplow, and E. S. G. Shaqfeh. Experimental investigation of the sedimentation of a dilute fiber suspension. *Physical Review Letter*, 77(2):290–293, 1996.

[63] E. J. Hinch and L. G. Leal. Effect of brownian motion on rheological properties of a suspension of non-spherical particles. *Journal of Fluid Mechanics*, 52:683–, 1972.

[64] E. J. Hinch and L. G. Leal. Rotation of small non-axisymmetric particles in a simple shear flow. *Journal of Fluid Mechanics*, 92:591–608, 1979.

[65] B. P. Ho and L. G. Leal. Inertial migration of rigid spheres in two-dimensional unidirectional flows. *Journal of Fluid Mechanics*, 65:365–400, 1974.

[66] B. P. Ho and L. G. Leal. Migration of rigid spheres in a 2-dimensional unidirectional shear-flow of a 2nd-order fluid. *Journal of Fluid Mechanics*, 76:783–799, 1976.

[67] Y. Iso, D. L. Koch, and C. Cohen. Orientation in simple shear flow of semi-dilute fiber suspensions 2. highly elastic fluids. *Journal of Non-Newtonian Fluid Mechanics*, 62:135–153, 1996.

[68] Yoichi Iso, D. L. Koch, and C. Cohen. Orientation in simple shear flow of semi-dilute fiber suspensions 1. weakly elastic fluids. *J. Non-Newtonian Fluid Mechanics*, 62:115–134, 1996.

[69] J. Israelachvili. *Intermolecular and surface forces*. Academic Press, second edition edition, 2002.

[70] K. M. Jan and S. Chien. Influence of the ionic composition of fluid medium on red blood cell. *The Journal of General Physiology*, 61:655–668, 1973.

[71] K. M. Jan and S. Chien. Ultrastructural basis of the mechanism of rouleaux formation. *Microvascular Research*, 5(2):155–166, 1973.

[72] G. B. Jeffery. The motion of ellipsoidal particles immersed in a viscous fluid. *Proc. Roy. SOCA.*, 102(161), 1922.

[73] S. M. Jogun and C. F. Zukoski. Rheology and microstructure of dense suspensions of plate-shaped colloidal particles. *Journal of Rheology*, 43(4):847–871, 1999.

[74] Robert E. Johnson and Theodore Y. Wu. Hydromechanics of low-reynolds-number flow. part 5. motion of a slender torus. *Journal of Fluid Mechanics*, 95:263–277, 1979.

[75] V. Kantsler and V. Steinberg. Orientation and dynamics of a vesicle in tank-treading motion in shear flow. *Physical Review Letter*, 95(25), 2005.

[76] A. Karnis, H. L Goldsmith, and S. G. Mason. The flow of suspensions through tubes.v. inertial effects. *The Canadian Journal of Chemical Engineering*, 44, 1966.

[77] A. Karnis, S. G. Mason, and H. L. Goldsmith. Axial migration of particles in poiseulle flow. *Nature*, 200:159–, 1963.

[78] K. L. Kasperski, C. T. Hepler, and L. G. Hepler. Viscosities of dilute aqueous suspensions of montmorillonite and kaolinite clays. *Canadian Journal of Chemistry*, 64:1919–1924, 1986.

[79] J. S. Ketchel and P. M. Larochelle. Collision detection of cylindrical rigid bodies using line geometry. *Proceedings of IDETC/CIE*, 2005.

[80] S. Kim and P. V. Arunachalam. The general-solution for an ellipsoid in low reynolds number flow. *Journal of Fluid Mechanics*, 178:535–547, 1987.

[81] S. Kim and S. J. Karilla. *Microhydrodynamics*. Dover Publications, 1991.

[82] D. L. Koch and E. S. G. Shaqfeh. The instability of a dispersion of sedimenting spheroids. *Journal of Fluid Mechanics*, 209(521), 1989.

[83] D. L. Koch and G. Subramanian. Collective hydrodynamics of swimming microorganisms: Living fluids. *Annual Review of Fluid Mechanics*, 43:637–659, 2011.

[84] S. H. Koenig. Brownian motion of an ellipsoid - correction to perrin's results. *Biopolymers*, 14(11):2421–2423, 1975.

[85] M. Krishnan, Z. Petrasek, I. Moench, and P. Schwille. Electrostatic self-assembly of charged colloids and macromolecules in a fluidic nanoslit. *Small*, 4:1900–1906, 2008.

[86] M. Krishnan, M. T. Tolley, H. Lipson, and D. Erickson. Directed hierarchical self assembly - active fluid mechanics at the micro and nanoscales. *Proceedings of ASME International Mechanical Engineering Congress and Exposition (IMECE)*, 2007.

[87] Madhavi Krishnan, Nassiredin Mojarad, Philipp Kukura, and Vahid Sandoghdar. Geometry-induced electrostatic trapping of nanometric objects in a fluid. *Nature*, 467:692–696, 2010.

[88] S. K.Veerapaneni, Y.-N. Young, P. M. Vlahovska, and J. Blawzdzeiwicz. Dynamics of a compound vesicle in shear flow. *Physical Review Letters*, 106(15), 2011.

[89] O. A. Ladyzhenskaya. *The mathematical theory of viscous incompressible flow*. Gordon and Breach: New York, 1963.

[90] R. G. Larson. Arrested tumbling in shearing flows of liquid crystal polymers. *Macromolecules*, 23:3383–3392, 1991.

[91] R. G. Larson. *The structure and rheology of complex fluids*. Oxford University Press, 1999.

[92] H. M. Laun. Orientation effects and rheology of short glass fiber-reinforced thermoplastics. *Colloid and Polymer Science*, 262(4):257–269, 1984.

[93] L. G. Leal. On the effect of particle couples on the motion of a dilute suspension of spheroids. *Journal of Fluid Mechanics*, 46(2):395–416, 1971.

[94] L. G. Leal. The slow motion of slender rod-like particles in a second-order fluid. *Journal of Fluid Mechanics*, 69:305–337, 1975.

[95] L. G. Leal. Particle motion in viscous fluid. *Annual Review of Fluid Mechanics*, 12:435–476, 1980.

[96] L. G. Leal. *Advanced transport phenomena*. Cambridge University Press, 2007.

[97] L. G. Leal and E. J. Hinch. The effect of weak brownian rotations on particles in shear flow. *Journal of Fluid Mechanics*, 46(685-703), 1971.

[98] S. H. Lee and L. G. Leal. The motion of a sphere in the presence of a deformable interface. ii. a numerical study of the translation of a sphere normal to an interface. *Journal of Colloid and Interface Science*, 87(1):81–106, 1982.

[99] J. A. lewis. Direct ink writing of 3d functional materials. *Advanced Functional Material*, 16:2193–2204, 2006.

[100] M. J. Lighthill. *An introduction to Fourier analysis and generalised functions*. 1958.

[101] B. Lim, P. A. J. Bascom, and R. S. C. Cobbold. Simulation of red blood cell aggregation in shear flow. *Biorheology*, 34(6):423–441, 1997.

[102] S. B. Lindstrom and T. Uesaka. A numerical investigation of the rheology of sheared fiber suspensions. *Physics of Fluid*, 21, 2009.

[103] R. St. J. Manley and S. G. Mason. Particle motions in sheared suspensions 2. collisions of uniform spheres. *Journal of Colloid Science*, 7:354–369, 1952.

[104] Qingjun Meng and Jonathan J.L. Higdon. Large scale dynamic simulation of plate-like particle suspensions. part i: Non- brownian simulation. *Journel of Rheology*, 52(1):1–36, 2008.

[105] L.J. Michot, I.Bihannic, S.Maddi, S.S.Funari, C.Baravian, P.Levitz, and P.Davidson. Liquid-crystalline aqueous clay suspensions. *Proceedings of the National Academy of Sciences of the United States of America*, 130(44):16101–16104, 2006.

[106] N. A. Mody and M. R. King. Three-dimensional simulations of a platelet-shaped spheroid near a wall in shear flow. *Physics of Fluid*, 17, 2005.

[107] N. A. Mody and M. R. King. Platelet adhesive dynamics. part ii: High shear-induced transient aggregation via gpib alpha-vwf-gpib alpha bridging. *Biophysical Journal*, 95:2556–2574, 2008.

[108] T. Murata and T. W. Secomb. Effects of shear rate on rouleau formation in simple shear flow. *Biorheology*, 25:113–122, 1988.

[109] B. Neu and H. J. Meiselman. Depletion-mediated red blood cell aggregation in polymer solutions,biophysical journal,volume 83,2002,2482-2490. *Biophysical Journal*, 83:2482–2490, 2002.

[110] A. Nir and A. Acrivos. Creeping motion of 2 arbitrary-sized touching spheres in a linear shear field. *Journal of Fluid Mechanics*, 59:209–223, 1973.

[111] A. Okagawa, R. G. Cox, and S. G. Mason. The kinetics of flowing dispersions vi. transient orientation and rheological phenomena of rods and discs in shear flow. *Journals of Colloids and Interface Science*, 45(2), 1973.

[112] A. Okagawa and S. G. Mason. The kinetics of flowing dispersions vii. oscillatory behavior of rods and discs in shear flow. *Journal of Colloid and Interface Science*, 45(2):330–358, 1973.

[113] P. Olla. Simplified model for red cell dynamics in small blood vessels. *Physical review letters*, 82(2):453–456, 1999.

[114] L. Onsager. The effects of shape on the interaction of colloidal particles. *Annals of the New York academy of sciences*, 51(4):627–659, 1949.

[115] W. H. Pell and L. E. Payne. On stokes flow about a torus. *Mathematika*, 7:78–92, 1960.

[116] F. Perrin. The brownian movement of an ellipsoid-the dielectric dispersion of ellipsoidal molecules. *Journal De Physique Et Le Radium*, 5:497–511, 1934.

[117] M. P. Petrich, D. L. Koch, and C. Cohen. An experimental determination of the stress-microstructure relationship in semi-concentrated fiber suspensions. *Journal of Non-Newtonian Fluid Mechanics*, 95:101–133, 2000.

[118] A. P. Philipse and A. M. Wierenga. On the density and structure formation in gels and clusters of colloidal rods and fibers. *Langmuir*, 14:49–54, 1998.

[119] O. Pironneau. On optimum profiles in stokes flow. *Journal of Fluid Mechanics*, 59:117–128, 1973.

[120] P.K.Tillett. Axial and transverse stokes flow past slender axisymmetric bodies. *Journal of Fluid Mechanics*, 44:401, 1970.

[121] C. Pozrikidis. *A practical guide to boundary element methods with the software library BEMLIB*. Chapman and Hall/CRC, 2002.

[122] Salima Rafai, Levan Jibuti, and Philippe Peyla. Effective viscosity of microswimmer suspensions. *Physical Review Letters*, 104, 2010.

[123] M. Rahnama, D. L. Koch, and E. S. G. Shaqfeh. The effect of hydrodynamic interactions on the orientation distribution in a fiber suspension subject to simple shear flow. *Physics of Fluid*, 7(487), 1995.

[124] A. Ramachandran, T. H. Anderson, L. G. Leal, and J. N. Israelachvili. Adhesive interactions between vesicles in the strong adhesion limit. *Langmuir*, 27:59–73, 2010.

[125] S. Roman, S. Lorthois, P. Duru, and F. Risso. Velocimetry of red blood cells in microvessels by the dual-slit method: Effect of velocity gradients. *Microvascular Research*, 84:249–261, 2012.

[126] W. B. Russel. The rheology of suspensions of charged rigid spheres. *Journal of Fluid Mechanics*, 85(2):209–232, 1978.

[127] R. W. Samsel and A. S. Perelson. Kinetics of rouleau formation i. a mass action approach with geometric features. *Biophysical Journal*, 37:493–514, 1982.

[128] V. Singh, D. L. Koch, and A. D. Stroock. Ideal rate of collision of cylindrical particles. *Langmuir*, 27:1813–1823, 2011.

[129] V. Singh, D. L. Koch, and A. D. Stroock. Rigid ring shaped particles that align in simple shear flow. *Journal of Fluid Mechanics*, 722:121–158, 2013.

[130] V. Singh, D. L. Koch, G. Subramanian, and A. D. Stroock. Rotational motion of a thin axisymmetric disk in a low reynolds number linear flow. *Physics of Fluids (in preparation)*, 2012.

[131] R. Skalak, P. R. Zarda, K. M. Jan, and S. Chien. Mechanics of rouleaus formation. *Biophysical Journal*, 35:771–781, 1981.

[132] G. G. Stokes. On the effect of internal friction of fluid in motion. *Cambridge Philisophical Society Transactions*, 9:8–, 1851.

[133] Carl A. Stover and C. Cohen. The motion of rodlike particles in the pressure-driven flow between two flat plates. *Rheologica Acla*, 29:192–203, 1990.

[134] Carl A. Stover, D. L. Koch, and C. Cohen. Observations of fibre orientation in simple shear flow of semi-dilute suspensions. *Journal of Fluid Mechanics*, 238:277–296, 1992.

[135] A. D. Stroock, S. K. W. Dertinger, A. Ajdari, I. Mezic, H. A. Stone, and G. M. Whitesides. Chaotic mixer for microchannels. *Science*, 295(5555):647–651, 2002.

[136] G. Subramanian and D. L. Koch. Inertial effects on fibre motion in simple shear flow. *Journal of Fluid Mechanics*, 535:383–414, 2005.

[137] G. Subramanian and D. L. Koch. Inertial effects on the motion of nearly spherical particles in simple shear flow. *Journal of Fluid Mechanics*, 557:257–296, 2006.

[138] R. R. Sundararajakumar and D. L. Koch. Structure and properties of sheared fiber suspensions with mechanical contacts. *Journal of Non-Newtonian Fluid Mechanics*, 73:205–239, 1997.

[139] C. M. Tchen. Motion of small particles in skew shape suspended in a viscous liquid. *American Institute of Physics*, 25:463–473, 1954.

[140] R. M. Thaokar, H. Schiessel, and I. M. Kulic. Hydrodynamics of a rotating torus. *The European Physical Journal*, 60:325–336, 2007.

[141] E. Tombacz, T. Nyilas, Z. Libor, and C. Csanaki. Surface charge heterogeneity and aggregation of clay lamellae in aqueous suspensions. *Progr. Colloid Polym Sci*, 125:206–215, 2004.

[142] S. Torza, R. G. Cox, and S. G. Mason. Particle motions in sheared suspensions xxvii. transient and steady deformation and burst of liquid drops. *Journal of Colloid and Interface science*, 38(2):396–411, 1972.

[143] B. J. Trevelyan and S. G. Mason. Particle motion in sheared suspensions. i. rotations. *Journal of Colloid Science*, 6:354–367, 1951.

[144] F. M. van der Kooij, A. P. Philipse, and J. K. G. Dhont. Sedimentation and diffusion in suspensions of sterically stabilized colloidal platelets. *Langmuir*, 16:5317–5323, 2000.

[145] P. Vasseur and R. G. Cox. The lateral migration of a spherical particle in two-dimensional shear flows. *Journal of Fluid Mechanics*, 78:385–413, 1976.

[146] M.Z. von Smoluchowski. *Zeitschr. Phys. Chem.*, 92(129-168), 1917.

[147] G. M. Whitesides and M. Boncheva. Beyond molecules: Self-assembly of mesoscopic and macroscopic components. *Proc. Nat. Academy of Sciences*, 99(8):4769–4774, 2002.

[148] D. G. Willis. Kinematic model of preferred orientation. *Geological Society of America Bulletin*, 88(6):883–894, 1977.

[149] H. Yamakawa and J. Yamaei. Application of kirkwood theory of trans-

port in polymer solutions to rigid assemblies of beads. *Journal of Chemical Physics*, 58, 1973.

[150] S. Yamamoto and T. Matsuoka. A method for dynamic simulation of rigid and flexible fibers in a flow field. *Journal of Chemical Physics*, 98(1):644–650, 1993.

[151] G. K. Youngren and A. Acrivos. Stoke flow past a particle of arbitrary shape- numerical-method of solution. *Journal of Fluid Mechanics*, 69:377–403, 1975.